UNIVERSITY OF SOUTHAMPTON

Faculty of Engineering and Physical Sciences
Computational Engineering and Design Research Group

Finite element analysis and material property modelling of thin-strut polymeric bioresorbable scaffolds

by

Ben Warwick Hoddy

MEng

ORCiD: 0000-0002-3918-9977

A thesis for the degree of
Doctor of Philosophy

August 2022

University of Southampton

Abstract

Faculty of Engineering and Physical Sciences
Computational Engineering and Design Research Group

Doctor of Philosophy

Finite element analysis and material property modelling of thin-strut polymeric bioresorbable scaffolds

by Ben Warwick Hoddy

Bioresorbable coronary scaffolds (BRS) offer a potential fourth revolution in interventional cardiology. Despite poor initial results, improvements in pre-processing technologies have facilitated a second generation of thin-strut designs which have shown promise in pre-clinical and early clinical trials. Therefore, the investigation of BRS design via *in-silico* and *in-vitro* methods is critical to maximise their clinical efficacy. After a review of the literature concerning the mechanical performance of coronary stents/scaffolds, the following aims were decided upon to; (i) investigate the equivalent plastic strain (PEEQ) within the struts of BRS and its relationship with scaffold design; (ii) achieve an improved consensus upon which material model(s) may be most appropriate for capturing the mechanical response of thin-strut BRS; and (iii) deploy a BRS into coronary artery geometry and design a novel BRS for use in a challenging clinical scenario.

Firstly, finite element analysis was conducted of the crimping, expansion and radial crushing of 20 scaffold designs comprising variations in ring length and strut width. Surrogate models were developed to explore the effect of the design variables upon the radial strength, post-expansion diameter, percentage recoil and cell area. The PEEQ distribution was observed along paths in critical locations. PEEQ was up to 2.4 times higher in the wide-strut designs and these also exhibited a twisting behaviour at the scaffold end rings. Whilst the post-expansion scaffold diameter was found to be accurately predicted by the *in-silico* tests, the radial strength and percentage recoil predictions were inaccurate, necessitating an improved material model.

A study was then conducted to explore the effect of different isotropic and anisotropic linear-elastic plastic models in predicting BRS mechanical behaviour. Stress-strain data obtained at different displacement rates, the use of isotropic and transversely isotropic elastic theories, the use of isotropic and anisotropic hardening, as well as the implementation of stress relaxation in the plastic regime of the material, were all explored.

A novel anisotropic material model, the Hoddy-Bressloff (HB) model, was developed which achieved prediction of the specific radial strength within 1.1% of the *in-vitro* result and the scaffold's post-expansion diameter within 6.7%. The viscoelastic-plastic Bergstrom-Boyce (BB) model was also investigated and this achieved prediction of the post-expansion diameter and radial strength within 2% of the *in-vitro* result. A multi-step crimping process that utilised holding to facilitate stress relaxation and increased ambient temperature were found to improve prediction of the post-crimping scaffold diameter in *silico*.

The baseline BRS successfully revascularised a diseased arterial model after *in-silico* balloon expansion and exerted both lower maximum and volume averaged stresses on the vessel wall compared to a metallic stent. This investigation highlighted the isotropic limitation of the BB model which resulted in the post-expansion strut configuration being misrepresented and so did not capture certain phenomena predicted by the anisotropic HB material model. Lastly, the novel scaffold for use in the clinically challenging scenario of a left main coronary artery bifurcation was deployed both in *silico* and in *vitro* into a patient specific model. The BRS was found to successfully revascularise the diseased part of the vessel but fracture did occur in the proximal rings and strut twisting was also evident, both of which were predicted by the HB model.

Contents

List of Figures

List of Tables

Declaration of Authorship

I declare that this thesis and the work presented in it is my own and has been generated by me as the result of my own original research.

I confirm that:

1. This work was done wholly or mainly while in candidature for a research degree at this University;
2. Where any part of this thesis has previously been submitted for a degree or any other qualification at this University or any other institution, this has been clearly stated;
3. Where I have consulted the published work of others, this is always clearly attributed;
4. Where I have quoted from the work of others, the source is always given. With the exception of such quotations, this thesis is entirely my own work;
5. I have acknowledged all main sources of help;
6. Where the thesis is based on work done by myself jointly with others, I have made clear exactly what was done by others and what I have contributed myself;
7. Parts of this work have been published as:

   B Hoddy, N Ahmed, K Al-Lamee, N Bullett, N Curzen, and NW Bressloff. Investigating the material modelling of a polymeric bioresorbable scaffold via in-silico and in-vitro testing. *Journal of the Mechanical Behavior of Biomedical Materials*, 120, 2021a

   B Hoddy, N Ahmed, K Al-Lamee, N Bullett, N Curzen, and NW Bressloff. Computational modelling of brs deployment into a patient-specific lm bifurcation. *EuroPCR Abstract Book*, 2021b. URL: https://eposter.europa-organisation.com/2021/europcr/

   B Hoddy, N Ahmed, K Al-Lamee, N Bullett, N Curzen, and NW Bressloff. Investigating the equivalent plastic strain in a variable ring length and strut width thin-strut bioresorbable scaffold. *Cardiovascular Engineering and Technology*, pages 1–16, 2022b. ISSN 1869-4098

B Hoddy, N Ahmed, K Al-Lamee, N Bullett, and NW Bressloff. Exploring a parallel rheological framework to capture the mechanical behaviour of a thin-strut polymeric bioresorbable coronary scaffold. *Journal of the Mechanical Behavior of Biomedical Materials*, 130, 2022a

Signed: Date:

Acknowledgements

Firstly, I would like to thank my supervisor Professor Neil Bressloff for his guidance and support over the past three years. Professor Bressloff's constructive criticism has no doubt greatly improved the research I have been able to undertake and has helped to provide a clear direction when this has been a challenge to discern for myself. I've very much enjoyed working with Professor Bressloff and will also miss discussing (although more often commiserating) the state of English test cricket which, as I come to the end of my PhD, has sunk to an all-time low. In the words of D:Ream, 'things can only get better...'

I would also like to give my thanks to Professor Nick Curzen. Professor Curzen's clinical expertise has significantly strengthened my research in maintaining its clinical relevance and helped me to remember that behind the material models, simulations and analysis lie patients that we hope to ultimately benefit from this research. Professor Curzen's encouragement has always left me feeling re-energised and excited to work in such a fascinating field. I must also thank Dr Kadem Al-lame, Dr Nial Bullett and Dr Naveed Ahmed of Arterius Ltd for the support they have provided to the project, both in terms of the funding of scaffold manufacturing and testing, as well as their time and expertise. I am incredibly grateful to the team at Arterius as without their input much of the research would not have been possible.

To Mum, Dad and my wife, Becky. Mum and Dad, thank you for your love, support and encouragement over the last 28 years, everything I've achieved is thanks to you both. I couldn't have asked anything more of you. Becky, starting a PhD six months before getting married is not a common scenario (for good reason!) and so I will always be grateful for your encouragement, not only to start the PhD but also in supporting me through every step - in the lows of COVID home working to the highs of being offered a job! For everything, Becky, thank you.

And lastly, to God - for His guidance, grace and enduring love.

To Mum, Dad and Becky

Nomenclature

Abbreviations

BMS	Bare Metal Stent
BRS	Bioresorbable Scaffold
BVS	Bioresorbable Vascular Scaffold
CA	Cell Area
CABG	Coronary Artery Bypass Grafting
CAD	Coronary Artery Disease
CD	Post Crimping Diameter
CFD	Computational Fluid Dynamics
CSA	Cross Sectional Area
DES	Drug Eluting Stents
DOF	Degrees of Freedom
EBC	European Bifurcation Club
FD	Final Diameter
FEA	Finite Element Analysis
FEM	Finite Element Method
FS	Foreshortening
HDL	High Density Lipoprotein
LAD	Left Anterior Descending
LCB	Left Circumflex Branch
LDL	Low Density Lipoprotein
MACE	Major Adverse Cardiovascular Events
MD	Maximum Diameter
MI	Myocardial Infarction
MRI	Magnetic Resonance Imaging
NURBS	Non-Uniform Rational Basis Spline
OCT	Optical Coherence Tomography
OD	Outer Diameter
PCI	Percutaneous Coronary Intervention
PEEQ	Equivalent Plastic Strain
PTCA	Percutaneous Transluminal Coronary Angioplasty

PLLA	Poly-L-Lactic Acid
RCA	Right Coronary Artery
RCP	Radial Collapse Pressure
RHS	Right Hand Side
SAR	Stent-to-Artery Ratio
SRS	Specific Radial Strength
ST	Stent Thrombosis
TLF	Target Lesion Failure
UMAT	User Material Subroutine
UTS	Ultimate Tensile Stress
UTSn	Ultimate Tensile Strain
VUMAT	V-User Material Subroutine
WHO	World Health Organisation

Units

atm	atmosphere
GPa	gigaPascal
KPa	kiloPascal
kg	kilogram
μm	micrometer
mm	millimeters
mmHg	millimeters of mercury
MPa	megaPascal
N	Newtons
N/mm^2	Newton per unit square millimeter
Pa	Pascal
s	second

Operators

cos	Cosine
$det[C]$	Determinant of the matrix/tensor C
$dev[C]$	Deviatoric operator on the matrix C
$\mathcal{L}^{-1}$	The inverse Langevin function
$a : b$	Double dot product of a and b
δ	Incremental value in a quantity
$[C]^{-1}$	Inverse of matrix C
$\int_a^b C\, dt$	Integral of C with respect to t, between a and b

$[C]$	Matrix C
$\sum_a^b C$	Sum of C between a and b
$\{C\}$	Vector C
$\|\|C^{(1)} - C^{(2)}\|\|$	Euclidean distance between $C^{(1)}$ and $C^{(2)}$

Latin Symbols

A	Amplitude of Higgs-Henne bump function
a	acceleration (m/s^2)
a_n	Amplitude of the n^{th} ring (mm)
b^*	Distortional left Cauchy-Green tensor
c	Material constant in the Bergstrom-Boyce material model
$[C]$	Damping matrix (kg/s)
C_{width}	Crown width (mm)
$C_{[]0}$	Hyperelastic sixth order polynomial function coefficient
d	Nodal displacements (mm)
$\dot{d}$	Nodal velocities (mm/s)
$\ddot{d}$	Nodal accelerations (mm/s)
E	Young's modulus (MPa)
E_P	Young's modulus in the plane of isotropy (MPa)
E_T	Young's modulus in the transverse direction (MPa)
$\hat{e}$	Elastic deviatoric strain
d_v	Vessel diameter (mm)
F	Deformation gradient tensor
$\hat{F}, \hat{G}, \hat{H}$	Direct stress ratios in Hill's yield function
$\hat{L}, \hat{M}, \hat{N}$	Shear stress ratios in Hill's yield function
F_i	Force magnitude of the i^{th} node (N)
f	Nodal forces (N)
F_{RL}	Ring length factor
F_{SW}	Strut width factor
h	Current isotropic hardening
$[I]$	Identity matrix
$\bar{I}_1$	First deviatoric strain invariant
i	Integer counter
j	Integer counter
J	Determinant of the deformation gradient tensor
$[K]$	Stiffness matrix (N/mm)
l	Scaffold length (mm)
$\bar{L}$	Characteristic length of an element
L_{ring}	Ring length (mm)

L_v	Vessel length (mm)
L_{stss}	Length of stenosis
m	Material constant in the Bergstrom-Boyce material model
$[M]$	Mass matrix (kg)
$[N]$	Shape function matrix
n	Ring number
nn	Direct material direction
nm	Shear material direction
N_{cc}	Total crimping cylinder nodes
p	Pressure (MPa)
$\bar{q}$	Deviatoric Kirchoff stress (MPa)
q	Weighting of terms in Morris-Mitchell criterion
q_0	Material constant in the Bergstrom-Boyce material model
S	Deviatoric Cauchy stress (MPa)
s	Material constant in the Bergstrom-Boyce material model
S_{width}	Strut width (mm)
t	Time
t_b	Base thickness of plaque layer
U	Strain energy density
V	Volume
v	velocity (m/s)
w	Width of Higgs-Henne bump function
$\hat{w}_i$	Coefficient of the i^{th} term in a surrogate model
x_p	Peak location for Higgs-Henne bump function
y	Objective function value for training data supplied to radial basis function
z	Variable basis function parameter

Greek Symbols

α	Weighting factor of acceleration between between two time steps
β	Weighting factor of acceleration between between two time steps
Δ^i	The i^{th} combination of each design variable in polynomial regression model
ϵ_{nn}	Direct strain in direction nn
ϵ_{nm}	Shear strain in direction nm
ϵ_{eng}	Engineering strain
ϵ_{true}	True strain
γ_{nm}	Engineering shear strain
ζ	Distances between points in latin hypercube

η	The number of points separated by each discrete distance in the latin hypercube
κ	Bulk modulus (MPa)
$\bar{\lambda}^*$	Effective chain stretch in the Bergstrom-Boyce material model
λ^{lock}	Maximum chain stretch in the Bergstrom-Boyce material model
λ^{cr}	Principle macroscopic stretch state
λ_i	Principle stretch in direction i
μ	Shear modulus (MPa)
ν	Poisson's ratio
ν_{tp}	Poisson's ratio for the plane of isotropy when displaced in the transverse direction
ν_{pt}	Poisson's ratio for the transverse direction when displaced in the plane of isotropy
ξ	Material constant in the Bergstrom-Boyce material model
ρ	Density (kg/m^3)
σ	Cauchy stress (MPa)
$\bar{\sigma}$	Current yield stress for a given plastic strain (MPa)
σ_A	Cauchy stress in network A of the Bergstrom-Boyce material model (MPa)
σ_B	Cauchy stress in network B of the Bergstrom-Boyce material model (MPa)
σ_{eng}	Engineering stress (MPa)
σ_{true}	True stress (MPa)
σ_{nn}	Direct stress in direction nn (MPa)
$\hat{\sigma}_{nn}$	Direct stress in direction nn for stress ratio in Hill's yield function (MPa)
σ_{VM}	Von Mises stress
σ_0	Reference stress for stress ratio in Hill's yield function (MPa)
τ_{nm}	Shear stress in direction nm (MPa)
$\bar{\tau}_{nm}$	Shear stress in direction nm for stress ratio in Hill's yield function (MPa)
Φ	Morris-Mitchell space filling criterion
Φ	Gramm matrix
ψ	Radial basis function
ω	Phase parameter

Chapter 1

Introduction

1.1 A Revolution in Interventional Cardiology?

The advent of a non-permanent coronary stent yielded much interest amongst cardiologists. Revascularising a stenosed coronary artery using a temporary scaffold offered the possibility of improved long-term outcomes for patients by lowering the risk of late-thrombus formation (blood clotting), reducing the potential complication of repeat interventions and increasing the likelihood of the artery regaining its vasomotion (Ang et al., 2017; Bink et al., 2019). Clinicians and engineers alike aspired to design a device that supports the diseased vessel for as long as necessary before resorbing into the vessel wall once the artery has undergone positive remodelling, a process in which the outer layers of the artery expand to facilitate an increase in lumen area. However, this aspiration was not easily achieved and so began a long story, which remains ongoing, in the quest for an effective bioresorbable scaffold (BRS).

The first drug eluting BRS to be granted widespread regulatory approval was the Abbott Vascular Absorb BVS (bioresorbable vascular scaffold) (PR Newswire, 2011). This proceeded the creation of the Igaki-Tamai biodegradable stent (Tamai et al., 2000) which was investigated in clinical trials but not employed widely in clinical practice. Initially, the Absorb BVS demonstrated acceptable levels of safety and efficacy with high levels of procedural and device success, as well as low rates of major adverse cardiac events (MACE) (Ormiston et al., 2008; Onuma et al., 2010). However, as longer term data became available for the Absorb BVS, it became apparent that it was less effective than its permanent counterparts and could not demonstrate non-inferiority to state-of-the-art drug eluting stents (DES) (Serruys et al., 2016). Indeed, higher rates of adverse clinical events, in particular blood clotting, were reported at greater than one year post intervention and so gradually the appetite for the Absorb BVS waned, culminating in withdrawal of the device from production in September 2017. Thick scaffold struts of over 150 µm, necessitated by the inferior material properties of the polymer scaffold

(low elastic stiffness and yield strength), in comparison to typical metallic DES, in order to attain sufficient radial strength were attributed as the primary cause of high rates of very late thrombosis (Sakamoto et al., 2018).

Whilst sceptics saw the withdrawal of the Abbott Vascular Absorb as the curtailment of a potential revolution in interventional cardiology, others have remained optimistic. Recently, thanks to improvements in polymer pre-processing and scaffold design, a second generation of thin-strut BRS have undergone development and begun pre-clinical and, in some cases, first-in-man trials (Katagiri et al., 2019; Koltowski et al., 2020; Song et al., 2021). Broadly, these have provided encouraging data and once again, like the first generation of designs, demonstrated non-inferiority to leading DES at an early stage.

One such device is the ArterioSorb^{TM} BRS by Arterius Ltd (Leeds, UK). The ArterioSorb^{TM} is a drug-eluting thin-strut (95 µm) polymeric BRS comprising a poly-l-lactic acid (PLLA) backbone. This scaffold has already shown non-inferiority to a modern DES in pre-clinical trials, in which the ArterioSorb^{TM} demonstrated similar acute recoil, luminal dimensions and endothelial shear stress as the Abbott Vascular XIENCE stent (Katagiri et al., 2019). This promising initial data, along with the imminent commencement of first-in-man clinical trials, are important steps in demonstrating the efficacy of the scaffold towards gaining regulatory approval for use in routine clinical practice. Arterius Ltd hold expertise in polymer science and the pre-processing of polymers to improve their mechanical properties. They are able to conduct in-house material testing of polymer specimens along with physical testing of scaffolds to assess their mechanical performance. To date, Arterius Ltd have collaborated with the University of Southampton for expertise in scaffold design, simulation and optimisation and continue to do so in this doctoral research. Utilising accurate stress-strain data for the calibration of material models within finite element analysis (FEA) and the ability to compare the results of FEA with bench-test data are essential if simulations are to accurately explore the mechanical behaviour of BRS and lessen the reliance upon slow and expensive *in-vitro* and *in-vivo* testing (Mincarone et al., 2021).

Therefore, in this thesis, the behaviour of BRS is explored via FEA to understand the relationship between geometry and scaffold performance with particular emphasis given to the development and exploration of material property modelling. Additionally, a greater understanding of the distribution of equivalent plastic strain (PEEQ) was sought, given the inherent reliance of a stent/scaffold upon plastic deformation. To fully utilise the *in-vitro* testing capabilities provided by Arterius Ltd, a new material model was developed along with the detailed exploration of a material model which used the parallel rheological framework in Abaqus/Explicit to seek to improve the prediction accuracy of the mechanical response of BRS. Lastly, this improved understanding was leveraged to investigate scaffolds in clinically realistic scenarios including the

development of a new scaffold design for use in a highly tapered bifurcation which presents a significant and clinically relevant challenge for contemporary BRS.

1.2 Research Aims and Objectives

There are three over-arching aims in this thesis linking material property modelling of PLLA, the relationship between scaffold design, PEEQ and scaffold performance and, third, the development of a BRS that harnesses the insight gained from the analysis of material properties and scaffold performance for a clinically challenging tapered bifurcation scenario.

Material property modelling of poly-l-lactic acid in finite element analysis.

To date, several material property models, with a significant range of complexity, have been used to simulate BRS deployment in FEA. However, no clear consensus has been reached upon which models are most appropriate to obtain an accurate prediction of the scaffold mechanical response, despite the large variety in model complexity and functionality.

Objectives:

- The material property models explored in the review of literature will be systematically compared and explored, with reference to *in-vitro* data, to ascertain if they provide a suitable level of accuracy to capture the mechanical response of next generation thin-strut BRS.
- A new material property model will be developed to provide an improvement in functionality over the existing models in use.

Equivalent plastic strain, scaffold geometry and mechanical performance.

Whilst many engineering applications consider the yielding of a material into its plastic regime to be detrimental, in the case of coronary stents and scaffolds, plastic deformation of the structure is inherently relied upon for the device to retain its dilated diameter. Therefore, the relationship between the equivalent plastic strain (PEEQ), the scaffold geometry and its mechanical response is important in understanding BRS behaviour.

Objectives:

- FEA will be used to observe the distribution of equivalent plastic strain (PEEQ) across critical locations such as the crown apex where high stress levels develop in balloon expansion. The patented ArterioSorb^{TM} design will be utilised to explore

the PEEQ distribution as well as other mechanical metrics that define the scaffold performance in multiple design instances.

- Comparison of *in-silico* and *in-vitro* data will also be made to assess the levels of plastic strain in the scaffold struts and understand other reported structural phenomena that occur in the expansion of BRS.

Scaffold design for a highly tapered bifurcation.

Until now, BRS have generally been considered for use in concentric lesions in straight non-tapered vessels. Indeed, the literature only considers the free expansion of BRS, with one exception (Schiavone et al., 2016). The stenting/scaffolding of tapered bifurcations, particularly those with non-expendable side branches, such as the left-main bifurcation, currently presents a significant challenge for interventionists. Therefore, the deployment of a BRS using FEA in clinically realistic scenarios beyond simple idealised cases is important in assessing their potential efficacy.

Objectives:

- Deployment using *in-silico* balloon expansion into coronary artery geometry will be conducted to assess the mechanical response of a BRS.
- Findings from the aforementioned research aims will be utilised to develop a scaffold design that can be deployed *in-silico* into a highly tapered arterial bifurcation. Ideally, a patient specific geometry will be used.
- To validate the *in-silico* findings an *in-vitro* deployment of the scaffold will also be undertaken into the same arterial geometry. This will help to inform where improvements to the initial design should be made.

1.3 Coronary Artery Disease

In this section, the anatomy of the cardiovascular system and coronary arteries is described before the physiology of and risk factors associated with coronary artery disease (CAD) are discussed. Lastly, the evolution of treatment methods for CAD, with a particular focus upon percutaneous coronary intervention, is presented.

1.3.1 The Cardiovascular System

The heart is a vital organ constructed of two pumps; the left and right chambers, used to circulate blood around the body. These chambers consist of an atrium through which blood flows into the ventricle that provides the main pumping force for blood to be

distributed away from the heart. The mitral and tricuspid valves regulate blood into their respective ventricles whilst the aortic and pulmonary valves regulate blood out of their respective ventricles. Oxygenated blood enters the left atrium via the pulmonary veins from the lungs and then moves into the left ventricle before it flows into the aorta for peripheral circulation. De-oxygenated blood enters the right atrium from the vena cava, into the right ventricle and then is pumped to the lungs to be re-oxygenated via the pulmonary arteries (Hall, 2010). This function is displayed in Figure 1.1.

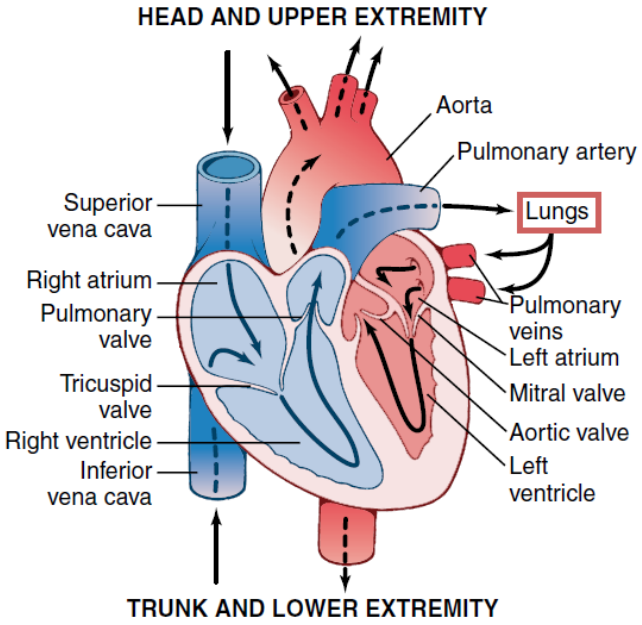

FIGURE 1.1: The anatomy of the heart. Both the left and right chambers are shown along with the major blood vessels. The arrows indicate the direction of blood flow (Hall, 2010).

1.3.2 The Coronary Arteries

In order to carry out the cardiac cycle, the muscles within the heart must themselves be supplied with oxygenated blood via the coronary arteries. These consist of; (i) the left coronary artery, which sub-divides into the left circumflex branch (LCB) and the left anterior descending (LAD) and (ii) the right coronary artery (RCA). These arteries branch off the aorta, above the aortic valve and wrap around the heart muscle. As the arteries reduce in size they begin to penetrate the heart to supply muscle located deeper inside the organ with oxygenated blood. The vast majority of the heart muscle is oxygenated in this way, only a tiny fraction of the muscle can obtain oxygenated blood from the chambers directly. Approximately 5% of the total cardiac output of blood is utilised by the heart itself (Hall, 2010). Figure 1.2 shows the anatomy of the coronary arteries. Increased cardiac activity causes an increase in blood flow through the coronary arteries to supply the extra demand in oxygenated blood. Interestingly, the mechanism by which vessels dilate due to oxygen demand is subject to debate but it is clear that

oxygen demand is a significant factor in coronary blood flow regulation (Hall, 2010). Arteries consist of three layers from the inner most; the intima, to the middle; media and through to the outermost layer; the adventitia, whilst the area through which blood flows, at the centre of the artery, is termed the lumen. The arterial layers are shown in Figure 1.3.

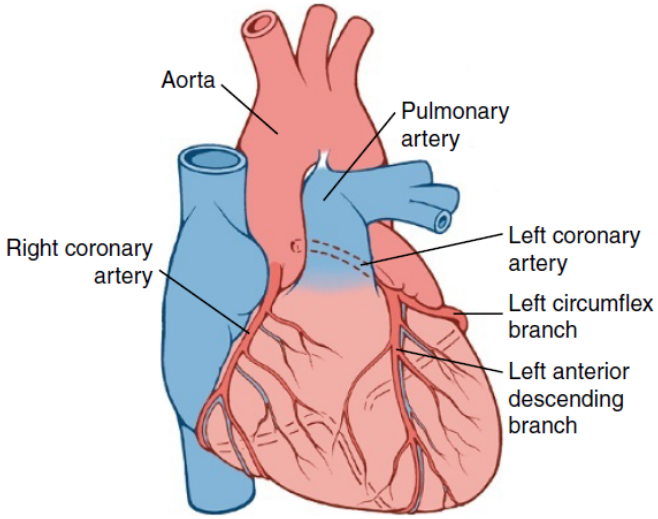

FIGURE 1.2: Anatomy of the left and right coronary arteries that supply the heart muscle with oxygenated blood (Hall, 2010).

1.3.3 Coronary Artery Disease

Global Impact

CAD is the leading cause of death worldwide and over 66,000 people, one third of which are under the age of 75, die annually in the UK due to CAD (British Heart Foundation, 2018). The world health organisation (WHO) estimates that CAD is responsible for seven million deaths a year globally and that 83% of the future increases in deaths due to CAD will occur in developing nations (Barrett et al., 2006). From these statistics alone it is clear that CAD is a significant problem in our global society that is unlikely to subside in the near future.

The Pathophysiology and Effects of CAD

Atheromateous narrowing (atherosclerosis) is the almost exclusive cause of CAD. This narrowing occurs due to the build-up of low density lipoprotein (LDL), commonly known as cholesterol, between the intima and media layers of the coronary artery. This process is initiated by damage to the endothelium (vessel wall) which increases the level of adhesion of macro-molecules, platelets and monocytes, a type of white blood cell. This results in monocytes passing through the endothelium and into the intima layer. As this occurs, the monocytes become macrophages which ingest and oxidize

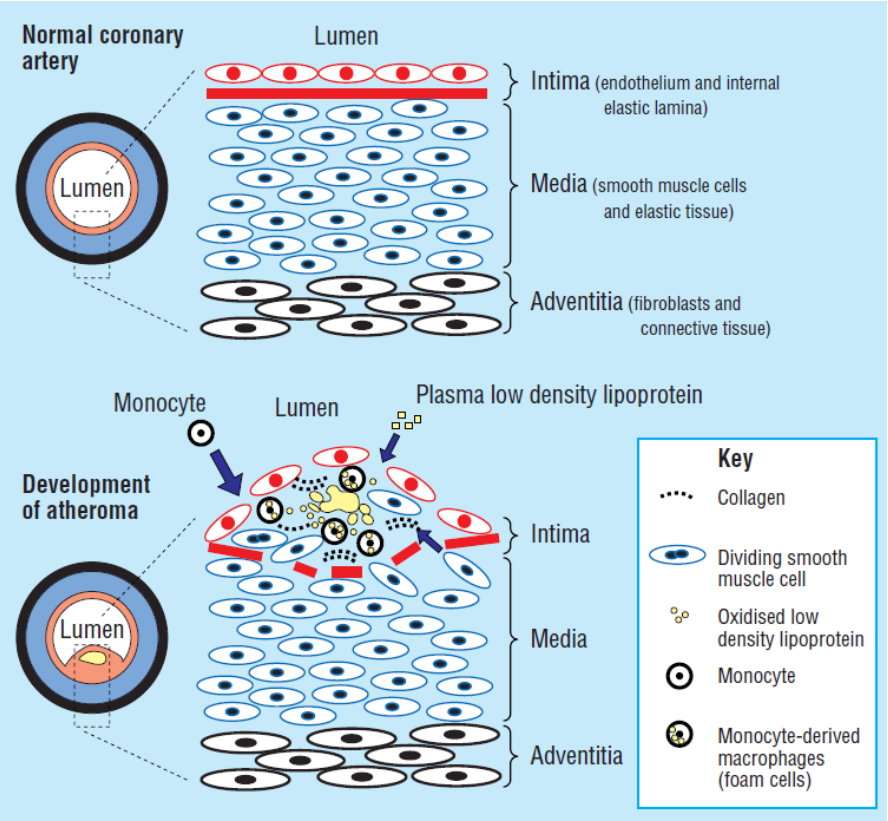

FIGURE 1.3: Comparison of healthy and diseased artery cross sections, showing the three layers, at a cellular level (Grech, 2011). The migration of monocytes into the intima followed by ingestion of LDL to form macrophages with the subsequent proliferation of smooth muscle cells is shown. This leads to the formation of plaque which protrudes into the lumen.

the LDL present in the blood. Once this has taken place, the macrophages are referred to as foam cells and become visible as fatty streaks in the vessel. Following this, the surrounding constituents of the media layer of the artery, the smooth muscle cells and fibrous tissue, greatly increase in number to form an increasingly large plaque. This process, shown in Figure 1.3, can self perpetuate as the foam cells release substances that further increase inflammation and expedite the increase of smooth muscle cells and fibrous tissue. As the plaque grows, the lumen will be reduced, causing a reduction in blood flow rate through the partially occluded vessel. The rough surface of a plaque protruding into the lumen can induce platelets in the blood to adhere to it and develop a thrombus (blood clot) which can completely occlude the vessel and prevent all blood flow. Alternatively, thrombus formation can also be induced via the rupturing of the plaque (Hall, 2010).

Once the atheromateous narrowing has caused >75% reduction in the lumen area, myocardial ischemia, a process by which the heart receives insufficient oxygen is likely to follow. The narrowing of the coronary artery, leading to reduced blood flow, is shown in Figure 1.4.

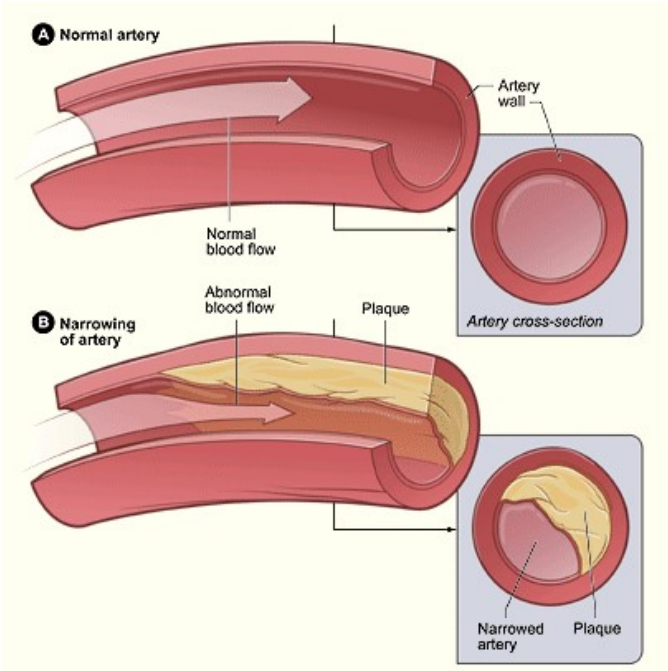

FIGURE 1.4: Comparison of healthy and diseased arteries and the plaque's effect to reduce blood flow due to narrowing of the lumen (Rapetto and Leoncini, 2017).

The reduction in blood flow in the partially occluded vessel can be quantified through Poiseuille's law which gives the resistance to flow in a pipe due to viscous forces of the wall as a function of diameter (Caro et al., 2012). However, it should be noted that Poiseuille's law is valid only for when the flow is steady, fully developed and laminar. Additionally the fluid must be considered in-compressible and Newtonian and such approximations are not always valid for blood flow in the cardiovascular system. This law is illustrated in Figure 1.5 and given by Equation 1.1, whereby, δp gives the change in pressure, μ_v is the viscosity of the blood, L_v is the length of the vessel and d_v is the vessel diameter.

$$\delta p = \frac{8\mu_v L_v}{\pi d_v^4} \tag{1.1}$$

As is evidenced in Equation Figure 1.1, a reduction in vessel diameter of 50% leads to a 16 fold increase in the resistance to flow. However, the downstream resistance of the vascular system could be multiple orders of magnitude higher than the resistance posed by the narrowed vessel in question. Therefore, a stenosis of this size would lead to reduced blood flow along this coronary artery, but not by as great a factor as 16. Regardless, this results in a deficit of oxygenated blood flowing through the vessel with a reduced diameter. The blood will follow the path of least resistance at each coronary bifurcation.

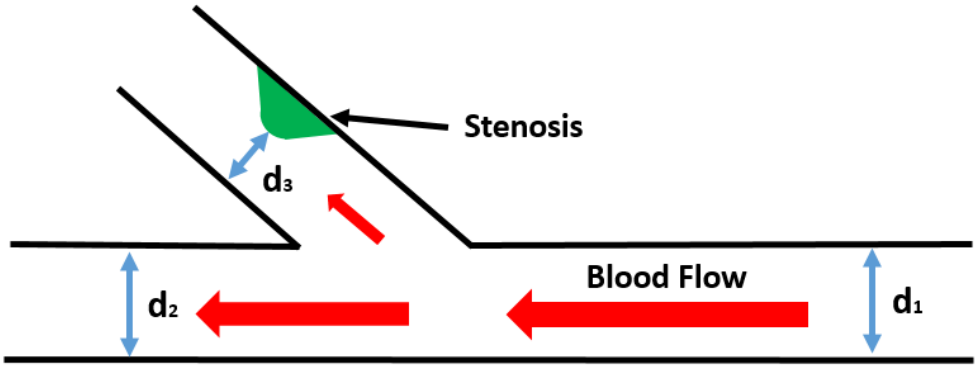

FIGURE 1.5: The blood flow through a coronary artery bifurcation. The reduction in diameter, due to the stenosis (shown in green), results in reduced blood flow rate in the branch of diameter d_3, due to the increase in resistance to flow.

Ischemia will manifest as angina, a condition where the patient experiences pain and a 'tightening' feeling across their chest. More severe coronary events such as a myocardial infarction (MI) or stroke will occur if the vessel becomes completely occluded due to the plaque itself or thrombus formation (Grech, 2011).

Risk Factors of CAD

Unsurprisingly, increased levels of LDLs in the blood will cause an increased risk of CAD. Conversely, a large ratio of high density lipoprotein (HDL) to LDL in the blood is considered to reduce the risk of developing atherosclerosis, although the exact mechanism by which this works is unknown.

Whilst increased levels of LDL in the blood can be induced through a poor diet containing a large amount of saturated fat or a very sedentary lifestyle, leading to obesity, there are also hereditary factors to consider. Familial hypercholesterolemia causes a deficiency in the receptors of LDL resulting in the liver being unable to absorb LDLs. The liver will then produce too many LDLs and release them into the blood as it is unable to discern the feedback from the already excessive amount of LDLs in the blood (Hall, 2010).

A number of other factors also greatly increase the proportion of LDLs in the blood and thus increase the risk of developing atherosclerosis. These are; diabetes, hyperlipidemia (excessive lipid content in the blood) and hypertension. Hypertension (high blood pressure) induces damage to the endothelium which, as previously discussed, will make blood vessels more susceptible to the build up of plaque. Sufferers of hypertension are twice as likely to develop CAD, whilst combining this with diabetes can increase risk by a factor of eight (Grech, 2011).

1.4 Treatment of Coronary Artery Disease

The two over-arching categories of interventional procedure used for coronary revascularisation are coronary artery bypass grafting (CABG) and percutaneous coronary intervention (PCI). CABG uses healthy vessels found elsewhere in the patient's body to provide a bypass route for the diseased coronary arteries. Such an invasive surgical procedure is only employed when the diseased coronary arteries cannot themselves be revascularised. PCI provides a less invasive method of coronary revascularisation when it is deemed that healthy blood flow can be restored within the diseased vessels. Percutaneous is defined as 'made, done or effected through the skin' and it is, in part, this less invasive nature that makes PCI a preferable alternative to CABG when circumstances permit (Grech, 2011). As well as the reduced risk of complications associated with surgery, many patients recovering from PCI can return home the day following the intervention or in some cases the same day.

In current clinical practice, PCI uses either a balloon to conduct percutaneous transluminal coronary angioplasty (PTCA) and/or a coronary stent; a scaffold like structure consisting of interlinked concentric rings to revascularise the diseased artery. The stent is crimped on to a balloon and catheter-guidewire assembly prior to the intervention. This is then inserted directly, often into the femoral or radial artery, up the aorta and round the aortic arch into the coronary arteries to the diseased site. The balloon is inflated to expand the stent, forcing the plaque against the vessel wall thus increasing the lumen area and blood flow through the vessel. The balloon is then deflated and removed with the catheter-guidewire whilst the stent remains in place to support the artery, continuing to squash the plaque against the vessel wall, as shown in Figure 1.8.

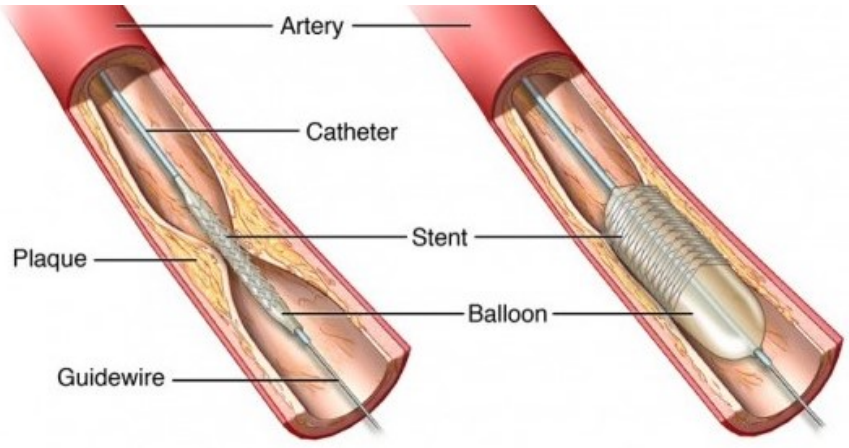

FIGURE 1.6: The stent is crimped onto the balloon on the catheter-guidewire assembly, inserted into the femoral or radial artery of the patient and guided along the network of vessels leading to the plaque. The balloon is then inflated to expand the stent to its target diameter. The balloon is then deflated and removed along with the catheter-guidewire assembly whilst the stent remains in place restoring the vessel patency (Cardiac Institute of the Palm Beaches, 2015).

1.4.1 Transluminal Coronary Angioplasty

Percutaneous transluminal coronary angioplasty (PTCA), first conducted in 1977 by Andreas Guentzig, was the precursor to coronary stenting. The primary difference in this procedure being the absence of a permanent stent that remains in the diseased artery indefinitely. Therefore, the balloon is inflated to dilate the artery to restore normal bloodflow before it is deflated and removed from the patient on the catheter-guidewire. Whilst the quality of surgical equipment initially limited the procedure to only a small proportion of patients (<10%), improvements in catheter and guidewire profiles, as well as balloon inflation pressures, allowed PTCA to become available to a broader range of patients (Grech, 2011). Whilst a significant number of successful PTCA procedures have been undertaken, there are a number of clinical effects that patients can suffer. These are acute vessel closure and restenosis, both of which are defined below (Kahn et al., 1990).

Acute vessel closure: The plaque that has been compressed against the vessel wall collapses back into the lumen, reducing the blood flow to its pre-revascularisation level. This complication is most likely to occur within 24 hours post intervention and is caused by the elastic properties of the plaque and artery. It occurs in 3-5% of patients and necessitates immediate revascularisation (Grech, 2011).

Restenosis: The response to injury in the vessel, in the case of PTCA due to the balloon, that causes a subsequent narrowing of the lumen, thus reducing the blood flow. In contrast to acute vessel closure this process may take many months to fully manifest. Restenosis develops in three stages; elastic recoil, negative remodelling and neointimal hyperplasia. Elastic recoil occurs due to the natural elastic properties of the artery. Negative remodelling is the healing process by which the adventitia contracts towards the centre of the artery. Neointimal hyperplasia is an inflammatory response due to injury at the vessel wall where smooth muscle cells migrate into the intima and proliferate (Grech, 2011). This three stage process causes a reduction in the lumen area, generally defined as a reduction of more than 50% in the lumen diameter (Zhou et al., 2017). Restenosis generally manifests as angina but can, on occasions cause MI depending on the severity of lumen loss (Levine et al., 1995).

1.4.2 Bare Metal Stents

To overcome the possibility of acute vessel closure, bare metal stents (BMS) were developed as a means of maintaining the lumen diameter post balloon angioplasty. BMS are a scaffold structure consisting of a single metal or alloy only. These devices were initially made of 316L stainless steel due to its favourable mechanical properties of a high elastic stiffness and yield strength. However, 316L stainless steel is non-magnetic resonance imaging (MRI) compatible and is not visible under fluroscopy. There are

also concerns around the biocompatability of 316L stainless steel due to the release of nickel. Therefore, alternative grades of stainless steel have been introduced along with a number of alternative metals including cobalt chromium, nitinol and titanium (Mani et al., 2007). BMS were found to reduce restenosis by 50% compared to balloon angioplasty (Ruygrok, 1997). Whilst bare metal stenting has shown improvements in terms of restenosis compared to PTCA, it did initiate the problem of stent thrombosis (ST). This complication occurs due to the presence of a stent in the artery providing a site for thrombus (blood clotting) formation. In the case of BMS, stent thrombosis is infrequent, around 1.5% of patients have suffered from this at three years post intervention. However, many cases of stent thrombosis are fatal as it can lead to MI (Tada et al., 2013).

Stent thrombosis: The formation of a blood clot in the diseased artery due to the presence of a coronary stent. ST can be fatal as it prevents blood flow to the heart muscle via the coronary arteries which can induce a MI. Late ST is considered as a thrombus formation that occurs between 30 days and one year after intervention whilst very late ST occurs in excess of one year post intervention. The three main causes of ST are discussed below (Modi and Bhimji, 2017).

Stent thrombosis is caused by:

- Alteration of haemodynamics, caused by the stent struts. Thicker and wider stent struts will interfere with the haemodynamics to a greater extent and hence increase the likelihood of ST. Under-expanded scaffolds and malapposed struts, as well as small artery diameters and large lesions, will exacerbate the changes in blood flow dynamics. A number of studies consider the alteration of wall shear stress in the vessel as a result of the stent structure and assume this has a clinically detrimental effect on the patient (Wentzel et al., 2003; LaDisa et al., 2003; Dehlaghi et al., 2008; Pant et al., 2011).
- Injury to the vessel wall due to the stent/scaffold or fracture of the stent/scaffold can both provide a site for thrombus formation. Damage to the vessel wall will also be worsened by the antiproliferative drugs used in drug eluting stents (DES) to inhibit restenosis which reduce the inflammatory response to damage of the vessel wall.
- Hypercoagulability, a largely hereditary factor that defines the tendency of blood to coagulate (form a clot) will naturally affect the likelihood of ST.

A number of different terms can be used to describe the design of coronary stents, namely whether they are considered open or closed cell and the location of the connectors. A cell is the area contained between the stent rings and connectors. If connectors are present between adjacent crowns, the curved parts of the stent struts (thus making the cell area as small as possible), then the design is considered closed cell. Open cell

designs give greater conformability to the shape of diseased arteries and aide the delivery procedure as they can match the vessel tortuosity when delivered through the guide catheter. However, open cell designs will not be as strong both longitudinally and radially and are prone to greater recoil (the elastic relaxation of the device after crimping and expansion) (Sakamoto et al., 2018). The location of the connectors can be described as peak to peak, peak to trough or trough to trough, this describes which side of the crown the connectors attach to. Figure 1.7 depicts a typical open cell coronary stent with offset peak to peak connectors.

FIGURE 1.7: The Boston Scientific REBEL BMS, an open cell design with offset peak to peak connectors (Boston Scientific, 2018)

Figure 1.8 shows a diagram of a typical coronary stent with peak to peak connectors with the stent anatomy labelled for reference.

1.4.3 Drug Eluting Stents

Since the introduction of drug eluting stents (DES), occurrences of restenosis post PCI have markedly reduced - less than 5% of interventions now result in this complication (Hamid and Coltart, 2007). Not only is the patient relieved of the potential symptoms of restenosis, but repeat revascularisation which may itself cause further complications is made redundant. DES secrete a drug over a given time period to reduce the severity of restenosis. The device may contain one or more layers of coatings to deliver the drug and tailor its elution profile. These coatings can act as an adhesive primer and a substrate which contains the antiproliferative drug to inhibit the biological process of neointimal hyperplasia, limiting restenosis (Grech, 2011).

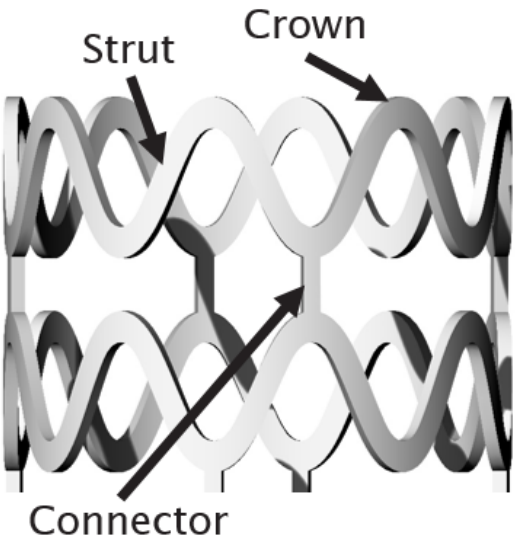

FIGURE 1.8: A labelled diagram of a typical coronary stent, showing a crown, straight strut section and connector labelled.

The first generation of DES employed either sirolimus or paclitaxel as the antiproliferative drug. Sirolimus was initially intended to treat fungal infections but its immunosuppressive properties became apparent and was trialled as a drug for DES which led to the development of the Cypher stent. Paclitaxel was first used in the treatment of ovarian cancer but similarly to Sirolimus was trialled in DES, in this case as part of the TAXUS trials (Halkin and Stone, 2004). Subsequent studies compared the efficacy of these drugs and concluded that the use of sirolimus reduced rates of restenosis and MI, as well as improved target vessel revascularisation when compared to paclitaxel (Simard et al., 2014).

The introduction of DES saw heightened debate surrounding the issue of late and very late ST. Studies assessing the first generation of DES found evidence pointing towards an increase of ST at >30 days to 3 years post intervention compared to BMS. At three years the rate of ST was found to increase from 1.5% (in BMS) to 2.2% (in first generation DES). The increase in late ST was associated with the use of thicker stent struts in DES (due to the polymer coating) as well as the biochemical effect of the polymer coating and antiproliferative drug themselves. This necessitated the development of a second generation of DES to overcome this increase in ST. Second generation DES have improved rates of late ST, reducing the observed incidents of ST at three years to 1% of interventions, lower than that of BMS. Improvements in scaffold design allowing for thinner struts, improved elution kinetics of the antiproliferative drug as well as changes in the biocompatability of the polymer substrate and antiproliferative drug have facilitated this (Tada et al., 2013).

The antiproliferative drugs and their elution profiles utilised in second generation DES were improved compared to first generation devices. The release kinetics of paclitaxel

were improved through use of a different polymer substrate that ensures the majority of the drug is eluted within the first 12 weeks. Zotarolimus, an analogue of sirolimus, uses a new phosphorylcholine polymer substrate that not only provides faster elution of the drug to facilitate normal repair of the artery wall but improved biocompatability compared to equivalent polymer coatings. Everolimus is also a derivative of sirolimus used on second generation DES. Both zotarolimus and everolimus show reduced levels of restenosis and rates of MI when compared to paclitaxel. Some studies did highlight an increase in rates of restenosis in the case of zotarolimus but this was countered by a significant reduction in MI due to late stent thrombosis (Simard et al., 2014). Drugs with improved clinical results appear to utilise a shorter elution duration whereby the antiproliferative drug is delivered within the first few months of stent placement allowing later healing of the arterial wall, thus reducing the likelihood of thrombus formation.

The Promus ELITE by Boston Scientific is shown in Figure 1.9(A). This is an everolimus-eluting platinum chromium coronary stent. The Resolute Onyx by Medtronic, shown in Figure 1.9(B), is a zotarolimus-eluting stent manufactured from a composite material of cobalt alloy and platinum-iridium alloy. These are both second generation DES that are commonly used in routine clinical practice in 2021.

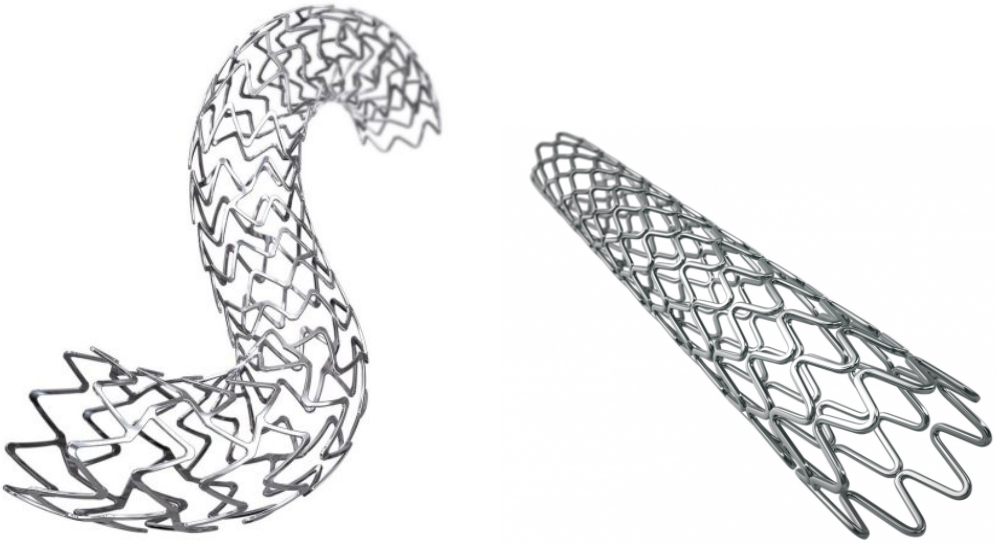

(A) (B)

FIGURE 1.9: (A) The Boston Scientific Promus ELITE DES (Boston Scientific, 2018) and (B) the Resolute Onxy DES by Medtroninc (Diagnostic and Interventional Cardiology, 2017).

1.5 Bioresorbable Scaffolds

1.5.1 Motivation

Whilst DES have reduced the rates of restenosis and ST, the medical community has sought a further improvement in very late ST through the introduction of bioresorbable scaffolds (BRS). These cardiovascular implants are delivered to the stenosis site using the same method as their permanent counterparts; via a balloon catheter. However, after 18 months the scaffold is completely resorbed into the vessel wall resulting in the structure not being present indefinitely in the vessel and so the risk of very late thrombus formation is negated (Simard et al., 2014). This type of implant also provides a benefit if repeat interventions are required as the presence of a device in a coronary artery will likely cause further complications. Recovery of vasomotion, the ability of an artery to contract and dilate, is also thought to be a potential benefit of this type of scaffold (Tan and Ananthakrishna, 2017).

1.5.2 The Evolution of Polymeric and Metallic BRS

Two main categories of bioresorbable scaffolds are currently under development; those manufactured from polymers and those manufactured from metallic alloys.

Polymers, such as the commonly used poly-l-lactic acid (PLLA), provide a biologically inert platform for scaffolds as they breakdown via hydrolysis into water and carbon dioxide in the absorption process (Wiltz, 2013). The primary drawback associated with polymer scaffolds is their inferior mechanical properties when compared with metallic devices, which has necessitated larger thickness and width in the scaffold struts. This is considered to have been the cause of sub-optimal clinical outcomes, most notably in the Abbott Vascular BVS whose production has been discontinued. In general, polymers exhibit an elastic stiffness that is approximately 100 times lower and a tensile strength around 10 times lower than measured in the metallic alloys used to manufacture DES (Sakamoto et al., 2018). Whilst initial data appeared promising for the device (Ormiston et al., 2008), data for clinical outcomes after one year post intervention indicated a higher rate of ST compared to current DES (Serruys et al., 2016; Kereiakes et al., 2016). ST occurring less than one year post intervention and in patients with smaller target vessels was attributed to the thicker strut profiles, whilst later ST was likely caused by exposed struts protruding into the luminal area as the device underwent bioresorption (Sakamoto et al., 2018). The subsequent withdrawal of the Abbott Vascular BVS, shown in Figure 1.10, from production led to significant scepticism concerning the efficacy of bioresorbable vascular scaffolds and their ability to realise any potential clinical benefits. However, more recent data observing a 5 year follow-up of patients in the ABSORB

III trial has shown the risk of target lesion failure (TLF), target vessel MI and ST is reduced in the BVS relative to permanent stents between 3 and 5 years post intervention (Kereiakes et al., 2019).

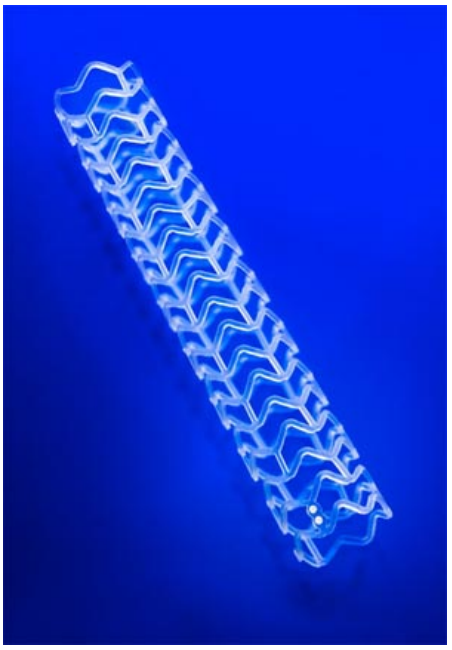

FIGURE 1.10: The Abbott Vascular BVS (bioresorbable vascular scaffold) (Medgadget, 2010)

Encouraging pre-clinical trial results from the latest generation of BRS have rekindled interest in a non-permanent treatment of atherosclerosis. The Arteriosorb^{TM} BRS, a sub-100 µm strut thickness scaffold has shown non-inferiority to the XIENCE metallic drug eluting stent (DES) (Katagiri et al., 2019) by demonstrating similar post expansion lumen area, percentage recoil of the scaffold and shear stress at the vessel wall. The Fantom scaffold by Reva Medical was deemed to have acceptable safety and efficacy after a first-in-man clinical trial after displaying no cases of ST, target lesion revascularisation (TLR) or death in a 30 day follow-up of a ten patient study. However, the financial burden of developing BRS led to Reva Medical filing for bankruptcy and stating that they would withdraw attention from the cardiovascular device sector (Koltowski et al., 2020; Taylor, 2020). Most recently, the results of the first-in-man clinical trial of the FireSorb BRS were presented in the FUTURE II study. The scaffold developed by MicroPort was found to have demonstrated non-inferiority to an everolimus-eluting cobalt-chromium stent by displaying similar levels of late lumen loss, strut coverage and target lesion failure (TLF) at one-year follow-up (Song et al., 2021). Prior to this, the industry scepticism surrounding BRS has led to many other device manufacturers halting the development of polymeric BRS. Indeed, in addition to the ArterioSorb^{TM}, it appears the DESolve, shown in Figure 1.11, by Elixir medical, the MeRes100 by Meril Life and the FireSorb by MicroPort are the only polymeric BRS currently under development. Whilst more long term data is required, the DESolve has also provided encouraging signs, proving

its safety and efficacy in early clinical trials (Nef et al., 2018). The MeRes100, a thin-strut BRS has also demonstrated encouraging results displaying favourable efficacy in treating patients with de novo coronary artery stenoses in a multi-centre trial (Abizaid et al., 2019).

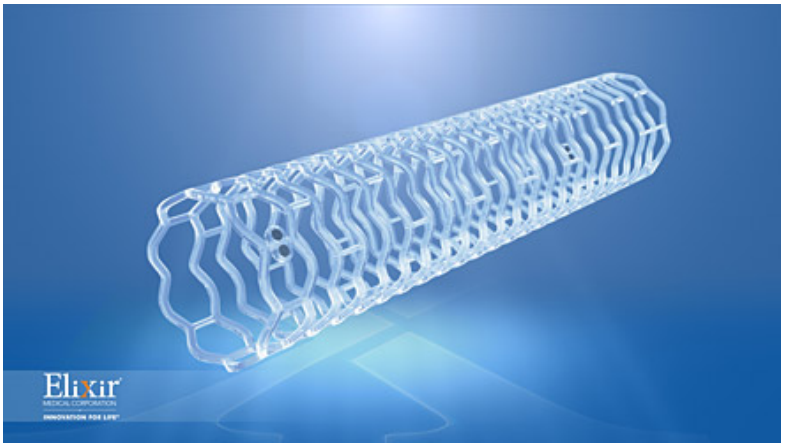

FIGURE 1.11: The DESolve BRS by Elixir

Whilst resorbable metallic scaffolds provide improved mechanical properties, they have been found to cause complications due to the by-products of their biodegradation. They also possess an inherently fast degradation time that can lead to premature break-down of the scaffold causing a loss of support for the artery. The Magmaris magnesium bioresorbable scaffold by Biotronik, shown in Figure 1.12, has provided some encouraging results after early clinical trials. Not only does it exhibit good performance in terms of biocompatibility, but very favourable performance relating to target lesion failure and ST which are both low. No probable or definite ST was found at six months post intervention in the study reported by Rapetto and Leoncini (2017) and ST rates have been reported at 0.5% at 12 months post intervention. It was also found that at four months post intervention Magmaris was almost completely resorbed which led to significant recoil of the artery. This fast degradation time could be viewed positively as it reduces the prospect of late and very late ST. However, this appears to be at the expense of support for the vessel when it is most needed, which is concerning. Moreover, a recent study published the occurrence of very-late restenosis around 20 months after the initial intervention which led to clinical symptoms and the requirement for re-intervention at the original stenosis site. In this case it appeared that portions of the scaffold struts were not resorbed and induced negative remodelling and neointimal proliferation (Bayón et al., 2020). Recently, the Iron Bioresorbable Scaffold (IBS), an ultra thin-strut BRS (70 µm) by LifeTech Scientific has released encouraging early data after delivery into porcine coronary arteries. The scaffold's safety and efficacy was found to be comparable to that of the state-of-the-art XIENCE stent (Abbott Vascular) at 6 months post implantation (Zheng et al., 2019).

Table 1.1 details the BRS currently believed to be under development. Ascertaining whether a manufacturer is continuing the development of a BRS can be challenging due to the long lead times prior to clinical data publication. Also, preliminary design concepts are often communicated by manufacturers but the decision to no longer pursue these can be withheld.

FIGURE 1.12: The Biotronik Magmaris magnesium bioresorbable stent (Biotronik, 2019).

Manufacturer	Model	Material	Most Recent Data
Arterius	ArterioSorb^{TM}	PLLA	July 2019
Biotronik	Magmaris	Magnesium	August 2020
Elixir	DESolve	PLLA	March 2018
LifeTech Scientific	IBS	Iron	February 2019
Meril Life	MeRes100	PLLA	September 2019
MicroPort	FireSorb	PLLA	May 2021

TABLE 1.1: Bioresorbable scaffolds that are believed to be currently under development due to recent publication of data or communications from the manufacturer.

1.5.3 Failure Modes of BRS

Poor clinical outcomes in BRS are ultimately caused by the mechanical response of the scaffold, its interaction with the vessel and influence upon the haemodynamics. Therefore, it is important to consider the mechanical failure modes of BRS such that these can be quantified and further understood to improve scaffold design.

Large strut dimensions have been necessary in BRS to ensure sufficient radial strength. However, it is evident that the thickness of the struts must be reduced to decrease the risk of ST (Sakamoto et al., 2018). Minimising the strut width to reduce the scaffold area

in contact with the vessel wall to lessen the risk of restenosis, as well as the haemodynamic disturbance, will also impact the radial strength. Therefore, the crushing of the scaffold once delivered *in-vivo* is a potential mode of failure. The radial strength of a coronary stent/scaffold, quantifies its efficacy in fulfilling its primary objective; to restore patency to a compromised vessel when subjected to a crushing force caused by a narrowing of the artery.

Secondly, BRS are vulnerable to brittle and ductile failure in balloon expansion whereby the strain in the scaffold struts exceeds their ultimate tensile strain. In particular, significant concern surrounded the over-expansion capabilities of first generation BRS (Foin et al., 2016b). Over-expansion is commonly undertaken in clinical practice using a post-dilatation balloon to optimise the vessel diameter. Commonly, a stent or scaffold of manufactured diameter 2.5 mm may be required to be expanded to a diameter in excess of 4 mm. However, the Abbott Vascular BVS was only recommended for use with very modest over-expansions of approximately 0.7 mm greater than the nominal diameter, which severely limited its efficacy (Abbott Vascular, 2017; Kereiakes et al., 2016). Whilst strut fracture will inevitably lead to a reduction in radial strength it will also increase the risk of ST as the fractured struts will be likely to protrude into the blood flow and act as a site at which a blot clot can form. Therefore, the ability of a BRS to tolerate significant over-expansions is a significant factor in determining the scaffold performance and in turn patient outcome.

The apposition of the scaffold struts against the vessel wall will greatly impact the scaffold performance *in-vivo*. Whilst this is not strictly considered a failure mode, the tendency of a scaffold to be evenly resorbed into the endothelium without struts protruding into the blood flow is important to reduce the risk of ST (Boeder et al., 2019). This is not only a function of the scaffold design but delivery strategy used by the interventionist.

Whilst not explicitly considered herein, fatigue failure also exists as a potential failure mode for coronary scaffolds due to the pulsatile stresses exerted on the scaffold *in-vivo*. Late failure of the struts can occur, leading to the same adverse effects as caused by the short term brittle or ductile failure that may manifest in scaffold expansion (ul Haq et al., 2017).

1.5.4 Fabrication of Bioresorbable Scaffolds

Whilst each BRS developer will utilise a different process to manufacture the scaffold, particularly in terms of material post processing, there will be commonality amongst different scaffold manufacturing processes.

Generally extruded tubes of the appropriate diameter will be used as the starting point for scaffold manufacture. Material post processing will then be applied to the extruded

tubes to improve their mechanical properties. The scaffold geometry will then be laser cut from the extruded tubes. The direction of the polymer chains within the scaffold will significantly affect the anisotropy of the device. Greater alignment of the chains in a particular direction will lead to greater strength and stiffness in that direction.

In the case of the ArterioSorb^{TM} extruded PLLA tubes were processed by solid phase orientation using biaxial die drawing whereby they were heated above the glass transition temperature, then drawn over an expanding mandrel (Al-Lamee et al., 2019). This induces crystallinity and orientates the polymer chains in both the axial and circumferential directions. As a result, the PLLA displays significant anisotropy with higher strength and stiffness in the axial direction, due to increased polymer chain crystallinity in this direction.

1.5.5 The ArterioSorb^{TM}

The ArterioSorb^{TM} BRS, shown in Figure 1.13, is a thin-strut (95 µm) coronary scaffold constructed from a PLLA backbone. The scaffold is coated with the anti-proliferative drug Sirolimus (Arterius Ltd, 2015). The most notable feature of the ArterioSorb^{TM} BRS is the central closed cell, designed such that radial strength is maximised where the stenosis is largest. Open cell rings either side of the central closed ring facilitate good side-branch access and flexibility to aid the deliverability of the scaffold and ensure it can conform to the vessel geometry to minimise strut malapposition. The scaffold utilises peak to peak connectors which form a helical pattern. The patent encapsulates a small increase in cell area (the area contained within each cell) progressively moving from the central closed rings to the end rings of the scaffold (Bressloff et al., 2017) via an increase in the open cell ring lengths. Once delivered to the site of the stenosis the scaffold resorbs into the vessel wall and is no longer present from between 12 to 24 months post intervention. Dual radio-opaque markers are located at either end of the scaffold.

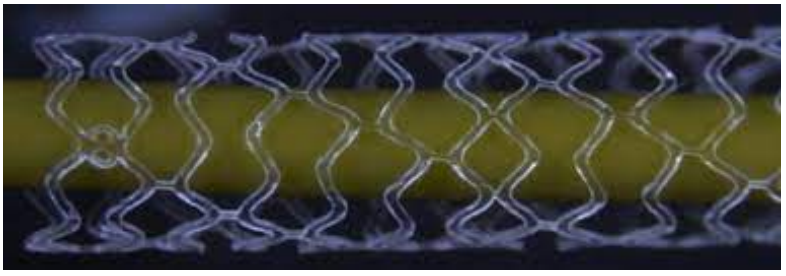

FIGURE 1.13: A microscope image of the ArterioSorb^{TM} scaffold expanded on a balloon/catheter. The central closed ring is evident along with the subsequent open cells and helical pattern of connectors.

1.5.6 The Ideal Bioresorbable Scaffold

The ideal characteristics of a coronary BRS are defined below. A BRS is required to revascularise a stenosed coronary artery without the introduction of clinical side effects. These criteria, with the exception of bioresorbtion are also applicable to permanent metallic stents.

A bioresorbable coronary scaffold should, in approximate order of importance:

- Provide sufficient radial strength to resist the compression forces exerted on it by the diseased artery. This is of fundamental importance as it is the scaffold's primary role to restore patency to the vessel allowing increased blood flow.
- Resorb evenly by minimising the malapposition of struts to the vessel wall. This will reduce the number of struts protruding into the lumen that could provide a site for thrombus formation.
- Tolerate significant over-expansion without strut fracture as post dilation of BRS is commonplace in clinical practice to maximise the post expansion diameter.
- Minimise alteration of the haemodynamic environment through minimisation of strut thickness and width.
- Minimise damage to the artery wall once in place. This is facilitated through the improvement of scaffold shapes to minimise tissue damage and prolapse which in turn will reduce restenosis.
- Facilitate good side-branch access to minimise the complexity of repeat interventions.
- Minimise post expansion recoil due to its own elastic properties as this could lead to greater restenosis as the scaffold is unable to maintain its target diameter.
- Possess good conformability to follow the natural curvature of the artery.

It is also important that the following criteria can be achieved by a stent/scaffold. These criteria are binary in nature and so if a stent/scaffold cannot achieve these then the design is unviable.

- Be able to be crimped to a diameter of approximately 1mm with good adhesion to the folded balloon-catheter such that it can be percutaneously delivered to the site of the stenosis.

- Secrete an anti-proliferative drug to suppress the response to injury in the vessel to lessen the extent of restenosis. This drug should not only be effective in its immunosuprecency but also have an optimised elution profile to allow late healing of the vessel such that the scaffold does not remain exposed and induce thrombus formation.

Evidence has shown that the ArterioSorb^{TM} possesses many of the traits required of an ideal coronary scaffold. It displays low recoil both post crimping and expansion meaning it secures well to a balloon/catheter and has a large post-expansion diameter. The closed cell ArterioSorb^{TM}, a design which utilises closed cells along the scaffold length, has also demonstrated comparable radial strength to a market leading DES, whilst the open cell design, focused upon herein, offers excellent vessel conformability and side branch access. Most notably, the ArterioSorb^{TM} is also able to withstand significant over expansion, without evidence of strut fracture. Therefore, the ArterioSorb^{TM} design appears promising in delivering a successful solution to the temporary scaffolding of coronary arteries. It is this scaffold design upon which the work in this thesis is based.

Chapter 2

Review of Literature

This chapter describes prior research largely themed by the three over-arching aims of this thesis. Firstly, the use of finite element analysis (FEA) to explore stent and scaffold design is presented with a focus upon, when possible, the exploration of PEEQ. Secondly, the focus shifts to the material property modelling of PLLA from the inception of a key material model through to the application of a variety of material property models in FEA. Finally, the modelling of stents and scaffolds in clinically realistic scenarios is presented; these depart from the idealised free expansion cases in which scaffolds are often investigated in *silico*.

2.1 FEA of Coronary Stents/Scaffolds

2.1.1 FEA Strategies

This section considers earlier FEA of coronary stents, which developed effective modelling strategies, through to more contemporary work that considers polymeric BRS.

One of the earliest FEA studies that focused on coronary stents was carried out by Etave et al. (2001) to calculate and compare a number of mechanical properties of two different types of stent, a study, which, by contemporary standards, appears relatively simple. However, since this research, numerous studies utilising FEA have been conducted to investigate stents/scaffolds through simulating their expansion. As FEA software has gained functionality and computational processing power has increased, ever more complex and realistic simulations of the deployment of coronary stents/scaffolds have been made possible.

Following this, a study by Migliavacca et al. (2002) modelled the free expansion of multiple slotted tubular stents to develop an understanding of how the strut thickness, metal-to-artery surface ratio, as well as the longitudinal and radial cut lengths affect

the device performance. Additionally, two further stent designs were considered resembling the Multi-Link Tetra (Guidant, Indianapolis, IN, USA) and the Carbostent (Sorin Biomedica, Saluggia, Italy). The stents were expanded to a diameter of 3 mm via a pressure applied to their internal face, a simplification of modelling balloon expansion, before allowing them to elastically recoil. It was found that the metal-to-artery ratio was proportional to the pressure required to expand the stent to a given diameter. In addition, this is one of the few FEA studies of coronary stents to consider the equivalent plastic strain (PEEQ), which also developed proportionally to the metal-to-artery ratio.

Migliavacca et al. (2005) then conducted free expansion of the Cordis BX Velocity (Johnson & Johnson Interventional System, Warren, NJ, USA) coronary stent using FEA. A uniform linearly increasing pressure was applied to the inside face of the stent to expand it. Post expansion, the stent was assessed in terms of the magnitude of its radial expansion, radial elastic recoil (both centrally and at the distal end of the device) and longitudinal elastic recoil. The study concluded that in order to predict the transient behaviour of the device in expansion, it is necessary to expand stents via balloon inflation in *silico*. The omission of a balloon model was attributed as the primary reason for the discrepancies between the *in-silico* and *in-vitro* validation data. However, the study also concludes that if the *in-vitro* and *in-silico* scaffolds are expanded to the same diameter then the stress fields at their final state are comparable. Such a result suggests the use of a cylinder with a radial displacement applied to it to expand a coronary stent in FEA provides a reasonable and computationally efficient expansion method if only the final state of the device is of interest.

Subsequently, these findings were confirmed by De Beule et al. (2008) in their investigation of the effect of balloon folding upon the *in-silico* expansion of coronary stents. Application of pressure to the internal stent face was found to be an oversimplification, which resulted in an inaccurate prediction of the transient and final stent shape. Use of a displacement driven cylinder was found to be a computationally efficient method of stent expansion but this was also found to compromise the predicted stent shape in the course of the expansion process. A comparison of the three expansion techniques investigated is shown in Figure 2.1. Whilst a dilatation balloon operates under pressure, this differs from direct application of pressure to the internal surface of the scaffold. In this case the pressure is equally applied across the scaffold structure which leads to the difference in results shown in Figure 2.1. Whilst these findings are insightful, the available processing power as a result of modern computing clusters means it is generally not prohibitive to utilise a folded elastic balloon model to expand a coronary stent/scaffold in *silico*.

The aforementioned studies by Etave et al. (2001), Migliavacca et al. (2002), Migliavacca et al. (2005) and De Beule et al. (2008) investigate stents' mechanical behaviour in the context of a free expansion scenario, discounting the interaction between the stent and

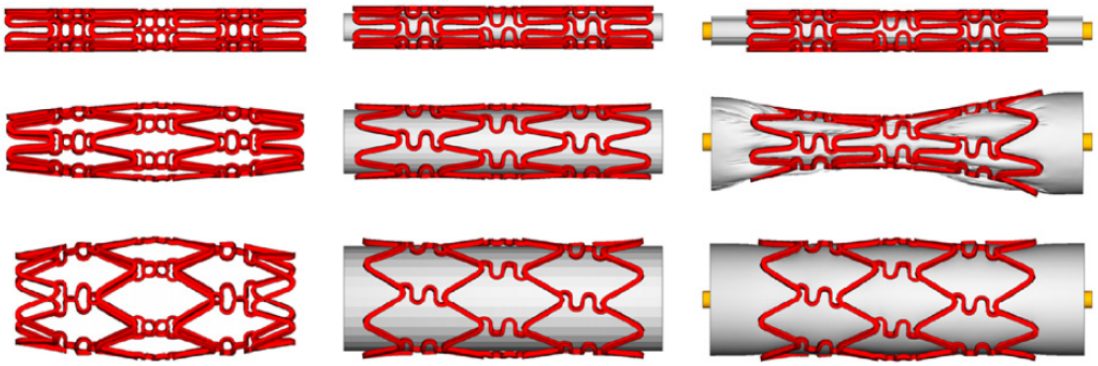

FIGURE 2.1: *In-silico* expansion of a coronary stent using pressure applied to its internal surface (left), a displacement driven cylinder (middle) and a tri-folded pressurised balloon (right) (De Beule et al., 2008).

artery. Naturally, this represents a significant simplification compared to a clinical scenario. However, such a technique dramatically reduces the complexity of the simulation, particularly in terms of the contact definitions required and so significantly shortens the solution time. Despite this simplification, this technique is used numerous times throughout the following literature to obtain comparable metrics of stent/scaffold mechanical behaviour.

The rise in interest in BRS led to an increase in studies assessing their mechanical performance and appropriate simulation strategies. Debusschere et al. (2015) investigated the effect of balloon deployment rate on a BRS via the use of an implicit finite element solution method. A scaffold model, based on the Abbott Vascular Absorb BVS, along with a cylindrical hyperelastic balloon was used. The simplified balloon model was justified in order to reduce the complexity of the contact interaction and facilitate use of the Abaqus/Implicit solution method. Unlike the explicit solution method, utilised by the majority of quasi-static coronary stent/scaffold deployment simulations, the implicit method does not lend itself to the solution of problems with complex nonlinear contact interactions but can facilitate faster solution times due to larger stable time increments compared to the explicit solution method. This means the natural time period of the expansion could be preserved, which is convenient when using a time dependent material model. The scaffold's material behaviour was characterised using a model based upon the Bergstrom-Boyce parallel network material model (Bergström and Boyce, 1998, 2000) comprising a viscoelastic plastic branch alongside a hyperelastic branch implemented using the user material (UMAT) sub-routine. The study concluded that using a step-wise inflation procedure reduces the maximum stress in the scaffold struts, shown in Figure 2.2, but does not significantly affect the final diameter of the scaffold. Whilst the study also demonstrates that the implicit solution method can be used for the expansion of a BRS in FEA, it is unable to validate the accuracy of the results of the scaffold expansion as no *in-vitro* data was provided.

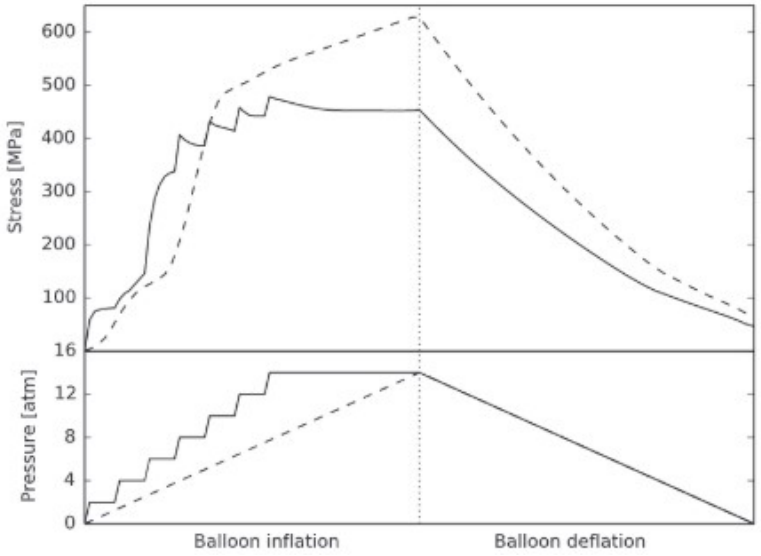

FIGURE 2.2: The maximal maximum principle stress in the struts of BRS, expanded via cylindrical balloon inflation in FEA using the Abaqus/Implicit solution method. The step-wise inflation method, shown by the solid lines, results in a significant reduction in stress compared to the direct inflation method, shown by the dashed line, which will reduce the likelihood of strut fracture for a BRS when expanded via balloon inflation (Debusschere et al., 2015).

Schiavone et al. (2016) simulated the deployment of a metallic stent, based upon the Abbott Vascular XIENCE V, and a polymeric BRS, based upon the Abbott Vascular Absorb BVS. The stent and scaffold were expanded into idealised coronary arterial models containing concentric and eccentric stenoses. The stenoses were located in a three-layer arterial model. The material behaviour of the BRS was modelled using an elasto-plastic model, although the stress-strain data to which it was calibrated to was not detailed. After expansion via a linear elastic balloon, the final diameter of the polymeric BRS was 2.22 mm compared to 2.37 mm in the metallic stent. In both the concentric and eccentric plaques, the Absorb scaffold also induced a lower level of stress in the plaque-artery system. Whilst lower levels of stress were exhibited in the Absorb device, the study does not emphasise the importance of the final stented diameter of the vessel, which is inferior in the case of the Absorb scaffold. Also, the BRS displayed significant non-uniformity in expansion in the eccentric plaque and took on a more eccentric shape itself when compared with the metallic stent. Whilst the paper concludes that polymeric BRS are preferable to metallic devices in highly eccentric stenoses, due to the reduced vessel stress they induce, this fails to recognise the inferior final diameter of the vessel and the non-uniformity in expansion, which are both significant factors that could adversely effect patient outcome. Moreover, the lower level of stress induced by the BRS is a result of its lower radial strength and so will negatively impact the patient outcome in terms of its efficacy in restoring the vessel patency. Additionally, this work does not consider the area in which the scaffold is in contact with the plaque-artery, which will exceed that of the metallic stent. Whilst lower levels of stress may be induced by the

BRS, the area over which an elevated stress level is induced will be larger than the stent. This should be quantified to give a fair comparison of the scaffold and stent. This study clearly shows the challenge BRS must overcome if they are to demonstrate acceptable mechanical performance comparable to that of metallic DES.

2.1.2 Studies Utilising *In-Vitro* Data

Whilst *in-silico* modelling of coronary stents/scaffolds can provide useful insight, the validation of these models via *in-vitro* evidence is critical to maximise confidence in the computational simulations. Therefore, the most relevant studies of BRS which utilise *in-vitro* validation data are reviewed in this section.

Radu et al. (2012) were the first to report the phenomenon of stress crazing in the struts of polymeric BRS. Until this point, FEA of BRS was limited, most likely due to the infancy of the Absorb BVS (Abbott Vascular, IL, USA). This report highlighted the whitening effect that can occur in high strain locations in polymers and noted that crazing is identifiable in optical coherence tomography (OCT) due to the increased scattering of light at the crazing site. A link between structural fracture of the struts in expansion, a relatively common occurrence in early generation BRS, and stress crazing was suggested. Microscope and OCT images of the expanded scaffold are shown in Figure 2.3 along with FEA of a simplified scaffold based upon the Absorb BVS. This highlights the importance of understanding the effect of the strain distribution in the scaffold struts of BRS.

Following this, Foin et al. (2016a) conducted a similar study comparing the XIENCE V stent and the Absorb BVS using *in-vitro* and *in-silico* testing to compare the acute recoil of the devices. *In-vitro* balloon expansion of the stent and scaffold into identical stenosis models was undertaken and assessment via OCT highlighted the lower minimum lumen area of the BVS (4.92 mm^2) compared to the XIENCE V (5.40 mm^2), as shown in Figure 2.4. In both cases post-dilatation of the devices was required to reduce malapposition of the struts. The aforementioned findings of Schiavone et al. (2016) are affirmed from the FEA, which concludes that lower levels of stress are induced on the vessel wall in the case of the BRS, as per Figure 2.5, albeit at the expense of greater acute recoil. The study also highlighted the difference in mechanical properties of metallic stents compared to polymeric scaffolds which result in the requirement for significantly different strut geometries to achieve sufficient radial strength. The importance of developing clinically relevant models is also stated as whilst idealised models can provide comparable data and a useful assessment of the stent/scaffold mechanical response, they may not accurately predict the likelihood of a successful clinical outcome in *vivo*.

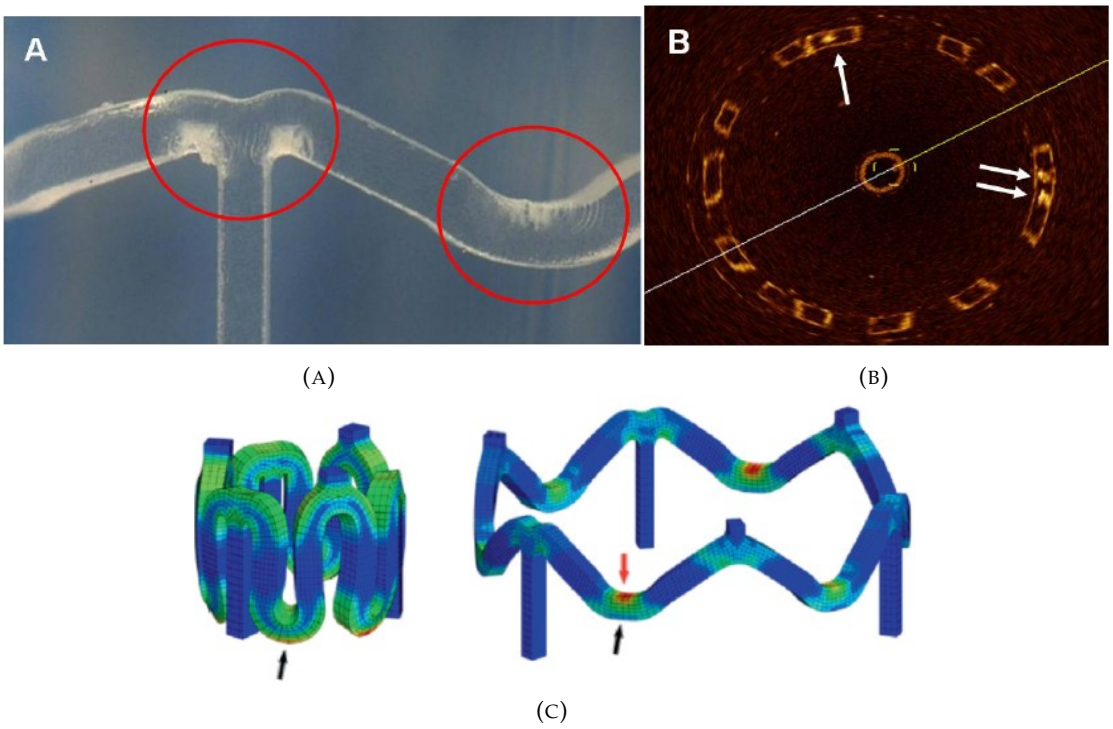

FIGURE 2.3: (A) A microscope image of the expanded Absorb BVS (Abbott Vascular, IL, USA) with stress crazing evident at the inside of the crown apex; (B) an optical coherence tomography image with the stress crazing highlighted in both cases and (C) the stress contours for the crimping and expansion of the scaffold using finite element analysis (Radu et al., 2012).

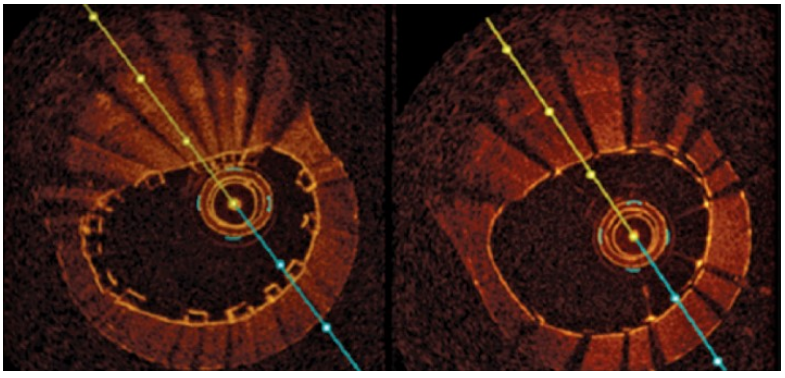

FIGURE 2.4: Optical coherence tomography of the Abbott Vascular Absorb BVS (left) and XIENCE V stent (right) expanded *in-vitro* under their nominal pressures of 7 and 10 atm respectively into a stenosed coronary artery model. The minimum lumen area is greater for the metallic stent as well as improved apposition of the scaffold struts to the vessel wall (Foin et al., 2016a).

Foin et al. (2016b) also investigated the over expansion behaviour of the Absorb BVS via *in-vitro* deployment into a stenosed coronary artery model, as well as in a free expansion scenario. 3 mm and 3.5 mm diameter scaffolds were tested using three different expansion regimes of increasing balloon size, as shown in Figure 2.6. Both the scaffolds show greater tolerance of over expansion in the free expansion scenario compared to expansion in the stenosed artery model. In the stenosed artery model, both scaffolds

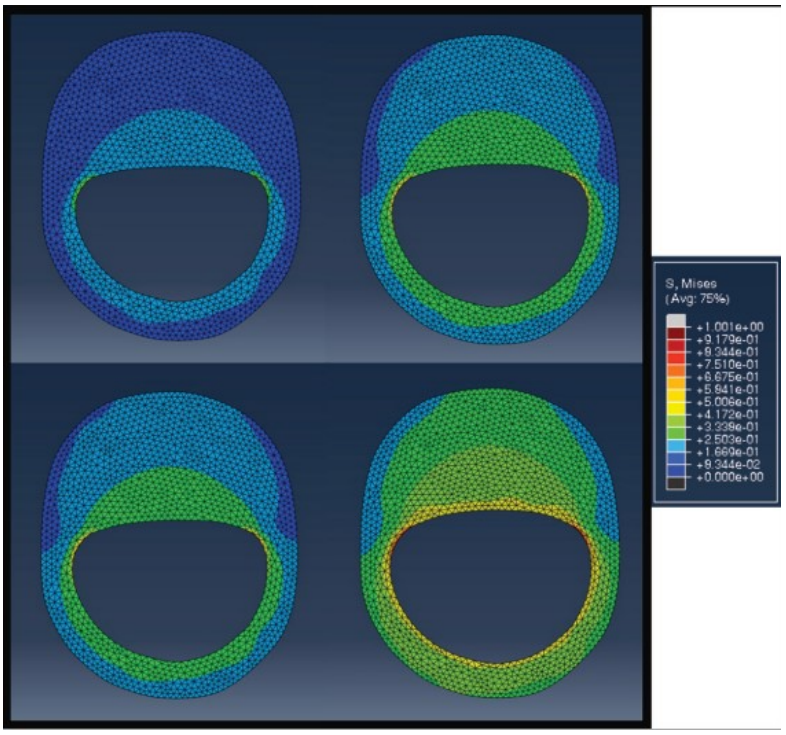

FIGURE 2.5: Finite element analysis of the wall stress of the artery for the Abbott Vascular Absorb BVS (left) and XIENCE V stent (right) expanded using a balloon model inflated at nominal pressure (top) and 18 atm (bottom). It is evident that the stresses are lower in the case of the BRS (Foin et al., 2016a).

could only tolerate an over expansion of 0.5 mm above their nominal diameter, whilst in the free expansion case they could achieve an over expansion of 0.65 mm above their nominal diameter. This is a result of the stenosis concentrating stress on the scaffold structure which led to fracture of the compressed struts. As per Foin et al. (2016a), this highlighted the importance of investigating BRS in clinically relevant scenarios and to avoid sole reliance upon free expansion data. The effect of over expansion and fracture upon the radial strength of the scaffold was also analysed. Unsurprisingly, as shown in Figure 2.7, the radial strength of rings containing a fractured strut was found to be compromised. Interestingly, in contrast to the recent findings of Arterius Ltd (Leeds, UK), scaffold struts that were over expanded were observed to also exhibit a reduction in radial strength compared to struts that were expanded to their nominal diameter.

Wang et al. (2017) then investigated the performance of a polymeric BRS via FEA and *in-vitro* testing. The percentage recoil, radial strength and flexibility of a scaffold similar to the Absorb BVS were assessed. A simplified two ring geometry was analysed using the Abaqus/Implicit solver to crimp, expand and crush the scaffold via cylindrical surfaces. A flexibility simulation was also conducted to bend the scaffold about its longitudinal axis. Samples of PLLA were tested in uniaxial tension to obtain the stress-strain curves at two different temperatures. Crimping was undertaken at a higher temperature of 48°C to improve the material's formability, whilst expansion was undertaken at 37°C. However, the direction from which the material was cut from the

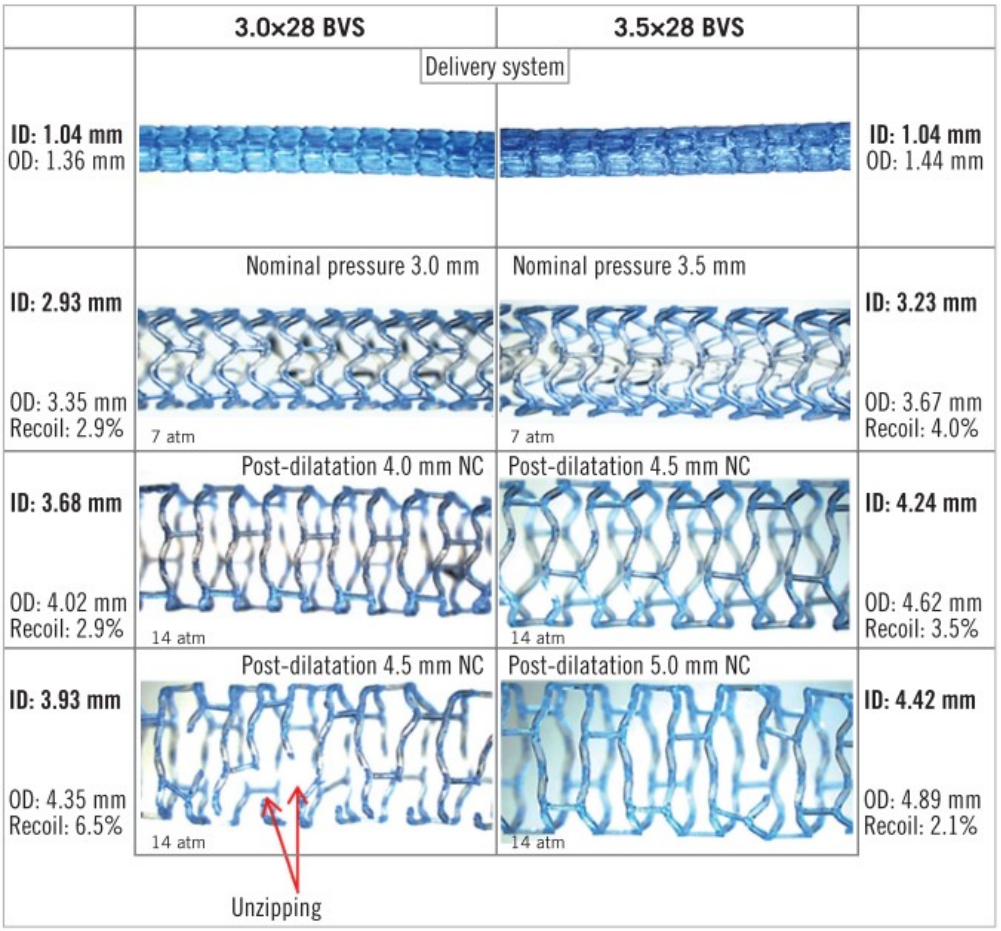

FIGURE 2.6: Free expansion of the 3 mm and 3.5 mm diameter Abbott Vascular Absorb BVS using three expansion regimes. In each case the over expansions which are ≥ 1 mm above the nominal expansion diameter result in strut fracture. (Foin et al., 2016b).

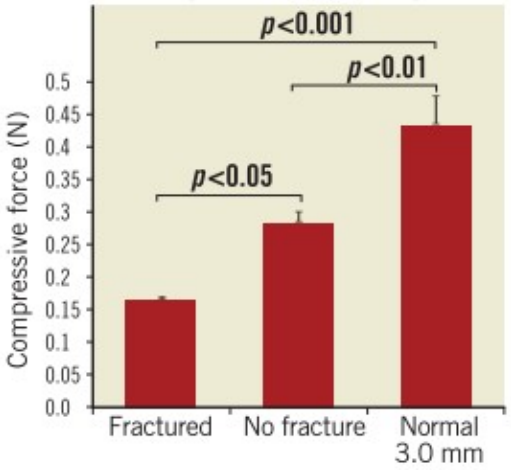

FIGURE 2.7: The radial strength of the 3 mm nominal diameter Abbott Vascular Absorb BVS tested via a point force applied to a fractured overexpanded ring (left), non-fractured overexpanded ring (central) and a non-fractured nominally expanded ring (right) (Foin et al., 2016b).

extruded PLLA tube was not divulged. The material was modelled as homogeneous and isotropic using linear elasticity and von Mises plasticity without consideration of anisotropy. During the crimping process, a concentration of plastic strain was observed on the inside faces of the crowns with the authors reporting the onset of stress crazing, shown in Figure 2.8. Areas of low stress were observed at the top of each connector and so the scaffold geometry was altered to reduce the area in this vicinity, creating a notch at the outside of the crown, as shown in Figure 2.9. This served to reduce the scaffold area in contact with the vessel whilst ensuring the scaffold structure is better utilised. This also resulted in a reduction in maximum stress and strain at the inside of the crown on either side of the connector and so homogenised the stress distribution around the crown/connector interface. In terms of radial recoil, the simulations were found to agree well with the *in-vitro* tests where all values were reported to be less than 5%. The specific radial strength was calculated as 1.46 N/mm in the simulation whilst the *in-vitro* tests indicated a radial strength of 1.55 N/mm which is particularly notable given the simple material model used and the low and accurate levels of percentage recoil predicted in *silico*. Unfortunately, very limited details are provided regarding the *in-vitro* testing of the scaffold and the pre-processing of the PLLA. This makes seeking a deeper understanding of the results reported here difficult as it is unclear how an elasto-plastic material model can achieve such accurate predictions of the scaffold mechanical behaviour. Additionally, the scaffold struts are thick (150 μm) and so the design would be considered clinically unviable in terms of the elevated thrombus risk presented in *vivo*.

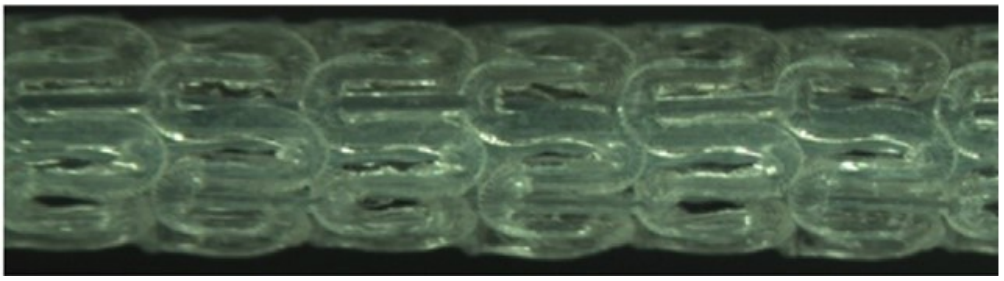

FIGURE 2.8: The scaffold crimped to an outer diameter of 1.41 mm inducing the onset of stress crazing in the scaffold struts Wang et al. (2017).

More recently, Wang et al. (2020) conducted a comparison of *in-silico*, *in-vitro* and *in-vivo* testing of bioresorbable coronary scaffolds. *In-vitro* and *in-silico* multi-modal mechanical loading was used to assess the efficacy of two scaffold designs and predict their performance in *vivo*. Prototype open-cell PLLA scaffolds were provided by Boston Scientific (MA, USA) that comprised two designs; 'slotted' and 'non-slotted'. The slotted design featured an arc-shaped slot removed close to the inner radius of the crown. Six pigs were used for the *in-vivo* testing where three scaffolds per animal were delivered into the LAD, LC and RCA respectively. These were then observed after 30 days, once surgically removed from the heart. Scaffolds were also delivered *in-vitro* to mock silicon vessels before the loading modes were exerted on the scaffold via the silicon vessel.

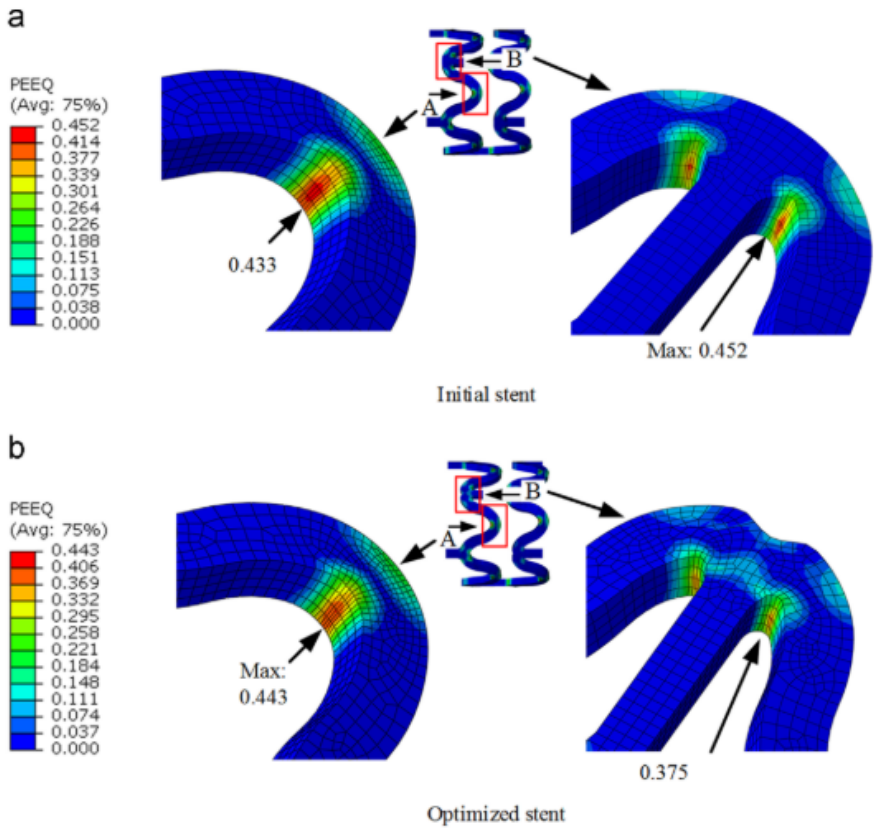

FIGURE 2.9: The equivalent plastic strain (PEEQ) in the crown apex of a scaffold based upon the Abbott Vascular Absorb BVS expanded to an inner diameter of 3.1 mm. A reduction in PEEQ is evident in the optimised scaffold due to the alteration of the geometry in the vicinity of the connector at the outside of the crown (Wang et al., 2017).

The loading modes comprised axial compression (A), bending (B) and torsion (T), each delivered separately in varying combinations, stress distributions of which for the non-slotted design are shown in Figure 2.10. The *in-silico* simulation mimicked delivery of the scaffold to the silicon vessel via crimping and balloon expansion before applying the loading in the same manner as the *in-vitro* tests. 54 strut fractures were reported *in-vivo* in the 'non-slotted' case, across eight tested scaffolds, compared to 25 *in-vitro* that were subjected to all three loading modes, across seven tested scaffolds. Only two fractures were reported *in-vivo* in the slotted design, compared to one *in-vitro* after bending and axial compression only. Stress concentrations were found to vary greatly between different loading scenarios. Most notably, axial compression was found to be beneficial to the scaffold performance in *silico* by reducing stress concentrations, which was consistent with the *in-vitro* results. The 'slotted' design showed fewer strut fractures *in-vivo* and *in-vitro* and lower stress levels *in-silico*, shown in Figure 2.11, indicating that this design can lessen the risk of strut fracture. The location of high stress areas varied greatly depending on the combination of loading mechanism. However, it was clear that a combination of axial compression and bending was necessary to align the number and location of strut fractures *in-vitro* with *in-vivo* results. Whilst this research

provides significant insight into the importance of including multi-modal loading in *in-silico* and *in-vitro* testing to detect scaffold fracture, the study does not reliably predict fracture likelihood from the *in-silico* testing. Indeed, the study considers the volume fraction of elements that show stress beyond the UTS but does not discuss whether this correlates with *in-vivo* and *in-vitro* results which would be a useful output.

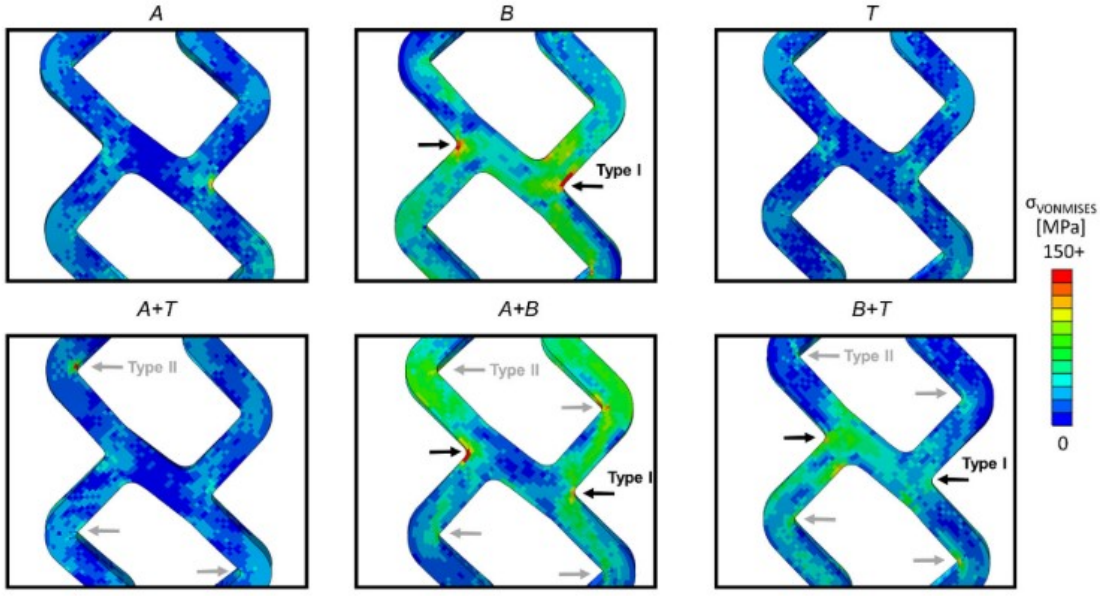

FIGURE 2.10: The von Mises stress distribution for the non-slotted scaffold design after application of different combinations of the loading modes; axial compression, (A); bending, (B) and torsion, (T). The location of potential fracture sites was categorised as; type 1, a connected crown; type 2, an unconnected crown and type 3, a connector (Wang et al., 2020).

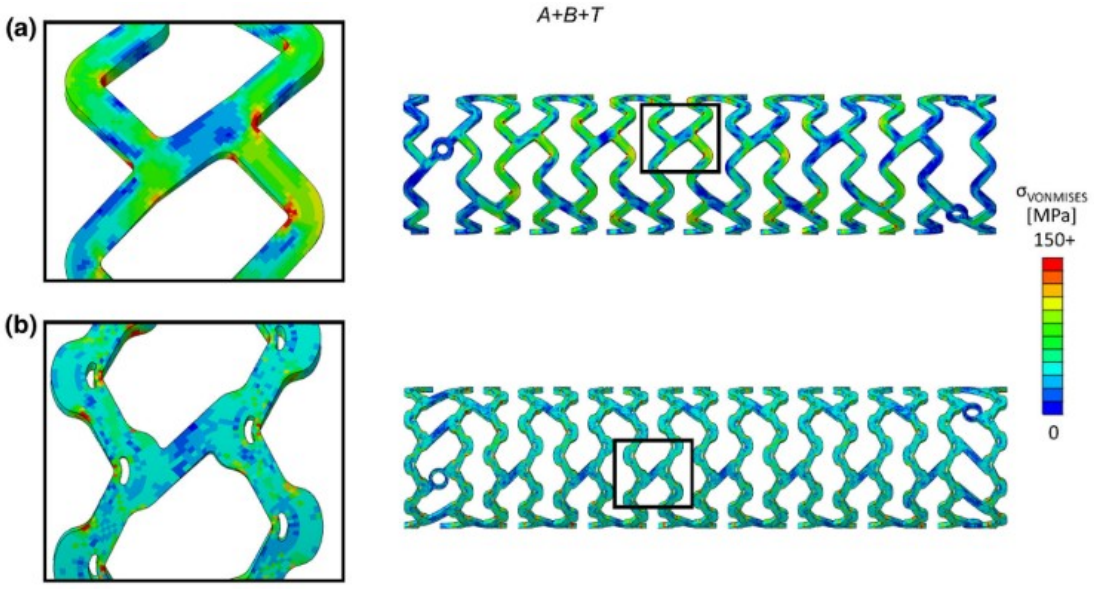

FIGURE 2.11: A comparison of the von Mises stress distribution between the non-slotted design, (A) and the slotted design, (B) after *in-silico* deployment into an idealised vessel followed by axial compression, bending and torsional loading (Wang et al., 2020).

Filipovic et al. (2021) conducted the *in-silico* and *in-vitro* comparison of the SYNERGY^{TM} BP platinum-chromium stent and a BRS provided by Boston Scientific (MA, USA), similar in appearance to that considered by Wang et al. (2020). The crimping and balloon expansion of the devices was conducted both *in-vitro* and *in-silico*, via FEA, prior to radial compression and crush resistance tests being undertaken. Whilst the SYNERGY^{TM} BP stent's material properties were described via linear elasticity and von Mises plastic theory, a more advanced material model was developed to accurately describe the mechanical response of the BRS, based upon stress-strain data provided by the manufacturer. However, details of the material model developed for the BRS are very limited and so the constitutive theory upon which the model was based and its general characteristics are unclear. In addition, the stress-strain curves predicted by the model do not appear to resemble the tensile test stress-strain curves provided by the manufacturer. Most notable in this study is the claim by the authors that the radial strength of the stent and scaffold is accurately predicted by their corresponding *in-silico* test. However, upon closer inspection of the force-diameter graphs, shown in Figure 2.11, the *in-vitro* results to which the simulation results are compared appear to vary significantly between each test case. Whilst the *in-vitro* results for the stent appear to follow the expected shape (an exponential increase in force, followed by a linear section which reaches a peak, followed by a gradual reduction after the maximum value), the force-displacement curves for the BRS take on a very different profile whereby the load increases throughout the duration of the test in two of the cases. Particularly in the case of the BRS, the spread of *in-vitro* results is so great, it is difficult to know to which set of *in-vitro* data the *in-silico* data should be compared meaning that validation of the *in-silico* data is not possible. Whilst it is beneficial to conduct multiple *in-vitro* studies perhaps further understanding of the large variation in results should be sought. Additionally, the values of radial strength in the compression tests appear low for a full length scaffold compared to comparable contemporary devices (Foin et al., 2016a; Wang et al., 2017; Hoddy et al., 2021a).

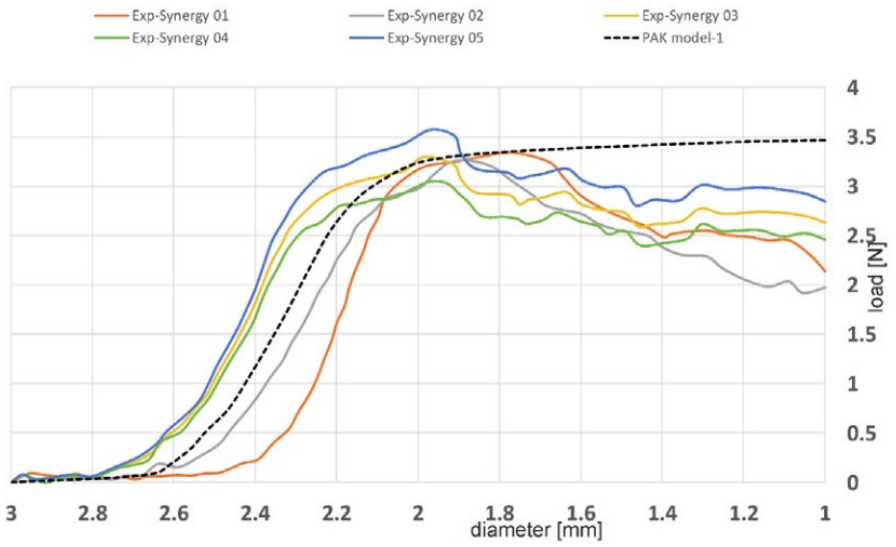

(A)

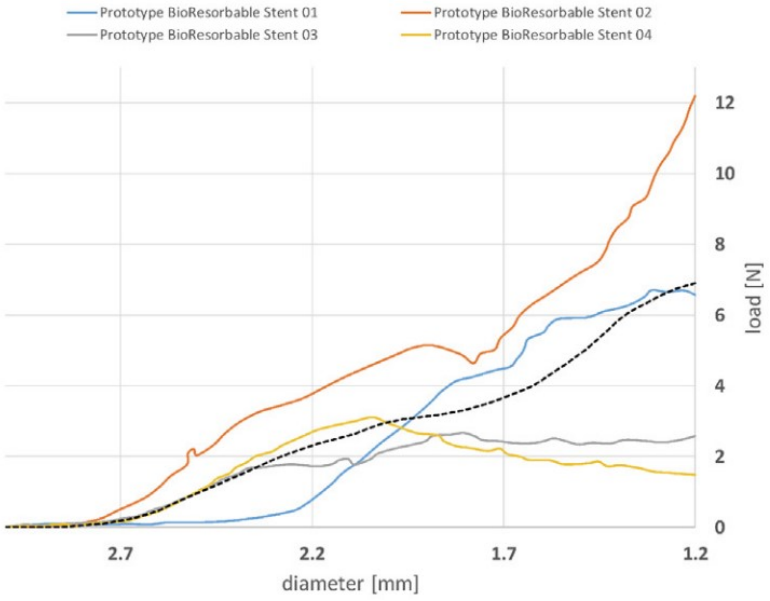

(B)

FIGURE 2.12: (A) The force-diameter curves for the radial compression test for the SYNERGY^{TM} BP stent and (B) the BRS provided by Boston Scientific (Boston, MA, USA). A large spread of results is evident in both *in-vitro* scenarios, particularly in the case of the BRS, which limits confidence in the accuracy of the *in-silico* predictions (Filipovic et al., 2021).

2.1.3 Design Optimisation of Coronary Stents / Scaffolds

Whilst numerous studies claim to optimise stent/scaffold designs, the studies presented here are considered the most comprehensive in terms of their optimisation strategy. The work by Pant et al. (2011) represents pivotal work in the space of multi-physics modelling of coronary stents, whilst the work by Blair et al. (2019b) considers a contemporary polymeric BRS and so is particularly relevant to this thesis.

In their seminal multi-physics research, Pant et al. (2011) presented a multi-objective design optimisation of the Cypher Select stent (Cordis Corporation, FL, USA), manufactured of stainless steel 316L. The stent was parameterised such that the ring height, connector height and strut width could be manipulated. Firstly, the delivery of the device was simulated via balloon expansion in an idealised stenosed arterial model, such that the stress distribution in both the artery and stent could be assessed, as well as the post-expansion recoil, shown in Figure 2.13(A) and Figure 2.13(B). Computational fluid dynamics (CFD) was used to simulate the blood flow over the stent once deployed to understand the level of wall shear stress in the vicinity of the device, shown in Figure 2.13(C). Thirdly, the drug diffusivity was simulated to study the concentration of the anti-restenosis drug within the arterial tissue post delivery, shown in Figure 2.13(D). Lastly, the stent flexibility was tested using structural FEA. From these simulations, six metrics were extracted to inform the optimisation process. These were; acute recoil, tissue stress, haemodynamic disturbance, drug delivery, uniformity of drug distribution and flexibility. A surrogate modelling approach was then used to search for optimised designs which were presented under different criteria. Two non-dominated designs were highlighted in the conservative paradigm as they avoided poor performance in all metrics. The updated designs both showed a reduced strut width and increased connector height when compared to the Cypher platform. Further optimised designs were also suggested under different paradigms. Multi-physics studies of this nature are very uncommon in the literature. Whilst the research did not provide validation data for the models and used simplified stent and artery models it does present some of the most comprehensive considerations of the requirements of a coronary stent and accordingly how the design of a commercial device can be systematically improved.

Blair et al. (2019b) conducted design optimisation for a PLLA scaffold by evaluating the cross-sectional area (CSA), foreshortening (FS), stent-to-artery ratio (SAR) and radial collapse pressure (RCP) using FEA. Both the scaffold geometry and pre-processing of the material were considered as design variables in this study. Biaxial stretching of the PLLA alters both the Young's modulus and yield strength of the material in different directions, leading to anisotropic behaviour of the PLLA. This was encapsulated in a number of empirical equations developed by Blair et al. (2019a). A 5 mm length, four ring open cell device with peak-to-trough connectors was parameterised in its crimped state with an outer diameter of 1.8 mm. The strut width, ring length and thickness could all be varied parametrically along with the design variable A_r, which defined the biaxial stretch ratio. The scaffold was expanded via a displacement driven cylinder from a diameter of 1.8 mm to 3.5 mm and then allowed to recoil. The design space was populated with 40 designs to be simulated using the Abaqus/Implicit solution technique (Dassault Systemes, France). Response surface plots were used to visualise the effect of pairs of design variables on the performance metrics. A single objective function containing each of the performance metrics equally weighted was formulated. The optimisation of this objective function was constrained by a minimum value of radial

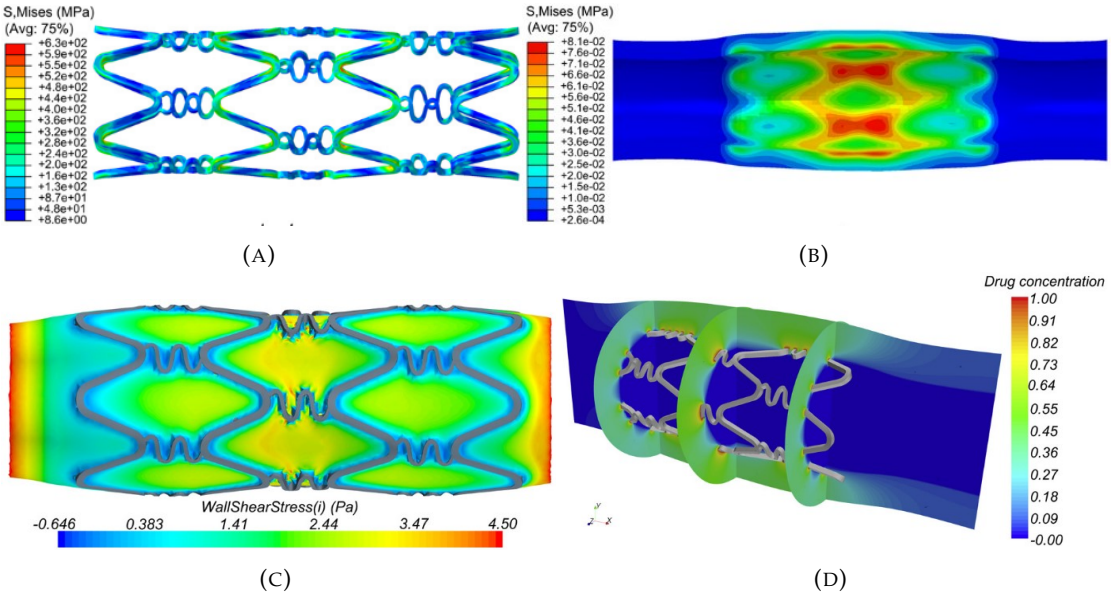

FIGURE 2.13: Multi-physics analysis of a simplified design of the Cypher Select stent. Finite element stress analysis for; (A) the stent and (B) the artery, is shown along with computational fluid dynamics (CFD) of the wall shear stress in; (C) the artery and (D) a diffusivity simulation also conducted using CFD (Pant et al., 2011).

collapse pressure of 40 kPa and maximum value of the strut thickness of 150 µm. The optimised device, shown in Figure 2.14, had an A_r value of 2.3, strut width of 173 µm, strut thickness of 150 µm and strut length of 900 µm. This study provides a comprehensive consideration of both the material processing and important geometric parameters in the design of a BRS. Whilst consideration of the material processing is useful and accounts for the anisotropy of PLLA, the assumption of perfect plastic behaviour in both the axial and circumferential directions is unlikely to represent the true stress-strain response of PLLA. The study also assumes a strut thickness of 150 µm is commonplace among BRS. However, given the findings of the Absorb II trial (Serruys et al., 2016), and the conclusion that BRS should seek thinner strut designs, without compromise to radial strength to become clinically viable (Sakamoto et al., 2018), a strut thickness of sub 100 µm is necessary for next generation BRS. Moreover, whilst the weightings of the respective objective functions are subjective, the cross sectional area and radial collapse pressure describe the primary objectives of a coronary stent/scaffold and so these should perhaps be more highly weighted in the objective function. Lastly, whilst optimisation of a scaffold design in an idealised scenario has led to an improved scaffold design, many simplifying assumptions have been made which limit the applicability of the optimisation to a realistic clinical scenario. Deployment of the scaffold into a stenosed vessel section would be beneficial to understand the malapposition of the scaffold struts, which is a key determinant of patient outcome (Boeder et al., 2019). *In-vitro* validation data would also serve to improve confidence in the accuracy of the finite element model.

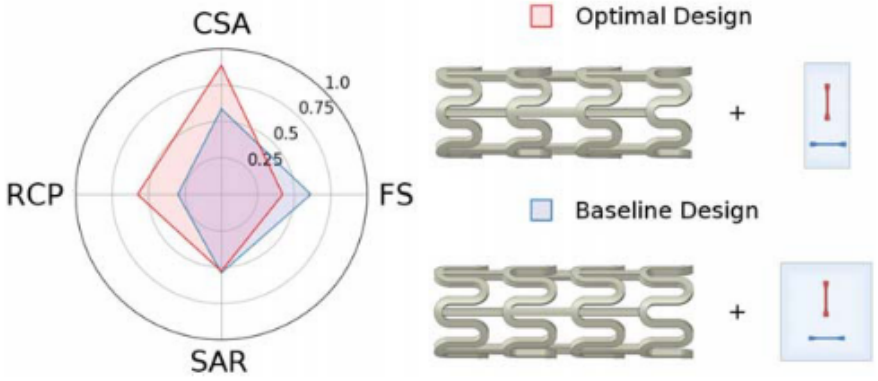

FIGURE 2.14: A visual comparison of the baseline and optimised designs with the performance for each metric (left) and the biaxial stretch ratio (right) visually represented. The baseline design shows equal stretching in both directions leading to isotropic behaviour whilst the optimised design shows greater pre-stretch in the axial direction (Blair et al., 2019b).

2.2 Material Property Modelling of PLLA

This section considers the development of a key material model to determine the stress response of polymers; the Bergstrom-Boyce parallel network model. The use of this model, in a variety of forms, along with other relevant material property models that seek to capture the mechanical response of polymeric BRS in FEA, are also explored.

Prior to the conceptualisation of BRS, research by Bergström and Boyce (1998, 2000) sought to capture the non-linear time dependant behaviour of elastomers via a constitutive material theory. *In-vitro* experiments using carbon filled chloroprene rubber were initially used to develop a material model via compression tests at different strain rates. Subsequent research by Bergström and Boyce (2001) focusing upon elastomers and soft biological tissues updated this original model which has then provided the foundation for the models used in contemporary FEA of BRS. Utilising parallel network rheology to decompose the total stress into elastic and viscoelastic plastic components is a defining characteristic of the resulting Bergstrom-Boyce model. Whilst the implementation of this model into finite element software and the additional complexity of calibration to material data has, in some cases, limited its use in contemporary simulations, the Bergstrom-Boyce model and models developed as a result of its inception are generally regarded as the optimal choice in polymer modelling, superseding isotropic linear elasticity combined with von Mises plasticity and isotropic hardening (Bergström, 2015).

Eswaran et al. (2011) conducted the calibration, development and validation of a parallel network material model directly based upon the work of Bergström and Boyce (1998, 2000, 2001). Firstly, uniaxial tensile tests were conducted on dogbone shaped specimens cut from PLLA tubes used for the manufacture of the Abbott Vascular Absorb BVS. To capture anisotropy, specimens from the axial and circumferential directions were tested and their stress-strain response to failure were recorded for three

different strain rates. The material model consisted of two networks, one containing an isotropic neo-Hookean element along with a viscoplastic power law flow element, whilst the second contained an anisotropic eight chain hyperelastic element to capture large strain behaviour. The model parameters were calibrated to the stress-strain data obtained from the uniaxial tests. A single ring of a scaffold based upon the Absorb BVS was used to validate the material model. The ring was tensioned via two cylindrical rods that moved in opposite directions to a given displacement. One set of experiments monotonically loaded the ring to failure, whilst another set carried out cyclic load-unload testing. The physical experimental setup was mimicked via FEA simulations and the results of the tests compared. The force-displacement curves for the different experiments were recorded and are shown in Figure 2.15. The ring tension validation confirmed that the model appeared to capture the behaviour of the scaffold very accurately with the force-displacement curves showing minimal disparity in results. To date, this remains the most complex material model to be utilised in the case of FEA of a BRS, albeit in a highly simplified scenario. It should also be remembered that not only is the scaffold geometry greatly simplified but the scaffold undergoes tension without its pre-stressed state due to crimping and balloon expansion which may significantly affect the force-displacement response.

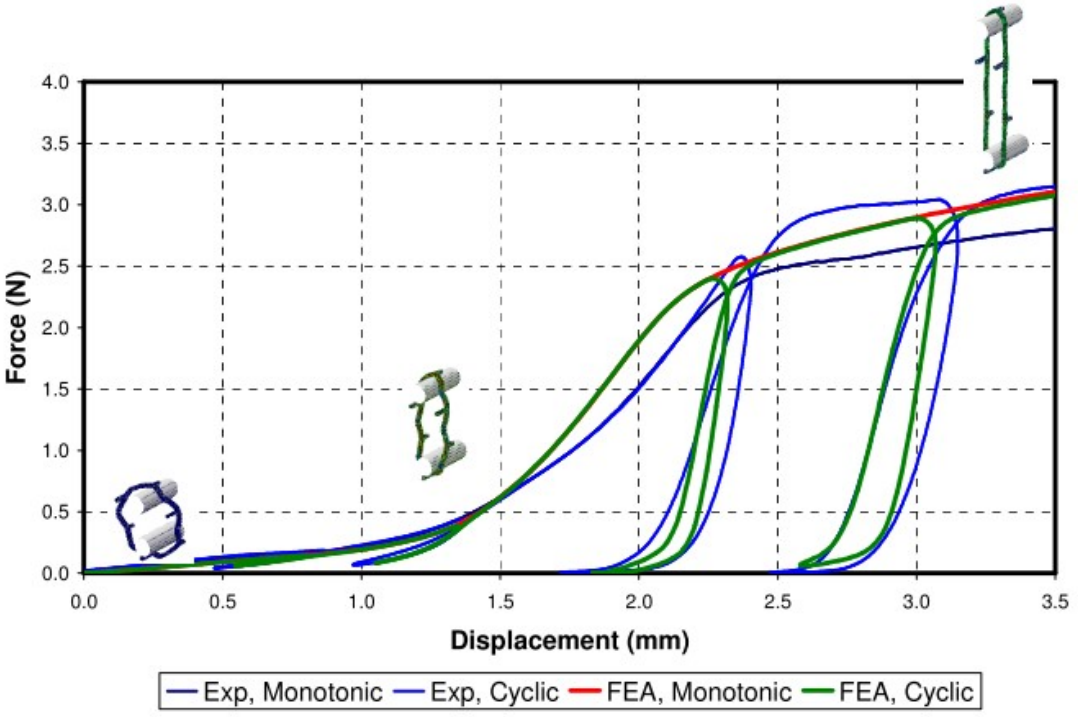

FIGURE 2.15: The *in-vitro* and *in-silico* single ring tension experiments for monotonic loading to failure and loading-unloading which utilise the parallel network Bergstrom-Boyce material model (Eswaran et al., 2011).

Bobel et al. (2015) employed the parallel rheological framework, a set of material models implemented in Abaqus/Explicit, partly based upon the work of Bergström and Boyce (1998, 2000, 2001) to simulate the deployment of coronary stents/scaffolds in

FEA. Simulated bench testing of the Multilink stent, the Abbott Vascular Absorb BVS and the Zig-Zag by Igaki-Tamai was conducted to obtain their radial strength, flexibility and longitudinal resistance. The scaffolds were manufactured in a post crimping state with pre-stresses applied to them before they were expanded via a displacement boundary condition, after which the scaffold was allowed to recoil. The first network arm of the isotropic viscoelastic plastic material model, used to capture the stress response of the PLLA, was represented by an Arruda-Boyce hyperelastic element, whilst the second contained a hyperbolic sine creep law element, representing the viscous term, in addition to the hyperelastic element. In terms of radial strength, the Absorb BVS design was the most successful and was the only design that could meet the minimum acceptable radial strength criteria of 0.04 MPa, whilst the Zig-Zag design fared worst. Both the Absorb BVS and Zig-Zag designs were compared to *in-silico* data from Grogan et al. (2012) in which the predicted radial strength agreed in both cases. A range of strut thicknesses and Young's moduli were also simulated for the Absorb BVS platform. A minimum thickness of 140 µm and minimum Young's modulus of 4 GPa were necessary to obtain the minimum acceptable radial strength. However, as previously discussed, a strut thickness of 140 µm is likely to be clinically unfavourable in terms of inducing late stent thrombosis in *vivo* (Foin et al., 2014; Sakamoto et al., 2018). In addition, a Young's modulus of 4 GPa lies at the upper end of the range of Young's moduli in the majority of published data. Therefore, whilst this research was the first to explore parallel network rheology implemented in Abaqus/Explicit for BRS, the suggested parameter values to obtain a BRS with acceptable mechanical performance are unlikely to be achievable.

Pauck and Reddy (2015) conducted FEA on three BRS designs employing an elasto-plastic material model calibrated to stress-strain data obtained from uniaxial tensile tests. Notably, this study was the first to utilise the Hill's yield function (Hill, 1948) to capture the anisotropy of PLLA in BRS, which, prior to this, was often disregarded. In addition, the model can be easily calibrated to *in-vitro* data without the requirement for an iterative process. The study sought to investigate the mechanical properties of three bioresorbable polymer scaffolds in terms of their percentage recoil, radial stiffness and radial strength after crimping and free expansion via displacement driven boundary conditions. In the case of each scaffold design, four Young's moduli were investigated, these were 0.9, 1.8, 3.6 and 9 GPa. Only the design based upon the Abbott Vascular Absorb BVS using a Young's modulus of 9 GPa achieved the minimum acceptable radial strength, quoted as 300 mmHg. Much like the study by Bobel et al. (2015), this research provides valuable insight into the use of a previously unused material model in the context of assessing the mechanical response of BRS using FEA. However, the comparative results of different scaffold designs only explore arbitrary changes in Young's modulus without discussion of the viability of achieving these values or indeed, detailed discussion of the reasoning behind differences in performance between the scaffold designs. Moreover, no *in-vitro* data was provided to validate the numerical findings.

Bobel et al. (2016) conducted experimental testing of dogbone shaped thin-film PLLA samples manufactured using the solvent casting method. The specimens were subjected to a number of mechanical tests to determine their pre-degradation characteristics. Uniaxial tensile testing in which the samples were loaded to a given strain before being rapidly unloaded was conducted, the results of which are shown in Figure 2.16. From this test it was evident that the material subjected to the fastest strain rate became significantly more brittle as it failed before unloading. The recovery of the material was tested in a similar way but unloading was conducted slowly by incrementally reducing the force over a given time. Cyclic loading and relaxation-creep tests were also undertaken. Testing was carried out at a variety of temperatures, shown in Figure 2.17 and Figure 2.19, respectively. As the temperature was increased from 25°C to 37°C, modest changes were evident in the stress strain response. Increasing the temperature to 42°C, above the glass transition temperature of PLLA, showed a significant drop in yield stress and initial elastic modulus. These temperatures represent room temperature (for reference), body temperature (where the scaffold is deployed) and a higher temperature at which scaffold crimping is undertaken. The displacement rate was varied between 1 and 100 mm/min, in Figure 2.16, which subtly increases the yield stress as this parameter was increased due to polymer chains having less time to rearrange to facilitate stress relaxation. However, displacement rates of 100 mm/min are likely to be counter to scaffold manufacturer advice as slow deployment of the scaffold is often recommended in clinical practice. Generally, very large levels of elastic and viscoelastic recovery are reported, as per the recovery test shown in Figure 2.19. This indicates that very large levels of recoil should be expected in BRS. However, this has not been reported in contemporary BRS in terms of the minimum lumen area achieved in *vivo* (Katagiri et al., 2019; Song et al., 2021). This study provides excellent insight into the behaviour of PLLA under different conditions which is beneficial when seeking to calibrate material models for *in-silico* testing. However, it must be remembered that the mechanical properties of PLLA will vary greatly depending upon the manufacturing method and pre-processing of the material. As previously discussed, PLLA has been observed to display anisotropy (Bergström and Hayman, 2016), which this research did not consider.

Bobel and McHugh (2018) sought to exploit the shape memory effect within PLLA to improve the deployment and recoil of polymeric BRS, using the parallel rheological framework in Abaqus/Explicit. Whilst shape memory effects of PLLA usually occur at temperatures much higher than 37°C, it was explored as to whether this can occur at lower temperatures. The material model varied from the previous work of Bobel et al. (2015), utilising a Neo-Hookean hyperelastic element, the Bergstrom-Boyce viscoelastic element and an isotropic hardening plastic element (although it is generally recommended that it is unnecessary to use the isotropic hardening model to capture the stress response of PLLA (PolymerFEM, 2021)). The natural time period of the simulation was preserved by simplifying the contact definitions, using displacement driven

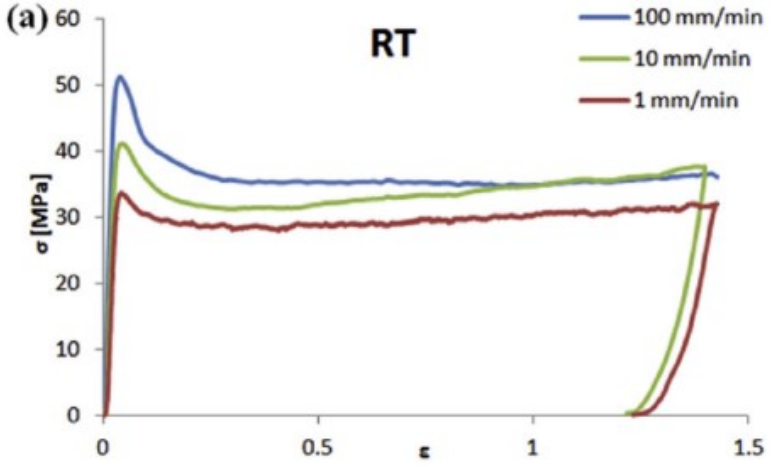

FIGURE 2.16: Uniaxial tensile tests conducted at three different strain rates on dogbone shaped samples of PLLA at 25°C. (Bobel et al., 2016).

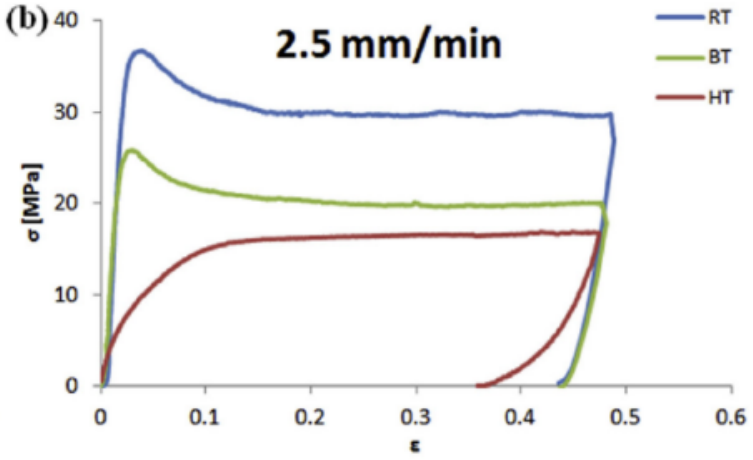

FIGURE 2.17: Load-unload tests for dogbone shaped samples of PLLA in which the sample is loaded and unloaded at a strain rate of 2.5 mm/min. The three tests are conducted at different temperatures of 25°C (RT), 37°C (BT) and 42°C (HT) (Bobel et al., 2016).

cylinders to crimp and expand the scaffold, which facilitated a coarse time increment of 1 x 10^{-4} s. Unfortunately, no *in-vitro* validation was undertaken to assess the model's accuracy. However, this study demonstrates the use of a high fidelity parallel network model to capture the behaviour of a BRS in FEA.

Wang et al. (2018) conducted *in-silico* and *in-vitro* testing of a thin-strut polymeric coronary scaffold provided by Boston Scientific. Firstly, dogbone specimens were cut from the axial direction of PLLA tubes used to manufacture the scaffold and tested via uniaxial tensile tests, which were conducted in both air and submerged in water at three different strain rates. A viscoplastic material model using linear isotropic behaviour and Johnson-Cook plasticity was calibrated to the stress-strain data obtained from the tensile testing. The model was then verified using FEA simulations to mimic the uniaxial tensile testing which showed good correlation. Simulations to replicate the crimping,

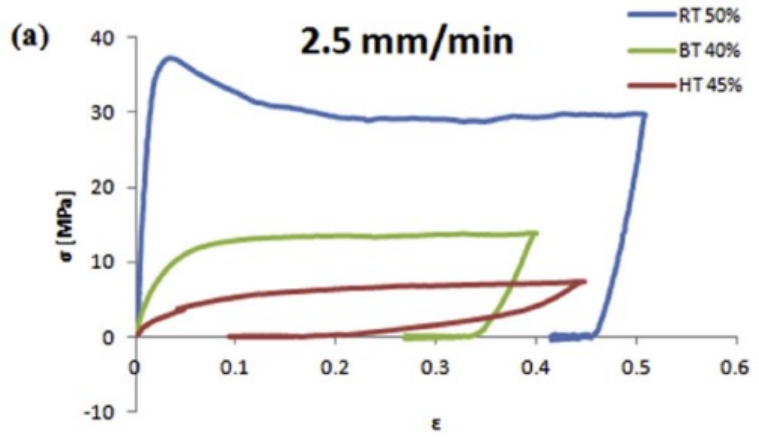

FIGURE 2.18: Recovery tests for dogbone shaped samples of PLLA in which the sample is loaded and unloaded at a strain rate of 2.5 mm/min. The three tests are conducted at different temperatures of 25°C (RT), 37°C (BT) and 42°C (HT) (Bobel et al., 2016).

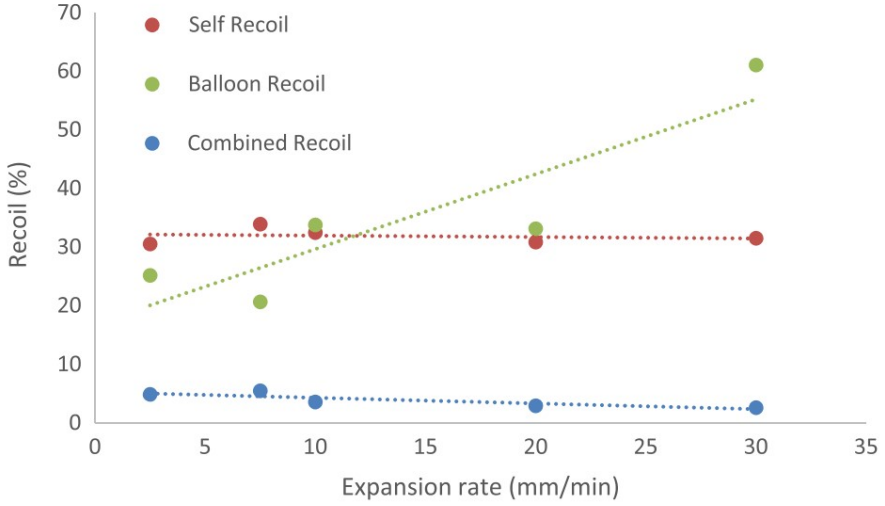

FIGURE 2.19: The effect of strain rate and deployment method on the percentage recoil of a BRS from *in-silico* testing conducted in Abaqus/Explicit using the parallel rheological framework (Bobel et al., 2016).

expansion, radial crushing and longitudinal stretching of the scaffold were conducted. These were all subsequently validated via *in-vitro* bench testing of the Boston Scientific scaffold. Interestingly, in the dry environment, scaffolds that were crimped at slower strain rates displayed a significantly lower level of stress compared to those crimped at a faster strain rate. However, in the submerged condition the number of elements containing high stress appeared not to be a function of strain rate, as shown in Figure 2.20. Although generally, the submerged condition showed lower stress levels in the crimped scaffold compared to the dry condition. In both dry and submerged cases a significant number of elements in the scaffold appear to exceed their fracture points. The study also observed micro-fractures in the scaffold after expansion *in-vitro*, shown in Figure 2.21, the number and severity of which would be a useful metric to evaluate

the clinical efficacy of BRS as strut fracture will be detrimental to the patient outcome. In conclusion, the study suggests that whilst interventionists are recommended to use low inflation rates when deploying BRS, the efficacy of this technique to reduce the stress state of the scaffold may be limited when submerged in the haemodynamic environment. This is an important finding and indicates that whilst significant time has been invested in modelling the strain rate dependency of polymers, in the case of simulating BRS delivery, this may be unnecessary in balloon expansion.

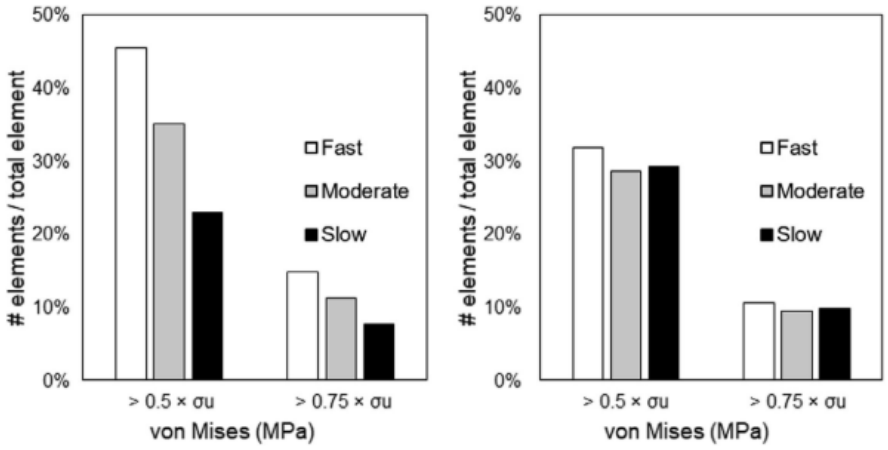

FIGURE 2.20: The percentage of elements that experience greater than 50% and 75% of the ultimate tensile stress, respectively. The left-hand plot shows the simulation for dry expansion of the scaffold, whilst the right-hand plot shows the simulation utilising the material model that assumes conditions resemble the haemodynamic environment (Wang et al., 2018).

FIGURE 2.21: Micro-cracks visible after the *in-vitro* expansion of a BRS at the inside of the crown apex. These could lead to strut fracture in *vivo* (Wang et al., 2018).

Blair et al. (2019a) conducted material model characterisation of biaxially stretched PLLA. The relative impact of biaxial stretching, temperature and strain rate on the Young's modulus and yield strength were assessed via *in-vitro* uniaxial tensile testing of dogbone shaped specimens of PLLA. A formalised design of experiments methodology was utilised to conduct experiments for the aforementioned design variables. It was ascertained that whilst the strain rate was found to have very little impact on both

the Young's modulus and yield strength, the post-processing temperature and ratio of stretching of the PLLA was found to greatly affect the material properties. Simple analytical equations were then developed for the Young's modulus and yield strength as a function of the biaxial stretch ratio and post-processing temperature which all achieved r-squared values of greater than 0.75. An anisotropic elasto-plastic material model, assuming transverse isotropy in the elastic region, was then calibrated for a single unit cube element in FEA using stress-strain data obtained from *in-vitro* testing. This showed good agreement between the physical and simulated data, as per Figure 2.22. Only in the case of the most severe anisotropy did the model deviate from the physical test data in the plastic regime, due to the limitation of the model to display only a single rate of plastic hardening for the two different material directions. This research usefully proposed a simple model to predict the Young's modulus and yield strength of PLLA after biaxial stretching at an elevated temperature. However, the study does not discuss the use of this pre-processing step in the commercial manufacture of BRS. Commonly, BRS are manufactured from extruded PLLA tubes which are then subjected to a pre-processing method. Unlike many previous studies, the anisotropy of PLLA is considered here, which is an important characteristic of the polymer behaviour, particularly when subjected to large levels of strain as is the case in scaffold expansion.

Antonini et al. (2021a) developed an *in-silico* simulation strategy to investigate the mechanical performance of the Fantom Encore BRS (Reva Medical, CA, USA). The focus of the study sought to investigate whether a material model can be developed despite a lack of stress-strain data to which the material model can be directly calibrated to. The parallel rheological framework was used in Abaqus/Explicit and Abaqus/Implicit to capture the viscoelastic-viscoplastic behaviour of the PLLA via a viscoelastic arm consisting of a hyperelastic Neo-Hookean element with a viscous plasticity power law in parallel with a viscoelastic arm consisting of a Neo-Hookean hyperelastic element with a power law strain hardening creep element. An *in-silico* simulation was setup to calibrate the parameters of the material model which comprised a tension test of a single repeating unit of the scaffold. Initial parameter values were selected based upon the literature before three values for each of the nine parameters were selected. This resulted in 19,683 tension simulations being undertaken. The force-displacement curves of these simulations were analysed to obtain the closest fit to the analogous *in-vitro* test that was conducted and the appropriate parameter values were selected. Subsequently, the final diameter of the scaffold is predicted after balloon expansion with a percentage error of less than 5%. The study also conducts a radial strength test of the expanded scaffold in *silico* which was calculated as 0.29 N/mm compared to a published value of 0.22 N/mm. Whilst the authors claim these values are comparable, the *in-silico* test represents a percentage error of 32%. This highlights that whilst it may be possible to replicate force-displacement curves between *in-silico* and *in-vitro* tests in simplified scenarios, predicting a metric such as radial strength for the entire scaffold provides an

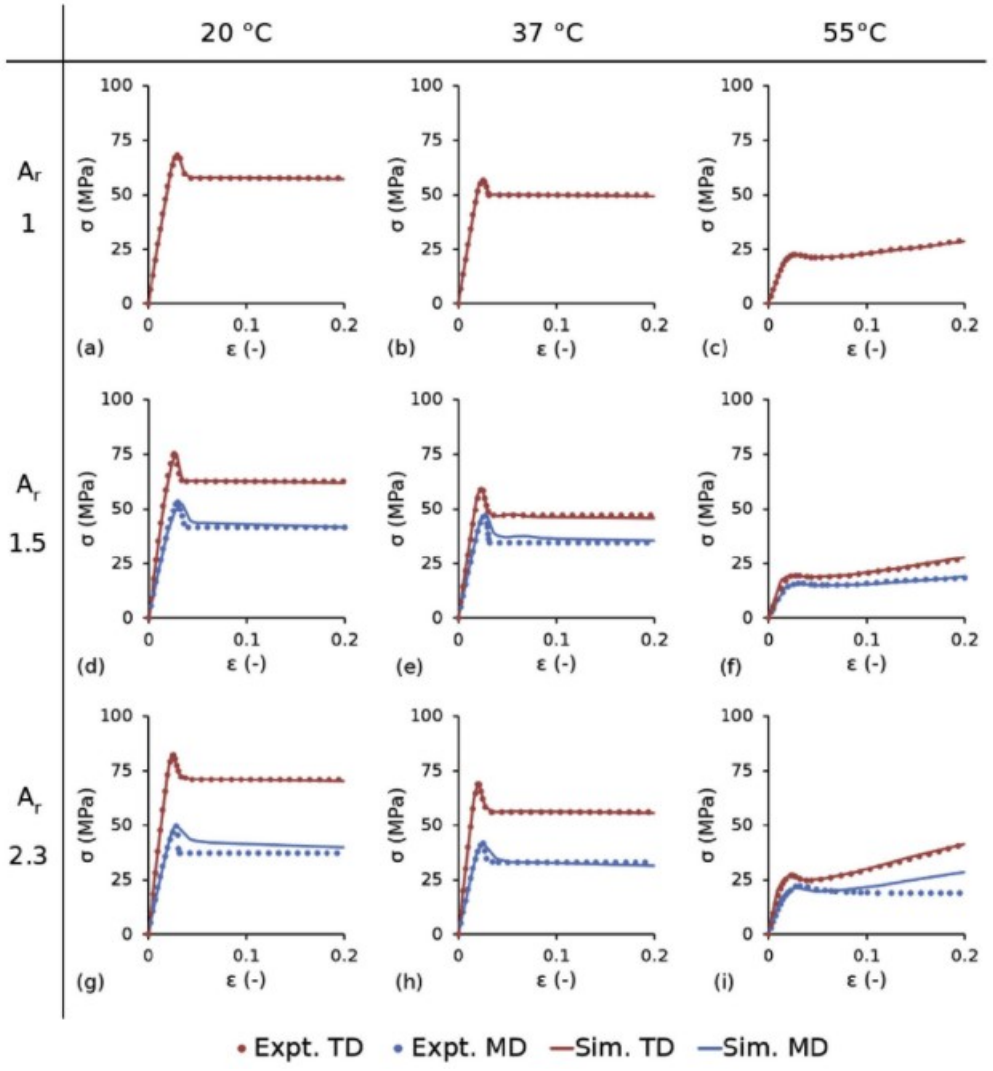

FIGURE 2.22: The effect of bi-axial stretching and temperature on PLLA samples subjected to uniaxial tensile testing. The bi-axial stretch ratio is given by A_r whilst *TD* refers to the transverse direction of the material and *MD* refers to the machine direction of the material. Excellent agreement is evident between the *in-vitro* and *in-silico* tests (Blair et al., 2019a).

additional challenge. Moreover, whilst this study demonstrates it is possible to replicate the behaviour of a BRS without the provision of stress-strain data, the methodology employed is convoluted. A huge number of FEA simulations were conducted and analysed, a process which could be greatly simplified by cutting a dogbone sample from the PLLA scaffold and subjecting it to uniaxial tensile testing to obtain stress-strain data. This would facilitate a simple analytical implementation of the model to be calibrated to this data using an iterative optimisation and would remove the need for the vast number of finite element simulations.

Following this, Antonini et al. (2021b) investigated the effect of temperature and strain rate on the crimping procedure of BRS, using *in-silico* testing of a scaffold based upon the Abbott Vascular Absorb BVS in Abaqus/Explicit. An elasto-viscoplastic strain rate

dependant Johnson-Cook material model was used. Several crimping simulations of varying complexity were undertaken. These ranged from simple loading and unloading through to a multi-step process that closely followed the manufacturers recommendations, including partial inflation of the expansion balloon to avoid strut distortion. The study highlights the importance of crimping the scaffold at a slow rate to minimise the risk of strut fracture due to excessive stress levels induced in the crimping process. This is consistent with the findings of Wang et al. (2020) as whilst they suggest the effect of strain rate is limited in a submerged environment, its effect is more pronounced in the dry conditions to which the scaffold is subjected in crimping. Therefore, if an accurate crimping simulation of the scaffold is to be undertaken then strain rate dependency is an essential feature of the material model. In addition, increased temperature was found to facilitate lower levels of stress in the scaffold struts, as shown in Figure 2.23 whereby the crimping temperature increases from left to right. Also of note are the levels of percentage recoil predicted which were in excess of 30% in *silico*. Values as large as this would not be feasible in clinical practice as this would result in unacceptable securement of the scaffold to the balloon-catheter, leading to slippage of the scaffold in *vivo*. Therefore, it is likely this metric was over-predicted. The study provides significant insight into the relative changes in stress levels that can be induced in polymeric scaffolds when crimped at different strain rates and temperatures.

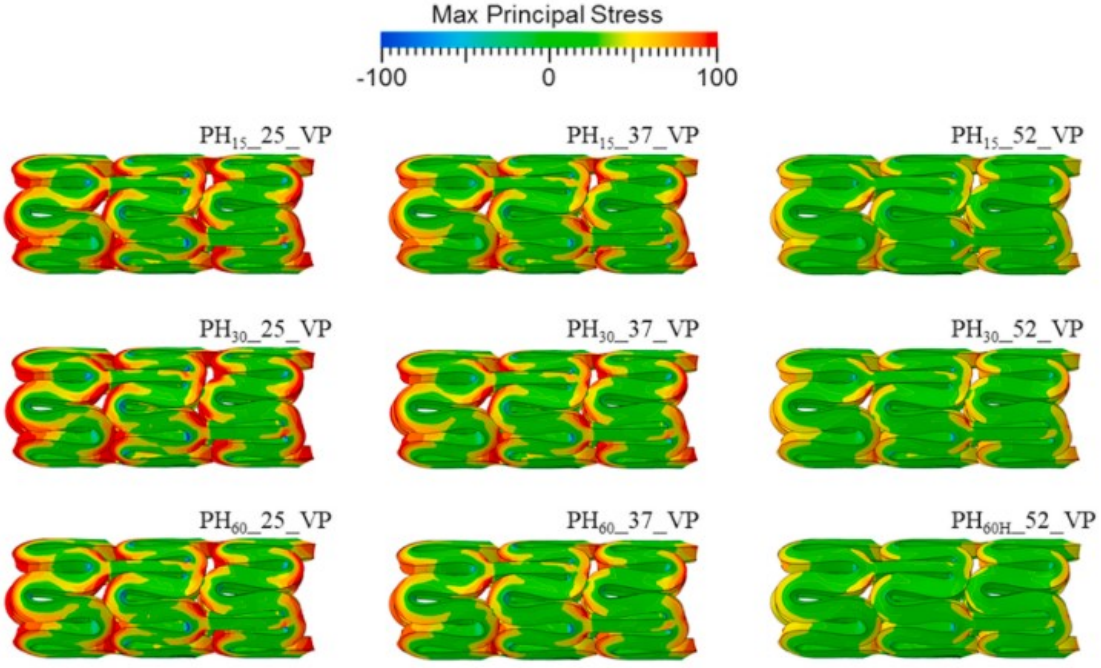

FIGURE 2.23: The stress levels within the struts of a scaffold based upon the Abbott Vascular Absorb BVS, crimped using different ambient temperatures and strain rates. The first subscript refers to the crimping duration in seconds (15, 30 or 60) whilst the second subscript refers to the ambient temperature in Celsius (25, 37 or 52). It is evident that an increase in temperature leads to a reduction in stress in the scaffold struts (Antonini et al., 2021b).

2.3 Clinically Realistic Scenarios

This section focuses upon FEA of coronary stents and scaffolds deployed *in-silico* into non-idealised scenarios. Whilst many studies neglect the scaffold/artery interaction and use free expansion to assess the mechanical response of the scaffold, this does present a significant simplification compared to the *in-vivo* situation. Therefore, *in-silico* deployment into realistic arterial segments is an important step in evaluating the performance of BRS.

In one of the earliest studies to advance upon the free expansion of coronary stents, Lally et al. (2005) assessed the stress field exerted by a stent on the wall of a coronary artery. This is an important consideration, given that restenosis is initiated by the response to damage to the vessel wall (Grech, 2011; Zhou et al., 2017). Two commercially available scaffolds; the S7 scaffold (Medtronic, Dublin, Rep. Ireland) and the NIR (Boston Scientific, MA, USA) were expanded inside an atherosclerotic coronary artery model and the stress on the arterial wall compared. The artery was modelled as an idealised cylindrical vessel of 4 mm outer diameter with a stenosis reducing the lumen diameter to 2 mm. Firstly, the tissue prolapse of the two devices was compared and found to reach a maximum value of 0.056 mm in the S7 stent compared to 0.124mm in the NIR stent. The percentage area of highly stressed (>4 MPa) arterial tissue was also assessed and found to be 4% in the S7 scaffold compared with 21% in the NIR stent. This is largely attributed to the higher recoil observed in the S7 device. The stress exerted on the vessel wall by the two stents is shown in Figure 2.24. The study concluded that whilst the recoil is slightly higher in the S7 stent (leading to a 4% decrease in the cross-sectional area, compared to an 8% increase in the case of the NIR stent), the S7 maintains sufficient patency to hold the artery open without being over rigid and causing excessive tissue prolapse leading to highly stressed arterial tissue. The study highlights the importance of a stent's ability to balance maintenance of the luminal area without causing excessive stresses within the arterial wall. Minimisation of recoil is a common objective function in the optimisation of coronary stents/scaffolds. However, the potential of a stent/scaffold to induce higher levels of restenosis due to very low radial recoil should certainly be considered as a result of these findings. The main limitation of the work concerns the idealised vessel geometry. Coronary arteries naturally exhibit significant curvature and tapering which increase the stress exerted on the arterial wall by the stent/scaffold.

Capelli et al. (2009) also studied the effect of stent design on tissue prolapse and stresses induced on the artery wall after delivery of the scaffold. The study noted that restenosis is influenced by the extent of damage to the vessel wall, the composition of the plaque, the stent design, the method of stent expansion and the fluid dynamics in the vicinity of the stent. It is asserted that structurally induced damage to the vessel wall is likely to be a function of the tissue prolapse through the cells of the stent which in turn can affect

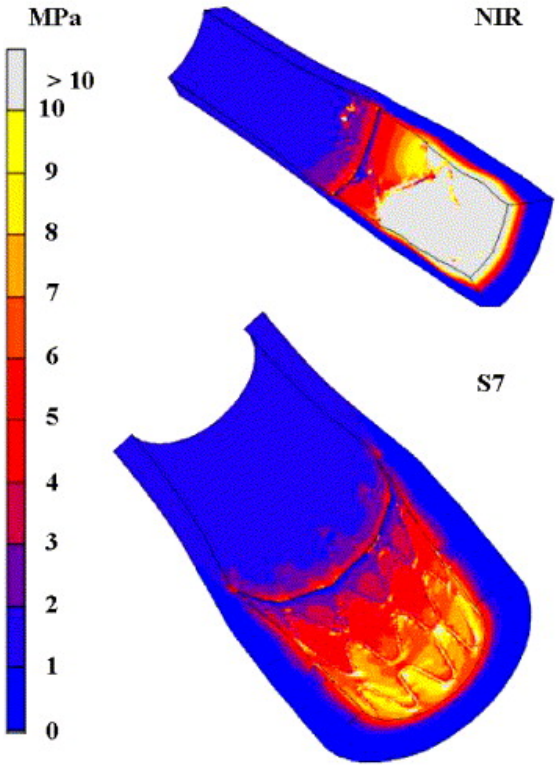

FIGURE 2.24: The stress exerted on sections of the arterial wall model by the NIR and S7 stents, expanded in *silico* (Lally et al., 2005).

the local haemodynamics. Five different stents were chosen to be deployed via the inflation of an elastic expansion balloon in a cylindrical arterial model. The printed area of the scaffold was not found to correlate with the maximum tissue prolapse. However, the prolapse index (PI) metric was developed to predict the level of tissue prolapse that occurs due to the stent struts. This was defined by the largest inscribable convex quadrilateral in the 'printed area' of a stent cell. The metric correlated well with the tissue prolapse observed in each design. No clear trend was ascertained between the restenosis and the geometrical design of a device, although the study noted that the results obtained could be compared to a clinical trial that evaluates restenosis for the same scaffolds. Whilst this study presents a number of significant simplifications over a realistic clinical situation, it displays an effective method of predicting maximum tissue prolapse from the stent cell geometry which could be employed in future studies and considered in ongoing stent/scaffold design.

Mortier et al. (2010) advanced upon an idealised coronary artery model by simulating the delivery of three different stent designs into a curved coronary artery bifurcation, shown in Figure 2.25. The arterial geometry was obtained from angiographic data of a patient's left main bifurcation. The Cypher Select (Cordis, CA, USA), Endeavour (Medtronic, Dublin, Rep. Ireland) and Taxus Liberté (Boston Scientific, MA, USA) stents were investigated. Two design modifications were made to the Cypher stent, one of which reduced the strut thickness for all rings to 100 µm from 140 µm, referred to as

CS_{thin} and the other reduced the end rings only to a thickness of 130 µm, referred to as CS_{end}. This was intended to reduce the maximum stress in the end rings and in the case of the first modification produce a device with greater flexibility to reduce straightening of the vessel as a result of the implant. After expansion of the device, each model was subjected to a radial strength test. The stents CS_{thin} and CS_{end} showed lower levels of circumferential stress than the baseline Cypher Select stent, which should lead to a reduced restenosis response. The circumferential stresses for the five stent designs are shown in Figure 2.26. Given its closed cell design, the Cypher Select showed the greatest radial strength of 0.15 MPa compared to 0.10 MPa in the case of both the Endeaver and Taxus Liberté. The altered Cypher stents displayed reduced radial strength of 0.11 in the case of CS_{thin} and 0.14 in the case of CS_{end}. Therefore, it was noted that CS_{end} represents a good design compromise as it did not show a significant reduction in radial strength but did reduce the circumferential stress in the end rings. The study highlights the extent to which vessel straightening occurs in curved sections of vessels, which significantly increased the circumferential stress on the artery in this case. However, there is no consideration of side branch access, which is imperative in the case of a bifurcation stent in order to ensure sufficient access to the side branch can be attained if further interventions are required.

Wei et al. (2019) studied the effect of plaque eccentricity and composition on the stent mechanical performance using FEA. Five different plaque eccentricities and four plaque compositions, as shown in Figure 2.27, were modelled to assess the recoil, plastic strain, foreshortening and stress distributions in the artery, plaque and stent. The five different eccentricities consisted of a range of circular plaques from 0% (a concentric lesion) to 80% eccentricity in increments of 20%. Effectively, this moves the lumen from the centre of the artery-plaque model radially outwards. The four plaque compositions range in complexity from a simple generalised plaque model described by a sixth-order reduced polynomial strain energy density function (also used to define the arterial behaviour), to a plaque consisting of the general plaque material, a lipid pool, calcified zones and a fibrous cap, the latter three described by the second-order Mooney-Rivlin equation. The stent was described by a simple isotropic elasto-plastic material model and deployed into the artery via a pressure applied to its inner face. Larger eccentricity resulted in greater recoil and plastic strain in the stent, whilst stent foreshortening increased above 20% eccentricity but then plateaued. Plaque von Mises stress was larger than in the artery and both were proportional to eccentricity. Notably, the low stiffness of the lipid pool was found to induce higher levels of plastic strain in the stent which led to lower recoil. The composition of the plaques was not found to greatly influence the von Mises stress on the artery or plaque, this was largely driven by plaque eccentricity. Overall, the study indicated that greater plaque eccentricity and complex composition led to a more vulnerable plaque with a greater percentage of highly stressed tissue that could present an increased risk of rupture.

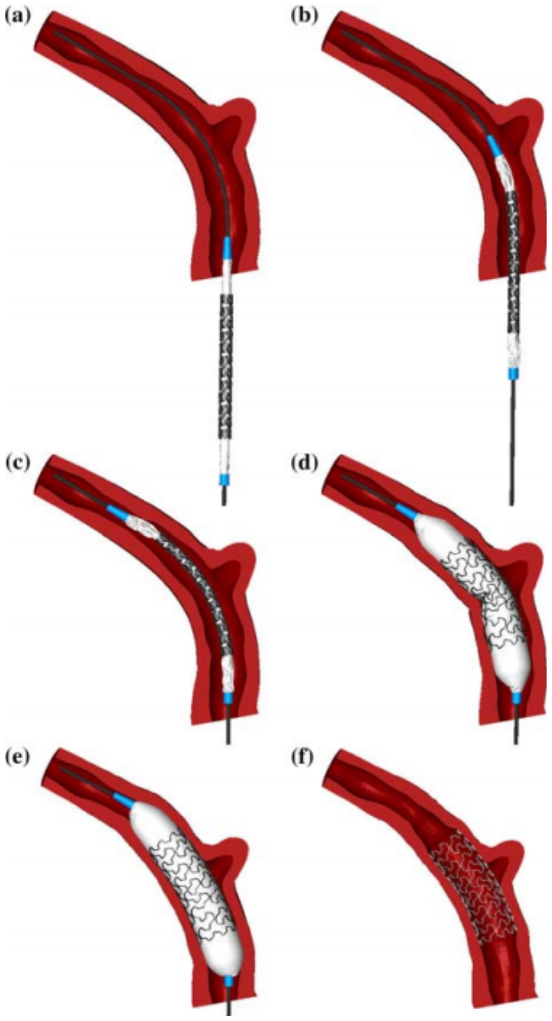

FIGURE 2.25: The *in-silico* delivery and expansion of a coronary stent into the left main and left anterior descending coronary arteries. Steps **(a)** to **(f)** detail the process of positioning the scaffold through to expansion and removal of the balloon Mortier et al. (2010).

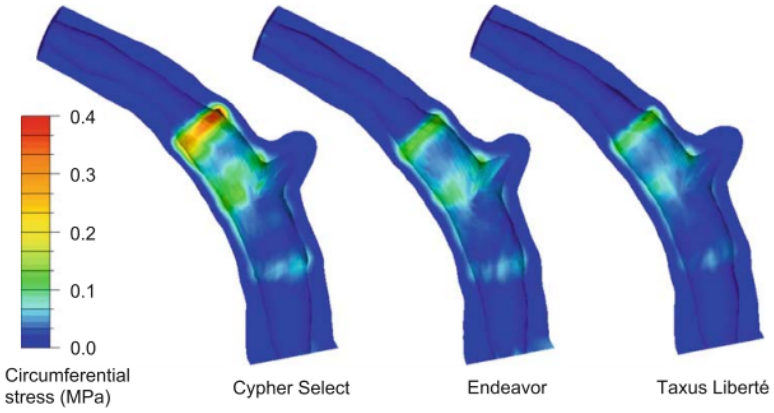

(A)

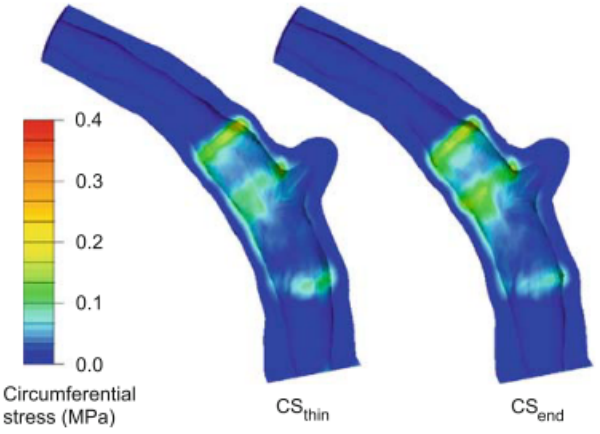

(B)

FIGURE 2.26: (A) The circumferential stresses for the three baseline stent designs and (B) the amended Cypher Select stent designs (Mortier et al., 2010).

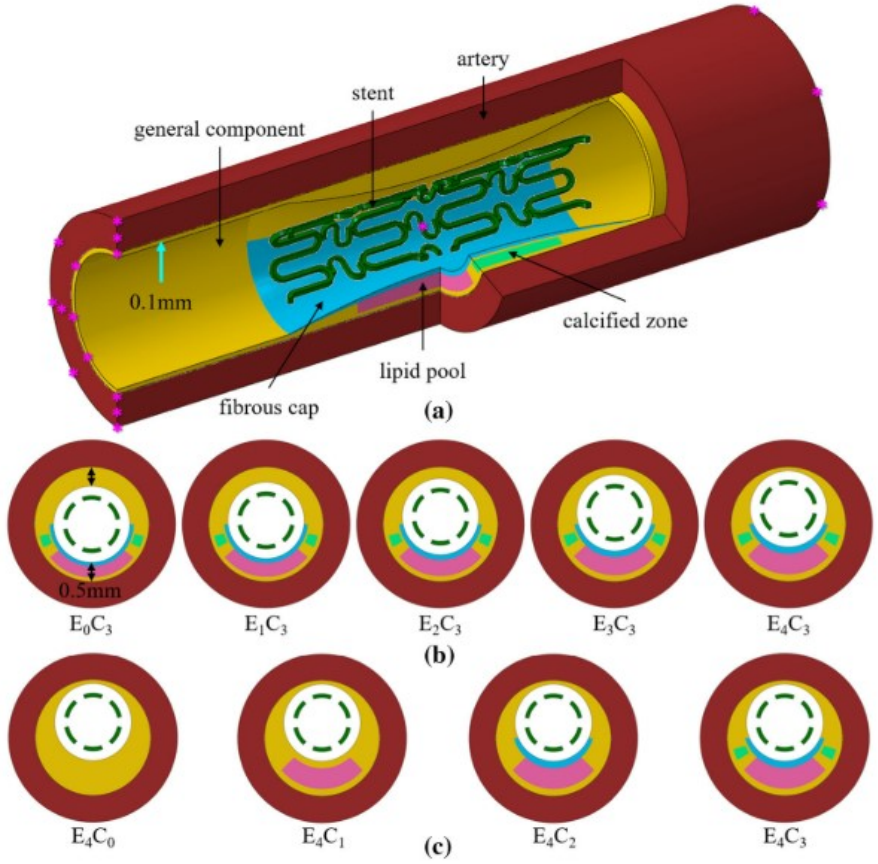

FIGURE 2.27: A 3D diagram of the complex plaque composition, (A), the range of plaque eccentricities, (B) and the range of different plaque compositions, (C), from the most simple generalised plaque (left) to the complex calcified plaque (right) used to investigate the stent/artery/plaque interaction (Wei et al., 2019).

2.4 Summary of Findings

In this section a summary of the findings from the review of literature is provided for each over-arching aim of the thesis.

2.4.1 FEA of Coronary Stents/Scaffolds

- The comparison of generic or commercially available stents/scaffolds and their mechanical properties is prolific. Work by Wang et al. (2006); Capelli et al. (2009); Li et al. (2014); Bobel et al. (2015); Pauck and Reddy (2015) and Qiu et al. (2017) are just a few examples. FEA of coronary stents/scaffolds is a well understood and mature field.
- Efforts to understand the underlying mechanics of the scaffold performance are limited, particularly since the work of Migliavacca et al. (2005). Stress and strain distributions are sometimes considered but rarely are their impact on clinical performance deduced or explained. This results in a limited understanding of how geometrical parameters impact the stress and strain distribution of the device and in turn how clinical outcomes and performance are affected.
- The equivalent plastic strain (PEEQ) is occasionally considered by studies but without the necessary detail to drive real insight into the cause of particular device performance.
- Foin et al. (2016b), Foin et al. (2016a), Wang et al. (2017) and Wang et al. (2020) all demonstrate the importance of using *in-vitro* data in addition to computational simulations to investigate scaffolds' mechanical response.

2.4.2 Material Property Modelling of PLLA

- The systematic comparison of different material models to ascertain their appropriateness is limited. To date, no clear consensus has been reached regarding which material model yields sufficiently accurate results to model the deployment of next generation BRS in *silico*.
- PLLA has demonstrated anisotropic behaviour which is recognised in some studies but without significant exploration or discussion, with the exception of Blair et al. (2019b), as to the necessity of modelling this behaviour.
- The strain rate dependency of PLLA is only necessary to model in crimping, as its effect upon the stress response of the scaffold has been shown to be minimal by Wang et al. (2018) when submerged in the haemodynamic environment, as is the case in balloon expansion.

- Several studies have utilised parallel network material property models to capture the viscoelastic-plastic behaviour of PLLA. The fundamental research of Bergström and Boyce (1998, 2000, 2001) was then applied in FEA studies by Eswaran et al. (2011), Debusschere et al. (2015), Bobel et al. (2015) and Bobel and McHugh (2018). These models were intended to supersede the use of simple isotropic linear elastic and Mises plasticity models, although these continue to be used in FEA of BRS.
- Wang et al. (2017) used an isotropic elasto-viscoplastic model which captured the mechanical behaviour of the scaffold when compared with *in-vitro* data. However, this study did not consider a thin-strut scaffold and provided very little detail regarding the *in-vitro* testing methodology.
- Validated *in-silico* results are yet to be presented that accurately predict the post-crimping diameter, post-expansion diameter and radial strength of a next generation thin-strut BRS.

2.4.3 Clinically Realistic Scenarios

- The topic of bifurcation scaffolding in the context of BRS is not explored in the literature. Previous studies by Mortier et al. (2009, 2010) provide good insight into coronary stenting in bifurcations but without detailed work considering how the design could be improved to facilitate better side branch access without compromising other structural properties.
- Whilst Blair et al. (2019b) and Pant et al. (2011) provide good examples of a systematic optimisation process, they both contain simplifying assumptions that may limit the efficacy of the optimised scaffolds in *vivo*. Therefore, *in-silico* studies should seek to simulate the scaffold in clinically realistic scenarios in addition to free expansion and expansion into idealised coronary arteries.

As a result of these findings, the doctoral research in this thesis will seek to explore the relationship between the design parameters of a next generation thin-strut BRS and its mechanical performance predicted via *in-silico* testing. An understanding of why particular mechanical phenomena occurs in crimping and balloon expansion will be sought to inform future scaffold design. Particular attention will be given to assess the equivalent plastic strain developed in the scaffold struts, as this is often not considered in the literature. A consensus upon the appropriateness of the material models investigated to date will be sought via a comparison of these different constitutive frameworks including both elasto-plastic and parallel network models. The importance of capturing the anisotropic behaviour of PLLA will also be investigated. This work will be underpinned by comparison with *in-vitro* data to validate computational findings and help derive greater insight into the scaffold mechanical response in both free expansion and expansion into arterial geometry. It is evident that exploring the scaffold

mechanical response beyond free expansion scenarios is necessary both in *silico* and in *vitro* to improve the prediction of scaffold performance and subsequent patient outcome. Therefore, *in-silico* scaffold deployment will be conducted into both idealised and patient specific coronary artery geometry and subsequently validated via analogous physical bench testing.

Chapter 3

Methodology

This section describes the employed methodology that is common across multiple chapters of this doctoral thesis. The computer aided design methodology, setup and underling theory of the finite element analysis, metrics used to describe the scaffold performance as well as the underlying constitutive laws of the material models investigated are discussed here.

3.1 Computer Aided Design Parameterisation

To perform parametric studies in FEA, it is necessary to first consider how best to parameterise the geometry in the computer aided design package.

The periodic shape of a single repeating unit of a coronary stent/scaffold is analogous to that of a trigonometric function. This can be parameterised using control point curves in which the position of each control point is defined by a 3D coordinate. However, such a method will result in many design variables which is impractical, particularly in the case of a design study when many design instances are required. Therefore, to minimise the number of design variables, a cosine term was used to describe the repeating unit's shape, given in Equation 3.1. This allows the amplitude of the repeating unit to be described by the coefficient a_n only, whilst ω, the phase parameter, describes the width of the repeating unit, tuned to ensure a scaffold outer diameter of 2.54 mm, as per the ArterioSorb^{TM} design. Use of a cosine term to describe the underlying shape of the scaffold rings affords significant flexibility to the scaffold parameterisation as further trigonometric functions can be superimposed upon the cosine term to form a Fourier series and describe alternative scaffold shapes without greatly increasing the number of design variables if required to do so.

$$f(x) = a_n cos(\omega x) \tag{3.1}$$

The following coefficients were derived to attain the approximate shape of the ArterioSorb^{TM} repeating units:

$$a_1 = 0.35 \tag{3.2}$$

$$\omega = 6.299 \tag{3.3}$$

A Python script was developed to parameterise the ring shape via the variables in Equation 3.1, as well as the crown and strut widths, such that they could be altered independently. The Python script calculates control lines orthogonal to the cosine curve at the midpoint of the crowns (local minima and maxima) and the mid-points of the sections between each crown (roots of the line). Two further lines are added equidistant from the straight section midpoints to maintain the strut width along the length of the straight section of the repeating unit. Control lines either side of the crown midpoints were also added to enforce tangency and ensure a smooth contour at the crown. A diagram of this construction geometry is shown in Figure 3.1. Each of the vertices of the control lines are then joined via interpolated third order NURBS curves (the line vertices acting as their control points) that define the 2D shape of the scaffold profile.

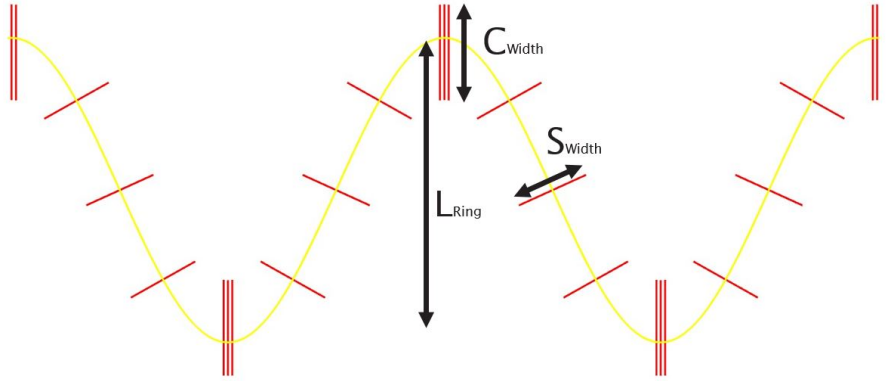

FIGURE 3.1: A repeating unit of the scaffold based upon the ArterioSorb^{TM} as constructed in Rhinocerus 5.0. The spine of the scaffold, defined by a cosine function is highlighted yellow whilst the control lines that define the 2D strut profile are highlighted red. The parameters L_{Ring}, S_{Width} and C_{Width} are labelled.

The Python script also provides the ability to vary the ring length and strut width along the scaffold length, the former of which is a feature contained within the ArterioSorb^{TM} patent (Bressloff et al., 2017). Design variables termed, the ring length factor (F_{RL}) and strut width factor (F_{SW}) define the rates of change of the ring length and strut width. The ring length (L_{Ring}) and strut widths at the crown, (C_{width}) and at the strut midpoint, (S_{width}) for each ring are given by:

$$L_{Ring} = a_1(F_{RL})^n \tag{3.4}$$

$$S_{width} = 0.17(F_{SW})^n \tag{3.5}$$

$$C_{width} = 0.22(F_{SW})^n \tag{3.6}$$

where n denotes the ring number starting at zero from the central rings and increasing symmetrically towards the scaffold end rings in unit increments. When F_{RL} and F_{SW} are set to unity a uniform ring length and strut width scaffold is defined. The baseline strut width value of 0.17 mm and crown width value of 0.22 mm, as per Equation 3.5 and Equation 3.6, respectively are variables that can be altered within the Python script.

The coordinate data of the vertices of the control lines, calculated from the Python script, was then passed to a Python script interpreted by Rhinoceros 5.0, a NURBS-based CAD modelling tool (1993–2008, Robert McNeel & Associates), to construct the geometry. Third order NURBS curves were used to interpolate the coordinate data and create the 2D scaffold profile.

The connector geometry was then added to the 2D scaffold outline. Straight sections joining every adjacent set of crowns at the central ring along with alternate sets of adjacent crowns at the subsequent open cell rings were defined. Flexibility of the connector layout was maintained within the Rhinoceros script to allow different configurations of open and closed cell designs. A scaffold configuration based upon the open cell ArterioSorb^{TM}, the design referred to herein as the 'baseline' design, is shown in Figure 3.2.

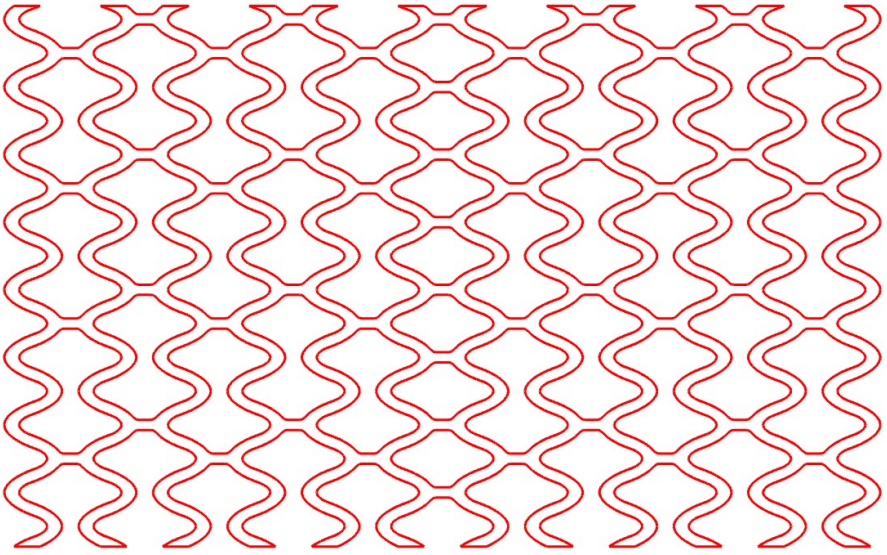

FIGURE 3.2: The 2D outline of the baseline scaffold design, based upon the open cell ArterioSorb^{TM} BRS.

The scaffold was then extruded to a uniform thickness of 0.095 mm and flowed into a cylindrical shape of outer diameter (OD) 2.54 mm. The finalised 12 ring scaffold is shown in Figure 3.3.

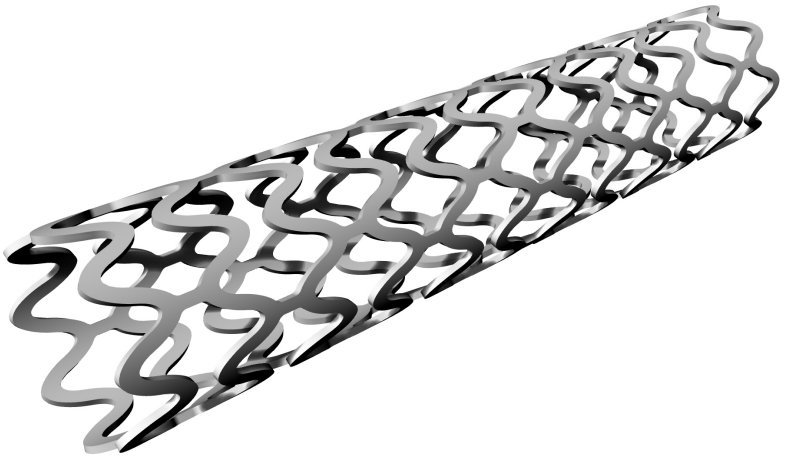

FIGURE 3.3: The open cell scaffold design, based upon the ArterioSorb^{TM} BRS. The scaffold consists of 12 rings, has a length 12.95 mm and a radial thickness of 0.095 mm.

3.2 Principles of Finite Element Analysis

3.2.1 Introduction

Finite element analysis (FEA) is a powerful technique, used to conduct analysis in a variety of physical domains including structural mechanics, electromagnetism, fluid dynamics and heat diffusion. In this thesis, FEA is used to predict and analyse the mechanical response of BRS. The underlying principles of the finite element method (FEM) are discussed here before a comparison of the explicit and implicit solution methods are presented.

The FEM is predicated upon the principle of minimum total potential energy (PMTPE). This is given in 3.7 and assumes that the potential energy in a system (Π) is the sum of the strain energy (U, stored energy that can be recovered) and the potential energy of external loading (V), which is the negative of the work done by external forces. The PMTPE assumes the static equilibrium of a system is the system with the minimum total potential energy and so this method seeks the minimum possible energy state of the system.

$$\Pi = U + V \tag{3.7}$$

Considering a dynamic problem, Hamilton's principle, given in 3.8, is applied and uses variational calculus, via the Euler-Lagrange equations to obtain the dynamic equation of motion for a system in which T is the kinetic energy and U is the potential energy. Further information regarding the underlying mathematics of the finite element method can be found in Zienkiewicz et al. (2005).

$$\mathcal{L} = T - \bar{U} \tag{3.8}$$

FEA spatially descretises the domain under investigation. That is, in the case of structural mechanics, the structure being analysed is split into smaller elements whose vertices are referred to as nodes. This is analogous to replacing the geometry under investigation with a series of interlinked springs and dampers representing the elements, whilst the interface between the elements are the nodes. This is a major approximation made by the FEM as the solution will be dependant upon the mesh density and how accurately the original geometry is captured. Boundary conditions are then imposed on the mesh to constrain it or apply forces, pressures or displacements in defined directions. In a 3D problem there are at most six possible directions of displacement at each node (three translational and three rotational), known as the degrees of freedom (DOF). The total DOF in the system is given by the number of nodes multiplied by the number of DOF at each node and provides a simple measure of the complexity of the system. Although, as boundary conditions are imposed on the system the DOF will reduce, so this should be accounted for prior to calculating the system complexity via the DOF. The solution process then calculates the respective displacements of each of the nodes. To do this, each element is assigned a shape function, that is, an assumed shape of the displacement field that describes its deformation. Once again, this is a key approximation made by the FEM as the assumed shapes of deformation may not accurately reflect reality. Therefore, elements with appropriate shape functions for the geometry must be chosen. Additionally, as the mesh is refined then the geometry of the structure will be more accurately captured and so a reduction in this type of error is guaranteed. Commercial FEA packages contain several element types with different shape functions and so appropriate selection of the element type is an important factor in the problem formulation. Once the displacement field can be calculated from the nodal displacements, via the shape functions, the strains and stresses within the geometry can be calculated. To formulate the problem as described above, a number of equation sets are required, these should relate:

1. Nodal displacements and displacement field
2. Displacement field and strain
3. Strain and stress

3.2.2 Dynamic Analysis

Two over-arching categories of FEA exist; static analysis and dynamic analysis. Whilst static analysis provides a simpler formulation of the problem that is faster to solve, dynamic analysis accounts for inertial effects and solves the problem temporally as well as spatially. The deployment of coronary stents/scaffolds in FEA is generally regarded as a quasi-static process in which the kinetic energy of the domain remains low throughout the analysis as a proportion of the internal energy of the system and so inertial forces are not dominant. This is ultimately a subset of dynamic problems that still demands a time dependant solution. Additionally, the problem is considered to contain nonlinear effects due to:

1. The complex contact interactions between the scaffold and balloon, and in more realistic deployment scenarios, the scaffold and artery.
2. Large displacements of the scaffold structure.
3. Material non-linearity due to the plastic deformation within the scaffold structure.

The governing equation of motion, resulting from the application of Hamilton's principle to a system, to be solved for the displacements in the the dynamic formulation of the FEM is given by 3.9. The DOF vector $\{d\}$, the vector of nodal displacements, is, in contrast to the static formulation, a function of time. Equation 3.9 gives the equation of motion to be solved for $\{d\}$. $[K]$ represents the stiffness matrix, $[M]$ the mass matrix, $[C]$ the damping matrix and $\{f\}$ the vector of forces acting on the structure.

$$[M]\{\ddot{d}\} + [C]\{\dot{d}\} + [K]\{d\} = \{f\} \tag{3.9}$$

The solution is obtained by marching forwards in time to calculate the DOF vector at the next time step using the DOF vectors at the current and previous time steps. There are two solution methods used in dynamic FEA; the implicit and explicit methods. Both methods have their relative merits and it is down to the user to decide upon the most appropriate for their analysis. These are now discussed before the chosen solution method is justified. Details of the explicit and implicit solution methods can be found in Appendix B.

3.2.3 Implicit vs Explicit

The stable time increment (δt, given in 3.10) is dependant upon the wave propagation speed of an element. Here, ρ is the density of the element, E is the element stiffness

and $\bar{L}$ is the characteristic length of the element. The minimum stable time increment must be less than or equal to the time it takes a stress wave to propagate the element, otherwise the simulation will become unstable and fail to solve.

$$\delta t \leq \sqrt{2}\frac{\bar{L}}{\sqrt{\frac{\rho}{E}}} \tag{3.10}$$

The explicit solution method will reach a solution more quickly than the implicit method for a given stable time increment as it does not need to carry out matrix inversion (which occurs in some numerical methods) or multiple iterations per time increment to solve for the DOF vector. However, the explicit method generally requires a small δt to ensure a solution can be obtained. Too large a time increment in the implicit method can lead to inaccurate results due to the many iterations required within each increment, causing a steady build up of numerical error. Additionally, the implicit method often uses significantly more system resources than the explicit method. Therefore, it is generally considered that the implicit methodology is best suited to long duration events where δt does not need to be small whilst the explicit method is better suited to impact events where very small time increments are necessary.

The deployment of a coronary stent/scaffold is considered a longer duration event as the crimping and expansion may happen over a time scale in the order of one second, with only a few millimeters of displacement. As previously mentioned, this results in relatively low kinetic energy throughout the process. However, the contact interactions between the stent/scaffold, crimping tool, balloon and artery must be accounted for. The Abaqus/Explicit solver facilitates the use of the general contact algorithm, considered more appropriate for complex contact interactions than the surface-to-surface contact algorithm, utilised in Abaqus/Implicit, which is likely to induce instability for complex interactions. As the explicit solution method requires such small time increments (in the order of 1e-7 s), the solution time for crimping and balloon expansion of a scaffold could become prohibitively large if simulated in its natural time scale. Therefore, the duration of the simulation can be reduced to a fraction of its real duration whilst ensuring that the inertia does not increase significantly. It is recommended that the kinetic energy of the system remains less than 5% of the internal energy for the duration of the simulation to maintain its quasi-static status. This reduction in period duration reduces the computation time without compromising the stability or accuracy of the simulation (DS SIMULIA, 2018). Abaqus/Explicit also utilises the mass scaling feature to improve the stability of the simulation. This increases the mass of some elements at the start of each step to increase the stable time increment. Naturally, this process must be controlled to ensure the increase in element mass does not result in a significant increase in kinetic energy of the system. A typical plot of the internal vs kinetic energy is shown in Figure 3.4.

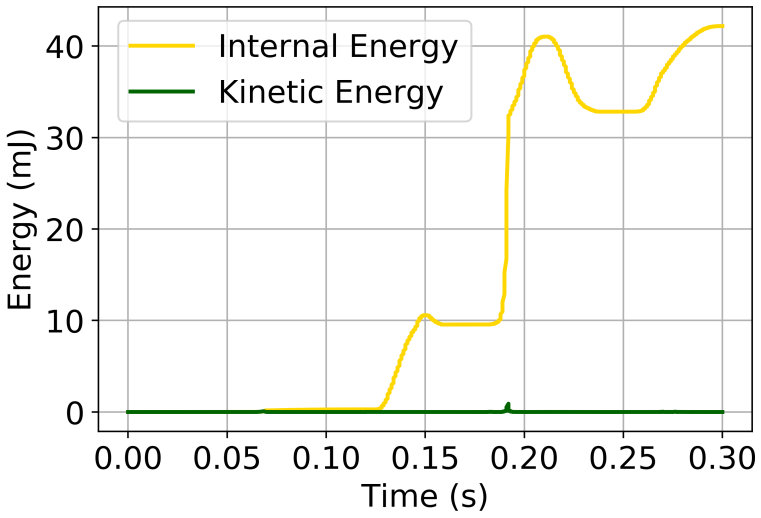

FIGURE 3.4: The internal vs kinetic energy for a FEA simulation of the crimping, balloon expansion and radial compression of a BRS in Abaqus/Explicit. The kinetic energy remains less than 5% of the internal energy, ensuring the simulation can be considered quasi-static.

Given the complexity of the contact interactions for the simulations undertaken herein, it was decided that the Abaqus/Explicit solution method would be used to simulate the deployment of BRS in FEA. This would ensure the simulations remain stable, can attain reasonable solution times and accurately represent the *in-vitro* testing to be conducted.

3.3 Setup of FEA Simulations

In this section, the setup of FEA simulations in Abaqus/CAE (DS SIMULIA) is detailed. Firstly, the mesh and time-step verification studies are presented before setup details of the free expansion simulations are discussed.

3.3.1 Mesh and Time-Increment Verification

A major approximation made within FEA is the discretisation of a continuous structure into a finite number of elements. Therefore, the results of FEA are dependant upon the mesh size and so a study was undertaken to ascertain the point at which mesh convergence is achieved. Similarly, for a dynamic simulation, the temporal discretisation of the problem into discrete time increments will also affect the results as this defines the number of increments in loading of the structure. Therefore, a time-increment refinement study was also undertaken.

In this case, a simple simulation setup was devised consisting of a single scaffold ring crimped from an OD of 2.54 mm to 1.1 mm and expanded to 3.5 mm OD using a rigid

cylindrical surface. The scaffold was meshed with C3D8R elements. Linear hexahedral elements are generally regarded as the optimum choice for this type of analysis, compared to linear tetrahedral elements as fewer are required to capture the same number of DOF and so a faster solution time will be achieved. Although fewer elements will not reduce the size of the finite element matrices there is generally a gain in efficiency in reducing the number of element computations. Whilst second order tetrahedral elements are available in Abaqus/Explicit, the Abaqus user guide recommends the use of linear hexahedral elements when the meshing algorithm allows due to the reduced computational cost (DS SIMULIA, 2018). A bilinear elasto-plastic material model was selected which had a Young's modulus of 4000 MPa, a yield strength of 100 MPa and an ultimate tensile strength 300 MPa at a plastic strain of 0.16. This was based upon initial tensile stress-strain data provided by Arterius Ltd.

The average von Mises stress, a metric commonly observed in mesh refinement studies, from two paths shown in Figure 3.5, around the scaffold structure was chosen as the metric to monitor the effect of the element size and time-step. In the case of the time-step refinement study, the results of which are shown in Figure 3.6(A), a mesh seed size of 0.04 mm was used. In the mesh refinement study, the results of which are shown in Figure 3.6(B), a time-step of 2e-7 s was used based upon previous experience in the research group.

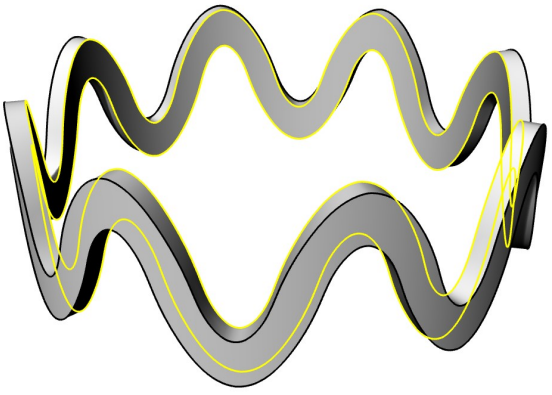

FIGURE 3.5: A single ring of the baseline scaffold design based upon the ArterioSorb^{TM} BRS. The paths used to monitor the mesh and time-step refinement are highlighted yellow.

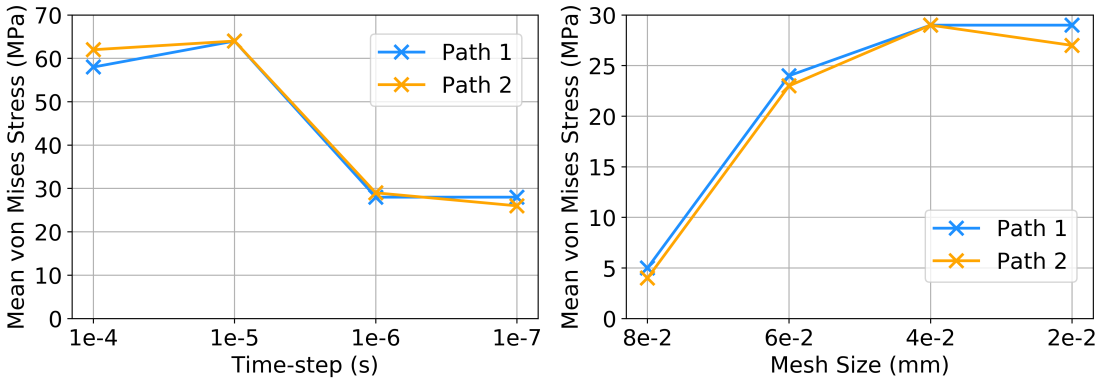

(A) (B)

FIGURE 3.6: (A) The time-step and (B) mesh refinement studies for a single ring scaffold, crimped and expanded via a rigid cylindrical surface. The mean von Mises stress is used to monitor convergence as the respective independent variables are refined.

It is evident in Figure 3.6(A) that refining the time-step beyond 1e-6 s leads to only fractional changes in the mean von Mises stress for the two paths. Therefore, it was decided that a time-step of 2e-7 s would be used for the subsequent simulations undertaken in Abaqus/Explicit. Previous experience of quasi-static simulations with complex contact interactions within the research group confirmed that this would be an appropriate value. A mesh size of 4e-2 mm was also decided upon as Figure 3.6(B) indicates convergence is achieved as the mesh reaches 4e-2 mm. The mean percentage change in mean von Mises stress of the two paths was just 3% as the mesh was refined from 4e-2 mm and 2e-2 mm. Whilst this mesh size only facilitates two elements across the scaffold thickness, the stress gradients in the radial direction are low as the dominant loading modes in crimping and expansion are bending about the crown apex causing tension/compression in the circumferential and axial directions. This mesh size achieved 5 elements across the scaffold width.

3.3.2 Free Expansion Simulations

The expansion of a stent/scaffold with the absence of arterial geometry provides a convenient method of comparison for the mechanical behaviour of coronary stents/scaffolds. Whilst, due to their simplified nature, they do not provide a complete assessment of the scaffold performance, they can help predict important metrics that contribute to the understanding of the scaffold mechanical response. Free expansion is used throughout the literature from early studies considering metallic stents through to contemporary studies considering polymeric BRS (Antonini et al., 2021b; Blair et al., 2019b; Bobel and McHugh, 2018; De Beule et al., 2008; Etave et al., 2001; Filipovic et al., 2021; Migliavacca et al., 2005; Wang et al., 2017). The free expansion simulations were devised to mimic the *in-vitro* testing of BRS conducted by Arterius Ltd such that the *in-silico* and *in-vitro* results were compared.

The free expansion simulations consisted of four parts within the assembly, which are shown in Figure 3.7.

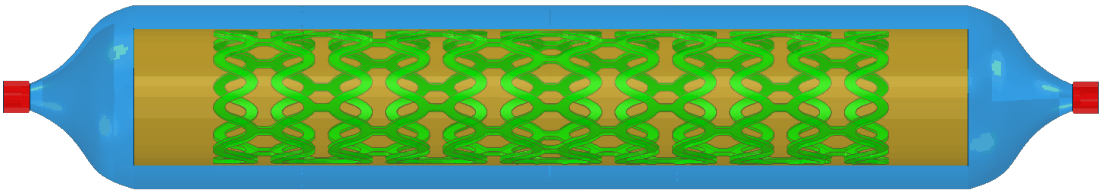

FIGURE 3.7: The assembly of the baseline scaffold (green), based upon the ArterioSorb^{TM} BRS, expansion balloon (blue), crimping cylinder (orange) and catheter tips (red) in Abaqus/CAE.

Scaffold Model

The scaffold was meshed using C3D8R reduced integration elements using the swept mesh algorithm. These are 8-node 3D stress elements with trilinear shape functions, with, as discussed in Subsection 3.3.1, a seed size of 0.04 mm.

Folded Balloon Model

A tapered balloon model, similar to that used by De Beule et al. (2008) of length 20 mm and diameter 3.5 mm was used to expand the scaffold. The isotropic elastic material model was used to describe the behaviour of the balloon where the Young's modulus, E and Poisson's ratio, ν were taken as 850 MPa and 0.4, respectively, similar to values used by Pant et al. (2012). Bilinear 4-node quadrilateral, reduced integration membrane elements were used to mesh the geometry. Whilst other studies do consider different balloon models as these will impact the scaffold mechanical response, this doctoral research assumes the same balloon material properties throughout.

Crimp Model

A cylindrical surface of length 20 mm was used to crimp and test the radial strength of the scaffold. The crimp was meshed using linear 4-node quadrilateral, reduced integration surface elements. The use of surface elements improves computational efficiency as the crimp is rigid and so does not have any structural properties associated with it, effectively it exhibits infinite stiffness.

Simulation Steps

The crimping, free expansion and radial crushing simulation consisted of the following steps to mimic the mechanical *in-vitro* testing of scaffold platforms conducted by Arterius Ltd (Leeds, UK):

1. Balloon compression. Two initial steps were required to ensure the expansion balloon resembled a tri-folded balloon as recommended by De Beule et al. (2008).

Three lines of nodes along the balloon's longitudinal axis, equally spaced circumferentially by 120° were constrained in all directions whilst three lines of nodes that intersperse the constrained nodes by 60° circumferentially were radially displaced inwards by 1.5 mm. The balloon compression process is shown in Figure 3.8(A) and Figure 3.8(B).

2. Balloon wrapping. The nodes displaced radially inwards were then constrained in all directions whilst a pressure was applied to one side of each of the three protruding balloon surfaces to wrap the balloon geometry. This process is shown in Figure 3.8(C) and Figure 3.8(D).

3. Crimping. The scaffold was crimped from its nominal diameter of 2.54 mm OD to 1.10 mm OD via the displacement driven crimping surface in which the nodes of the crimping surfaced were constrained from displacement in the circumferential and axial directions. The surface was then removed to allow the scaffold to elastically recoil.

4. Expansion. The scaffold was expanded by inflating the 3.5 mm balloon, pressurised to 7.5 atm. The balloon was then deflated to allow the scaffold to elastically recoil. Initial simulations confirmed this pressure gave a suitable and clinically relevant maximum scaffold OD of approximately 3.8 mm.

5. Crushing. The scaffold was crushed radially via the displacement driven crimping surface to a diameter of 2 mm. Again, the cylinder nodes were constrained to move in the radial direction only.

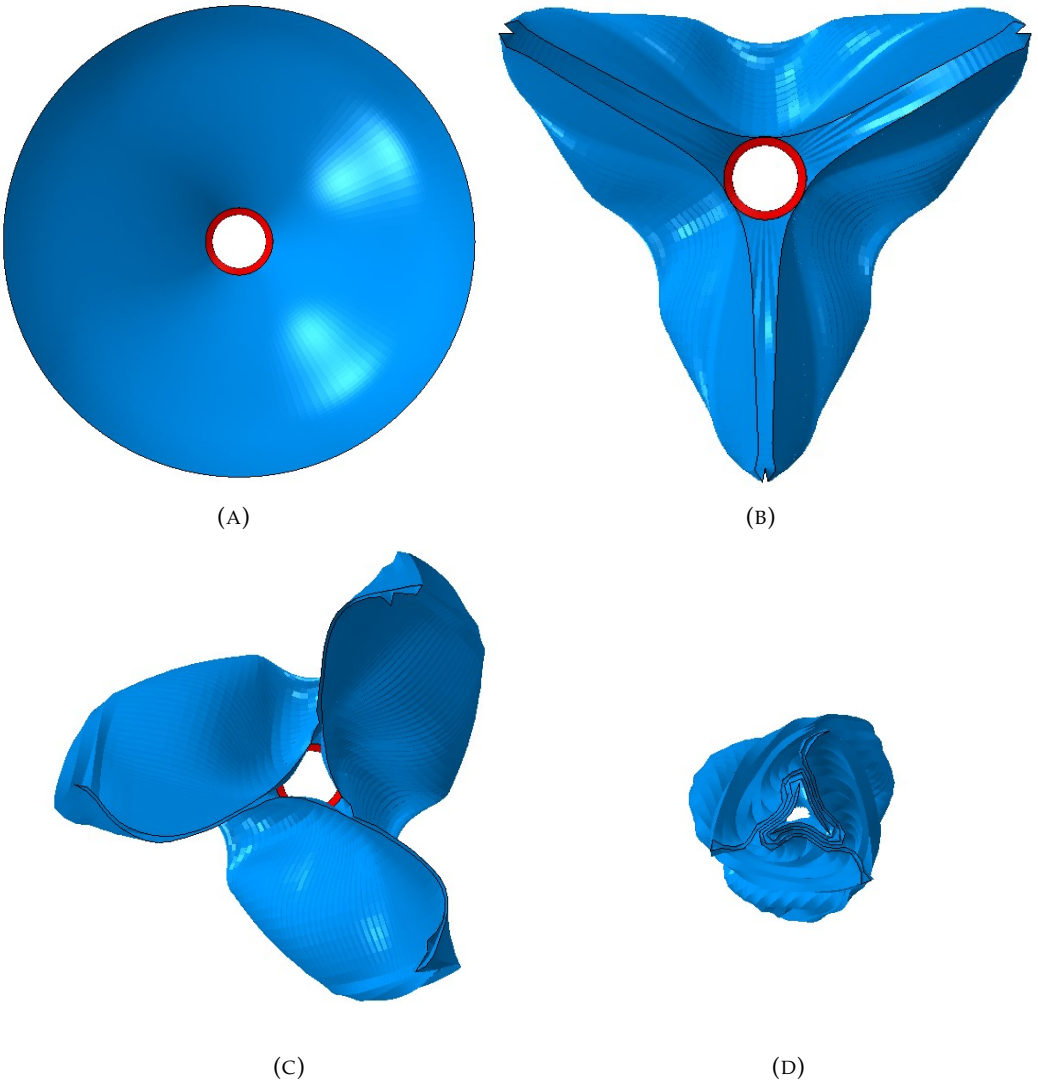

FIGURE 3.8: Cross-sectional views at the midpoint of the expansion balloon's longitudinal axis in the compression and wrapping steps showing; (A) the balloon prior to compression; (B) the balloon at the end of the compression step; (C) the halfway point of the wrapping process and (D) and the final state of the balloon after wrapping. The distal catheter tip, coloured red, is also visible.

As previously discussed, the Abaqus general contact algorithm was used in the simulations to define frictional tangential contact and non-penetration between the following pairs of surfaces:

- Crimp and Scaffold
- Scaffold (self contact)
- Balloon (self contact)
- Balloon and Scaffold

A friction coefficient of 0.1 was used, as per Debusschere et al. (2015). To improve the computational efficiency of the simulation, the contact pairs were switched off in the steps in which they were not required. A tie contact was also defined between the catheter tips and ends of the balloon whilst the catheter tips were themselves constrained in translation and rotation throughout the simulation. Four sets of nodes, each located on a crown apex at the central closed ring of the scaffold were constrained to move in the radial direction only throughout the duration of the simulation.

Each of the steps in the free expansion simulation had a duration of 0.06 s. This is significantly shorter than the natural time period of the scaffold crimping and expansion process. Running the simulation in its natural time period would lead to excessively long solution times, due to use of the conditionally stable Abaqus/Explicit solution method, as discussed in Subsection 3.2.3. Figure 3.9 shows the crimping, free expansion and radial crushing simulation for the baseline scaffold design.

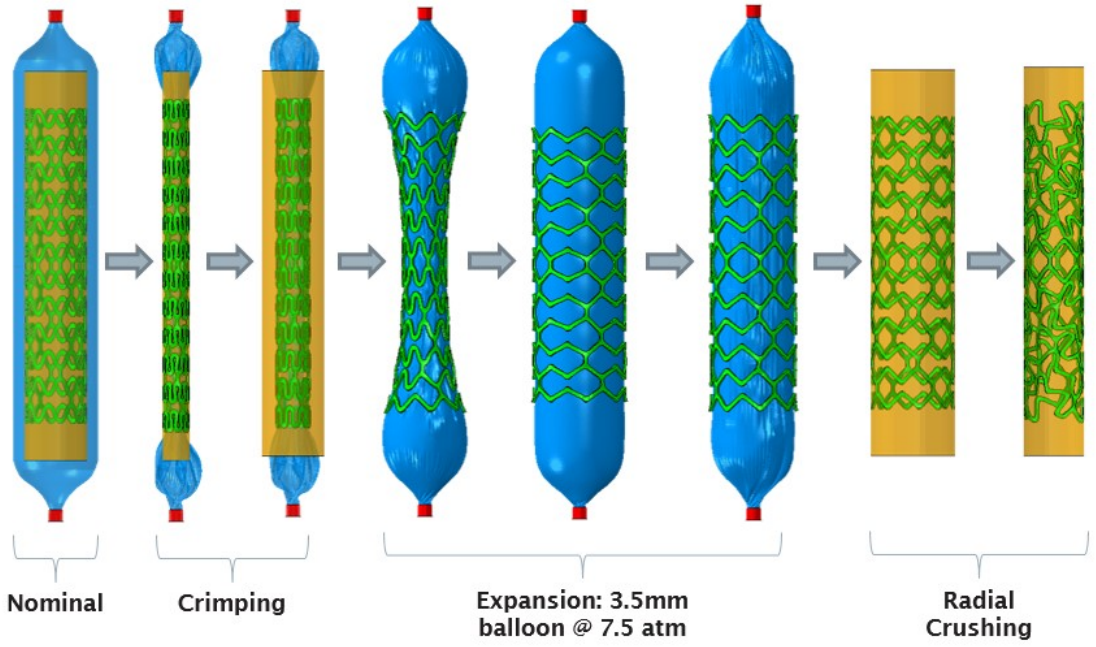

FIGURE 3.9: Free expansion simulation in Abaqus/CAE (DS SIMULIA) to mimic the *in-vitro* testing process undertaken by Arterius Ltd (Leeds, UK).

3.4 Assessment of Scaffold Mechanical Performance

Several metrics were chosen to assess the scaffold mechanical response in deployment and provide a quantifiable method of comparison between different material models and scaffold designs.

3.4.1 Performance Metrics

Specific Radial Strength

Radial strength defines the ability of a BRS to fulfill its primary objective of restoring the lumen area of a diseased coronary artery by resisting the crushing force of a plaque-/stenosis. Specific radial strength (SRS) is calculated by summation of the maximum reaction force of each of the nodes in the crimping cylinder in the final crushing step, divided by the scaffold length. This is defined as:

$$SRS = \frac{1}{l} \sum_{i=1}^{i=N_{cc}} F_i \tag{3.11}$$

where F_i is the reaction force of the i^{th} of the N_{cc} nodes that constitute the crushing cylinder and l is the length of the scaffold. The specific form of this metric is used to aid comparison between scaffold designs of different lengths which result if the variable ring length and strut width width parameters are exploited. Observation and accurate prediction of the radial strength of BRS is critical given the challenge of achieving acceptable radial strength in thin-strut BRS (Sakamoto et al., 2018; Bink et al., 2019).

Final Diameter

Final diameter (FD) measures the outer diameter of the scaffold once it has elastically recoiled post balloon expansion. This is a significant factor in predicting the post-procedural success as the interventionist will seek to achieve the greatest possible lumen area, a direct surrogate of FD in free expansion, to restore normal blood flow. The FD is dependant upon the SRS of the scaffold in the case of constrained expansion into coronary artery geometry and the elastic material behaviour that defines the acute recoil. The diameter of the scaffold rings was measured at multiple locations around the circumference and the mean value was calculated.

Percentage Recoil

Percentage recoil ($R_{\%}$) gives the percentage difference between the maximum diameter (MD) of the scaffold, when the balloon reaches the maximum inflation pressure and the final diameter (FD) post relaxation, defined as:

$$R_{\%} = (\frac{MD - FD}{MD}) * 100 \tag{3.12}$$

Recoil provides a convenient method of comparing the FD of different scaffold designs as each design will achieve a different MD for a given balloon inflation pressure, due to their different SRS. In the case of free expansion, the $R_{\%}$ is dependant upon the scaffold's elastic stiffness only whilst in constrained expansion this metric is also dependant

upon the radial strength of the BRS. Percentage recoil is commonly used to assess scaffolds' mechanical response in the literature (Schiavone et al., 2016; Bobel and McHugh, 2018; Antonini et al., 2021b).

Cell Area

Cell area (CA) is the space enclosed by a cell of the scaffold, as considered by Mortier et al. (2009). The CA is measured for a given ring number prior to deformation of the scaffold and so the cells around a scaffold's circumference are guaranteed to be of equal size. This defines the ease of access afforded by the scaffold to side branch vessels both for further interventions and blood supply to the distal coronary arteries. Whilst CA should be maximised to improve side branch access, the smaller cell area of BRS compared to metallic stents may be beneficial in terms of reducing tissue prolapse, as investigated by Lally et al. (2005).

Equivalent Plastic Strain

As discussed in Section 1.2, the equivalent plastic strain (PEEQ) is relied upon in BRS to maintain their post-expansion diameter and restore patency to a diseased coronary artery. Therefore, the magnitude and distribution of the PEEQ will greatly affect the scaffold's mechanical response and in turn the patient outcome. PEEQ is considered in the context of permanent metallic stents by Migliavacca et al. (2002, 2005) and more recently in the context of BRS by Wang et al. (2017).

The equivalent plastic strain is defined as:

$$\bar{\epsilon}^{pl} = \bar{\epsilon}^{pl}\Big|_0 + \int_0^t \dot{\bar{\epsilon}}^{pl} dt \tag{3.13}$$

where $\dot{\bar{\epsilon}}^{pl}$ is defined depending upon the material model in use, in this case utilising the Mises definition:

$$\dot{\bar{\epsilon}}^{pl} = \sqrt{\frac{2}{3}\dot{\epsilon}^{pl} : \dot{\epsilon}^{pl}} \tag{3.14}$$

where $\dot{\epsilon}^{pl}$ is the tensor containing the rate of plastic strain in each direction, subjected to the double dot product.

3.4.2 In-vitro Mechanical Testing

In-vitro testing was conducted by Arterius Ltd to validate the FEA simulations. The following process was used to deploy the scaffold and assess its mechanical response in free expansion:

1. The scaffold was crimped incrementally on to a balloon-catheter in a water bath heated to 42°C to an OD of 1.1 mm. The crimp was released and securement of the scaffold to the balloon-catheter was assessed.

2. The scaffold was then expanded in three stages whilst submerged in a water bath, heated to 37°C to mimic body temperature. A tri-folded balloon of diameter 3.0 mm inflated to 8 and then 16 atm of pressure was used followed by a 3.5 mm diameter balloon inflated to 7.5 atm. This multi-step process is similar to that used in a clinical scenario where post-dilation of the scaffold is commonplace. The OD of each ring in the scaffold was measured throughout the crimping and expansion process at the end of each step.

3. The expanded scaffold was radially crushed to an OD of approximately 2 mm using a Blockwise TTR2 radial force testing machine. The maximum force required in the crushing process was used to define the radial strength of the scaffold.

Referring to subsection 3.3.2, it is evident that there exists differences in the *in-silico* and *in-vitro* scaffold deployment methodologies. The use of a single balloon to expand the scaffold is employed to improve computational efficiency but it's effect compared to a multi-balloon strategy is subsequently explored in chapter 5. Additionally the use of an elevated temperature in crimping in *vitro* was not initially considered due to the limitations of test equipment available to conduct tensile testing of PLLA dogbone samples whilst in a heated water bath. However, the effect of this in silico is investigated in chapter 6.

3.5 Material Modelling of PLLA

The comparison of several material models along with the development of a novel material property model is undertaken in this doctoral research. Therefore, understanding of the underlying constitutive material theory is important if these models are to be exploited. In this section the constitutive theory of the relevant material models is discussed. The underpinning theory of continuum mechanics can be found in Sadd (2018) and Benham et al. (1996).

3.5.1 Isotropic Linear Elasticity with Mises Plasticity

Whilst generally considered most appropriate for the modelling of metallic alloys, the Mises yield function and isotropic hardening in combination with isotropic linear elasticity is used by a number of studies considering the deployment of polymeric BRS in

FEA (Wang et al., 2017; Qiu et al., 2017; Schiavone et al., 2016). It is important to consider this model due to its simplicity, ease of implementation and the fact it may provide a reasonable approximation of the macro-behaviour of the scaffold/PLLA combination.

Elasto-plastic models determine the stress state of a material as distinct elastic and plastic responses. In this case, the elastic response is calculated, based upon the linear isotropic elastic relations shown in Equation 3.15 in which σ_{nn} gives the direct stress, τ_{nm} the shear stress, ϵ_{nn} the direct strain and γ_{nm} the shear strain in each case where $n, m = 1, 2, 3$. The Young's modulus is given by E and the Poisson's ratio of the material is given by ν.

$$\begin{Bmatrix} \epsilon_{11} \\ \epsilon_{22} \\ \epsilon_{33} \\ \gamma_{12} \\ \gamma_{13} \\ \gamma_{23} \end{Bmatrix} = \frac{1}{E} \begin{bmatrix} 1 & -\nu & -\nu & 0 & 0 & 0 \\ -\nu & 1 & -\nu & 0 & 0 & 0 \\ -\nu & -\nu & 1 & 0 & 0 & 0 \\ 0 & 0 & 0 & 2+2\nu & 0 & 0 \\ 0 & 0 & 0 & 0 & 2+2\nu & 0 \\ 0 & 0 & 0 & 0 & 0 & 2+2\nu \end{bmatrix} \begin{Bmatrix} \sigma_{11} \\ \sigma_{22} \\ \sigma_{33} \\ \tau_{12} \\ \tau_{13} \\ \tau_{23} \end{Bmatrix} \tag{3.15}$$

It is convenient, in the context of coronary artery scaffold geometry, to define a cylindrical coordinate system, not only to aide application of the boundary conditions in FEA but also for the consideration of anisotropic material models. Therefore, herein direction 1 refers to the radial direction, direction 2 refers to the circumferential direction and direction 3 refers to the axial direction.

Returning to linear isotropic elasticity, after the elastic stress response has been calculated, the Mises yield function reduces the complex 3D stress state of the material and compares this to the material's yield stress, experimentally determined from the uniaxial tensile testing, to discern whether it has yielded and thus entered its plastic regime.

The Mises stress potential is given by:

$$f(\sigma)_{vm} = \sqrt{\frac{3}{2} S : S} \tag{3.16}$$

where S is the deviatoric stress, given by:

$$S = \sigma - \frac{1}{3} trace(\sigma)[I] \tag{3.17}$$

where σ is the Cauchy stress tensor and $[I]$ is the identity matrix.

If the Mises stress exceeds the current yield stress then the material is considered to have yielded. If yielding has not occurred then the stress is obtained via the linear elastic Hooke's law relations, stated in Equation 3.15. In the case of yielding, the equivalent plastic strain is defined by the approximation:

$$\bar{e}_{pl} = \frac{f(\sigma)_{vm} - \overline{\sigma}}{3\mu + h} \tag{3.18}$$

where $\overline{\sigma}$ is the current yield stress and h is the current hardening of the material. The shear modulus, given in Equation 3.19 is defined from the Hooke's law relations, stated in Equation 3.15.

$$\mu = \frac{E}{2(1+\nu)} \tag{3.19}$$

Whilst an iterative solution technique such as Newton's method may be used to calculate the equivalent plastic strain, for small increments such as those commonly used in the explicit solution technique Equation 3.18 is sufficient.

The updated yield stress is then calculated using the equivalent plastic strain. The total stress of the material is then updated using the relation:

$$\sigma = \frac{\overline{\sigma} 2G\hat{e}}{\overline{\sigma} + (3\mu\bar{e}_{pl})} + \sigma_{hyd} \tag{3.20}$$

where the term $2G\hat{e}$ gives the elastic deviatoric stress and σ_{hyd} gives the hydrostatic stress. The Abaqus user guide details the implementation of this constitutive theory (DS SIMULIA, 2018).

3.5.2 Anisotropic Linear Elasticity with Hill's Plasticity

As PLLA exhibits anisotropy, some computational studies have considered simple permutations of isotropic elasto-plastic theory to account for this (Pauck and Reddy, 2015; Blair et al., 2019b). PLLA can be conveniently described by approximating its elastic behaviour as transversely isotropic. Transverse isotropy specifies a single direction in which the material properties vary from an assumed plane of isotropy. This is most appropriate in the case of PLLA as the circumferential and radial directions can be assumed to have identical material properties whilst the axial direction deviates from these significantly, as evidenced in Appendix A.

E_p gives the Young's modulus in the plane of isotropy, whilst E_t gives the Young's modulus in the transverse direction, in this case, the axial direction of the scaffold. Equation

3.21 shows the stress-strain relationship for the elastic model whilst Equation 3.22 and Equation 3.23 define G_t, the shear modulus in the transverse direction and G_p, the shear modulus in the plane of isotropy in terms of the other parameters (Amadei, 1996; DS SIMULIA, 2018). The respective values of the Poisson's ratio, for the different loading directions are difficult to obtain experimentally, particularly for the radial direction. However, Equation 3.24 shows the relationship between ν_{tp} and ν_{pt}, which, in general are not equal and so assuming a value for ν_{tp}, ν_{pt} can be calculated. This is expected to be close to zero, given the increased stiffness in the transverse direction relative to the plane of isotropy.

$$\begin{Bmatrix} \epsilon_{11} \\ \epsilon_{22} \\ \epsilon_{33} \\ \gamma_{12} \\ \gamma_{13} \\ \gamma_{23} \end{Bmatrix} = \begin{bmatrix} \frac{1}{E_p} & \frac{-\nu_p}{E_p} & \frac{-\nu_{tp}}{E_p} & 0 & 0 & 0 \\ \frac{-\nu_p}{E_p} & \frac{1}{E_p} & \frac{-\nu_{tp}}{E_p} & 0 & 0 & 0 \\ \frac{-\nu_{pt}}{E_p} & \frac{-\nu_{pt}}{E_p} & \frac{1}{E_t} & 0 & 0 & 0 \\ 0 & 0 & 0 & \frac{1}{G_p} & 0 & 0 \\ 0 & 0 & 0 & 0 & \frac{1}{G_t} & 0 \\ 0 & 0 & 0 & 0 & 0 & \frac{1}{G_t} \end{bmatrix} \begin{Bmatrix} \sigma_{11} \\ \sigma_{22} \\ \sigma_{33} \\ \tau_{12} \\ \tau_{13} \\ \tau_{23} \end{Bmatrix} \tag{3.21}$$

$$\frac{1}{G_t} = \frac{1}{E_p} + \frac{1}{E_t} + 2\frac{\nu_{pt}}{E_t} \tag{3.22}$$

$$\frac{1}{G_p} = \frac{2(1+\nu)}{E_p} \tag{3.23}$$

$$\frac{\nu_{tp}}{E_t} = \frac{\nu_{pt}}{E_p} \tag{3.24}$$

Utilising the relations in 3.22, 3.23 and 3.24, the elastic response can be defined using the coefficients E_p, E_t, ν, ν_{tp} and ν_{pt} only.

The anisotropic plastic potential material model, first used by Pauck and Reddy (2015) in the context of polymeric BRS in FEA uses the Hill's yield function, an extension of the Mises function, to define the anisotropic yield of PLLA (Hill, 1948; DS SIMULIA, 2018). In Cartesian coordinates this is defined as:

$$f(\sigma) = \sqrt{\hat{F}(\sigma_{22}-\sigma_{33})^2 + \hat{G}(\sigma_{33}-\sigma_{11})^2 + \hat{H}(\sigma_{11}-\sigma_{22})^2 + 2\hat{L}\tau_{23}^2 + 2\hat{M}\tau_{31}^2 + 2\hat{N}\tau_{12}^2} \tag{3.25}$$

where the constants $\hat{F}$ to $\hat{N}$ are given by:

$$\hat{F} = \frac{\sigma_0^2}{2}\left(\frac{1}{\bar{\sigma}_{22}^2} + \frac{1}{\bar{\sigma}_{33}^2} - \frac{1}{\bar{\sigma}_{11}^2}\right), \hat{G} = \frac{\sigma_0^2}{2}\left(\frac{1}{\bar{\sigma}_{33}^2} + \frac{1}{\bar{\sigma}_{11}^2} - \frac{1}{\bar{\sigma}_{22}^2}\right), \hat{H} = \frac{\sigma_0^2}{2}\left(\frac{1}{\bar{\sigma}_{11}^2} + \frac{1}{\bar{\sigma}_{22}^2} - \frac{1}{\bar{\sigma}_{33}^2}\right) \tag{3.26}$$

$$\hat{L} = \frac{3}{2}\left(\frac{\tau_0}{\bar{\tau}_{23}}\right)^2, \hat{M} = \frac{3}{2}\left(\frac{\tau_0}{\bar{\tau}_{13}}\right)^2, \hat{N} = \frac{3}{2}\left(\frac{\tau_0}{\bar{\tau}_{12}}\right)^2 \tag{3.27}$$

the ratios $\bar{\sigma}_{nn}^2/\sigma_0^2$ and $\bar{\tau}_{nm}^2/\tau_0^2$ define the ratio of yield stress in the direction nm (where $n, m = 1, 2, 3$) to the yield stress in the tabulated stress-strain data used to define the plastic behaviour in the Abaqus/CAE implementation of this model. In the case of the transversely isotropic PLLA, this effectively facilitates a constant scaling of the stress in the plastic regime for the axial direction, by the factor $\bar{\sigma}_{33}^2/\sigma_0^2$, in which the reference stress is given by the yield stress in the circumferential direction.

3.5.3 Viscoelasticity

Developed prior to the conceptualisation of polymeric BRS, the Bergstrom-Boyce (BB) model is a viscoelastic-plastic material property model that has been demonstrated to accurately predict the stress-strain response of elastomeric polymers (Bergström and Boyce, 1998, 2000, 2001). The original model has been adapted and implemented within Abaqus/Explicit using the parallel rheological framework (DS SIMULIA, 2018). The rheology of the model explored in this doctoral research, shown in Figure 3.10, is represented by two network arms acting in parallel, one of which contains an eight chain hyperelastic element whilst the second contains the eight chain hyperelastic element in series with a viscous flow element. Variants of the BB model are explored in the context of BRS deployment in FEA by Eswaran et al. (2011), Debusschere et al. (2015) and Bobel et al. (2015); Bobel and McHugh (2018). Notably, the parallel rheological framework (PRF) implementation of the Bergstrom-Boyce model does not facilitate anisotropy, as per the model used by Eswaran et al. (2011).

Polymers used in medical applications, such as PLLA, exhibit nonlinear time-dependent behaviour such as viscoelastic recovery and strain rate dependency in addition to differences in stress response in loading and unloading and permanent deformation, which are all captured by the Bergstrom-Boyce material property model implemented in the PRF (Bergström and Hayman, 2016).

The BB model is predicated on the multiplicative decomposition of the deformation gradient. Given that the parallel networks act in tandem, the deformation gradient applied to network A, F_A, is equal to the deformation gradient applied to network B, F_B. F_B is then decomposed into two stages, an elastic step, F_B^e and a viscous step,

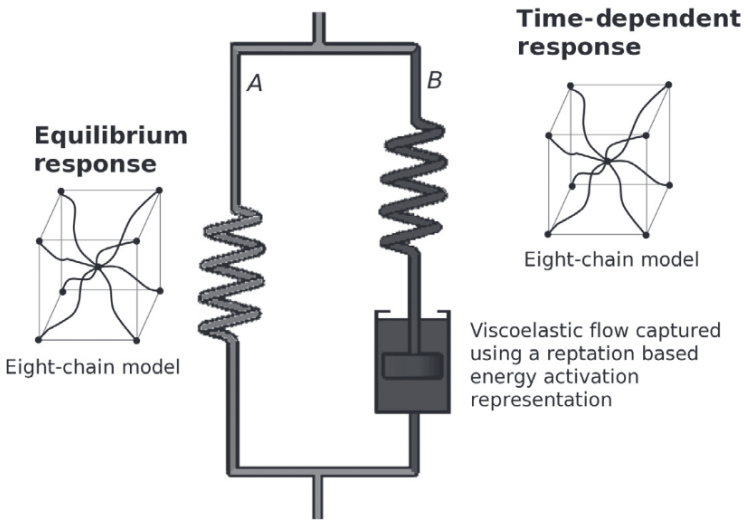

FIGURE 3.10: The parallel network rheology of the Bergstrom-Boyce model as implemented in Abaqus/Explicit. An eight chain hyperelastic element, network A, acts in parallel with another eight chain hyperelastic element in series with a viscoelastic flow element, network B (Bergström, 2015). Alternative hyperelastic and viscous elements are available to use in Abaqus/Explicit.

F_B^v, as per Equation 3.28. The total Cauchy stress is calculated by summation of the contributions from each network.

$$F_B = F_B^e F_B^v \tag{3.28}$$

The hyperelastic element in network A is given by the eight chain model, commonly referred to as the Arruda-Boyce hyperelastic model (Boyce and Arruda, 2000). The stress response of this element is given in Equation 3.29:

$$\sigma_A = \frac{\mu}{J\overline{\lambda^*}} \frac{\mathcal{L}^{-1}(\overline{\lambda^*}/\lambda^{lock})}{\mathcal{L}^{-1}(1/\lambda^{lock})} dev[b^*] + \kappa(J-1)[I] \tag{3.29}$$

where μ is the shear modulus, $\overline{\lambda^{lock}}$ is the maximum chain stretch and κ is the bulk modulus. These are all material parameters that must be calibrated to stress-strain data. $\mathcal{L}^{-1}$ gives the inverse Langevin function which can be approximated in numerous ways to ease implementation in a numerical code (Jedynak, 2015). The deviatoric operator is given by dev. $\overline{\lambda^*}$ is the effective chain stretch, b^* is the distortional left Cauchy green tensor, $J = det(\mathbf{F})$ and $[I]$ is the identity matrix (Bergström, 2015; DS SIMULIA, 2018).

The hyperelastic element in network B, the Cauchy stress response of which is shown in Equation 3.30, is similar to that in network A, with the shear modulus, μ, scaled by the dimensionless parameter, s. The superscript e denotes that the parameter relates to the elastic part of network B.

$$\sigma_B = \frac{s\mu}{J_B \overline{\lambda_B^{e*}}} \frac{\mathcal{L}^{-1}(\overline{\lambda_B^{e*}}/\lambda^{lock})}{\mathcal{L}^{-1}(1/\lambda^{lock})} dev[\mathbf{b}_B^{e*}] + \kappa(J_B^e - 1)[I] \tag{3.30}$$

The time dependent creep rate, $\overline{\dot{\epsilon}}^{cr}$, which is used to calculate the deformation gradient for the elastic part of network B, necessary to calculate the Cauchy stress defined in Equation 3.30 is defined in Equation 3.31:

$$\overline{\dot{\epsilon}}^{cr} = (\lambda^{cr} - 1 + \xi)^C \left(\frac{\bar{q}}{q_0}\right)^m \tag{3.31}$$

where

$$\lambda^{cr} = \sqrt{\frac{1}{3}(F_B^v : F_B^v)} \tag{3.32}$$

in which the operator ':' is the double dot product, $\bar{q}$ denotes the deviatoric Kirchhoff stress whilst ξ, C, q_0 and m are all material parameters. The time derivative of the viscous part of the deformation gradient for network B is calculated using Equation 3.33.

$$\dot{F}_B^v = \overline{\dot{\epsilon}}^{cr} (F_B^e)^{-1} \frac{\bar{q}}{||\bar{q}||_F} F_B \tag{3.33}$$

in which $||\bar{q}||_F$ gives the Frobius normal of the deviatoric Kirchhoff stress. Equation 3.33 is subsequently integrated with respect to time to obtain the deformation gradient for the viscous part of network B at the next time increment, given in Equation 3.34.

$$F_B^{v1} = F_B^{v0} + \int_{t_0}^{t_1} \dot{F}_B^v \, dt \tag{3.34}$$

Lastly the elastic part of the deformation gradient, necessary to calculate the Cauchy stress defined in Equation 3.30, is calculated via the expression:

$$F_B^{e1} = \frac{F_B}{F_B^{v1}} \tag{3.35}$$

A detailed mathematical description of the BB model can be found in Bergström (2015).

3.6 Summary

This chapter describes the methodologies employed across multiple chapters within this doctoral thesis. The free expansion of BRS in FEA is used in Chapters 4 - 7 with the addition of deployment into coronary artery geometry in Chapter 7, the methodology of which is explained there. Similarly, the metrics described in this chapter to quantify the scaffold performance are used in Chapters 4 - 7, with the PEEQ investigated in Chapter 4 only. Chapters 4 and 5 use the elasto-plastic material models with Chapter 6 exploring the PRF and Chapter 7 employing both model frameworks.

Chapter 4

Equivalent Plastic Strain in a Scaffold with Variable Ring Length and Strut Width

4.1 Introduction

The equivalent plastic strain (PEEQ), developed in the struts of BRS in crimping and balloon expansion, has been considered by very few previous studies. This metric is inherently relied upon by coronary stents/scaffolds to maintain their target diameter in the diseased vessel and avoid excessive elastic recoil. Migliavacca et al. (2002) investigated the effect of a number of design variables on the performance of a slotted tube stent, although in that case, only the maximum PEEQ was considered rather than its distribution across the scaffold struts. More recently, Wang et al. (2017) considered PEEQ to optimise the geometry of the crown apex of a BRS and predict the onset of crazing, validated with *in-vitro* data. We propose that PEEQ is an important but little understood metric in the case of coronary scaffolds, particularly as it may help to provide insight into the avoidance of brittle and ductile strut fracture. Excessive levels of strain, a surrogate of PEEQ, will lead to strut fracture whilst insufficient PEEQ will result in higher levels of elastic recoil, due to the limited amount of permanent deformation in the scaffold struts. Therefore, understanding the relationship between scaffold geometry, PEEQ and mechanical performance is important. Specifically, understanding the distribution of PEEQ across the crown width and around the scaffold ring, where PEEQ is greatest is critical. Moreover, the isotropic hardening model, employed herein, utilises the equivalent plastic strain as an internal state variable to determine the yield stress and hardening of a material.

Another important, but often neglected consideration for all coronary scaffolds is the side-branch access they facilitate. Maximising the open cell area of the scaffold could

help to improve side-branch access and minimise interventional techniques required in *vivo* to alter the shape of the expanded scaffold which can induce clinical complications, compromise scaffold structural integrity (leading to strut fracture) and exacerbate vessel wall damage. Excessive damage to the vessel walls is commonly linked with poor clinical outcomes, particularly restenosis (Hoffmann et al., 1999; Grech, 2011) due to the onset of neointimal hyperplasia (Farb et al., 1999; König et al., 2002). Fracture of the scaffold struts can provide a site for thrombus formation (blood clotting) which in many cases can be fatal. Moreover, BRS are likely to have small cell areas due to their short struts in comparison with metallic stents. Therefore, exploring how to improve this geometric property is critical if BRS are to be adopted into routine clinical practice.

In this chapter we utilise geometry control to investigate the PEEQ, specific radial strength (SRS), percentage recoil ($R_{\%}$) and cell area (CA) of a variable ring length and strut width BRS using a 25 point design study, representing modifications to the baseline scaffold design, based upon the ArterioSorb^{TM} BRS. The scaffold design was explored by exploiting the ArterioSorb^{TM} patent via variation of the ring length and strut width along the scaffold length. A more detailed study of five scaffold designs which observed the distribution of PEEQ in critical locations in the scaffold struts was also undertaken. Finite element analysis (FEA) was used to simulate the crimping and balloon expansion which mimicked the *in-vitro* free expansion of scaffolds by Arterius Ltd. Results from the bench testing of the baseline design were used to compare with the *in-silico* data for the crimped diameter (CD), maximum diameter (MD) and final diameter (FD) in addition to the aforementioned metrics. Additional *in-vitro* data including the over-expansion of the baseline design were considered to provide further insight into BRS mechanical behaviour, particularly related to the adverse effects observed in the excessive development of PEEQ.

4.2 Methodology

4.2.1 Scaffold Geometry

To explore variable ring length and strut width designs, the design variables F_{RL} and F_{SW} which define the rates of change of the ring length and strut width, as per the geometry parameterisation in Section 3.1, were both constrained between 1.04 and 0.96 to limit investigation into scaffolds with excessively wide/narrow and long/short struts. Initial simulations and observation of the scaffold geometry confirmed that exceeding these limits would not be beneficial for the scaffold design.

The following parameters remain constant across all 25 designs; ring length of the central closed rings (0.7 mm, measured peak to trough for the underlying cosine function used to define the ring shape), ratio of the crown to strut width (220/170), thickness in

the radial direction (0.095 mm), number of rings (12) and nominal outer diameter (2.54 mm). The 3D geometry of the baseline scaffold design is shown in Figure 4.1.

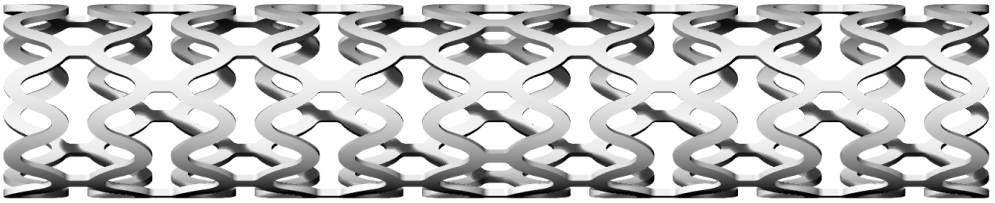

FIGURE 4.1: The baseline scaffold design based upon the open cell ArterioSorb^{TM} BRS.

One half of the four scaffold designs from each corner of the design space are shown in Figure 4.2. Observing this figure, the relative changes in ring length and strut width along the scaffold length, emanating from the central closed ring outwards are evident.

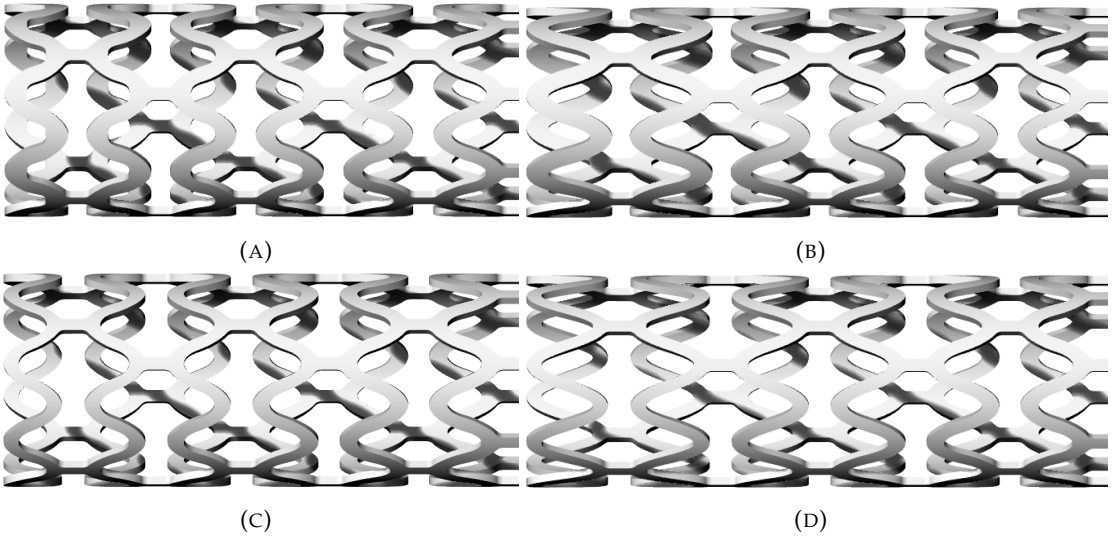

(A) (B)

(C) (D)

FIGURE 4.2: The scaffold designs located in each of the four corners of the design space given by; (A) design $F_{RL} = 0.96$ and $F_{SW} = 1.04$; (B) design $F_{RL} = 1.04$ and $F_{SW} = 1.04$; (C) design $F_{RL} = 0.96$ and $F_{SW} = 0.96$ and (D) design $F_{RL} = 1.04$ and $F_{SW} = 0.96$.

4.2.2 Sampling Plan

The optimised Latin hypercube is a commonly used method to design a sampling plan, the details of which can be found in Appendix C and Forrester et al. (2008). In this case, the optimised Latin Hypercube provided 20 sampling points in addition to the baseline configuration and the designs from each corner of the design space, totalling 25 design points. Whilst the population of a two parameter design space is relatively simple, using this technique ensured the sampling plan had good space filling properties, without using equispaced data points in a regular grid format which can be liable to misrepresenting the underlying functions.

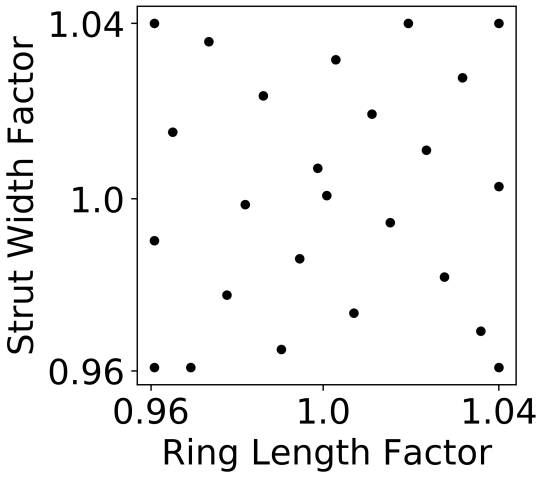

FIGURE 4.3: The sampling plan for a 25 point design study in a two parameter design space, using an optimised Latin hypercube.

4.2.3 FEA Setup

The finite element simulations consisted of the steps detailed in Subsection 3.3.2 in which the scaffold was crimped from its nominal diameter of 2.54 mm to 1.1 mm before being expanded via an elastic balloon at 7.5 atm. Lastly the scaffold was crushed from its post-expansion diameter to approximately 2 mm OD. The FEA simulations were conducted on the University of Southampton Iridis 4 high performance computing cluster. Each simulation was run on a 2.6 GHz Sandybridge 16-core node and took approximately 6 hours to complete.

The material behaviour was described by an elasto-plastic model containing linear elasticity and the Hill's yield function, as detailed in Subsection 3.5.2 and also used by Pauck and Reddy (2015). The Young's modulus (E) and Poisson's ratio (ν) were input into Abaqus/CAE (DS SIMULIA) using the data obtained from the 50 mm/min uniaxial tensile tests, presented in Figure 4.4. The Young's modulus, E is obtained from calculating the average of the slopes of the linear portions of the circumferential and axial directions for the 50 mm/min case. The Poisson's ratio, ν is assumed given the difficulty in measuring this parameter. Both of these elastic parameters are given in Table 4.1.

Young's Modulus (MPa) E	Poisson's Ratio ν
3250	0.3

TABLE 4.1: The values of the material parameters that define the elastic behaviour of the PLLA scaffold.

The data that defines the plastic behaviour of the PLLA scaffold is given in Table 4.2, obtained from the 50 mm/min uniaxial tensile tests for the circumferential direction of the PLLA tube (from which the scaffolds are cut), presented in Figure 4.4. The 50 mm/min data was used as this was provided prior to the slower displacement rate data and is the displacement rate used historically by Arterius Ltd to obtain the stress-strain response of dogbone samples. Slower displacement rate data was provided later and is utilised in subsequent chapters in this doctoral thesis. The ratio of yield stresses between the axial and circumferential directions, calculated from this data is given in Equation 4.1.

Plastic Strain ϵ^{pl}	**Yield Stress** σ_y
0.000	60
0.131	65
0.209	69
0.280	75
0.346	79
0.406	89
0.462	96
0.510	115
0.557	129
0.600	146
0.619	155

TABLE 4.2: Material data to define the plastic behaviour of the PLLA scaffold, obtained from the 50 mm/min uniaxial tensile tests for the circumferential direction of the die-drawn PLLA tube.

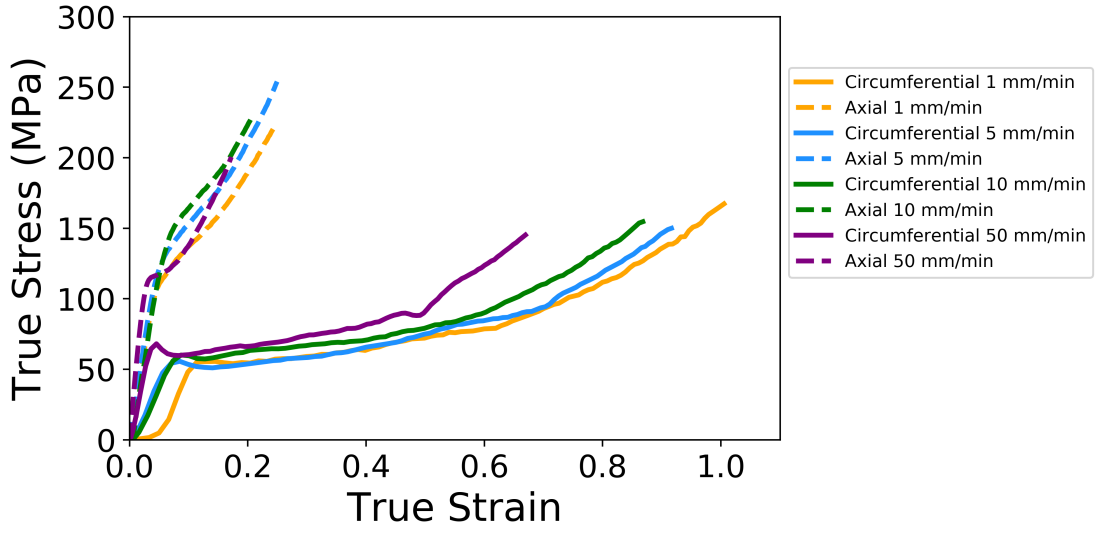

FIGURE 4.4: The stress-strain response from uniaxial tensile tests of dogbone shaped specimens cut from a die-drawn PLLA tube. Samples from both the axial and circumferential directions were tested at four independent displacement rates. In each case, the sample was strained until failure.

$$\bar{\sigma}_{33}^2/\sigma_0^2 = 1.72 \tag{4.1}$$

The resultant material model and underlying stress-strain data is given in Figure 4.5.

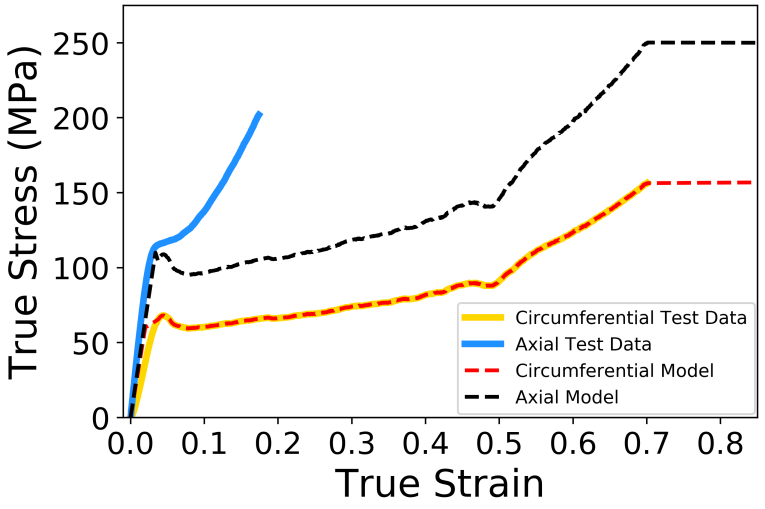

FIGURE 4.5: The resultant linear-elastic Hill's yield function material model, based upon stress-strain data obtained from uniaxial tensile tests of dogbone PLLA samples conducted at 50 mm/min.

4.2.4 Scaffold Performance and PEEQ Analysis Methods

The crimped diameter (CD), maximum diameter (MD), final diameter (FD), percentage recoil ($R_{\%}$), cell area (CA) and specific radial strength (SRS), as defined in Section 3.4.1, were all investigated with CA, SRS and $R_{\%}$ as part of the 25 point design study. Additionally, the average maximum PEEQ (PQ_{max}), defined as the average of the maximum PEEQ along the crown path for eight crowns located on an end ring of the scaffold was also considered. The average of the eight maximum values is used to lessen the effect of an artefact in the mesh distorting results. In this free expansion case it should be expected that each of the eight crowns will display broadly identical stress distributions, given the circumferential symmetry of the scaffold. This metric was devised to help characterise the PEEQ using a single variable in addition to the path data analysed. The PEEQ at the end ring of the scaffold was used as the geometry of the end rings will provide the most contrast between different scaffold designs. However, the maximum PEEQ for some designs could occur at the central rings.

The PEEQ distribution in the baseline design, along with a design from each corner of the design space was investigated in more detail using paths along which the PEEQ was observed. These were created by a series of Python scripts. Firstly, the coordinates of the underlying geometry were obtained from Rhinoceros 5.0 by extracting the location of a specified crown apex (for the crown path) or the underlying cosine function of a specified ring (for the ring path). The coordinate points were then passed to a Python script to translate them as required by the user. The crown path could be translated radially towards the inside or outside face of the scaffold whilst the ring path could be translated radially and/or axially towards the top or bottom face of the scaffold ring. Lastly, the translated 3D coordinates were passed to a Python function read by Abaqus/CAE in which they were provided as an argument for the in-built 'NearestNode' function which takes a 3D coordinate and obtains the node located closest to that point. A path was then created containing the located nodes along which the PEEQ could be observed and extracted.

The paths across the crown width and around an end ring of the scaffold are shown in Figure 4.6(A) and Figure 4.6(B), respectively. A scaffold end ring was chosen for the detailed PEEQ study as this provided the greatest contrast in geometry between the five scaffold designs. A path across the crown apex was used due to the large strain gradient across it in balloon expansion, from compressive strain at the outside of the crown to tensile strain at inside of the crown. The ring paths were created to highlight the lateral position and change in magnitude of the PEEQ, particularly in the region either side of the crown apex where the strain gradient was expected to be large. The paths were extracted for the mid-point of the balloon expansion step at which the balloon is at maximum inflation pressure.

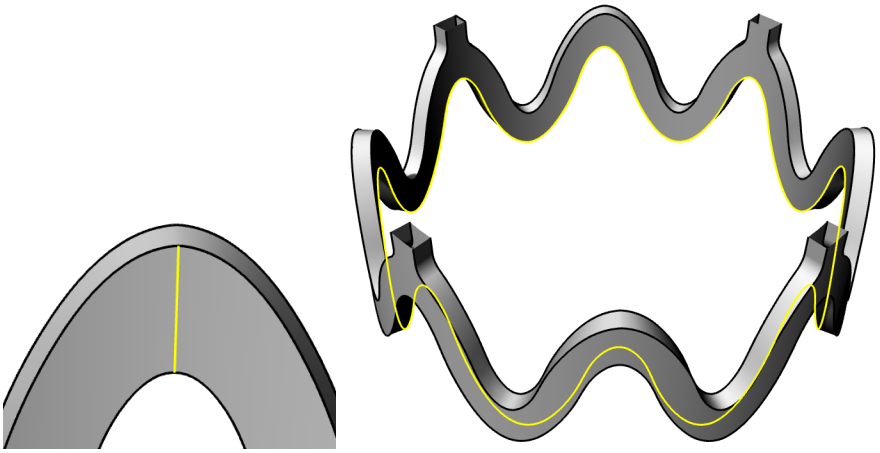

(A) (B)

FIGURE 4.6: The paths used to inspect PEEQ for; (A) the crown path which originates at the inside of the crown apex and traverses the width of the strut to the outer side of the crown and (B) the ring path.

Due to the circumferential symmetry of the scaffold geometry, the PEEQ data around the scaffold ring path was averaged across each of the four repeating units that constitute the scaffold ring.

To assess the PEEQ across the crown width, a fourth order polynomial regression model was selected to which the data was fitted, using the 'scikit learn' library in Python (Pedregosa et al., 2011). Calculating an average of the eight PEEQ values (one per crown) at each location across the crown width was not possible because of the differences in mesh discretisation between crowns due to the use of an irregular swept mesh. This limitation did not affect the ring paths and so an average value at each location along the repeating unit was used to aid visualisation of the ring path data. The data for the eight crown paths was divided into two groups for model fitting - those with and without a connector attached, as this significantly affected the resulting PEEQ distribution.

4.2.5 Surrogate Models

Surrogate models provide a method to predict the response of a metric to a set of design variables and hence gain an understanding of that metric's response across the entire design space. Classical engineering modelling techniques, such as regression modelling and radial basis functions (RBF) can facilitate accurate predictions of smooth, continuous functions when only a relatively sparse data set is available. A summary of the underlying theory of polynomial regression (PR) models and RBF, as used in this chapter, is provided in Appendix D in addition to Pedregosa et al. (2011) and Forrester et al. (2008).

The ability of each model to describe the underlying data set was quantified using the 'leave-one-out' technique to plot the actual vs predicted values and calculate the root-mean-squared (R^2) coefficient. The 'leave-one-out' technique provides a conservative estimate of the model fitness as each value is predicted when that data point is omitted and then the model is subsequently re-calibrated. This results in prediction of a point at which the density of underlying data points to which the model is trained is approximately half of elsewhere in the surrogate.

Figure 4.7 quantifies the quality of fit for each of the surrogate models in Figure 4.9. In each case an R^2 value of greater than 0.86 is achieved. Table 4.3 gives the details of the surrogate models used to capture each of the four metrics investigated. For each metric, both RBF and PR models of different orders were considered and their appropriateness for the underlying data set quantified using the R^2 metric. In the case of the RBF, only linear and cubic fixed basis functions were considered to simplify the parameter estimation process. Kriging surrogate models were also considered for each of the metrics in the design study although these did not improve the model fit to the underlying data and thus suggested variable basis function models (of which Kriging models are a generalisation) may not be appropriate. PR models of orders 1 to 6 were explored. In the case of PQ_{max} a first order PR model was used, which is a linear regression model. It is interesting to note that only the model for $R_{\%}$ uses a RBF. Use of a PR model in the case of $R_{\%}$ yielded an R^2 in excess of 0.9 but this was super-seeded by the third order RBF model.

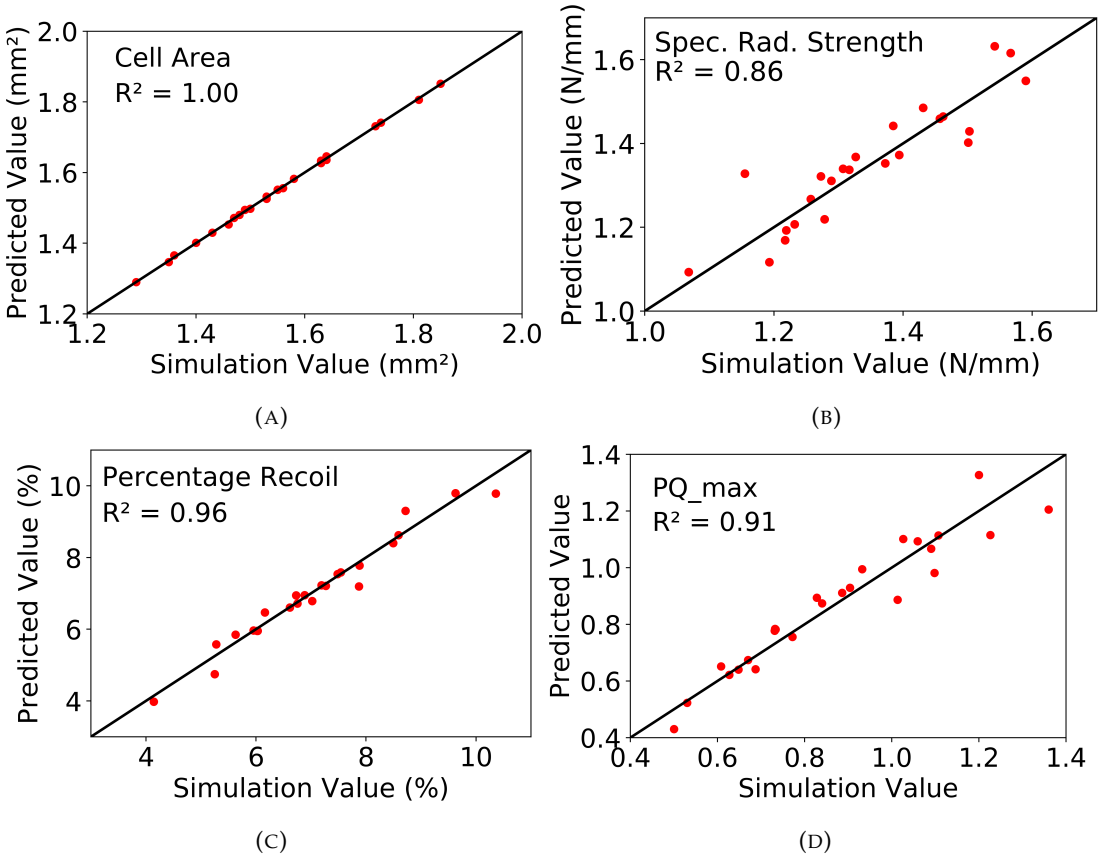

FIGURE 4.7: Actual vs predicted values for each of the surrogate models using the 'leave-one-out' strategy for; (A) cell area; (B) maximum diameter; (C) percentage recoil and (D) average maximum PEEQ.

Metric	Surrogate Model	Order
Cell Area	Polynomial	2
Specific Radial Strength	Polynomial	5
Percentage Recoil	Radial Basis Function	3
PQ_{max}	Polynomial	1

TABLE 4.3: The surrogate model details used to capture each of the four mechanical metrics.

4.3 Results & Discussion

4.3.1 Comparison of *In-Vitro* and *In-Silico* Results

Table 4.4 shows a comparison of the CD , MD and FD in addition to the $R_{\%}$ and SRS of the scaffold between the *in-silico* and *in-vitro* cases for the baseline scaffold design.

The MD of the scaffold is predicted within 1.1% of the *in-vitro* value, whilst the FD is predicted within 4%. The $R_{\%}$ predicted *in-silico* is almost three times greater than that

observed *in-vitro* whilst the SRS is over predicted by more than 50%. Whilst $R_{\%}$ and SRS deviate significantly from the *in-vitro* value, they provide a useful comparison between scaffold designs in terms of their relative post-expansion behaviour given the trends observed in mechanical metrics are explainable and the model is based upon a longstanding material constitutive theory implemented in a commercial FEA package. Particular phenomena exhibited by polymers will not be captured in the model, as is explored later in the thesis, but broad trends in mechanical behaviour as a result of changes in scaffold geometry will be captured by the model framework. Whilst an elasto-plastic model utilising the Hill's yield function has been employed in previous computational studies of polymeric BRS (Pauck and Reddy, 2015; Blair et al., 2019b), we subsequently demonstrate in Chapter 5 the challenge of accurately predicting both the percentage recoil and radial strength of a thin-strut BRS using this material model framework. To date, more advanced material models that capture the viscoelastic response of PLLA have been used to explore polymeric BRS in the context of FEA (Bergström and Boyce, 2001; Eswaran et al., 2011; Bobel and McHugh, 2018). However, viscoelastic models that utilise a parallel network rheology require greater effort in terms of calibration to the uniaxial tensile data and understanding of the material constitutive theory. Therefore, it was decided that the material modelling of PLLA would be investigated in subsequent chapters. Whilst the SRS and $R_{\%}$ are not accurately predicted by the elasto-plastic model their relative changes across different scaffold designs can still be explored using this model.

Scenario	Crimped Diameter (mm) CD	Maximum Diameter (mm) MD	Final Diameter (mm) FD	Percentage Recoil (%) $R_{\%}$	Specific Radial Radial (N/mm) SRS
In-vitro	1.18	3.81	3.71	2.62	0.89
In-silico	1.36	3.85	3.57	7.27	1.50

TABLE 4.4: A comparison of the crimped diameter, maximum diameter, final diameter, percentage recoil and specific radial strength for the baseline scaffold design for the *in-silico* and *in-vitro* tests.

Figure 4.8 shows a comparison of the *in-silico* and *in-vitro* expansion of the baseline scaffold at its MD and FD. The *in-silico* scaffold is shown as a red overlay upon an image of the *in-vitro* test. Observing Figure 4.8(B), it's evident that greater recoil occurs in *silico* compared to in *vitro*. Differences are noticeable in the scaffold shapes, particularly in Figure 4.8(B) at the central closed ring. In addition to the limitation of the material model, this discrepancy could also be a result of the interaction between the scaffold and balloon. In the *in-vitro* test, the crimped scaffold remains firmly in contact with the balloon after the crimp is removed whilst the *in-silico* test leaves a small gap between the crimped scaffold and balloon (although this is ultimately a result of the material

model), as indicated by the differences in CD in Table 4.4. However, this altered interaction between the balloon and scaffold may subsequently impact the post-expansion predictions. Moreover, the friction between the scaffold and balloon is set using a friction coefficient of 0.1 yet this value is difficult to validate and could contribute to the error. However, prediction of the scaffold shape generally appears most accurate at the end rings, the location at which the values of PEEQ are extracted. This gives improved confidence regarding the prediction of the local strains at this critical location, particularly at maximum balloon inflation pressure.

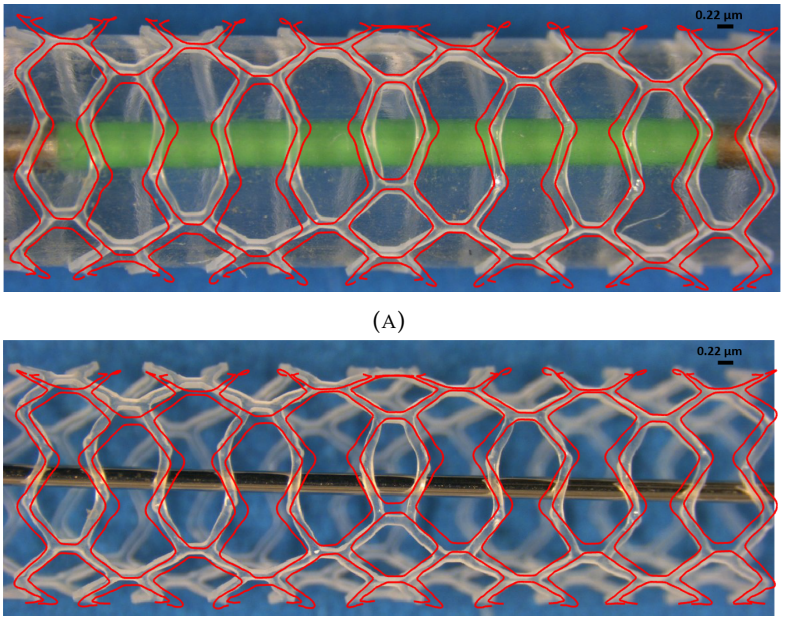

(A)

(B)

FIGURE 4.8: Comparisons of the scaffold shapes for; (A) the diameter at maximum balloon inflation pressure and (B) the final diameter. The *in-vitro* tests were conducted by Arterius Ltd.

Results for the 25 point design study are shown in Table 4.5. The change in ring length ($RL_{\%}$) and change in strut width ($SW_{\%}$) denote the change in these geometric parameters for an end ring of the scaffold relative to the same ring in the baseline scaffold design (design 1).

Design Number	Ring Length Factor	Strut Width Factor	Change in Ring Length (%)	Change in Strut Width (%)	Cell Area	Specific Radial Strength	Percentage Recoil	Average Maximum PEEQ
	F_{RL}	F_{SW}	$RL_{\%}$	$SW_{\%}$	CA	SRS	$R_{\%}$	PQ_{max}
1	1.000	1.000	0.0	0.0	1.55	1.50	7.27	0.84
2	0.960	0.960	-18.5	-18.5	1.46	1.27	5.25	1.67
3	0.960	1.040	-18.5	21.7	1.29	1.54	4.14	1.20
4	1.040	0.960	21.7	-18.5	1.85	1.01	10.23	0.50
5	1.040	1.040	21.7	21.7	1.63	1.15	7.87	1.09
6	0.960	0.989	-18.5	-5.4	1.40	1.59	5.28	1.01
7	0.964	1.015	-16.7	7.7	1.36	1.46	6.03	1.06
8	0.968	0.960	-15.0	-18.5	1.49	1.37	5.63	0.69
9	0.973	1.036	-12.8	19.3	1.35	1.46	5.95	1.36
10	0.977	0.977	-11.0	-11.0	1.50	1.50	6.02	0.77
11	0.981	0.998	-9.1	-1.0	1.47	1.57	6.16	0.89
12	0.985	1.023	-7.3	12.0	1.43	1.39	7.02	1.03
13	0.989	0.964	-5.4	-16.7	1.58	1.29	6.61	0.63
14	0.994	0.985	-3.0	-7.3	1.56	1.43	6.75	0.73
15	0.998	1.006	-1.0	3.0	1.53	1.38	7.19	0.90
16	1.002	1.032	1.0	17.1	1.48	1.31	6.73	1.11
17	1.006	0.973	3.0	-12.8	1.64	1.28	7.48	0.65
18	1.011	1.019	5.6	9.9	1.55	1.32	7.54	0.93
19	1.015	0.994	7.7	-3.0	1.64	1.33	7.88	0.73
20	1.019	1.040	9.9	21.7	1.53	1.19	6.88	1.23
21	1.023	1.011	12.0	5.6	1.63	1.26	8.49	0.83
22	1.027	0.981	14.2	-9.1	1.73	1.22	8.72	0.61
23	1.032	1.027	17.1	14.2	1.63	1.22	8.59	1.10
24	1.036	0.968	19.3	-15.0	1.81	1.07	10.36	0.53
25	1.040	1.002	21.7	1.0	1.74	1.23	9.63	0.73

TABLE 4.5: Cell area, specific radial strength, percentage recoil and average maximum PEEQ for the 25 design point study.

4.3.2 Surrogate Models

Figure 4.9 depicts the response surfaces predicted by the surrogate models constructed from the data in Table 4.5. Whilst Figure 4.9(A) represents a geometrical metric of the scaffold, rather than a mechanical metric measured in *silico*, it it useful to visualise this

via a surrogate model to aid comparison with the mechanical metrics. It is evident from Figure 4.9(A) that long narrow struts produce scaffolds with a larger open cell area that facilitate improved side-branch access. Figure 4.9(B) shows a particularly non-linear response which explains why a fifth order polynomial regression model was required to obtain the best fit. The baseline scaffold design appears to lie close to the optimum SRS with an SRS of 1.5 N/mm with the optimum value approximately 1.6 N/mm. Whilst it may be expected that decreasing the ring length, to reduced the bending moment arm about the crown, and increasing the strut width, to increase the second moment of area of the scaffold cross section, from the baseline design leads to greater levels of SRS, this does not appear to be the case. Figure 4.9(C) shows that long narrow strut scaffolds exhibit large levels of $R_{\%}$ whilst short wide strut scaffolds reduce the $R_{\%}$. However, the magnitude of $R_{\%}$ is likely to be lower in *vitro*, according to Table 4.4. These relative changes in recoil behaviour can be explained via observation of Figure 4.9(D) in which low levels of equivalent plastic strain develop in long narrow struts. The long struts do not need to open significantly to facilitate expansion to the target diameter meaning the development of tensile plastic strain at the inside of the crown apex is limited. This highlights that under-expansion of a BRS could be detrimental to its acute recoil performance. Therefore, it is critical BRS are fully expanded in *vivo* to their target diameter. Whilst Figure 4.9(A) and Figure 4.9(D) drive the scaffold design towards the bottom-right corner of the design space, Figure 4.9(C) displays the opposite trend to limit the $R_{\%}$ whilst Figure 4.9(B) indicates a design close to the baseline design is optimum in terms of SRS.

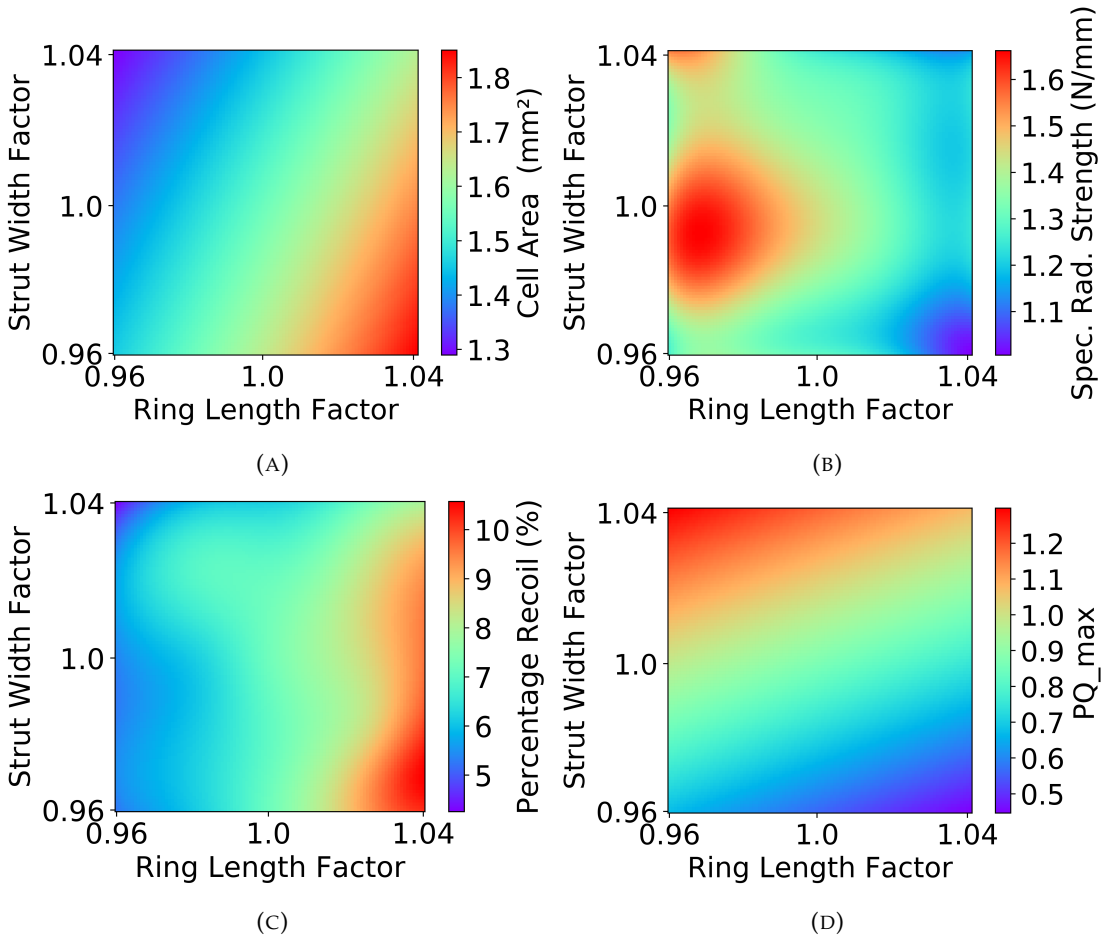

FIGURE 4.9: Surrogate models for the 25 point design study showing; (A) cell area; (B) specific radial strength; (C) percentage recoil and (D) average maximum PEEQ.

4.3.3 PEEQ Analysis

Figure 4.10 gives the PEEQ distribution in four rings of each of the five scaffolds investigated in detail when the expansion balloon is at maximum inflation pressure. It is evident that the difference in geometry between each design yields significantly different distributions of PEEQ. The short-wide strut design (design 3, Figure 4.10(A)) shows the greatest level of PEEQ and displays significant splaying of the crowns in the radial direction whilst design 5, Figure 4.10(B) shows twisting at the crown apex as the scaffold is expanded. Design 4, Figure 4.10(D) displays the lowest level of PEEQ development amongst the five designs where PEEQ at the inside of the crown does not exceed 0.5.

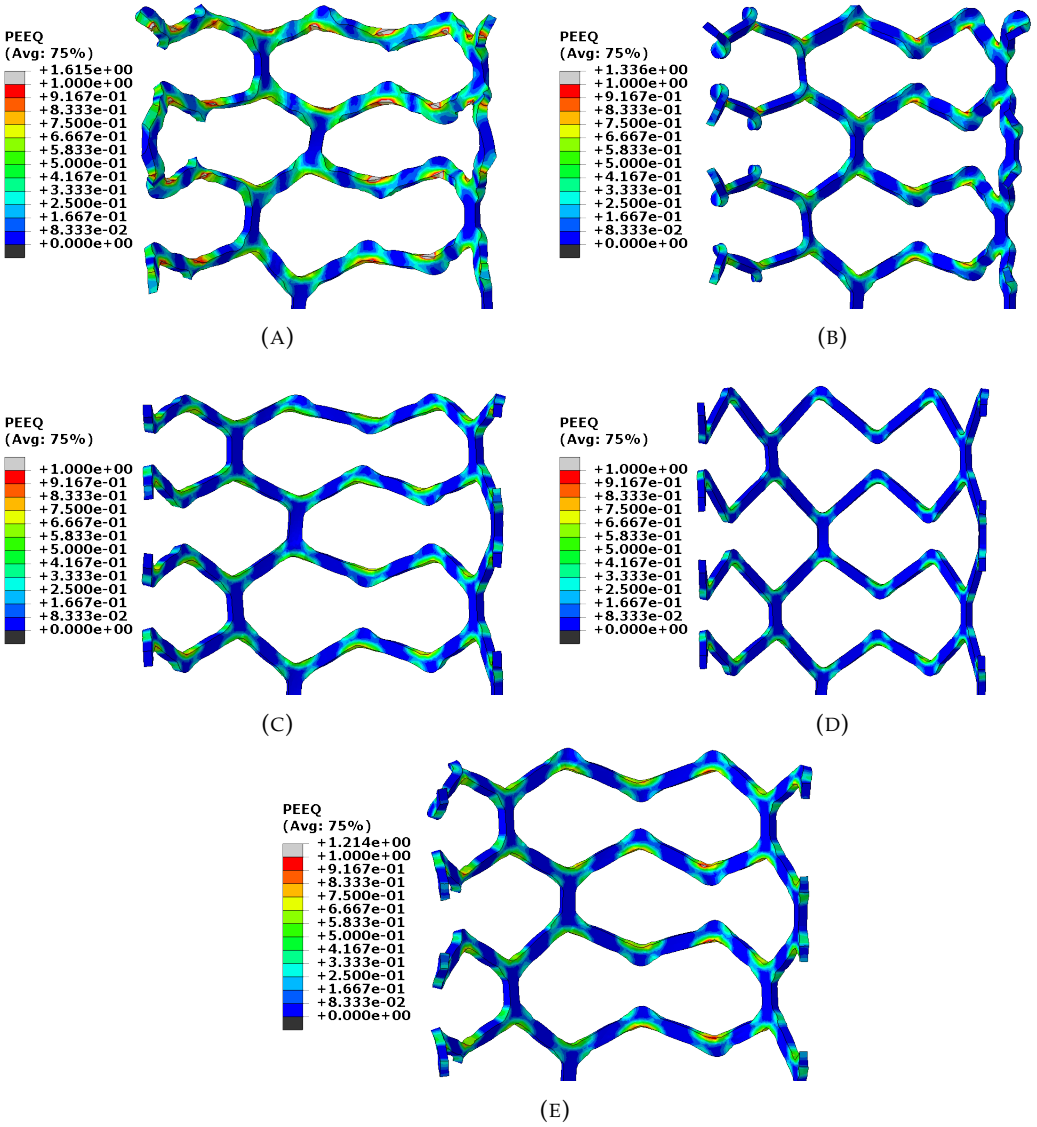

FIGURE 4.10: Equivalent plastic strain for each scaffold design at maximum inflation pressure for; (A) design 3; (B) design 5; (C) design 2; (D) design 4 and (E) design 1.

Figure 4.11 details the PEEQ along the path denoted in Figure 4.6(B), averaged for a single repeating unit, from an end ring of each of the five scaffold designs. The error bars show the maximum deviation of the average value from the data points. Designs 1, 3 and 5 in Figure 4.11(E), Figure 4.11(A) and Figure 4.11(B), respectively, show an alternating pattern of PEEQ at the inside of each crown due to the presence of a connector. This is evident in the two different amplitudes of the largest peaks which denote the inside of the crown, where the largest level of PEEQ exists. This effect does not appear to be present in the narrow strut designs, shown in Figure 4.11(C) and Figure 4.11(D), where the peaks denoting the inside of the crown are of equal amplitude. With the exception of design 5, the level of PEEQ on the outside of the crown in each design is symmetrical about the crown attached to a connector. Indeed, the small 'v' shaped

peaks are of equal amplitude on each side of the large amplitude peak. In the case of design 5, the PEEQ distribution on the outside of the crown is asymmetric about the connector. This is evident via the right side of each 'v' shaped peak in Figure 4.11(B) displaying a larger value than the left side. It is also evident that the wide strut designs show greater variability in maximum PEEQ compared with the narrow strut designs, evidenced in the larger error bars in Figure 4.11(A) and Figure 4.11(B). Figure 4.11(A) also confirms that the PEEQ in design 3 only drops to zero in a small portion of the straight section of the strut.

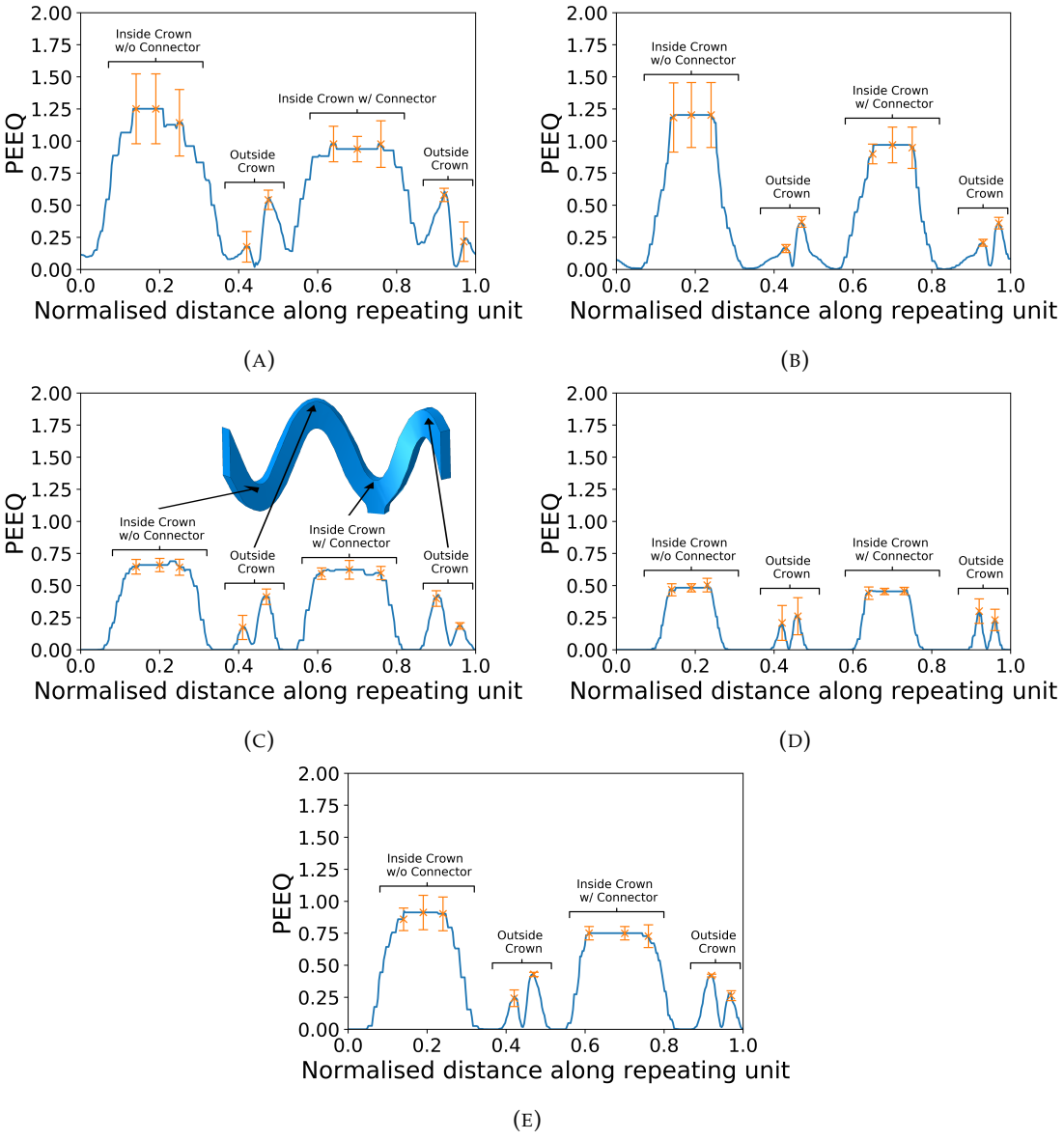

FIGURE 4.11: An averaged value of equivalent plastic strain for the four repeating units along paths around an end ring of each scaffold design for; (A) Design 3; (B) design 5; (C) design 2; (D) design 4; and (E) design 1.

Figure 4.12 displays the values of PEEQ across the two groups of crowns on the end ring of each scaffold design using the polynomial regression model to calculate an average

of the eight paths for each end ring, as shown in Figure 4.6(A). In Figure 4.10 and Figure 4.11, designs 3 and 5 display the largest level of PEEQ at the inside of the crown and show a greater level of penetration of PEEQ across the crown. As per Figure 4.11, the presence of a connector reduces the level of PEEQ developed at the inside of the crown. This is particularly evident in design 1, Figure 4.12(E) where there is a large difference in maximum PEEQ between the two cases. This is also present in designs 3 and 5 but less noticeable, in part due to the large variability of PEEQ.

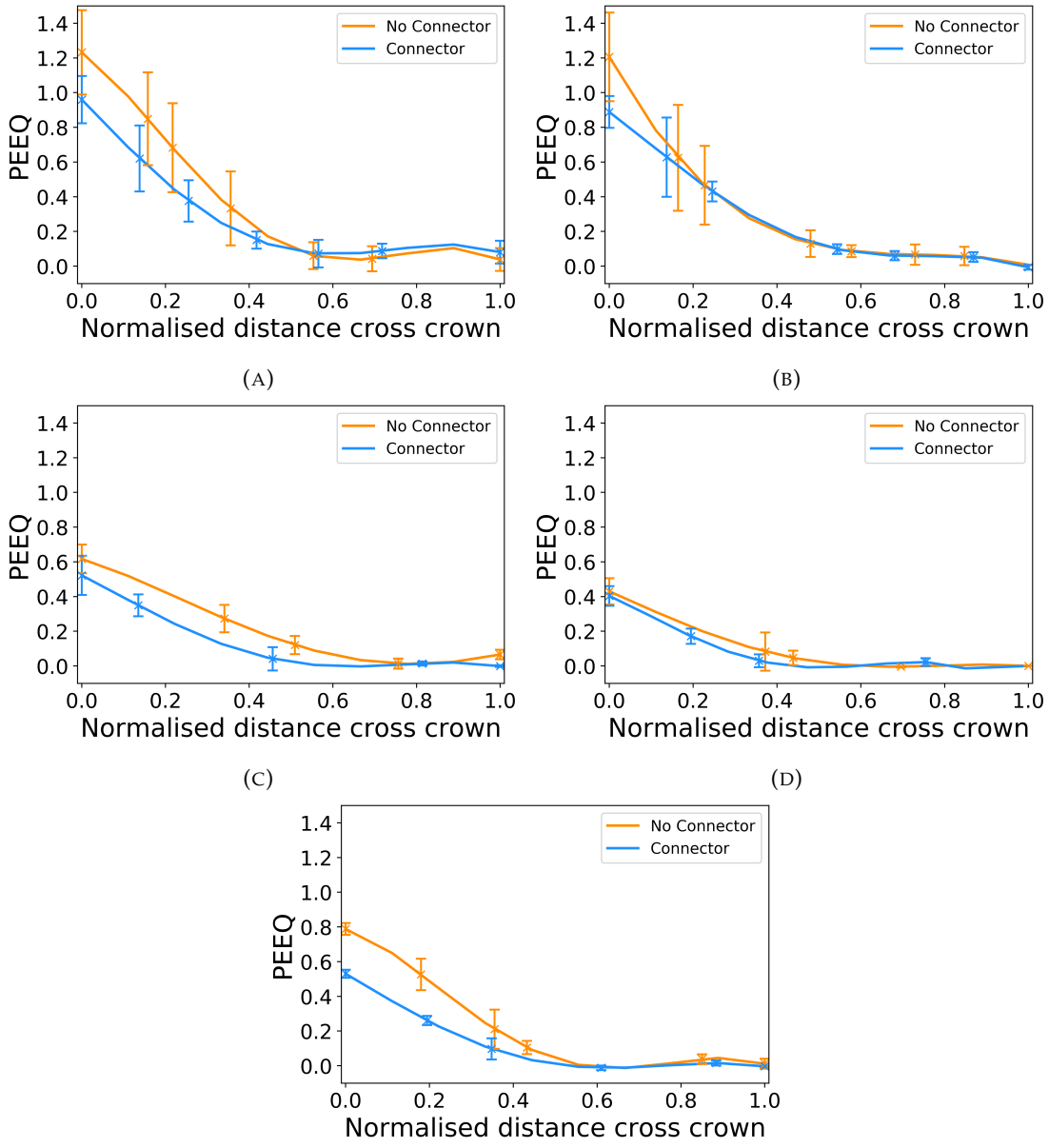

FIGURE 4.12: Equivalent plastic strain across the crown width of an end ring of each scaffold design for crowns with and without a connector. (A) Design 3; (B) design 5; (C) design 2; (D) design 4 and (E) design 1.

Observation of the five scaffold designs makes clear that variations in ring length and

strut width, of approximately +/- 20% from the baseline design, along the scaffold length yield a change in mechanical performance, as per Table 4.5. This results in $R_{\%}$ varying from 4.14% to 10.36% and SRS varying from 1.01 to 1.59 N/mm. There is also a significant variation in PQ_{max}, from 0.61 to 1.67. Short wide strut designs afford improved levels of $R_{\%}$ due to the increased levels of PEEQ developed at the crown apex whilst long narrow strut designs naturally accommodate superior side branch access with a reduced risk of strut fracture due to the lower levels of plastic deformation. Although, this will result in a lower value of radial strength as the struts become longer and easier to displace in cantilever bending given their larger moment arm.

The use of defined paths along which to observe the PEEQ, significantly aids the quantification and analysis of the subtle differences in PEEQ distribution between each scaffold design. Designs 1, 2 and 5 show similar distributions of PEEQ, according to Figure 4.10. This is unsurprising given they both have the same ratio of ring length to strut width. Design 1 exhibits approximately 30% lower $R_{\%}$ than design 4, due to the greater level of PEEQ developed at the crown apex, evidenced in Figure 4.12 and Table 4.5 where the PQ_{max} is 0.84 for design 1, compared with 0.5 for design 4. Interestingly, in the case of designs 3 and 4, PQ_{max} is greater than the ultimate tensile strain (UTSn) of PLLA, which is 0.7 in the circumferential direction, as per Figure 4.4. This indicates the ability of the scaffold to tolerate very large levels of equivalent plastic strain. Figure 4.13 strengthens this argument as it shows design 1 significantly over-expanded without displaying evidence of strut fracture despite the baseline design exhibiting a PQ_{max} of 0.84 at the inside of the crown apex when expanded in *silico*. Indeed, many of the crowns in Figure 4.13 appear to have been completely straightened yet do not display any whitening of the plastic known as 'crazing', first observed in BRS by Radu et al. (2012). This validates design 1 and by extension design 2 as viable designs that tolerate significant equivalent plastic strain, even when over-expanded, as is commonplace in clinical practice (Foin et al., 2016b).

Figure 4.12(A), Figure 4.12(B) and Figure 4.12(E) all show two distinct patterns of PEEQ penetration across the crown width depending upon the presence of a connector. It is evident that the presence of a connector attached to a crown restricts the ability of the crown to open in expansion, limiting the development of plastic strain. This will result in crowns in any given scaffold ring displaying alternating stress levels which could worsen uneven resorption of the scaffold where resorption occurs fastest at the highly stressed crowns (Soares et al., 2010; Luo et al., 2014). This in turn could exacerbate the long term blood clotting risk if scaffold struts protrude into the blood flow, providing sites for thrombus formation. Therefore, the use of a closed cell scaffold design, whilst reducing the cell area afforded by the scaffold, may improve the likelihood of even resorption of BRS. Such a design could be employed in a vessel in which there are no side branches or the side branches are expendable. The two patterns of PEEQ penetration

across the crown are not evident in the long ring length designs. This indicates the connector has less effect in reducing the relative opening of the scaffold struts in expansion in these scaffold designs.

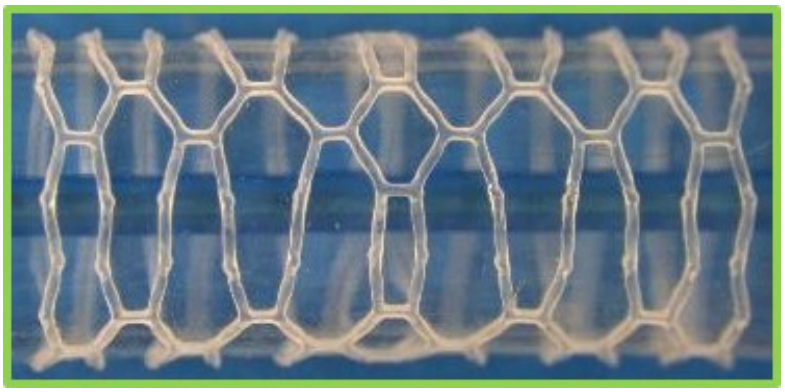

FIGURE 4.13: The baseline scaffold (design 1) over-expanded to an outer diameter of 4.39 mm without evidence of strut fracture occurring.

Design 4 displays a very low level of plastic strain developed in the scaffold struts. According to Figure 4.11 and Figure 4.12, the value of PQ_{max} does not exceed 0.5. Figure 4.12(D) shows that the PEEQ does not penetrate far into the straight sections of the strut in design 4 which leads to poor $R_{\%}$ performance. However, this design does have a large CA to facilitate improved side branch access.

Referring to the wide strut designs (designs 3 and 5), significantly more plastic strain is developed in the scaffold struts compared to the narrow strut designs. In addition to the reduced radius of curvature at the inside of the crown apex, this is due to the twisting and splaying of the crowns that occurs in expansion, highlighted in Figure 4.14 which shows designs 3 and 5 at maximum balloon inflation pressure. This behaviour is likely to occur due to the high ratio of strut width to strut thickness. As the scaffold is expanded, the conventional cantilever movement of the crown in the circumferential and axial directions is exchanged for twisting in the radial direction as this provides less resistance to the opening of the scaffold ring. This explains why lower than expected levels of SRS are observed in the short ring-length wide-strut designs. It is likely that any twisting of the scaffold struts will be detrimental to the radial strength as this exposes the crushing force to the weaker resistance of the strut thickness, rather than forcing the rings to close the struts via bending about the crown apex in the axial and circumferential directions. Therefore, it is generally desirable to increase the ratio of strut width to thickness but only prior to it inducing the onset of strut twisting about the crown apex.

It may be expected that twisting or splaying of the scaffold struts would be constrained by the vessel wall *in-vivo*. Regardless, the tendency of the struts to twist will heighten the stress exerted on the arterial lining, increasing the risk of neointimal hyperplasia

(Farb et al., 1999; König et al., 2002). Reducing stress exerted on the vessel wall is highly desirable. Indeed, this is highlighted by a number of studies that assess the stress exerted by coronary stents/scaffolds on the arterial layers (Lally et al., 2005; Mortier et al., 2010; Pant et al., 2011; Wei et al., 2019). Most importantly, the twisting behaviour exhibited in *silico* in scaffold design 5 has been observed in *vitro* in the constrained deployment of a long ring length BRS, as shown in Figure 4.15, in which the scaffold was deployed via balloon expansion into a mock silicon vessel. Observing the scaffold/artery interaction it is evident that the vessel wall did not prevent the radial twisting of the scaffold struts about the crown apex.

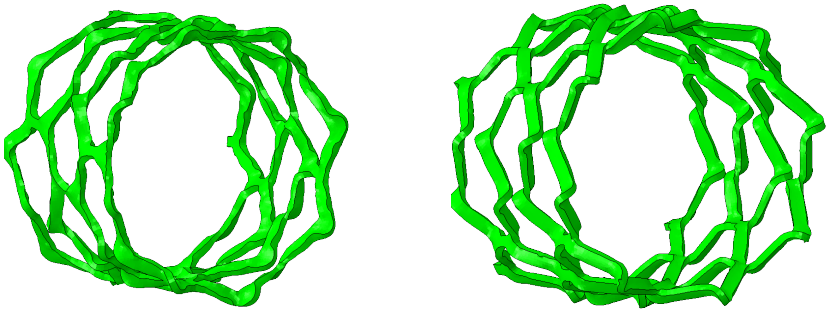

(A) (B)

FIGURE 4.14: Wide-strut scaffold designs that exhibit twisting when expanded for; (A) design 3 which shows some splaying of the crowns in the end ring and (B) design 5 which displays significant twisting in the radial direction about the crown apex in each of the four rings shown.

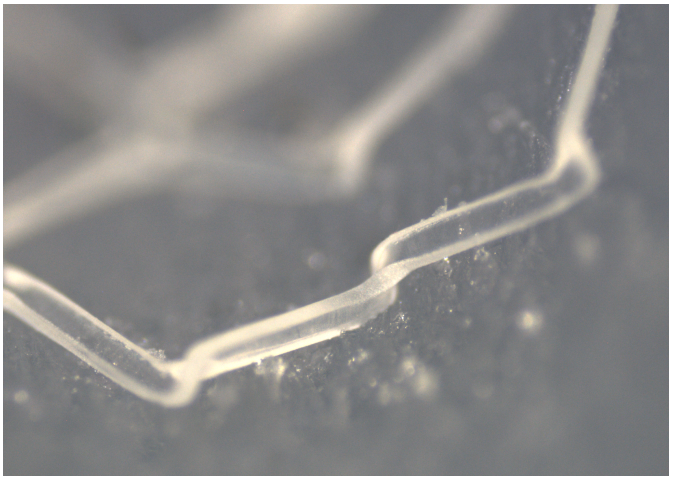

(A)

FIGURE 4.15: *In-vitro* evidence of strut twisting about the crown apex in the deployment of a long ring-length BRS into a mock silicon vessel. The initial scaffold expansion was conducted by Arterius Ltd whilst the image was obtained using an optical microscope at the University of Southampton's material laboratory.

As only a very small portion of the scaffold struts in design 3 appear to have developed no plastic strain, confirmed by Figure 4.10(A) and Figure 4.11(A) where the PEEQ has

penetrated far into the straight sections of the struts, this design presents a significant risk of strut fracture due to the high value of PQ_{max} at the inside of the crown apex. Referring to design 5 in Figure 4.11(B), it is evident that the PEEQ is contained more closely to the vicinity of the crown apex, compared to design 3. However, design 5 still presents a significant risk of strut fracture due to the large value of PQ_{max} which could initiate and propagate a crack at the crown apex.

Figure 4.12(A) and Figure 4.12(B) show that a significant level of PEEQ develops to around 50% of the crown width and some PEEQ even penetrates the entire crown width. This can be detrimental to the scaffold as it can induce the 'hinging' phenomenon, whereby plastic strain visibly penetrates across the entire width of the crown. This is evidenced by the whitening of the plastic from the inner to outer crown radius, similar to the aforementioned 'crazing' phenomenon reported by Radu et al. (2012). Figure 4.16 shows two previous generations of the ArterioSorb^{TM} BRS which utilise a helical pattern of connectors, deployed in free expansion in *vitro*. The scaffold depicted in Figure 4.16(A) shows the onset of 'hinging' even when expanded to a modest target diameter. This contrasts the scaffold in Figure 4.16(B) which shows no evidence of hinging when expanded to a similar target diameter. Whilst hinging has not been observed to initiate brittle or ductile fracture in scaffolds when expanded, it will initiate vulnerability to fatigue failure and, as previously mentioned, have implications upon the rate at which the scaffold resorbs in the crown region. In turn, this could lead to protrusion of the scaffold struts into the lumen, presenting an increased risk of thrombus formation.

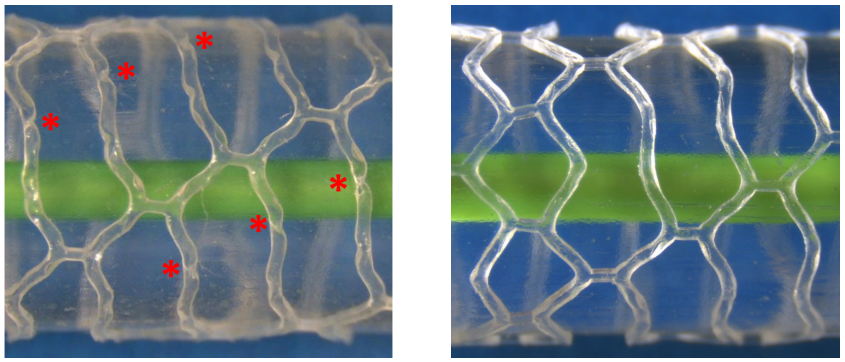

(A) (B)

FIGURE 4.16: A comparison of the penetration of equivalent plastic strain across the width of crowns using *in-vitro* testing conducted by Arterius Ltd. (A) shows the whitening effect of the plastic, termed 'hinging' (in the location of red asterisks) and leaves the scaffold vulnerable to fatigue failure. In contrast, (B) shows no evidence of hinging.

4.4 Conclusions

Variable ring length and strut width scaffolds were explored via *in-silico* testing to understand the effect of geometry upon several mechanical metrics and the side-branch access afforded by thin-strut BRS. Comparison with *in-vitro* data was also conducted to validate the simulations and deepen understanding of the adverse effects that manifest in BRS expansion. Particular attention was given to the development of equivalent plastic strain, PEEQ, in the scaffold struts. This was also observed along defined paths both across the crown widths and around the scaffold end rings which highlighted a number of subtle differences in PEEQ distribution between each design. Surrogate models of the cell area, percentage recoil, specific radial strength and PEEQ were also presented to understand the relative changes in these metrics that occur across the design space.

In this chapter, the following conclusions can be drawn:

1. The phenomenon of twisting about the crown apex in the radial direction, a result of the high strut width to strut thickness ratio in long ring-length and thin-strut designs, has been observed both in *silico* and in *vitro*. This effect will heighten the risk of damage to the vessel wall and explains why long ring length designs exhibited a relative decrease in specific radial strength according to the surrogate model and underlying *in-silico* data.

2. Variation of ring length and strut width along the scaffold length results in significantly different distributions of PEEQ around the scaffold ring. Long narrow struts cause an asymmetric distribution of PEEQ at the outside of the crowns, due to the twisting observed here. If variable ring length and strut width devices are to be explored to aid side branch access and facilitate over expansion, scaffold designs which utilise ring lengths and strut widths in the range of the relatively narrow strut designs: 1, 2 and 4, should be considered. If a different target diameter or strut thickness is to be considered then alternative ring lengths and strut widths may be viable.

3. Wide-strut scaffolds offer a significantly increased risk of strut fracture due to the development of high levels of equivalent plastic strain at the inside of the crown apex. The onset of 'hinging' may also occur in wide-strut designs if the plastic strain penetrates the width of the crown.

4. The maximum and final diameters of the scaffold post balloon-expansion were accurately predicted by the *in-silico* test with a percentage error of less than 4%. The specific radial strength and percentage recoil of the scaffold was poorly predicted by the *in-silico* testing, primarily due to the limitations of the material model.

5. Percentage recoil is in direct competition with the cell area and PQ_{max} in this scaffold parameterisation. Additionally, the baseline design lies close to the optimum specific radial strength.

6. The presence of a connector attached to a crown will reduce the PEEQ developed at that crown and alter the PEEQ distribution around the scaffold ring. This is particularly the case in over-expansion scenarios and for wide-strut designs. This impacts the likelihood of strut fracture and the manifestation of the hinging phenomenon. In turn, this effects the even resorption of the scaffold *in-vivo*.

Due to the short-comings of the simple elasto-plastic material model used in this chapter, it was decided that subsequent chapters would investigate alternative material models and seek to ascertain a greater understanding of which material model frameworks are appropriate to accurately predict the mechanical behaviour of thin-strut BRS in FEA. Multiple permutations of elasto-plastic models are investigated along with the development of a novel anisotropic material model and investigation of a parallel network viscoelastic-plastic model.

Chapter 5

Investigating Elasto-Plastic Material Modelling and Development of a Novel Material Model

5.1 Introduction

As highlighted in Chapter 4, the choice of constitutive material model used in FEA is important to accurately capture the mechanical behaviour of thin-strut polymeric BRS. PLLA is a biodegradable aliphatic polyester (Farah et al., 2016) in which viscoelasticity, anisotropy, strain rate dependence and temperature dependence have all been observed experimentally (Bergström and Hayman, 2016). However, the degree to which it is necessary to model each of these features remains subject to debate. Indeed, it is unclear whether simple material models, used appropriately, provide an acceptable first approximation to model the mechanical performance of BRS without the need for computationally expensive material models.

Several material models have been utilised in the FEA of polymeric BRS. Schiavone et al. (2016), Wang et al. (2017) and Wang et al. (2018) have all used isotropic linear elasticity with Mises plasticity and isotropic hardening models, whilst Pauck and Reddy (2015) attempted to capture the anisotropic behaviour of poly-l-lactic acid (PLLA) by employing the Hill's yield function to differentiate between the yield stress in the axial and circumferential directions. This was latterly used by Blair et al. (2019b), with the addition of a transversely isotropic elastic model, in the optimisation of a scaffold based upon the Abbott Vascular BVS. Eswaran et al. (2011) developed an anisotropic viscoplastic model, based upon the work of Bergström and Boyce (1998, 2001), in which the material model was validated via a force/displacement experiment of a single scaffold ring in both cyclic and monotonic tension. An isotropic permutation of this

model, implemented in Abaqus/Explicit and Abaqus/Implicit via the parallel rheological framework (PRF), was then used by Bobel and McHugh (2018) to investigate three different BRS designs. Moreover, in Chapter 4 we demonstrate the limited efficacy of simple elasto-plastic theory to predict the mechanical response of a thin-strut BRS. Therefore, it is clear that further investigation is required to understand the limitations of this constitutive material model and whether it can be used to model next generation BRS using FEA or if alternative material models are required.

Whilst several material models have been investigated in the literature, there is no apparent consensus upon which model provides a suitable approximation of the mechanical response of thin-strut BRS in the context of FEA, in part due to the lack of *in-vitro* validation, with the notable exception of Wang et al. (2020). Additionally, careful consideration of material anisotropy is lacking, and the benefit of capturing this in place of isotropic models does not appear to have been explored to date.

Therefore, in this chapter we present a study that compares isotropic, anisotropic and a new user defined material property model calibrated using the tensile stress-strain data obtained by Arterius Ltd. FEA was conducted to mimic the *in-vitro* mechanical testing of scaffolds. The *in-silico* data was compared to the physical bench testing results to ascertain the appropriateness of the respective material models. Firstly, we present the comparison of two simple isotropic linear-elastic Mises-plasticity material models and a variety of anisotropic material models that utilise the Hill's yield function. These anisotropic models explore the use of stress-strain data obtained from uniaxial tensile tests at different displacement rates. Also, the inclusion of the stress relaxation, or 'failure' data is explored in this constitutive model as well as considering whether to approximate the material's elastic regime as isotropic or transversely isotropic. Based upon these initial findings a new model was implemented via the Abaqus VUMAT subroutine. This utilised the Hill's yield function with several amendments made to increase the model's fidelity whilst retaining simplicity and minimising computational cost. Lastly, a higher fidelity simulation was set up to explore whether more accurate representation of the *in-vitro* balloon-expansion procedure leads to better prediction of the final shape and radial strength of the scaffold.

5.2 Methodology

5.2.1 Scaffold Geometry

The baseline scaffold geometry used in Chapter 4, the details of which are given in Section 4.2, was used to investigate the material models in *silico*.

5.2.2 Material stress-strain Data

The uniaxial tensile test data, given in Figure 4.4, was used to calibrate the isotropic, anisotropic and user-defined material models investigated here. The Abbott Vascular BVS product guidelines recommend a slow rate of expansion due to the relative reduction in stress that this technique induces (Abbott Vascular, 2017; Bobel et al., 2016). However, as previously discussed, Wang et al. (2018) proposed that the efficacy of this technique may be limited in the case of scaffold deployment in *vivo* due to the scaffold being submerged in a solution at an elevated temperature. The simulations were conducted using models calibrated to the 1 mm/min and 50 mm/min stress-strain data, respectively, shown in Figure 5.1 in each case for the two material directions of interest. The former of these displacement rates was considered the most clinically relevant whilst the latter provided a significant point of contrast to the slow clinically relevant displacement rate.

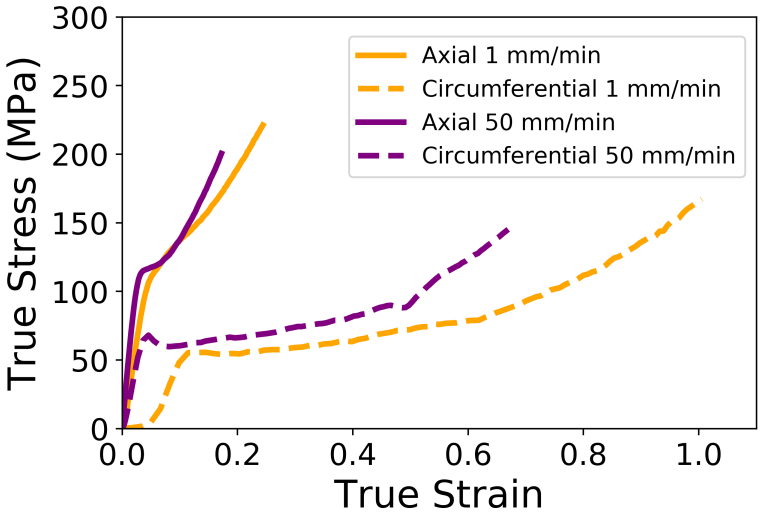

FIGURE 5.1: Stress-strain data from uniaxial tensile tests of dogbone shaped specimens cut from a die-drawn PLLA tube used to calibrate the isotropic, anisotropic and user-defined material models.

5.2.3 Isotropic Material Model

An isotropic elasto-plastic rate independent material model which employed the Mises yield function with isotropic hardening, the underlying constitutive theory of which is detailed in Subsection 3.5.1, was used to model the mechanical behaviour in two different cases. These were calibrated using the axial and circumferential material properties, respectively. This facilitated a comparison of the two material directions to understand which one was dominant in describing the mechanical behaviour of the scaffold. Only stress-strain data obtained at the displacement rate of 1 mm/min was used for these material models. It was hypothesised that the isotropic models' prediction would be

the least accurate of all the models to be evaluated. Therefore, comparison of models calibrated using stress-strain data obtained at a different displacement rate was deemed unnecessary.

The defining properties of each of the isotropic scenarios are shown in Table 5.1 and Table 5.2. The Young's modulus, E, defines the slope of the initial portion of the stress-strain curve, preceding the yield stress, σ_y, which gives the stress required to cause yielding for a particular strain. In the case of the Abaqus/CAE isotropic hardening model, the user defines the plastic behaviour by entering the yield stresses as a function of the plastic strain. The hardening is subsequently calculated from the gradient of the stress-strain data as a piece-wise linear hardening curve. The initial yield stress at zero plastic strain was calculated using the graphical 0.2% proof method in which the intercept of the data and line from 0.2% strain with the same linear gradient as the data itself defines the point at which yield is onset.

Material Direction	Young's Modulus (Mpa)
Axial	2985
Circumferential	759

TABLE 5.1: Elastic properties for the axial and circumferential isotropic scenarios.

Axial Direction 1 mm/min		Circumferential Direction 1 mm/min		Circumferential Direction 50 mm/min	
Plastic Strain ϵ^{pl}	Yield Stress σ_y	Plastic Strain ϵ^{pl}	Yield Stress σ_y	Plastic Strain ϵ^{pl}	Yield Stress σ_y
0.000	110	0.000	50	0.000	60
0.030	123	0.166	56	0.131	65
0.048	134	0.280	62	0.209	69
0.066	142	0.377	71	0.280	75
0.083	151	0.467	77	0.346	79
0.100	162	0.544	86	0.406	89
0.116	173	0.608	99	0.462	96
0.131	184	0.664	114	0.510	115
0.145	197	0.712	131	0.557	129
0.159	211	0.753	149	0.600	146
0.173	225	0.796	164	0.619	155

TABLE 5.2: Plastic properties for the isotropic scenarios utilising stress-strain data obtained at 1 mm/min. The circumferential data obtained at both 1 mm/min and 50 mm/min was also used to define the in-plane plastic behaviour of the PLLA for the anisotropic models.

5.2.4 Anisotropic Material Model

Eight variants of a material model using the Hill's yield function (Hill, 1948; DS SIMULIA, 2018), the constitutive theory of which is provided in Subsection 3.5.2, were investigated. These explored whether to model the elastic behaviour of the scaffold as isotropic or transversely isotropic. Transverse isotropy provides a convenient approximation for the elastic behaviour of PLLA as a plane of isotropy can be assumed for the radial and circumferential direction whilst the axial direction displays a significantly different stress response described by the transverse Young's modulus.

The modelling of failure of the material elements by including the stress relaxation that occurs above the UTSn was also investigated. This requires the addition of plastic stress-strain data to describe the reduction in stress that occurs as elements become overly strained. However, the elasto-plastic framework in Abaqus/CAE enforces the minimum value of plastic stress to be greater than or equal to the initial yield stress at zero plastic strain. Therefore, the stress will not relax to zero whilst the material is within its plastic regime as a result of excessive strain.

The features of each model are summarised in Table 5.3, comprising the 12 different material model variants investigated. Scenarios 3-10 denote the anisotropic Hill's yield function models whilst scenarios 11 and 12 utilise the Hoddy-Bressloff model, explained later in this chapter. The displacement rate at which the stress-strain data used to calibrate the model was obtained is detailed, followed by the elastic and plastic constitutive model theories and lastly whether the stress relaxation data is employed by the material model.

Test Scenario	Displacement Rate of Stress-Strain Data (mm/min)	Elastic Model	Plastic Model	Stress Relaxation Data Included
1 1-Ax-Iso-Mises-N	1 (Ax. Dir.)	Isotropic	Isotropic (Mises)	No
2 1-Cir-Iso-Mises-N	1 (Cir. Dir.)	Isotropic	Isotropic (Mises)	No
3 1-Cir-Iso-Hill-N	1	Isotropic	Anisotropic (Hill)	No
4 50-Cir-Iso-Hill-N	50	Isotropic	Anisotropic (Hill)	No
5 1-Cir-TrIso-Hill-N	1	Transversely Isotropic	Anisotropic (Hill)	No
6 50-Cir-TrIso-Hill-N	50	Transversely Isotropic	Anisotropic (Hill)	No
7 1-Cir-TrIso-Hill-Y	1	Transversely Isotropic	Anisotropic (Hill)	Yes
8 50-Cir-TrIso-Hill-Y	50	Transversely Isotropic	Anisotropic (Hill)	Yes
9 1-Cir-Iso-Hill-Y	1	Isotropic	Anisotropic (Hill)	Yes
10 50-Cir-Iso-Hill-Y	50	Isotropic	Anisotropic (Hill)	Yes
11 1-Cir-Iso-HB-Y	1	Isotropic	Anisotropic (Hoddy-Bressloff)	Yes
12 1-Cir-Iso-HB-Y*	1	Isotropic	Anisotropic (Hoddy-Bressloff)	Yes

TABLE 5.3: Test scenarios and descriptions of their respective material models. Each model is calibrated to stress-strain data which is obtained at one of two different displacement rates and comprises an elastic and plastic model to describe the material behaviour. For the plastic model, *Mises* refers to the Mises yield function with isotropic hardening, *Hill* refers to plastic potential theory with the Hill yield function and *Hoddy-Bressloff* refers to the Hoddy-Bressloff model which facilitates a variable plastic potential dependant upon the equivalent plastic strain. *Test scenario 12 (1-Cir-Iso-HB-Y*) used the more realistic multi-balloon expansion strategy.

The elastic material property parameters, obtained from the data in Figure 5.1, that

define the isotropic and transversely isotropic elastic models are shown in Table 5.4. In the case of the isotropic elastic models, the mean value of the Young's modulus for the two material directions, E_p and E_t, for the appropriate displacement rate was used whilst the Poisson's ratio, ν, was used. For the transversely isotropic models the value ν_{tp} was assumed in order to calculate ν_{pt} using 3.24.

Displacement Rate $\dot{u}$ (mm/min)	Young's Modulus In-plane E_p (MPa)	Young's Modulus Transverse E_t (MPa)	Poisson's Ratio ν (-)	Poisson's Ratio ν_{tp} (-)	Poisson's Ratio ν_{pt} (-)	Shear Modulus In-plane G_p (MPa)	Shear Modulus Transverse G_t (MPa)
1	759	2985	0.3	0.3	0.076	292	587
50	2035	4577	0.3	0.3	0.133	782	1189

TABLE 5.4: Elastic material model parameters for the anisotropic Hill's yield function models which use elastic transverse isotropy.

The resultant material property model is shown in Figure 5.2 for the two displacement rates. The model shown in Figure 5.2 represents the setup in test scenarios 1-Cir-TrIso-Hill-N and 50-Cir-TrIso-Hill-N. The model assumes perfect plasticity is exhibited after the last data point of the material's yield stress and plastic strain. Use of isotropic elasticity would result in the elastic portions of the graphs displaying the same slope for both directions. Use of the stress relaxation data shows a drop in the yield stress from its maximum value to the yield stress value at zero plastic strain before continuing to exhibit perfect plasticity for the circumferential directions for both strain rates via the black dashed lines. The line displaying larger stress values for each data set denotes the axial direction's response whilst the line displaying lower stress values denotes the circumferential direction's response.

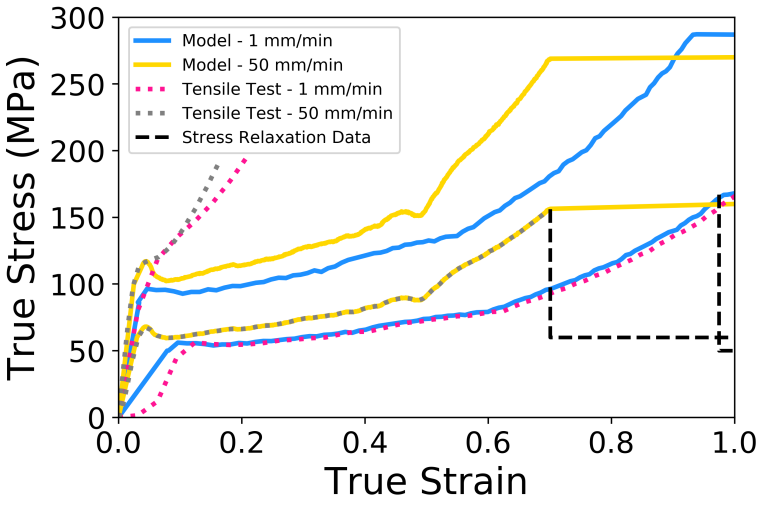

FIGURE 5.2: The anisotropic plastic potential material models and tensile test data for the 1 mm/min and 50 mm/min displacement rates. The line displaying lower stress values in each case denotes the response in the circumferential direction whilst the line displaying the larger stress levels in each case gives the axial direction's response. The black dashed line denotes the model's response if the failure data is included, in this case, for the circumferential direction only for both the 1 mm/min and 50 mm/min cases. Upon failure, an immediate drop in stress is evident followed by perfect plasticity as tensile strain continues.

The plastic hardening in the axial direction of both displacement rates is underestimated in the in-built Abaqus/CAE (DS SIMULIA) anisotropic models. This is a fundamental limitation within the material modelling capabilities of Abaqus in terms of describing anisotropy in the plastic regime. Only a constant ratio between the two directions can be used which does not allow the differences in hardening to be captured which bares no resemblance to the observed mechanical behaviour of PLLA. As per Chapter 4, this ratio is given by:

$$\bar{\sigma}_{33}^2/\sigma_0^2 = 1.72 \tag{5.1}$$

where direction 33 represents the axial direction and direction 0, the reference stress, is obtained from the circumferential direction.

5.2.5 Hoddy-Bressloff Material Model

The inherent limitation of the aforementioned anisotropic material model is evident in Figure 5.2 as the hardening in the plastic regime must remain constant between different material directions. Whilst the Hill's yield function can describe different yield stresses for a given plastic strain in the respective directions, it is unable to capture a difference in the gradients of the stress-strain curves. This is a significant approximation when considering the actual behaviour of PLLA, evidenced in Figure 5.1, where

anisotropy is most prolific in the material's plastic behaviour via a significant difference in plastic hardening of the PLLA.

To overcome this limitation, the Hoddy-Bressloff material model was developed, based upon the findings of the exploration of the in-built Abaqus anisotropic material models. The model is based upon the Hill's yield function but defines the yield ratio as a function of the equivalent plastic strain rather than a constant value. This facilitates independent rates of change of the yield stress for each material direction, overcoming the limitation of a constant yield potential. This model was implemented using the VUMAT sub-routine in Abaqus/Explicit and provides the same functionality as the aforementioned anisotropic material model with the addition of a variable yield ratio to describe the stress response in the plastic regime of the axial material direction.

A 1D Python implementation of the elasto-plastic Hill's yield function material model was constructed to facilitate development of the variable yield ratio. Firstly, rather than interpolating the stress-strain data input to Abaqus/CAE and calculating the gradient at a given plastic strain to define the material hardening, the plastic response was modelled using a third order polynomial function. This allowed it to be easily differentiated as it is a function of PEEQ only. The Python 'curvefit' function was used to train the polynomial coefficients to the stress-strain data. The function is shown in Equation 5.2.

$$\sigma_y = 540\bar{e}_{pl}^3 - 400\bar{e}_{pl}^2 + 130\bar{e}_{pl} + 50 \tag{5.2}$$

The PEEQ is denoted by $\bar{e}_{pl}$ and σ_y gives the yield stress. The variable yield ratio function was created using a similar method in which the coefficients were trained to the ratio of the stress-strain response in each material direction using a third order polynomial function. Third order polynomial functions were chosen to model the yield stress and stress ratio responses as only one independent variable, the PEEQ, was present in each case and the profile of the stress-strain curve of PLLA in the plastic regime resembles that of a relatively low order polynomial.

Equation 5.3 a shows the third order polynomial function that defines the ratio of the axial and circumferential yield stresses as a function of plastic equivalent strain.

$$\frac{\sigma_{33}^2}{\sigma_0^2} = 300\bar{e}_{pl}^3 - 50\bar{e}_{pl}^2 + 9\bar{e}_{pl} + 2.25 \tag{5.3}$$

The elastic behaviour was modelled via isotropic elastic theory using the parameters in Table 5 for the 1 mm/min displacement rate case. The reference plastic data, used to calculate the yield stress and hardening in the circumferential direction, approximated via the third order polynomial function in Equation 5.2 was calibrated to the stress-strain data obtained at 1 mm/min, as shown in Table 5.2.

The Hoddy-Bressloff model also facilitates the decrease in hardening and yield stress that occurs when elements exceed their UTSn. This allows the elements to effectively fail and thus provide no resistance to further deformation by enforcing the plastic hardening and current yield stress to be zero once the ultimate tensile strain for a given element is exceeded. This is in contrast to the in-built Abaqus anisotropic models that will allow a decrease in hardening and yield stress (although not below the value of the yield stress at zero plastic strain) and thereafter hold the yield stress constant, thus enforcing perfect plasticity upon the material after the UTSn is exceeded.

Figure 5.3 presents the true stress-strain response of the Hoddy-Bressloff model. The drop in stress whereby the UTSn of the material in the circumferential direction is exceeded is evident.

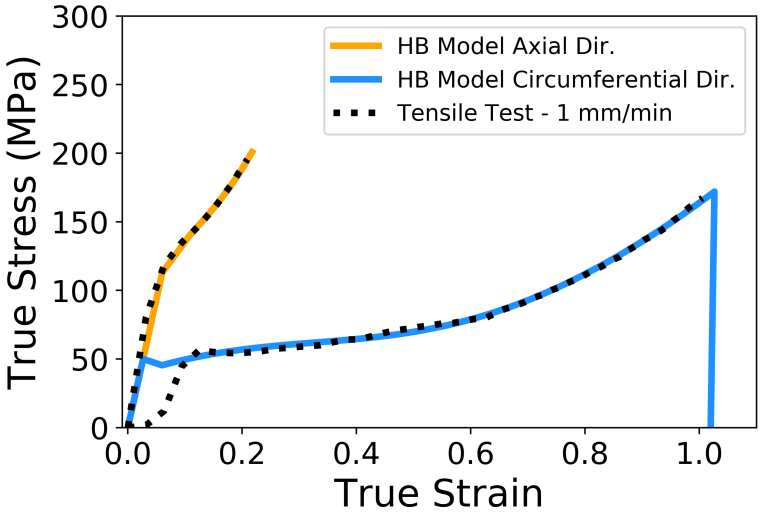

FIGURE 5.3: The Hoddy-Bressloff model calibrated using the stress-strain data obtained at 1 mm/min. This utilises a variable yield ratio, dependant upon the equivalent plastic strain which facilitates a differential in hardening in the plastic regime for the respective material directions. The elastic regime is modelled via isotropic linear elastic relations. The initiation of failure above a true strain of approximately 1.0 is evident whereby the stress and plastic hardening relaxes to zero.

5.2.6 FEA Setup

The free expansion simulation details are depicted in Figure 3.3.2. Additionally, a more realistic simulation setup provided two extra 'pre-expansion' steps to the *in-silico* test. This simulation utilised an extra balloon of diameter 3 mm. This smaller balloon was used to pre-dilate the scaffold firstly via inflation to a pressure of 8 atm, followed by inflation to 16 atm. The simulation then proceeded with step 3 (expansion using the 3.5 mm balloon) as previously described in Subsection 3.3.2. This method more closely followed the technique used by Arterius Ltd (Leeds, UK) in the *in-vitro* testing and was used once for the model described in Table 5.3, scenario 12. Scenarios 1 - 11 used only

a single balloon to expand the scaffold as described in steps 1 - 4. Figure 5.4 shows this realistic simulation setup, whilst the standard simulation setup used the 3.5 mm balloon only.

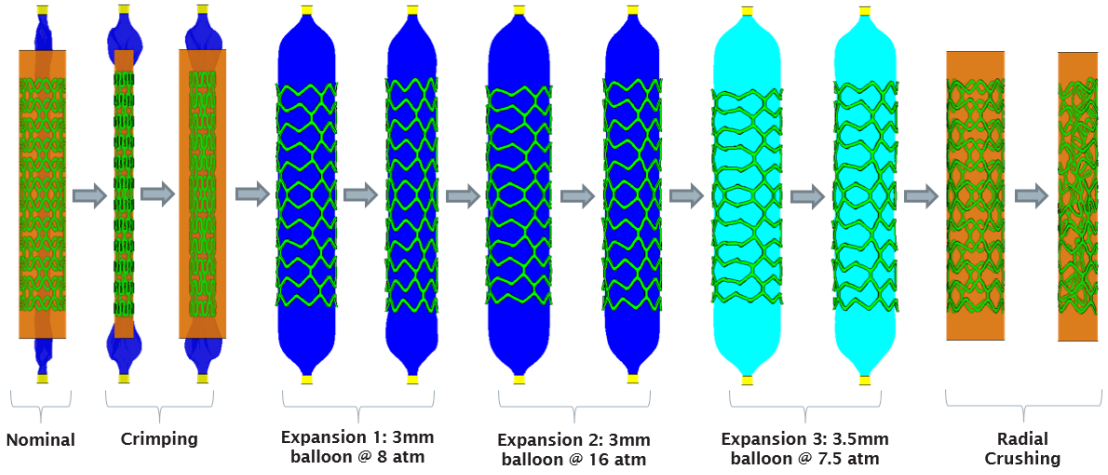

FIGURE 5.4: Realistic simulation setup in Abaqus/CAE (DS SIMULIA) to mimic the *in-vitro* mechanical testing of the BRS conducted by Arterius Ltd (Leeds, UK). The standard simulation setup used the 3.5 mm balloon only to expand the scaffold.

The multi-balloon simulation took approximately 20 hours to complete using the University of Southampton Iridis 4 high performance computing cluster whilst the standard simulation setup took approximately 6 hours to complete, as per Chapter 4.

5.2.7 Scaffold Performance

The metrics to quantify the performance of the scaffold's mechanical response in crimping, balloon-expansion and radial crushing are detailed in Section 3.4. Namely, these are the radial strength (RS, effectively the SRS multiplied by the nominal scaffold length), final diameter (FD) and percentage recoil ($R_{\%}$) of the BRS. The final diameter and percentage recoil are measured at two locations along the scaffold length; ring 1 refers to one of the central closed rings whilst ring 6 refers to one of the scaffold end rings. Given the different configurations of the central and end rings of the scaffold (closed and open cells, respectively), it was deemed necessary to observe these metrics at the two contrasting locations on the scaffold. Additionally the distribution of equivalent plastic strain was observed to help understand the likelihood of strut fracture in expansion and the difference in this metric as a result of different material models.

5.3 Results & Discussion

Results for the 12 test scenarios along with the *in-vitro* bench test are summarised in Table 6.4.

Test Scenario	Radial Strength (N)	Final Diameter Ring 1 (mm)	Percentage Recoil Ring 1 (%)	Final Diameter Ring 6 (mm)	Percentage Recoil Ring 6 (%)
in-vitro	11.52	3.66	2.92	3.71	2.62
1 1-Ax-Iso-Mises-N	26.42	3.05	17.71	3.14	16.28
2 1-Cir-Iso-Mises-N	6.35	3.14	18.71	3.23	16.71
3 1-Cir-Iso-Hill-N	13.99	3.47	9.88	3.46	10.36
4 50-Cir-Iso-Hill-N	19.30	3.60	6.14	3.57	6.92
5 1-Cir-TrIso-Hill-N	12.82	3.30	14.31	3.29	14.86
6 50-Cir-TrIso-Hill-N	20.33	3.69	4.52	3.53	7.95
7 1-Cir-TrIso-Hill-Y	12.56	3.30	14.29	3.28	15.04
8 50-Cir-TrIso-Hill-Y	19.17	3.60	6.49	3.51	8.47
9 1-Cir-Iso-Hill-Y	14.12	3.47	9.87	3.46	10.36
10 50-Cir-Iso-Hill-Y	15.54	3.69	4.78	3.63	5.96
11 1-Cir-Iso-HB-Y	11.00	3.51	9.65	3.46	11.07
12 1-Cir-Iso-HB-Y*	11.40	3.48	10.44	3.46	10.82

TABLE 5.5: Radial strength, final diameter and percentage recoil obtained for the 12 different testing scenarios along with the *in-vitro* bench test.

5.3.1 Isotropic Plastic Material Models

Observation of the isotropic plastic material model results shows their inferiority compared to anisotropic models. Utilising the axial stress-strain data only (model 1-Ax-Iso-Mises-N) significantly overestimates the RS of the scaffold compared to the *in-vitro* bench test, whilst the circumferential data (model 1-Cir-Iso-Mises-N) underestimates

this metric. In both cases the isotropic model provides a poor estimate of the final scaffold shape, predicting a $R_{\%}$ of approximately 18% and FD of approximately 3.1 mm at the central ring compared to 2.92% and 3.66 mm, respectively for the *in-vitro* test. Utilising data obtained at a faster displacement rate would likely further degrade the isotropic axial model and provide minimal improvement to the isotropic circumferential model's prediction, given that this would result in a Young's modulus similar to that used in model 1-Ax-Iso-Mises-N, test scenario 1.

Figure 5.5 shows the equivalent plastic strain developed in the vicinity of the crown apex at the scaffold end rings at maximum balloon inflation pressure using; (A) material model 1-Ax-Iso-Mises-N and (B) material model 1-Cir-Iso-Mises-N.

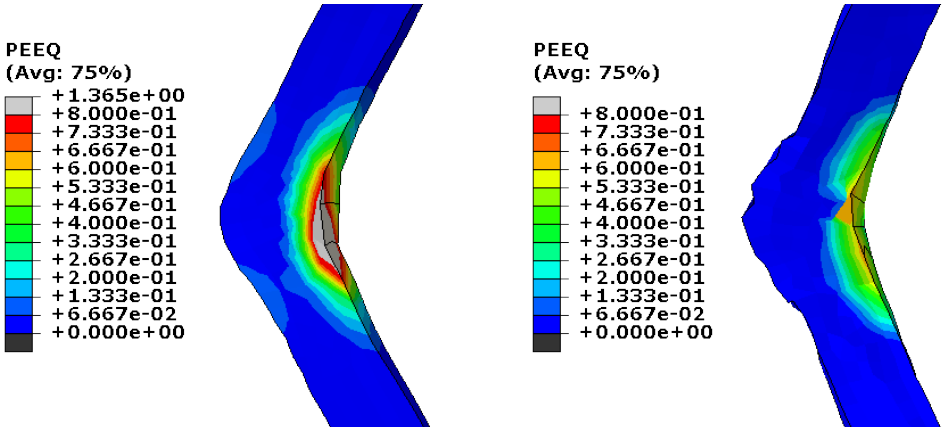

(A) (B)

FIGURE 5.5: Equivalent plastic strain distributions for the simulations using isotropic material models that utilise; (A) stress-strain data from the axial direction (model 1-Ax-Iso-Mises-N) and (B) stress-strain data from the circumferential direction (model 1-Cir-Iso-Mises-N).

A high level of PEEQ, in excess of the UTSn, is evident in Figure 5.5(A) at the inside of the crown apex. In contrast, the plastic strain on the outside of the crown is low, yet the *in-vitro* data suggests a significant amount of PEEQ develops either side of the crown apex where the plastic appears to whiten slightly on the outside of the crown. This is evident in Figure 5.6 where the outside edge of the crown apex becomes more pronounced whereby the smooth contour at the outside of the crown is disrupted, due to the adjacent areas of plastic strain as the scaffold opens in expansion. This could be described as 'pinching' of the crown apex. Therefore, it is unlikely that Figure 5.5(A) provides a realistic picture of the strain distribution in the scaffold. Figure 5.5(B) highlights some significant deformation around the outer edge of the scaffold whereby it appears jagged which seems non-physical, perhaps due to the low material stiffness inherent to the circumferential stress-strain data. There is also no development of PEEQ on the outside of the crown in 5.5(B). Therefore, it is clear that isotropic elasto-plastic material models provide limited insight into scaffold mechanical behaviour.

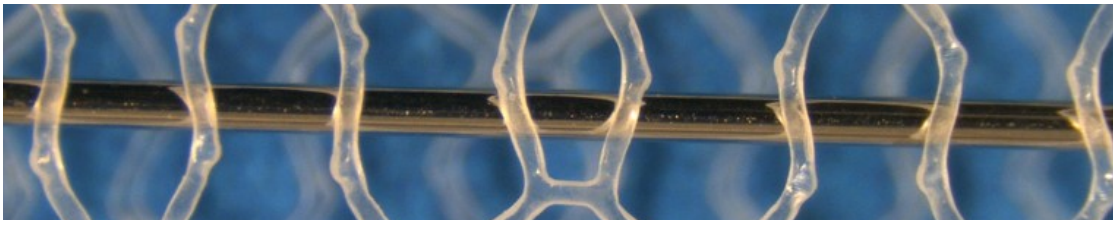

FIGURE 5.6: A section of the recoiled baseline scaffold design, based upon the ArterioSorb^{TM} BRS. Significant levels of plastic strain have been developed either side of the open-cell crown apexes at their outer edges resulting in 'pinching' of the crown. The *in-vitro* testing was conducted by Arterius Ltd (Leeds, UK).

For clarity, the terms hinging, crazing and pinching are defined here.

- Crazing is the whitening of PLLA that occurs when it is plastically deformed, first observed by (Radu et al., 2012).
- Pinching describes the increased pronouncement of the outside of the crown apex, whereby the smooth contour at the outside of the crown is disrupted.
- Hinging occurs when crazing of the polymer traverses the width of the scaffold strut and renders the scaffold vulnerable to fatigue failure.

5.3.2 Anisotropic Plastic Material Models

5.3.2.1 Comparison of Displacement Rate of Underlying Stress-Strain Data

Use of the anisotropic material models provided a clear step change in the predicted mechanical behaviour of the scaffold. Model 1-Cir-Iso-Hill-N significantly improved upon predicting the RS and FD compared to the isotropic material models, resulting in percentage errors of 21% and 6.7%, respectively from the *in-vitro* data. Model 50-Cir-Iso-Hill-N greatly improved upon the FD and $R_{\%}$ prediction, whereby the FD of the scaffold end ring was predicted to within 4% of the *in-vitro* value, yet over estimated the RS, by 40%, due to its high Young's modulus. Models 1-Cir-Iso-Hill-N and 50-Cir-Iso-Hill-N demonstrate the trade-off between prediction of the scaffold shape and radial strength, the former better described in each case by utilising the 50 mm/min stress-strain data to enforce a lower level of recoil while the latter preferring the use of the less-stiff slower displacement rate data.

5.3.2.2 Comparison of Elasticity Models

Considering the modelling of the material's elastic regime, utilising an isotropic approximation in the case of the slower displacement rate greatly improved prediction of

the scaffold shape (comparing models 1-Cir-Iso-Hill-N and 1-Cir-TrIso-Hill-N) whilst there is no significant difference in the case of the 50 mm/min data (comparing models 50-Cir-Iso-Hill-N and 50-Cir-TrIso-Hill-N). Model 50-Cir-Iso-Hill-N provided percentage errors of 1.64% and 3.77% for prediction of the FD of rings 1 and 6, respectively when compared with the *in-vitro* scenario. However, model 1-Cir-TrIso-Hill-N provided a marked improvement upon the prediction of RS when compared to model 1-Cir-Iso-Hill-N, although at the expense of predicting the scaffold's final shape. Once again, the trade-off between predicting the scaffold shape and RS is highlighted, in this case due to the modelling of the elastic regime of PLLA.

5.3.2.3 Use of Failure Stress-Strain Data

Figure 5.7 shows a comparison of the equivalent plastic strain developed in the two end rings of scaffolds using models 1-Cir-TrIso-Hill-Y, 50-Cir-TrIso-Hill-Y, 1-Cir-Iso-Hill-Y and 50-Cir-Iso-Hill-Y. Each of these models uses the failure stress-strain data to induce stress relaxation in the elements once the ultimate tensile strain is exceeded.

Inclusion of the failure data allied with the transversely isotropic elastic model, as per models 1-Cir-TrIso-Hill-Y and 50-Cir-TrIso-Hill-Y, did not significantly alter prediction of the scaffold shape compared to models 1-Cir-TrIso-Hill-N and 50-Cir-TrIso-Hill-N. However, a small improvement in RS prediction was achieved in both cases, due to the relaxation in stress that occurs as elements begin to exceed the UTSn. Interestingly, observation of Figure 5.7 suggests that only a very small number of elements exceeded the UTSn in model 1-Cir-TrIso-Hill-Y, shown in Figure 5.7(A). In model 50-Cir-TrIso-Hill-Y, shown in Figure 5.7(B), where a noticeable proportion of the scaffold appears to exhibit significant development of PEEQ, only 0.68 % of the scaffold structure actually exceeded the ultimate tensile strain (remembering that in this case the ultimate tensile strain is lower, approximately 0.65). Moreover, there were only modest changes to prediction of the scaffold's FD and RS when compared with not including the failure data for this model. Further, it is also evident in Figure 5.7(B) that the highly strained areas are generally not joined to a connector. This same trend is evident in a comparison of model 1-Cir-Iso-Hill-Y, Figure 5.7(C) and model 50-Cir-Iso-Hill-Y, Figure 5.7(D). Therefore, as suggested in Chapter 4 the connector geometry has a significant influence upon the behaviour of the scaffold. It is possible the mechanical performance of the scaffold is dominated by the geometry of the crowns attached to connectors as, despite the highly strained elements, the scaffold maintains good mechanical performance in the case of models 50-Cir-TrIso-Hill-Y and 50-Cir-Iso-Hill-Y. After comparing models 1-Cir-TrIso-Hill-Y and 1-Cir-Iso-Hill-Y as well as 50-Cir-TrIso-Hill-Y and 50-Cir-Iso-Hill-Y it was observed that utilising the isotropic elastic approximation led to greater development of equivalent plastic strain in both cases which resulted in improved FD predictions.

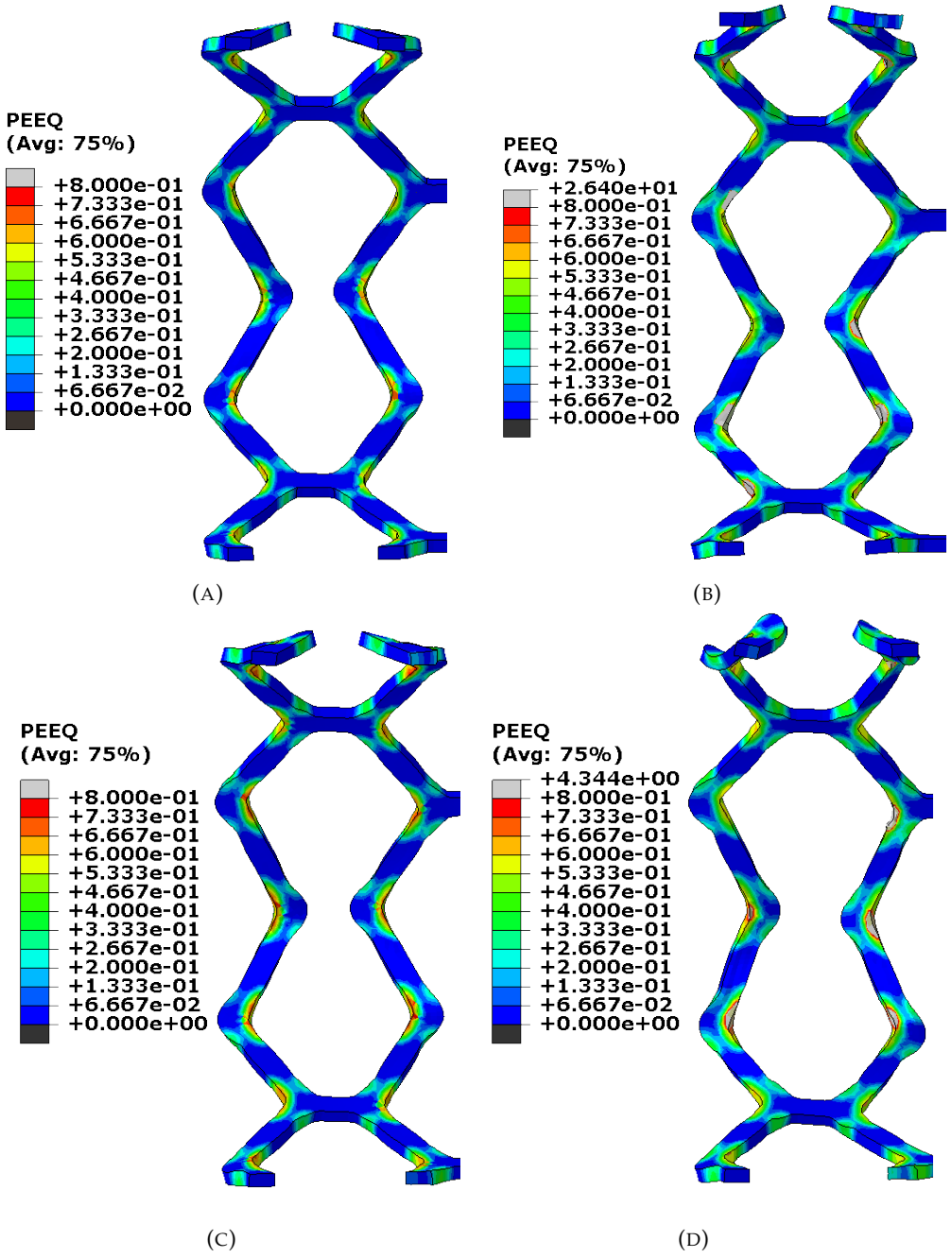

FIGURE 5.7: A comparison of the equivalent plastic strain in the end rings of the scaffolds for; (A) model 1-Cir-TrIso-Hill-Y; (B) model 50-Cir-TrIso-Hill-Y; (C) model 1-Cir-Iso-Hill-Y and (D) model 50-Cir-Iso-Hill-Y when the balloon is at maximum inflation pressure.

Returning to the distribution of equivalent plastic strain at the outside of the crown, Figure 5.7 shows a much more realistic picture compared to Figure 5.5. Significant development of plastic strain either side of the crown apex is evident in Figure 5.7 in all test scenarios which results in 'pinching' of the crown observed in the physical bench tests, as per Figure 4.13.

The equivalent plastic strain in the scaffold struts at maximum diameter for model 50-Cir-Iso-Hill-Y, test scenario 10, is presented in Figure 5.8. The plastic strain distribution shows the 'pinching' phenomenon, shown in Figure 4.13, where significant levels of PEEQ developed either side of the crown apex on its outer radius. However, very large maximum values of PEEQ, approximately 6 times greater than the UTSn observed in the tensile tests of PLLA conducted at 50 mm/min, develop at the inside of the crowns which would not manifest to such a high magnitude in *vitro* without strut fracture occurring.

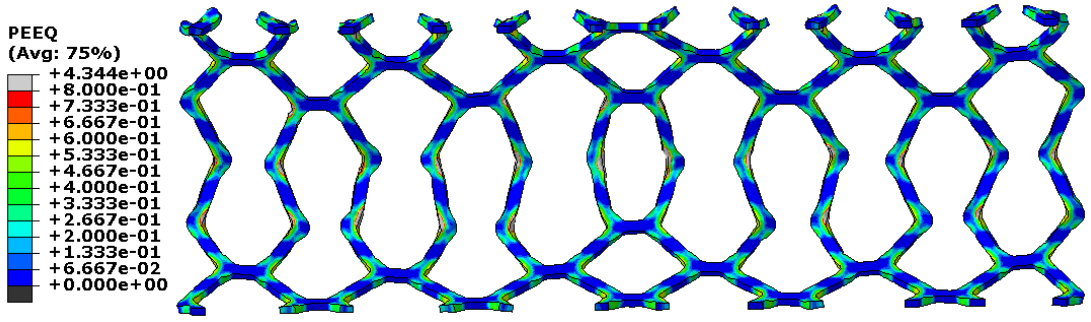

FIGURE 5.8: The equivalent plastic strain distribution for the scaffold at maximum diameter for model 50-Cir-Iso-Hill-Y, test scenario 10.

Figure 5.9 shows the force displacement curves for the *in-vitro* test and model 1-Cir-TrIso-Hill-Y, test scenario 7 which gives the best prediction of RS of all the in-built Abaqus anisotropic models investigated. The model predicts the initial gradient of the force-displacement graph well whilst the maximum force is over-predicted by 9%. The crimp makes contact with the scaffold at a different diameter due to the different FD achieved between the *in-vitro* and *in-silico* tests.

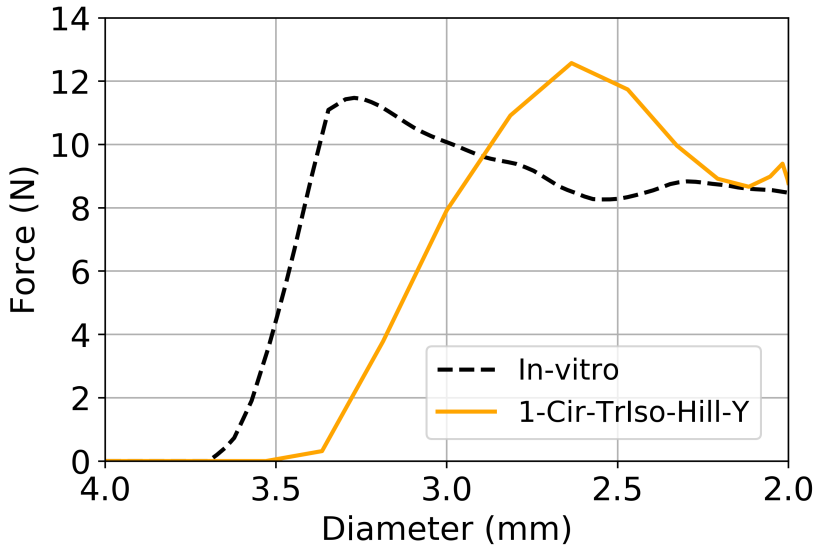

FIGURE 5.9: The force-displacement curves for the radial crushing test for the *in-vitro* and *in-silico* cases. The results for model 1-Cir-TrIso-Hill-Y, test scenario 7 are depicted. This material model comprises anisotropic plasticity and elastic transverse isotropy in addition to the failure stress-strain data, obtained at a displacement rate of 1 mm/min.

5.3.2.4 Summary of Anisotropic Plastic Models

Modelling the elastic behaviour of the scaffold using linear isotropy and including the failure data in the material model, as per models 1-Cir-Iso-Hill-Y and 50-Cir-Iso-Hill-Y, yielded a significant improvement in prediction of the final diameter of the scaffold, compared to models 1-Cir-TrIso-Hill-Y and 50-Cir-TrIso-Hill-Y, respectively. Scenario 50-Cir-Iso-Hill-Y also provided an improvement in the prediction of RS as this reduces from 19.17 N in model 50-Cir-TrIso-Hill-Y to 15.54 N. Model 1-Cir-Iso-Hill-Y achieved a good estimation of scaffold FD with percentage errors of 5.19% and 7.89% for rings 1 and 6, respectively. This is good considering the low Young's modulus of just 1872 MPa utilised in that model. However, the prediction of RS in the case of model 1-Cir-Iso-Hill-Y, yielded a percentage error of 22.47%, compared to the *in-vitro* test. Utilising an average of the Young's moduli for the axial and circumferential directions to describe the material stiffness, as performed in the implementation of the isotropic elastic models, resulted in an effective increase in stiffness in the circumferential direction. As the circumferential direction is the primary loading direction in expansion, albeit in combination with the axial direction due to the bending of the scaffold struts about the crown apex, the RS was overestimated, evidenced in models 1-Cir-Iso-Hill-Y and 1-Cir-TrIso-Hill-Y when compared to the *in-vitro* test.

After exploration of the models utilising the anisotropic Hill's yield function, considering isotropic and transversely isotropic elastic models, failure stress-strain and the displacement rate of the underlying stress-strain data, it is clear that none of the models can simultaneously capture both the final scaffold diameter and radial strength of

the baseline scaffold design. Use of the Hill's yield function in combination with elastic isotropy and the failure data (as per model 50-Cir-Iso-Hill-Y) gave the best prediction of final diameter with percentage errors, compared to the *in-vitro* data, of 0.82% and 2.16% for rings 1 and 6, respectively. However, the percentage error for RS prediction for this scenario was 34% which represents a significant overestimation. The recoiled scaffold for model 50-Cir-Iso-Hill-Y is presented in Figure 5.8. The maximum plastic strains reached approximately 4.4 at the inside of some crowns, in particular those not attached to a connector. It is noticeable that post recoil the scaffold struts remain relatively straight, particularly at the central closed ring due to the significant development of plastic strain at this location. Strains of this magnitude would not develop in *vitro* but lead to redistribution of the strain in the scaffold struts or result in failure of the scaffold struts due to ductile fracture. However, the scaffold presented no evidence of fracture from the physical bench test, even when significantly over-expanded, as shown in Figure 4.13.

In contrast, the best prediction of the RS was given by model 1-Cir-TrIso-Hill-Y which used the slower displacement rate stress-strain data, transverse isotropy as well as incorporating the failure data. This yielded a percentage error of 8.99% compared to the *in-vitro* test. The force-displacement curves for model 1-Cir-TrIso-Hill-Y and the *in-vitro* test are given in Figure 5.9. Observation of Figure 5.9 shows that material model 1-Cir-TrIso-Hill-Y captured the general force-displacement profile of the scaffold well although with a small over prediction in maximum force but a similar gradient of the initial portion of the curve.

Accurate prediction of both the post-expansion scaffold diameter and radial strength does not appear to be possible within the constraints of the constitutive theory using the in-built Abaqus anisotropic plastic potential models investigated. Therefore, it was decided an alternative material model should be explored.

5.3.3 Hoddy-Bressloff Material Model

Based upon the findings of the *in-silico* test scenarios 1 - 10, it was hypothesised that an alternative model may be able to achieve a more accurate estimation of the scaffold radial strength whilst minimising the compromise in prediction of the post-expansion scaffold diameter.

Thus the Hoddy-Bressloff model was devised to:

1. More accurately model the high strain behaviour of the axial direction.
2. Capture the stress relaxation and subsequent decrease in hardening in elements that become overly strained.

This HB model facilitates greater plastic strains to develop in some elements as they become overly strained and exhibit a large drop in stress whilst retaining radial strength in the scaffold overall via the increase in yield stress and hardening in the axial direction as the plastic strain develops.

The equivalent plastic strain distribution at MD for the model 1-Cir-Iso-HB-Y, test scenario 11, is shown in Figure 5.10. The maximum plastic strains developed at the inside of the crowns appear to greatly exceed UTSn of the PLLA. This is caused by the relaxation of stress when the ultimate tensile strain is exceeded as this effectively facilitates perfect plasticity to occur at zero stress. Elsewhere in the scaffold struts, the plastic strain appears more closely confined to the vicinity of the crown apex compared with the in-built anisotropic models in Abaqus.

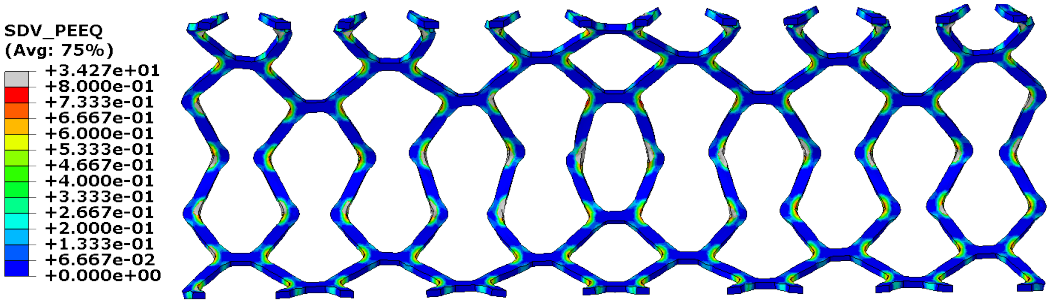

FIGURE 5.10: The distribution of plastic equivalent strain in the struts of the ArterioSorb^{TM} at maximum balloon inflation pressure for model 1-Cir-Iso-HB-Y.

Figure 5.10 highlights that the model allowed significant plastic strain to develop at the inside of the crowns to a maximum value of almost 35. However, less than 1% of the elements in the scaffold display a value of PEEQ greater than 1. The maximum values of PEEQ displayed in Figure 5.10 would not manifest in *vitro* as crack initiation and propagation would occur prior to such high levels of PEEQ developing. Again, it is interesting to note that the crowns joined to a connector display a much lower and more realistic distribution of PEEQ. This indicates that the crown geometry in the vicinity of a connector determines the mechanical performance of the scaffold. Otherwise RS may suffer considerably *in-silico* due to the significant levels of strain predicted at the inside of the crown. Also, it is noteworthy that the 'pinching' evident in the *in-vitro* test at the outside edge of the crown apex was also evident in model 1-Cir-Iso-HB-Y. Areas of modest but noticeable levels of PEEQ lie either side of the crown apex. However, the magnitude of PEEQ at the outside of the crown is certainly smaller than in the case of model 50-Cir-Iso-Hill-Y. Further, Figure 5.10 appears to show the PEEQ is more confined to the vicinity of the crown and less well distributed into the scaffold struts in comparison to Figure 5.7 and Figure 5.8 which depict the in-built anisotropic models from Abaqus.

Figure 5.11 shows the force-displacement curves for the *in-vitro* test, model 1-Cir-Iso-HB-Y (test scenario 11) and model 1-Cir-Iso-HB-Y* (test scenario 12). The simulations

both employ the Hoddy-Bressloff model but utilise different deployment strategies in the FEA. Both cases appear to predict the force required to crush the scaffold until the maximum force after which the scaffold is deemed to have failed due to buckling of the scaffold struts. At this point the crushing force prediction deviates significantly from the *in-vitro* test. The buckling of the scaffold is subject to many geometrical non-linearities that might initiate this, making it particularly hard (and unnecessary) to predict in this context. Once again the stiffness of the scaffold in the crushing process is accurately predicted. It is also evident in Figure 5.11 that the HB model more accurately predicts the FD of the scaffold as the crimp and scaffold appear to come into contact at a similar diameter.

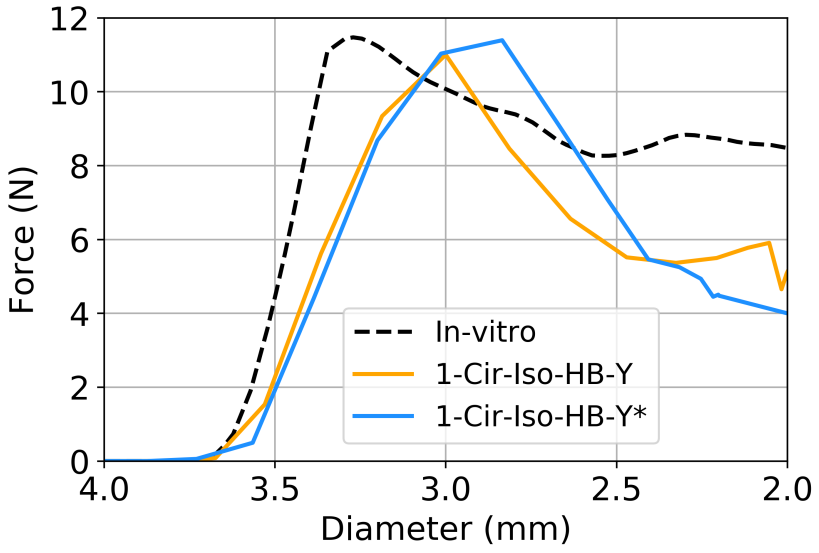

FIGURE 5.11: The force-displacement plots from the radial crushing test for the *in-vitro* test as well as models 1-Cir-Iso-HB-Y and 1-Cir-Iso-HB-Y*, both of which use the Hoddy-Bressloff model encompassing linear isotropy, the stress-strain failure data and calibration to the plastic stress-strain data obtained at a displacement rate of 1 mm/min.

Whilst model 1-Cir-Iso-HB-Y provides a reasonable prediction of the FD, Figure 5.12 shows that the scaffold recoiled more greatly *in-silico* than in the *in-vitro* test where the post-expansion recoil was low due to the HB model not utilising the stiffer axial component of the Young's modulus. Although this model framework would result in a reduction in accuracy of RS prediction if this were to be taken into account via orthotropic elastic relationships. This figure highlights the disparity in $R_{\%}$ between the *in-silico* and *in-vitro* cases. It is particularly clear in Figure 5.12(E) and Figure 5.12(F) where the central closed cells are dramatically different in shape due to the inherently low stiffness of the HB model which led to poor $R_{\%}$ prediction.

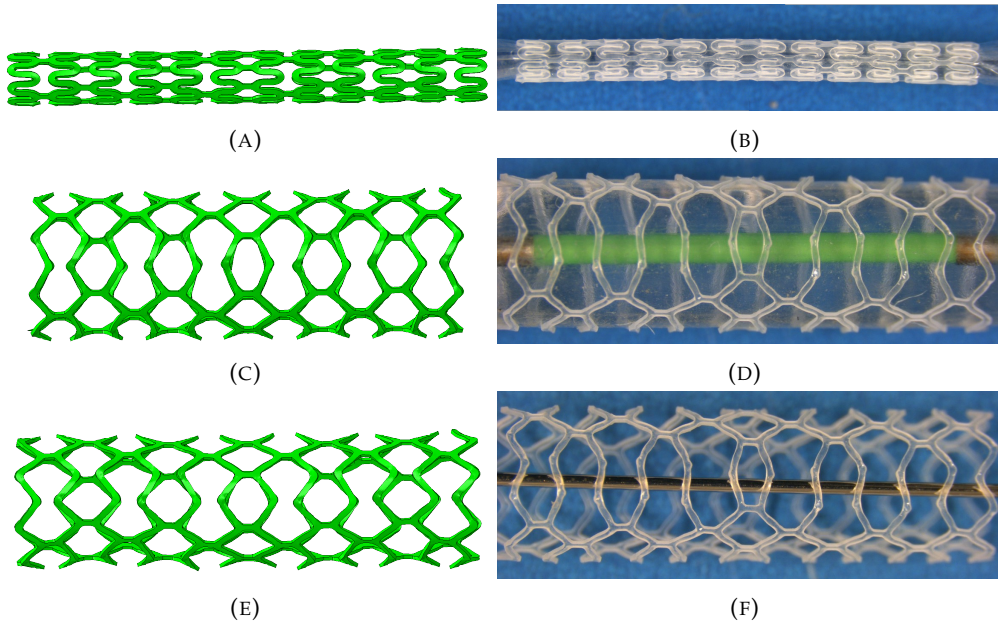

FIGURE 5.12: A comparison of the scaffold shapes for scenario 11 (left) and the *in-vitro* test (right). Scenario 11 utilises the Hoddy-Bressloff material model. Each stage of the deployment process is shown where; (A) and (B) depict the scaffold post crimping; (C) and (D) depict the scaffold on the balloon at maximum inflation pressure and; (E) and (F) depict the recoiled scaffold post expansion.

The Hoddy-Bressloff model achieved a good level of accuracy in predicting the final diameter of the scaffold post expansion, in particular for a model that utilises the stress-strain data obtained at the slower, more realistic displacement rate. Percentage errors for prediction of the FD of 5.46% and 5.39% for rings 1 and 6, respectively were achieved. The model also predicted the RS with an accuracy of 4.45% in test scenario 11 which represents the best estimation of this metric compared to all the aforementioned models. It should be noted that the elasto-plastic model utilised by Wang et al. (2017) in the expansion of a polymeric BRS achieves a similar level of percentage recoil. However, the scaffold width and thickness are far greater than that of the ArterioSorb^{TM} BRS. This is testament to the exceptional recoil behaviour of the ArterioSorb^{TM} which, as proven in this study, is difficult to capture in tandem with an accurate RS prediction. Therefore, this model appears to offer a good balance of both FD and RS prediction. The model also estimates these critical metrics conservatively by under-predicting the radial strength and over-predicting the elastic recoil which is favourable to over-estimating the performance of the device.

5.3.4 Realistic Simulation Strategy

Whilst it was hypothesised that the disparity in recoil behaviour of the scaffold between the *in-silico* and *in-vitro* scenarios was, in part, due to the multiple balloon expansion strategy used in *vitro*, this was not found to be the case. Multiple balloon expansions of

the scaffold is commonly used in clinical practice, known as pre/post-dilatation. The realistic simulation setup detailed in Subsection 5.2.6 was utilised to explore whether this strategy yields improved recoil results, for the Hoddy-Bressloff model, detailed in Table 5.3 (model 1-Cir-Iso-HB-Y*).

Model 1-Cir-Iso-HB-Y* yielded no significant improvement in prediction of the final scaffold diameter with very similar levels of $R_{\%}$ and FD compared to model 1-Cir-Iso-HB-Y. However, prediction of RS did improve and achieved a percentage error of just 1.1% compared to the *in-vitro* test. The force-displacement curve for this test case, shown in Figure 5.11 displays good agreement with the *in-vitro* data until the point of maximum force, after which, again, the curves diverge significantly. The final diameter of the scaffold was predicted with percentage errors of 4.9% and 6.7% compared to the *in-vitro* test for rings 1 and 6, respectively. However, the higher complexity of these simulations means that solution times were in the order of 20 hours, rather than 6 hours, achieved by the single balloon strategy. Therefore, this strategy is difficult to justify given the practicalities of long solution times and the volume of the results files produced.

These findings confirm that a mechanism exists in the PLLA, that is not currently captured by any of the aforementioned models, which results in the low recoil behaviour of the ArterioSorb^{TM} BRS. Therefore, the exploration of alternative material models to capture this low recoil behaviour without alteration of the RS prediction, should be undertaken. The use of parallel network models to capture the viscoelasticity observed in PLLA should certainly be considered. However, whilst a number of previous studies develop and utilise such constitutive material models (Bergström and Boyce, 1998; Eswaran et al., 2011; Debusschere et al., 2015; Bobel et al., 2015; Bobel and McHugh, 2018), it is unclear whether they would facilitate accurately capturing the recoil behaviour of a thin-strut second generation BRS, particularly given the very low values exhibited in the ArterioSorb^{TM} BRS. No previous studies appear to report a $R_{\%}$ of less than 3% for a thin-strut BRS deployed via balloon expansion.

Whilst the multi-balloon expansion technique has been modelled, a realistic multi-stage elevated temperature crimping process was not able to be explored in this work. It is possible that this process, conducted by Arterius Ltd, has a significant impact on the recoil behaviour of the scaffold due to the rearrangement of polymer chains that occurs throughout this process. Therefore, to explore this could also provide further insight into the low recoil behaviour exhibited by the ArterioSorb^{TM} BRS.

5.4 Conclusions

This work compares and contrasts a variety of material models, including a new user-defined model, calibrated with realistic stress-strain data obtained from uniaxial tensile

tests and validates them with clinically relevant *in-vitro* data. An improved simulation strategy that offers closer alignment with the *in-vitro* tests was also explored to attempt to further improve *in-silico* prediction of scaffold performance. From this, the following conclusions can be drawn.

1. A new material property model, the Hoddy-Bressloff model, provides an improved yet conservative estimation of radial strength with a percentage error of just 1.1% using a realistic multi-balloon expansion strategy. Post-expansion scaffold shape is predicted within 6.7% of the *in-vitro* data.

2. The realistic simulation setup indicates that a mechanism exists in the PLLA which causes the very low recoil behaviour of the ArterioSorb^{TM} BRS that is not captured in the by the material models investigated in this chapter. Therefore, higher fidelity, viscoelastic-plastic material models should be explored as well as exploration of the effect of the crimping process upon scaffold mechanical behaviour. It is also evident that use of a multi-balloon strategy to deploy coronary scaffolds in *silico* provides a small improvement in RS prediction at a significant computational cost.

3. Capturing both the post-expansion scaffold shape and radial strength in *silico* for the baseline scaffold design based upon the ArterioSorb^{TM} BRS cannot be achieved with the in-built Abaqus anisotropic models explored in this study.

4. An anisotropic description of the plastic behaviour of the scaffold is superior to an isotropic model to accurately capture the scaffold mechanical behaviour.

5. When using an anisotropic plastic potential model that incorporates the stress relaxation data along with isotropic elastic theory and stress-strain data obtained at a fast displacement rate of 50 mm/min, an improvement in accuracy for scaffold shape prediction can be achieved.

6. In contrast, when using an anisotropic plastic potential model that incorporates the stress relaxation data along with a transverse isotropy approximation, the model should utilise stress-strain data obtained at a slow, clinically relevant displacement rate, in this case 1 mm/min to more accurately capture the radial strength of the scaffold.

Chapter 6

Investigating a Viscoelastic-Plastic Material Model

6.1 Introduction

Chapters 4 and 5 conclude that predicting the mechanical behaviour of next generation thin-strut coronary scaffolds is challenging in the context of FEA. The use of simple elasto-plastic theory does not appear to be appropriate to capture both the scaffold's final diameter and an accurate prediction of its radial strength. Therefore, we now turn out attention to a high fidelity viscoelastic-plastic material model. Viscoelastic-plastic material models that utilise a parallel network rheology, have long been regarded as the gold standard for describing the stress-strain response of polymers (Bergström, 2015). However, the increased complexity of these models, compared to elasto-plastic theory, can hinder their adoption in FEA. Increased solution times and a scarcity of model availability in finite element software contribute to this. In addition, significantly more effort is required by the user to understand the model parameters and calibrate them to experimental data. In addition, whilst these models are proven at capturing the stress response of PLLA, whether they can accurately predict the mechanical metrics that quantify the performance of next generation thin-strut scaffolds is yet to be ascertained. In doing so, this will help to reduce the reliance on costly and time consuming *in-vitro* testing (Mincarone et al., 2021).

In Chapter 5 we demonstrated the limitations of elasto-plastic theory to accurately predict the FD and RS of a BRS based upon the ArterioSorb^{TM} without compromise to at least one of them. A viscoelastic-plastic material model may be able to more accurately capture the scaffold mechanical behaviour. In this case, the radial strength and elastic recoil are not both determined by a single parameter (the Young's modulus) as the material model can describe different gradients of the loading and unloading paths in the

stress-strain response. This should help facilitate an improvement in recoil prediction as well as radial strength.

The ability of *in-silico* tests to capture the post-crimping recoil of the scaffold also appears challenging from our investigation in Chapter 4. Recently, Antonini et al. (2021a) used the Johnson-Cook viscoplasticity model to simulate the behaviour of a BRS, based upon the Abbott Vascular Absorb GT1, to investigate the effect of temperature and strain rate upon the stresses developed in crimping. This also highlighted the difficulty in predicting the very low values of post-crimping recoil necessary in BRS to facilitate acceptable securement to the balloon-catheter.

Therefore, in this chapter we present an analysis of a variant of the Bergstrom-Boyce (BB) material model, a viscoelastic-plastic model (Bergström and Boyce, 1998, 2001; DS SIMULIA, 2018) as implemented in Abaqus/Explicit via the parallel rheological framework to assess its accuracy in predicting the radial strength, percentage recoil and post-expansion diameter of a second generation thin-strut BRS, based upon the ArterioSorb^{TM} platform. Additionally, the effect of a temperature dependent material model and a staged crimping technique upon the post-crimping diameter of the scaffold is investigated. The isotropic limitations of the material model are considered, along with calibration to uniaxial tensile data and the implications of using a time dependent model in an explicit solver. The results are validated with *in-vitro* data obtained from mechanical laboratory testing and are also compared with the Hoddy-Bressloff model developed in Chapter 5.

6.2 Methodology

6.2.1 Scaffold Geometry

The same scaffold geometry, detailed in Subsection 4.2.1, for the baseline scaffold design was used in this study.

6.2.2 Constitutive Material Model

The Bergstrom-Boyce model is a viscoelastic-plastic material model that has been demonstrated to accurately predict the stress-strain response of elastomeric polymers (Bergström and Boyce, 1998, 2001). Polymers used in medical applications, such as PLLA exhibit nonlinear time-dependent behaviour such as viscoelastic recovery and strain rate dependency when subjected to large strains, resulting in permanent deformation (Bergström and Hayman, 2016). The rheology of this model can be represented by two network arms acting in parallel. Whilst a variety of model elements can be used in the parallel rheological framework in Abaqus/Explicit, the model used herein was chosen to

align it as closely as possible to the original BB model and to the model explored by Bobel and McHugh (2018) in the context of a first generation BRS. The first network arm contains an eight chain hyperelastic element with Mises plasticity and isotropic hardening whilst the second contains an eight chain hyperelastic element in series with the Bergstrom-Boyce viscous flow element. The constitutive theory of this model is presented in Subsection 3.5.3. The plastic behaviour in the first network arm uses a yield stress of 50 MPa at zero plastic strain. However, this was expected to have minimal effect upon the model's stress response due to being dominated by the viscous branch. This is because the subsequent calibration of the material model to the tensile test data yielded a large value of s (as per 3.30), which scales the contributions of the two network arms to the total stress tensor and so the B network was found to dominate the response of the model. Indeed, it is rarely necessary to use an additional plasticity model in the hyperelastic branch to describe the behaviour of polymers and it is not necessary in order to capture permanent strains (PolymerFEM, 2021).

6.2.3 Material Model Calibration

To utilise a material model in FEA, stress-strain data obtained from an *in-vitro* test must be obtained to which the model parameters can be calibrated. Most commonly, uniaxial tensile tests of dogbone shaped specimens are conducted as these are relatively simple to undertake. Chapter 5 presented stress-strain data of uniaxial tensile tests under monotonic loading to failure at multiple strain rates. In this case, despite the PRF model facilitating strain rate dependency, only a slow, clinically relevant displacement rate of 1 mm/min was considered as strain rate dependency was not the focus of the research. In addition, the dogbone shaped specimens were not monotonically loaded to failure but rather, loading-unloading tests were undertaken, the results of which are shown in Figure A.3.

The uniaxial loading-unloading tests were conducted using the same equipment and methodology as the monotonic load-to-failure tests with the obvious exception that the samples were loaded incrementally at 1 mm/min to approximately 75% of their failure strain before being unloaded to zero stress at 1 mm/min.

Whilst the *in-vitro* data shows a maximum strain of 0.8, initial simulations using the BB model showed that the maximum strain in the circumferential direction only reached approximately 0.2 at the inside of the scaffold crowns in expansion. The model was calibrated over this strain range given its time dependency and so no such assumptions regarding the strain range were necessary in the calibration of models in previous chapters. It should also be noted that, unlike the elasto-plastic models investigated, the BB does not consider PEEQ. Additionally, the uniaxial loading-unloading tests did not consider holding the sample at a constant strain, the stress response of which is relevant in crimping and expansion where the stress relaxation of BRS is exploited. Elastomers

such as PLLA are known to undergo stress relaxation when held at a given strain due to the viscous time-dependant rearrangement of the polymer chains. Therefore, the stress-strain data was amended based upon evidence from literature (Bobel et al., 2016; Sweeney et al., 2019) to only consider the strain up to a maximum of 0.2, effectively truncating the *in-vitro* data to a smaller strain range. This was followed by a holding section in which the stress relaxes to approximately 25% of its maximum value, before the remaining stress is allowed to relax via elastic recoil within approximately 2% strain. The resulting data, used to calibrate the material model is shown in Figure 6.1.

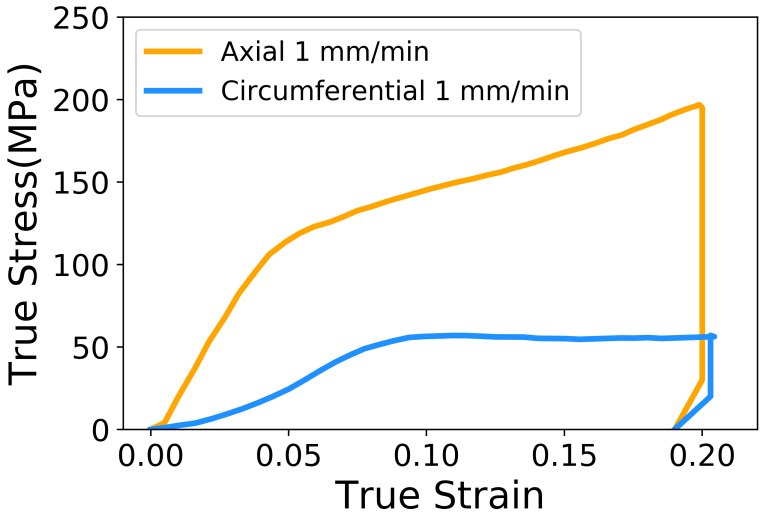

FIGURE 6.1: The amended stress-strain response for a uniaxial loading-unloading test for dogbone shaped samples cut from die-drawn PLLA tubes in the circumferential and axial directions in which the predicted stress relaxation and subsequent elastic recoil has been considered.

A 1D Python implementation of the BB model was used to calibrate the material model parameters (s, μ, $\overline{\lambda^{lock}}$, κ, ξ, C, q_0 and m, as per Chapter 3) to the uniaxial loading-unloading data in Figure 6.1, as well as a calculated data set comprising the mean stress response of the two directions. The model was evaluated for each permutation of the parameters and compared to the *in-vitro* data supplied. The parameter set that yielded the greatest R^2 value was chosen. Whilst PLLA exhibits highly anisotropic behaviour, the BB material model implemented in Abaqus/Explicit is limited to isotropic behaviour only. Therefore, it was hypothesised that calibrating a model to an average of the two directions' data sets would be the best compromise for predictions of the scaffold mechanical behaviour.

To validate the calibrated model, uniaxial tensile tests of dogbone shaped specimens were undertaken in *silico* to ensure that the model produced a similar stress response in Abaqus/Explicit as predicted by the 1D Python implementation. Given the time dependency of the model, the effect of the time period in tensile loading upon the model's stress response was also investigated.

The implementation of this model in Abaqus/Explicit allows calibration to additional state variables to define the material model parameters. Therefore, two sets of parameters were defined; those that referred to the room temperature data and those that referred to data obtained at an elevated temperature. Whilst uniaxial tensile tests at a range of temperatures were not able to be conducted, an estimate based upon the work of Antonini et al. (2021a) was used. This assumed a reduction in stress of approximately 50% when the temperature is increased from 25 °C (room temperature) to 42 °C, the temperature at which crimping is undertaken.

6.2.4 In-Vitro Bench Testing

The *in-vitro* testing utilised in this chapter to validate the *in-silico* models is the same as used in Chapters 4 and 5.

6.2.5 Simulation Setup

The initial crimping simulations were undertaken to investigate the effect of utilising an elevated temperature (42 °C), as per the *in-vitro* testing, as well as the loading profile of the crimping displacement upon the post-crimping scaffold diameter. Simulations were setup in which the scaffold was crimped from its nominal diameter to an outer diameter of 1 mm via a displacement driven crimping surface. This represents a slightly more aggressive crimping target diameter than used in *vitro* (1.1 mm) to help achieve an improvement in post-crimping recoil in *silico*. The time period of the crimping was 0.2 s to allow sufficient time for stress relaxation to stabilise. A predefined temperature field of 315 K (42°C) within the simulations' initial conditions was used to simulate the elevated temperature. The details of the four crimping simulations are given in Table 6.1 whilst the two loading profiles investigated are shown in Figure 6.2. The staged loading profiles facilitated stress relaxation throughout the crimping process at a constant strain. This was proposed as it maintained a given scaffold diameter but allowed the stresses to relax resulting in lower elastic recoil when the crimp was removed.

Simulation No.	Ambient Temperature	Displacement Profile
CRIMP-1	25°C	Direct
CRIMP-2	42°C	Direct
CRIMP-3	25°C	Staged
CRIMP-4	42°C	Staged

TABLE 6.1: Details of the four simulations undertaken to investigate the effect of an elevated ambient temperature and the displacement profile upon the post-crimping scaffold diameter.

A simulation of the crimping, balloon-expansion, relaxation and radial strength tests, as shown in Figure 6.3, was conducted to mimic the mechanical *in-vitro* testing of scaffold platforms undertaken by Arterius Ltd. The simulation varies from the setup used in Chapters 4 and 5, and consisted of the following steps:

1. Balloon folding. The tapered balloon was wrapped such that it resembled a standard tri-folded balloon.
2. Crimping. The scaffold was crimped from its nominal OD of 2.54 mm to 1 mm via a displacement driven crimping surface which used the staged crimping profile.
3. Expansion. The scaffold was expanded by inflating the 3.5 mm balloon, pressurised to 7.5 atm.
4. Holding. The balloon was then held at 7.5 atm for the same duration as the expansion step to facilitate stress relaxation.
5. Deflation. The balloon was deflated to allow the scaffold to elastically recoil.
6. Crushing. The scaffold was crushed radially via the displacement driven crimping surface to a diameter of approximately 2 mm.

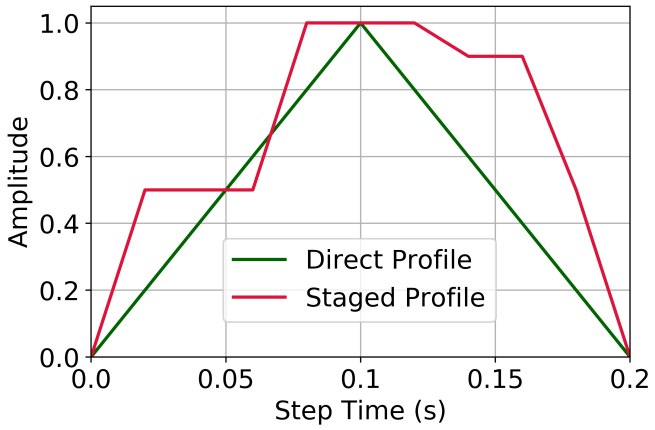

FIGURE 6.2: The two displacement profiles applied to the crimping cylinder in the initial crimping investigation. The direct profile displaces the cylinder linearly to its maximum displacement in half the time period and then relaxes it in half the time period. The staged profile utilises holding of the cylinder at points throughout the crimping and un-crimping process to facilitate stress relaxation.

A significant consideration when using the BB model in Abaqus/Explicit is the loading period due to the time dependent nature of the material model. A small change in the step length could significantly alter the stress response of the model. However, given the nature of the explicit solution technique where small time increments are required to achieve a stable solution, it is impractical to model the simulation in real time. This means the material model was calibrated to an artificial time vector to align

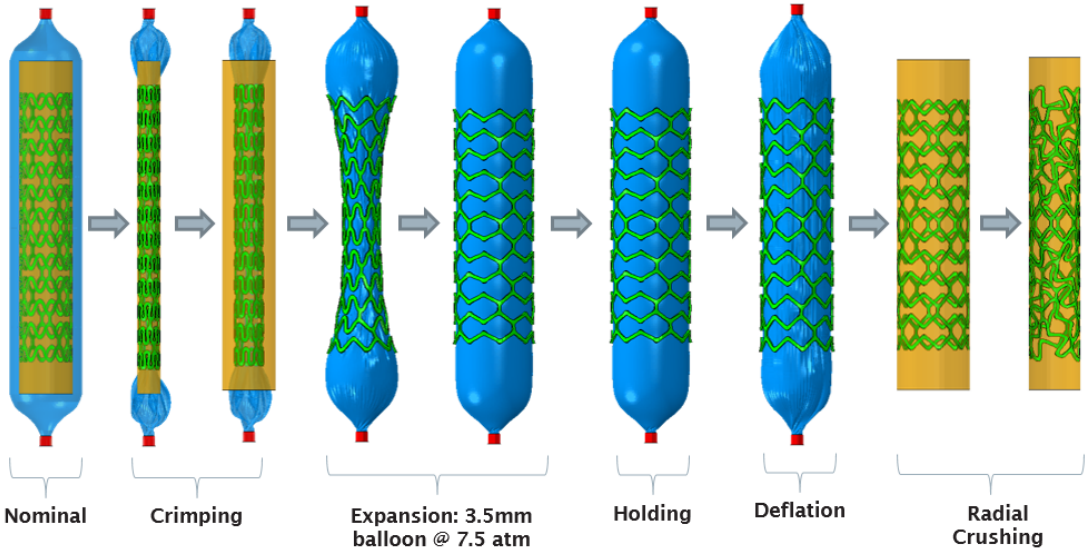

FIGURE 6.3: The simulation procedure in Abaqus/Explicit to mimic the *in-vitro* crimping, balloon expansion and radial strength testing of the BRS for the parallel rheological framework material model.

the stress response *in-silico* with the *in-vitro* data. The PRF material model was initially calibrated using a time period of 0.03 s for the expansion step, based upon the expected loading phase duration in Abaqus/Explicit, as per the previous simulations conducted. The effect of altering the step length was explored and is subsequently discussed in Subsection 6.3.2.

6.3 Results & Discussion

6.3.1 Isotropic Model Limitation

The Bergstrom-Boyce model, calibrated to the circumferential, axial and mean (the average stress response of the axial and circumferential directions) stress/strain data is shown in 6.4. Although PLLA has demonstrated anisotropic behaviour, it was hypothesised that, given the isotropic limitation of this implementation of the BB model, the model calibrated to the mean data would provide the most accurate predictions of the scaffold mechanical behaviour. The strain was applied in 0.03 s, as per the intended expansion time of the elastic balloon, the holding and recoil phases lasted 0.03 s and 0.24 s respectively. The recoil phase was given a large time increment to ensure the stress was fully relaxed.

There is excellent agreement between the BB models and *in-vitro* data, shown in Figure 6.4, particularly in the case of the mean data model which achieves an R^2 value of 0.98. Whilst the axial and circumferential data cannot be perfectly described by the model, due to the convex sections of the curves, they achieve R^2 values of 0.9 and 0.84,

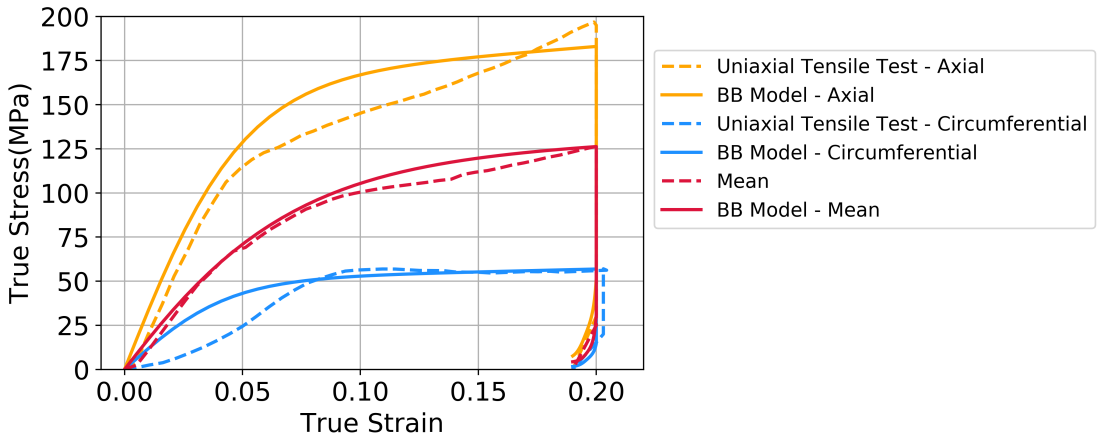

FIGURE 6.4: The Bergstrom-Boyce model calibrated to the axial, circumferential and mean stress-strain uniaxial tensile test data.

respectively. A higher fidelity model would be required to more closely describe the *in-vitro* data. However, this may be unnecessary to predict the mechanical behaviour of the BRS with suitable accuracy and will lead to increased solution times and increased complexity when calibrating the model as further model parameters would be required.

6.3.2 Effect of Time Period on Stress Response

To provide initial validation of the PRF model in Abaqus/Explicit, the uniaxial tensile test conducted on the dogbone specimen, the results of which are shown in Figure 6.1, was recreated in *silico* for the model calibrated to the circumferential data for three time periods. The relationship between the model's stress response and the time period of the tensioning of the sample in the *in-silico* test was investigated, with the sensitivity analysis shown in Figure 6.5.

Interestingly, a time period of half the value used in the 1D Python implementation was required to obtain the same stress response as the uniaxial tensile test in Abaqus/-Explicit. The disparity in the stress response between the 1D Python implementation and the *in-silico* dogbone test using a time period of 0.03 s in the tensioning step, as detailed in Figure 6.5, is of interest. In each case, the material models and time period to tension the sample to a true strain of approximately 0.24 were identical and so the stress responses were expected to be very similar. However, the maximum stress in the 1D Python implementation was approximately 60 MPa whilst in the case of the *in-silico* dogbone test, was approximately 45 MPa. Decreasing the time period for the tensioning step of the *in-silico* dogbone test to 0.015 s led to the stress responses aligning. The mass scaling used *in-silico* by the explicit solution technique to increase the minimum stable time increment will preserve the natural time period of the simulation and so this can be discounted as a source of error. As previously discussed, the simulation is

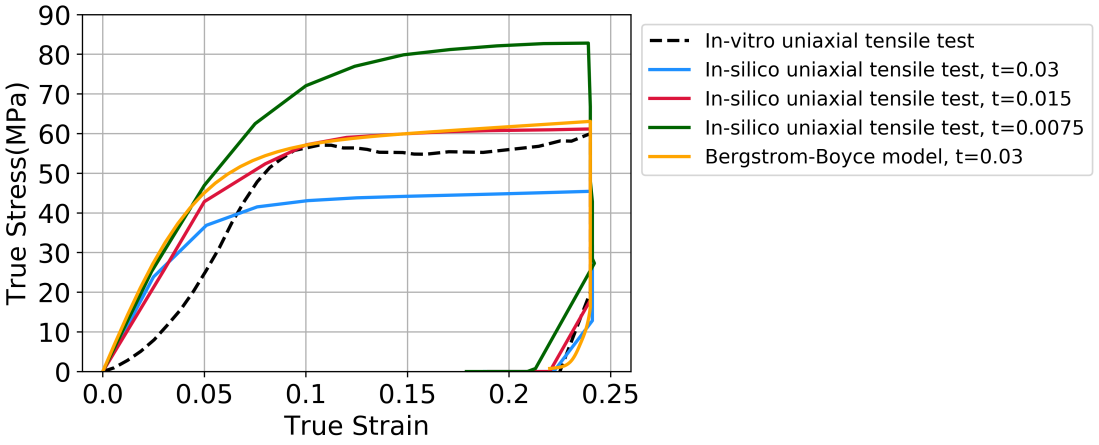

FIGURE 6.5: The Bergstrom-Boyce model implemented via the parallel rheological framework in Abaqus/Explicit calibrated to the circumferential data, using different time periods for the tensile tension step to investigate the sensitivity of this parameter with respect to the stress response for the *in-silico* uniaxial loading-unloading tests conducted on a dogbone shaped PLLA sample. The Bergstrom-Boyce model (yellow) refers to the 1D Python implementation, used for calibration of the model parameters.

quasi-static and so the kinetic energy is monitored to ensure it remains low throughout the simulation. Therefore, any small artificial increases in element mass will negligibly affect the model's stress response. The 3D effects of the *in-silico* simulation are minimal as the stresses in the directions orthogonal to the axis of the dogbone specimen (in this case, the scaffold's circumferential direction) are close to zero. This implies the only source of error which led to this difference in stress response between the two cases was due to the implementation of the BB model in Abaqus/Explicit. Relatively sparse information is available in the Abaqus user guide regarding the model (DS SIMULIA, 2018) but cross referencing with the 1D Python implementation (Bergström, 2015) leads to no obvious differences in the constitutive model theory. Therefore, it was deemed important to consider the effect of these stress differences upon the metrics that define the efficacy of the scaffold's mechanical behaviour.

To investigate the sensitivity of the scaffold FD and RS to the tensioning time period and in turn the maximum stress that manifests in expansion, the *in-silico* scaffold expansions were run using time periods in balloon expansion of both 0.015 s and 0.03 s. Observing the results of these simulations it was evident that whilst the model appeared sensitive to the time period in terms of its stress response, as shown in Figure 6.5, the scaffold mechanical metrics were less sensitive, with the FD and RS only altered by approximately 1% when the time period for the expansion step was doubled. Therefore, the faster expansion step of 0.015 s was considered thereafter, as it had been subsequently validated that the difference in scaffold mechanical performance between the two time periods was minimal yet it offered a faster solution time and alignment of the stress response with the *in-silico* dogbone tests. Whilst Bobel and McHugh (2018) used a very similar material model, the experimental data to which the material model

was calibrated, obtained by Bobel et al. (2016), was not attempted to be recreated via *in-silico* dogbone tests. Moreover, Bobel and McHugh (2018) conducted the simulations in their natural time period using simplified contact definitions to facilitate a very coarse time increment of 1e-4 s. A small disparity between the force-displacement curves of *in-vitro* and *in-silico* tensile tests conducted by Antonini et al. (2021b) on PLLA dogbone specimens is evident, although in this case the rate dependent elasto-plastic Johnson-Cook material model was used. No comparable studies were found that have sought to validate tensile dogbone tests in *silico* that also use the BB model implemented in Abaqus/Explicit. This highlights that whilst a model can be highly sensitive to a particular parameter in terms of its stress response, the predicted mechanical behaviour may be largely unaffected due to the relatively fast relaxation of stress that occurs as a result of the model's time dependency.

6.3.3 Scaffold Mechanical Response in Crimping

Once the model calibration for room temperature (mean stress-strain response) was finalised, the model parameters could be adjusted to facilitate the predicted reduction in stress response as a result of an increased ambient temperature in crimping. The resulting model for the elevated temperature scenario, along with the original room temperature model, are shown in Figure 6.6 whilst the values of the material model parameters are given in Table 6.2.

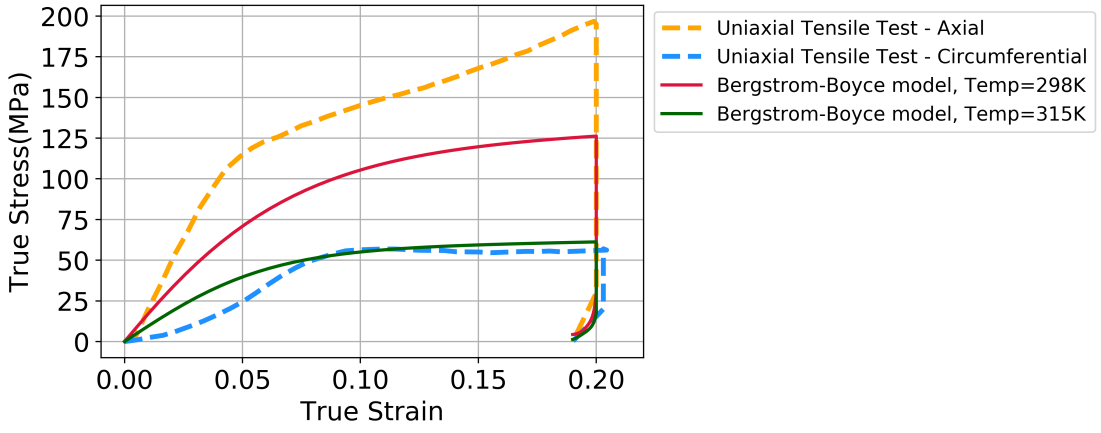

FIGURE 6.6: The temperature dependent Bergstrom-Boyce material models, implemented via the parallel rheological framework in Abaqus/Explicit, calibrated to the mean data at room temperature (red) and then adjusted to represent the reduced stress response as a result of increased ambient temperature (green).

The post-crimping diameter (CD) of the scaffolds for the *in-silico* and *in-vitro* crimping tests is detailed in Table 6.3. Whilst the *in-silico* models do not appear to capture the very low recoil post-crimping, there is a significant variation in the post crimping diameters as a result of the crimping technique and material model used.

	Hyperelastic Parameters				Viscous Parameters			
Amb Temp.	μ	λ^{lock}	κ	s	ξ	C	q_0	m
25°C	14.0	5.55	500	50	14.63	-0.51	10.86	1.58
42°C	7.0	5.55	500	50	10.00	-0.51	9.00	2.00

TABLE 6.2: Parameter values for the Bergstrom-Boyce material model, implemented via the parallel rheological framework in Abaqus/Explicit, for room temperature, at which the uniaxial tensile tests were undertaken, and adjusted for an elevated crimping temperature to yield a reduced stress response.

Simulation No.	Post-Crimping Diameter (mm) CD	Ambient Temperature	Displacement Profile
in-vitro	1.18	42°C	Staged
CRIMP-1	1.50	25°C	Direct
CRIMP-2	1.35	42°C	Direct
CRIMP-3	1.42	25°C	Staged
CRIMP-4	1.34	42°C	Staged

TABLE 6.3: The post-crimping outer diameter of the scaffolds from the four *in-silico* crimping tests and the *in-vitro* test.

The von Mises stress contours for the end rings of scaffolds in their fully crimped and post-crimped state are shown in Figure 6.7 and Figure 6.8, respectively, for the four crimping simulations. In the maximum crimping case there is approximately half the magnitude of stress in the vicinity of the crown in simulation CRIMP-4 compared to CRIMP-1. In the recoiled case the difference in stress response is less significant but still discernible between the four simulations.

Utilising the temperature dependency of the PRF model helps facilitate an improvement in prediction of the post-crimping scaffold diameter, shown in Table 6.3. The lower level of stress that develops in the scaffold struts, evident in Figure 6.7 and Figure 6.8, reduces the final diameter of the scaffold from 1.5 mm in CRIMP-1 to 1.35 mm in CRIMP-2. A lower stress magnitude will also reduce the risk of initiating strut fracture in the crimping process. Additionally, facilitating stress relaxation at a constant strain appears to benefit the predicted recoil, which was expected given this technique is also used *in-vitro*. In this case, the CD is reduced to 1.42 mm in CRIMP-3. However, using both the staged crimping and elevated ambient temperature does not have an additive effective and so the CD is only reduced to 1.34 mm. This does represent a significant improvement in post-crimping final diameter prediction, although there remains a percentage error of 14% compared to the *in-vitro* test. The post-crimping recoil is similar to that achieved by Antonini et al. (2021a), although this investigated a

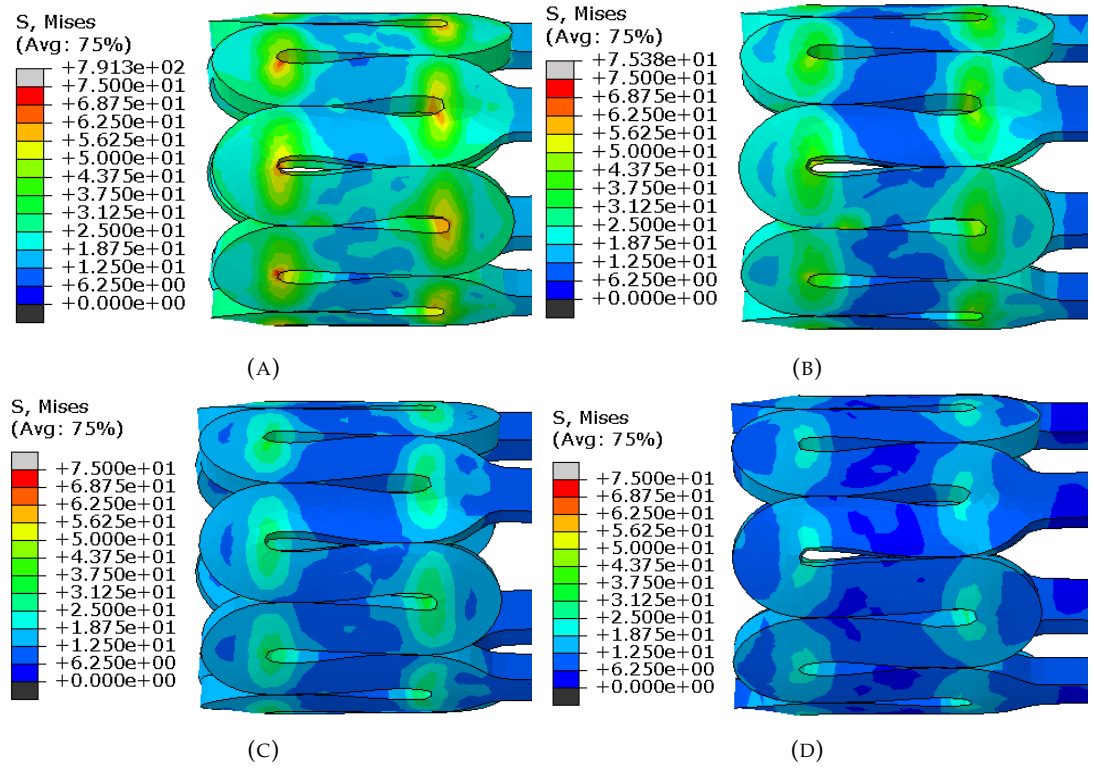

FIGURE 6.7: Von Mises stress contours for the scaffolds at their minimum diameter in crimping. Sub-figures (A)-(D) represent crimping simulations CRIMP-1 to CRIMP-4.

wider and thicker strut scaffold which results in larger post-crimping diameters of approximately 1.6 mm. Despite this improvement, it is clear that *in-silico* prediction of the post-crimping scaffold shape remains a challenge in the case of the PLLA used by the ArterioSorb^{TM} due to its specific micro-structural behaviour which likely necessitates a bespoke material model to predict the very low recoil values achieved in *vitro*.

6.3.4 Effect of the Material Direction of the Underlying Stress-Strain Data

The maximum diameter, final diameter and percentage recoil for the scaffold end rings as well as the scaffold's radial strength for the *in-vitro* and *in-silico* free expansion tests are shown in Table 6.4. The difference in prediction of the FD and $R_{\%}$ between the mean and circumferential BB models is very small. The axial direction model predicts the $R_{\%}$ most accurately and shows a significantly lower prediction of MD and FD as a result of its higher elastic stiffness compared to the other two BB models.

The force/diameter curves for the three Bergstrom-Boyce models are given in Figure 6.9 along with the *in-vitro* validation test. The use of the BB model calibrated to the mean stress-strain data achieved the most accurate prediction of the RS with a percentage error of just 1.5%, evidenced in Table 6.4. However, it is evident that the model predicts the maximum force to occur at a smaller final diameter than exhibited in *vitro*. There

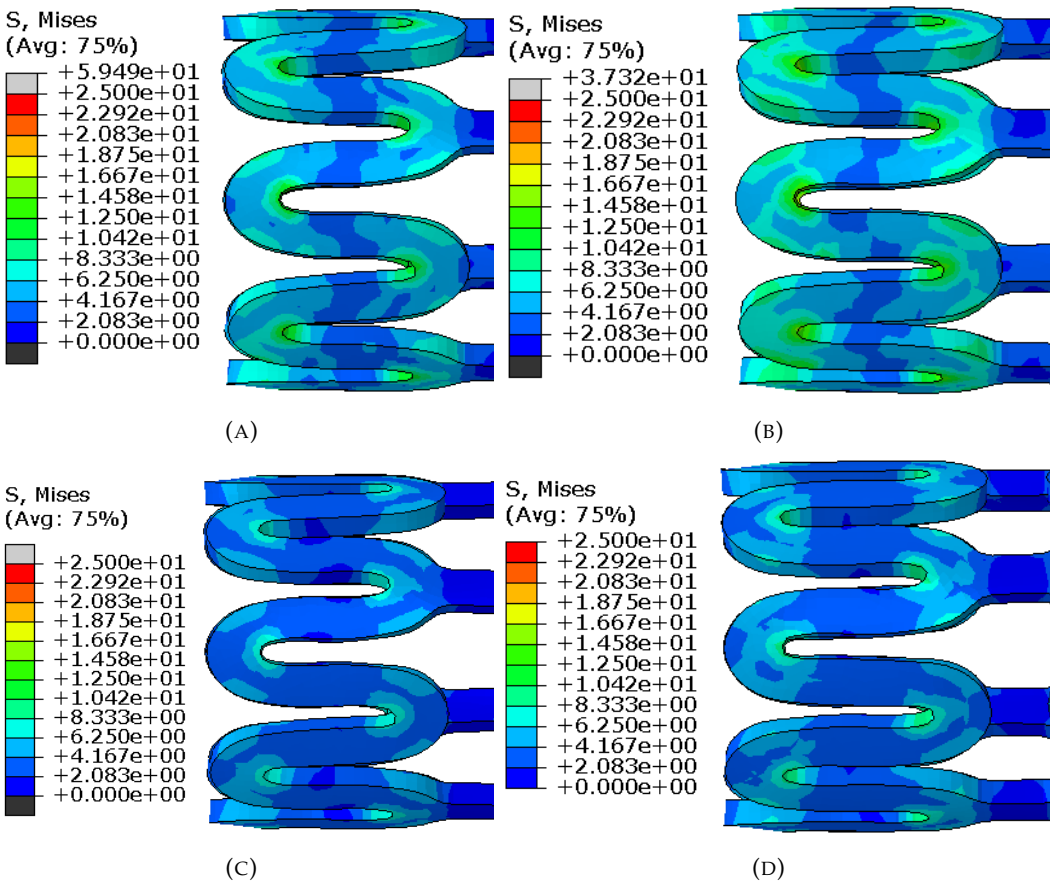

FIGURE 6.8: Von Mises stress contours for the scaffolds in their recoiled state post crimping. Sub-figures (A)-(D) represent crimping simulations CRIMP-1 to CRIMP-4.

Material Model	Maximum Diameter (mm) *MD*	Final Diameter (mm) *FD*	Percentage Recoil (%) $R_{\%}$	Radial Strength (N) *RS*
in-vitro	3.81	3.71	2.62	11.52
Hoddy-Bressloff	3.89	3.46	11.01	11.00
Bergstrom-Boyce (Mean)	3.89	3.65	6.17	11.35
Bergstrom-Boyce (Circumferential)	3.90	3.67	5.90	6.53
Bergstrom-Boyce (Axial)	3.73	3.63	2.68	19.63

TABLE 6.4: Results for the free expansion of the BRS using the Bergstrom-Boyce material model, implemented in Abaqus/Explicit via the parallel rheological framework, calibrated to each of the three stress-stain data sets, along with the analogous *in-vitro* test conducted by Arterius Ltd (Leeds, UK) and the Hoddy-Bressloff model, presented in Chapter 5 for comparison.

is a deviation of approximately +/- 40% for prediction of the RS from the *in-vitro* value for the three BB models, which is unsurprising given the significant difference in the

gradients of their stress response in loading. Whilst the model calibrated to the mean stress-strain data is based upon a fictitious set of data, it does provide a significant improvement relative to other isotropic models to capture the resultant mechanical behaviour of an anisotropic material when only an isotropic material model is available. Whilst the force-diameter plot in Figure 6.9 for the BB model calibrated to the mean data accurately predicts the RS, it does under-predict the stiffness, given by the initial gradient of the curve. The BB model, calibrated to the axial data, very accurately predicts the stiffness of the scaffold when subjected to radial crushing although it significantly overestimates the RS by approximately 100%.

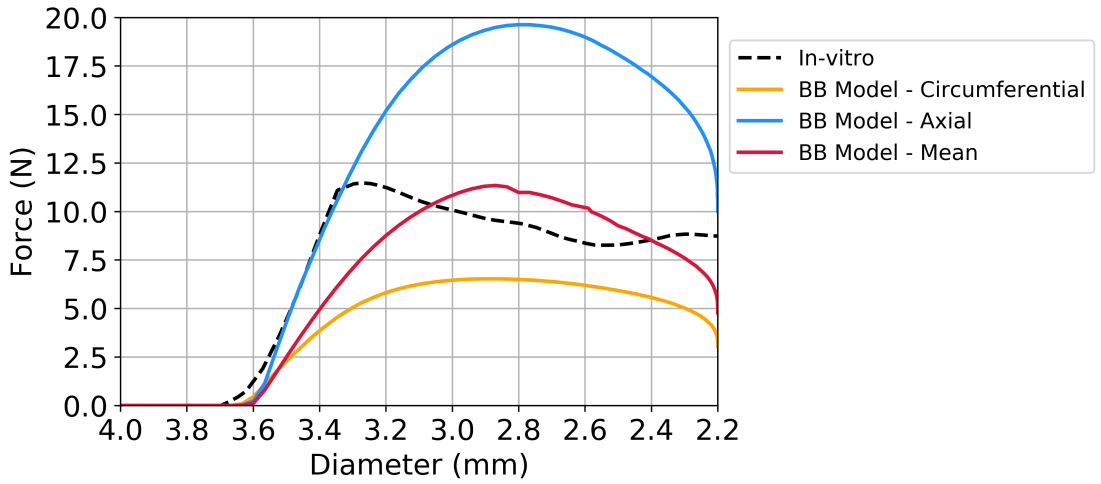

FIGURE 6.9: The force/diameter curves from the radial crushing tests for the three Bergstrom-Boyce models calibrated to each of the stress-strain data sets in addition to the *in-vitro* bench test.

6.3.5 Comparison of the BB Model with the HB Model

Figure 6.10 shows a comparison of the recoiled scaffold shapes post-expansion for; (A) the Hoddy-Bressloff model and (B) the Bergstrom-Boyce model (calibrated to the mean stress/strain data) overlaid upon an image of the recoiled scaffold in *vitro*. Both *in-silico* cases show a different recoiled strut configuration compared to the *in-vitro* test, despite the predicted final diameter, particularly in the case of the BB model, being very accurate.

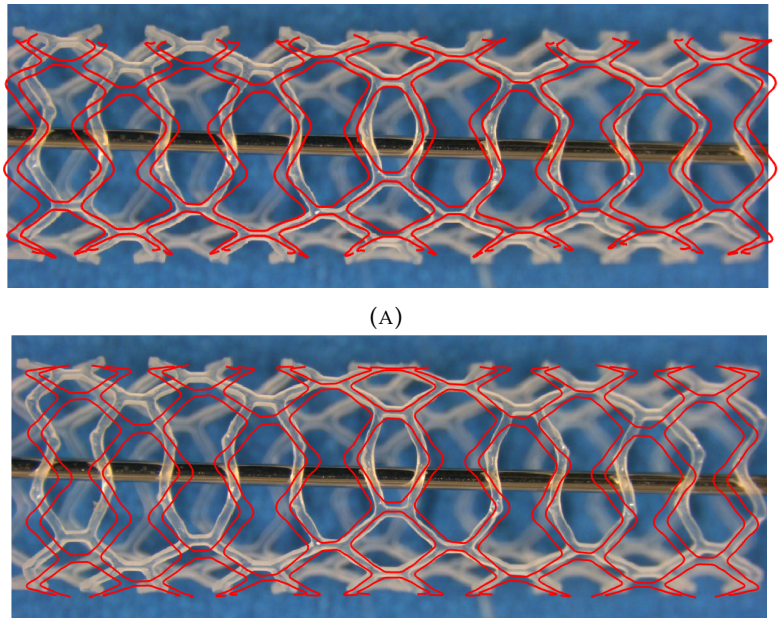

(A)

(B)

FIGURE 6.10: A comparison of the recoiled scaffold shapes for; (A) the Hoddy-Bressloff model and (B) the Bergstrom-Boyce model (calibrated to the mean stress/strain data), both of which are overlaid as a red outline upon an image of the recoiled scaffold in *vitro*.

Comparing the BB model calibrated to the mean stress/strain data to the HB model presented in Chapter 5, the BB model more accurately predicts the final diameter of the scaffold according to Table 6.4. Observing Figure 6.10, it can be seen that the central scaffold rings for the *in-silico* test using the BB model in Figure 6.10(B) appear to have recoiled more greatly than those in *vitro*. In the case of the BB model, the central ring cells around the scaffold's circumference all appear to be displaced by a similar amount post expansion. However, it is evident from the *in-vitro* images that the closed cells at the central rings should be displaced by less than the open cells at the central rings, as is evident in Figure 6.10(A) for the HB model. This is a result of the isotropic approximation of the PRF in which the BB material model is implemented. Whilst the overall mechanical behaviour of the scaffold can be accurately predicted using this approximation, the resistance to deformation in the axial and circumferential material directions will, in reality, be different. Therefore, it would be expected that in the case of a closed cell, the stiffer and stronger axial direction's material properties are more dominant, due to the presence of a connector at the crowns, than in an open cell whereby the weaker and less stiff circumferential properties are more dominant. This explains why the HB model displays less expansion of the closed cells in Figure 6.10(A) than the BB model in Fig.6.10(B). However, this result is compromised by the large level of acute elastic recoil that occurs in the HB model post-expansion, evidence by the greater foreshortening of the *in-vitro* scaffold compared to the scaffold in *silico*. Additionally, the open cell rings at the left-hand end of the *in-silico* scaffold in Figure 6.10(B) do not align

with the *in-vitro* scaffold which appears to have flexed along its longitudinal axis. This makes the prediction of the post-expansion strut configuration appear worse than it is for the BB material model.

With reference to Table 6.4, the FD and $R_{\%}$ prediction is much more accurate when using the BB model compared with the HB model. As hypothesized, this is due to the structure of the BB model facilitating different loading and unloading slopes in the stress/strain response, unlike simple elasto-plastic theory whereby the Young's modulus defines both the RS of the scaffold and the $R_{\%}$. In contrast, the BB model allows separate tuning of the loading and unloading behaviour which facilitates independent control of the RS and $R_{\%}$. The force-diameter curves in Figure 6.11 for the two *in-silico* models are consistent until the maximum force has been reached, at which point the scaffold is considered to have failed. The BB model provides an excellent estimate of the magnitude of the RS and greatly improves upon the most comparable study which reports a greater than 30% error in RS prediction, compared to data from the scaffold manufacturer (Antonini et al., 2021a). However, the location at which the maximum force is predicted displays a discrepancy in both cases. This suggests that prediction of the scaffold's final diameter is critical in predicting the diameter at which the maximum force occurs. A 2% error in FD prediction leads to a 12% error in prediction of the diameter at which the maximum force occurs in radial crushing of the scaffold. Additionally, the strut configuration may also contribute to this inaccuracy in the case of the BB model, which as already discussed, is compromised due to the isotropic limitation of the material model.

Given the aforementioned considerations it is evident that whilst the BB model incorporates increased complexity in terms of its calibration it also provides improved accuracy of the prediction of the scaffold's final diameter and radial strength compared to the best performing elasto-plastic model. However, the prediction of the exact strut configuration is compromised due to the isotropic approximation of the model.

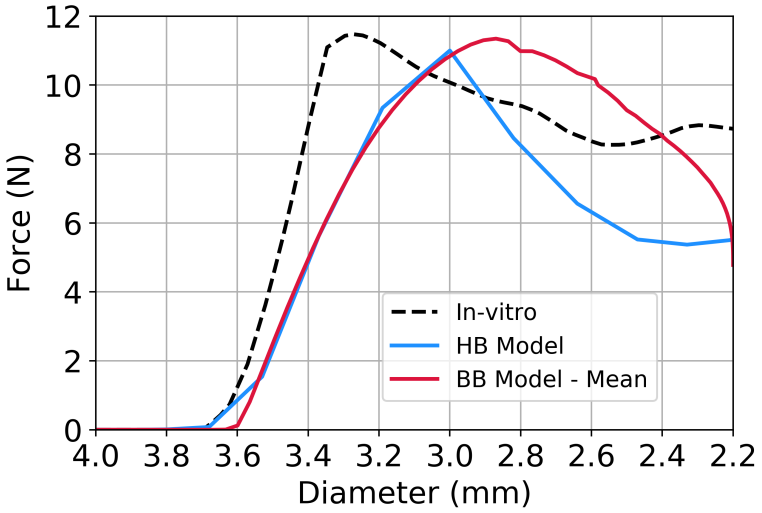

FIGURE 6.11: The force/diameter curves from the radial crushing tests for the Bergstrom-Boyce model calibrated to the mean stress-strain data, in addition to the *in-vitro* bench test and the Hoddy-Bressloff model for comparison.

6.4 Conclusions

The parallel rheological framework implemented in Abaqus/Explicit was explored via the Bergstrom-Boyce viscoelastic-plastic material model to capture the mechanical response of a thin-strut bioresorbable scaffold based upon the ArterioSorb^{TM} using finite element analysis to simulate the crimping, balloon expansion and radial crushing of the scaffold. The implications of a rate dependent material model in an explicit solver were discussed, along with the model's isotropic limitation. Additionally, the effect of the crimping strategy, including the use of a temperature dependent material model and stress relaxation steps, was investigated with respect to the post-crimping final diameter prediction. The following conclusions can be drawn.

1. Calibration of the Bergstrom-Boyce viscoelastic-plastic material model to the mean of the axial and circumferential directions' stress responses facilitates an accurate prediction of the scaffold's radial strength, within 1.5% of the *in-vitro* value and final diameter, within 2% of the *in-vitro* value which provides a significant improvement over the best performing elasto-plastic model.

2. The isotropic limitation of the parallel rheological framework in Abaqus/Explicit reduces the accuracy with which the post-expansion strut configuration of the scaffold is predicted.

3. Whilst maintaining the natural time period of the scaffold expansion in *silico* is impractical in an explicit solver, calibration of the model to a reduced time vector did not adversely affect the simulation. Comparison of uniaxial tensile tests conducted in *silico* and in *vitro* were found to exhibit different stress levels although

these were observed to relax quickly and did not alter the mechanical response of the scaffold significantly.

4. The post-crimping diameter prediction of the scaffold was greatly improved via use of a temperature dependant material model and a multi-staged crimping process which induced stress relaxation in the scaffold struts. However, the percentage recoil predicted in *silico* still greatly exceeded that observed in *vitro*, suggesting a micro-structural mechanism exists in the PLLA in crimping that is not captured by the Bergstrom-Boyce viscoelastic-plastic material model.

Drawing upon the insight gained into the behaviour of thin-strut BRS as a result of their design and the improvements in material modelling within finite element analysis from this chapter and those preceding it, it was decided that this would inform the development of a novel scaffold design for a clinically relevant scenario. Both the Hoddy-Bressloff model, which provides an anisotropic description of the material behaviour facilitating accurate prediction of the post expansion scaffold shape, and the Bergstrom-Boyce model, which accurately predicts the scaffold metrics investigated in this chapter, will be necessary to gain maximum insight into the new scaffold design in combination with further *in-vitro* testing.

Chapter 7

Realistic Clinical Scenarios

7.1 Introduction

Whilst free expansion simulations provide a useful method of comparing the mechanical performance of BRS designs and their constitutive material models in *silico*, the *in-silico* deployment of BRS into coronary artery geometry containing a stenosis can yield additional information about the predicted performance of the scaffold in *vivo*. Arterial geometry into which coronary stents are deployed in FEA is used throughout the literature (Lally et al., 2005; Ragkousis, 2016; Wei et al., 2019). Unsurprisingly, the deployment of BRS into realistic stenosed arterial geometry is rare, with as far as the author is aware, only the work by Schiavone et al. (2016) conducted to date. In this study, a simple elasto-plastic model was used to describe the stress response of the PLLA, which, as demonstrated in Chapter 5, is unlikely to be appropriate to accurately predict the scaffold's mechanical performance. The stress imparted to the artery wall was assessed, along with the percentage recoil and dogboning of the scaffold and compared with a state-of-the-art drug eluting metallic stent. Foin et al. (2016a,b) considered the use of BRS in realistic clinical scenarios predominantly through *in-vitro* testing. However, both the aforementioned studies considered thick-strut first generation BRS only.

Revascularising a coronary artery in the vicinity of a bifurcation is widely regarded as a challenging clinical scenario. The European bifurcation club (EBC), which seeks to improve interventional techniques for bifurcation lesions, recommends where possible the use of a single stent strategy to achieve favourable patient outcomes. However, several different stenting techniques can be used in bifurcation scenarios, many of which require significant deformation of the stent which could lead to loss of its mechanical integrity (Burzotta et al., 2020). Mortier et al. (2010) highlighted the importance of facilitating side-branch access when revascularising a diseased vessel in the presence of a bifurcation. Struts covering a vessel side branch not only provide a site for thrombus formation but also inhibit further interventions, located distally from the bifurcation.

Highly tapered vessels are also likely to present a more hostile environment for BRS. Given their limited overexpansion capability to date, as demonstrated by Foin et al. (2016b), there remains significant concern regarding the ability of BRS to be deployed into highly tapered vessels. In such a case the scaffold may be greatly overexpanded at one end whilst underexpanded at the other. The malapposition of scaffold struts to the vessel wall is also another important factor in determining the patient outcome (Boeder et al., 2019). These cannot be investigated or determined in free expansion scenarios.

Therefore, in this chapter, the *in-silico* deployment of the baseline scaffold design into an idealised coronary artery stenosis is presented. The stresses exerted upon the artery wall are analysed and the performance of the baseline scaffold is assessed. Secondly, a novel scaffold design is presented that exploits the ArterioSorb^{TM} patent to improve the design for use in a patient specific coronary artery bifurcation, as used by Ragkousis (2016). Free expansion and constrained deployment into the patient specific geometry are undertaken *in-silico* and compared with *in-vitro* bench testing conducted by Arterius Ltd to validate the findings. The free expansion simulation of the novel scaffold design was conducted using both the Hoddy-Bressloff and Bergstrom-Boyce material models in *silico* to facilitate their comparison in addition to validation against the *in-vitro* data.

7.2 Methodology

7.2.1 Scaffold Geometry

The baseline scaffold design, based upon the ArterioSorb^{TM} BRS was investigated for deployment into the concentric stenosis-artery model. The details of this scaffold geometry are provided in Subsection 4.2.1.

The second scaffold geometry was designed specifically for the left-main coronary artery bifurcation. With this in mind, the variable ring length and strut width, as explored in Chapter 4, was utilised to tailor the scaffold geometry to the highly tapered coronary artery. The scaffold comprised a compound growth in ring length of 5% from the central ring towards the proximal end whilst a 3% reduction in ring length was used from the central ring towards the distal end of the scaffold. The struts were maintained at a constant width along the length of the scaffold in the proximal direction to avoid excessively long wide struts that would be liable to twisting in the radial direction about the crown apex in balloon expansion, as exhibited in Chapter 4. A 3% compound decrease in strut width along the scaffold length was used in the distal direction to maintain the original ratio of ring length to strut width, as the struts become increasingly short. This was deemed the best course of action given the radial strength of the struts will increase as they become shorter. Therefore, reducing the strut width

in the distal direction would result in the radial strength remaining approximately constant along the scaffold length. Increasing the radial strength at the distal end was deemed unnecessary considering the stenosis is located close to the ostium of the side branch, as is often the case in *vivo*.

Additionally, to facilitate acceptable side branch access the central rings of the scaffold were significantly altered from the baseline design by increasing their ring length to provide four large openings at the central rings in the location of the side branch. Closed cells are present either side of the central rings to prevent twisting of the long ring-length central rings. The bifurcation scaffold geometry is shown in Figure 7.1; the proximal long ring-length rings are located on the left hand end and the distal short ring-length rings are located on the right hand end.

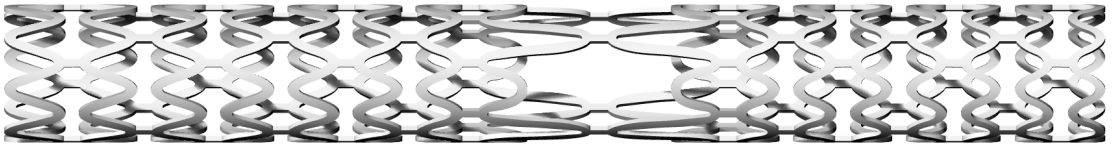

FIGURE 7.1: The geometry of the bioresorbable scaffold designed for the left main coronary artery bifurcation geometry. The proximal scaffold end is located to the left with the distal end located to the right.

7.2.2 Baseline Scaffold Deployment

Expansion of the baseline scaffold design into the idealised coronary artery stenosis model was undertaken first. This used the same setup as described in Subsection 3.3.2 with the addition of the coronary artery geometry.

An idealised two layer coronary artery model was constructed, containing a concentric stenosis which reduced the lumen area by 60%, as per Pant et al. (2012). The Hicks-Henne bump function (Hicks and Henne, 1978), shown in Equation 7.1, was used to parameterise the plaque geometry to ensure the profile resembled a realistic coronary artery stenosis. The artery consisted of an outer cylinder representing the intima, media and adventitia layers of 0.7 mm thickness and an inner plaque layer which facilitated a nominal lumen diameter of 3.5 mm, reducing to 2.2 mm at the centre of the stenosis.

The Hicks-Henne bump function is given by:

$$y = t_b + (A - t_b)\left[sin\pi\left(\frac{x}{L_{stss}}\right)^{(-ln2/lnx_p)}\right]^w \qquad (7.1)$$
$$where, 0 < x < L_{stss}$$

in which t_b is the base thickness (in this case the plaque thickness at nominal diameter), A is the amplitude of the bump, x_p is the location of the peak, w varies the width of the peak and L_{stss} is the length of the stenosis.

The two layer idealised coronary artery section was meshed using C3D8R elements in a structured layout after a single partition of the geometry along its longitudinal axis. A seed size of 0.1 mm was used. This ensured nine elements lay across the artery thickness at the thinnest part of the vessel, distal and proximal to the stenosis. The idealised coronary artery stenosis model is shown in Figure 7.2.

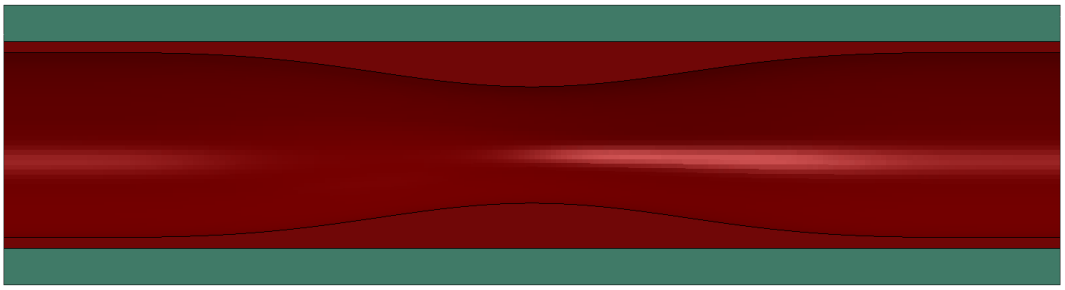

FIGURE 7.2: An idealised coronary artery stenosis model. The maximum lumen diameter of 3.5 mm reduces to 2.2 mm at the centre of the concentric stenosis which results in a 60% reduction in lumen area.

In addition to the setup detailed in Subsection 3.3.2, non-penetrating surface contacts were defined between the scaffold and plaque/artery as well as the balloon and plaque-/artery in which a frictional coefficient of 0.1 was used. Tie contacts were also defined between the artery and plaque layers to ensure they were effectively bonded throughout the balloon expansion process.

7.2.3 Bifurcation Scaffold Deployment

Subsequent simulations were also conducted on a patient specific coronary artery bifurcation model obtained from angiographic data. The model, shown in Figure 7.3 represents the left main coronary artery bifurcation, the junction of the LAD and LCB. The artery contains a 30% stenosis in the proximal LAD and significant tapering from approximately 5 mm at the left main branch to 2.5 mm at the distal LAD in addition to a large side-branch ostium of 4.5 mm. This geometry provides a good example of a challenging case for BRS given the large side branch ostium and vessel diameter mismatch between the proximal and distal ends. The arterial geometry was partitioned by Ragkousis (2016) to facilitate a structured hexahedral mesh.

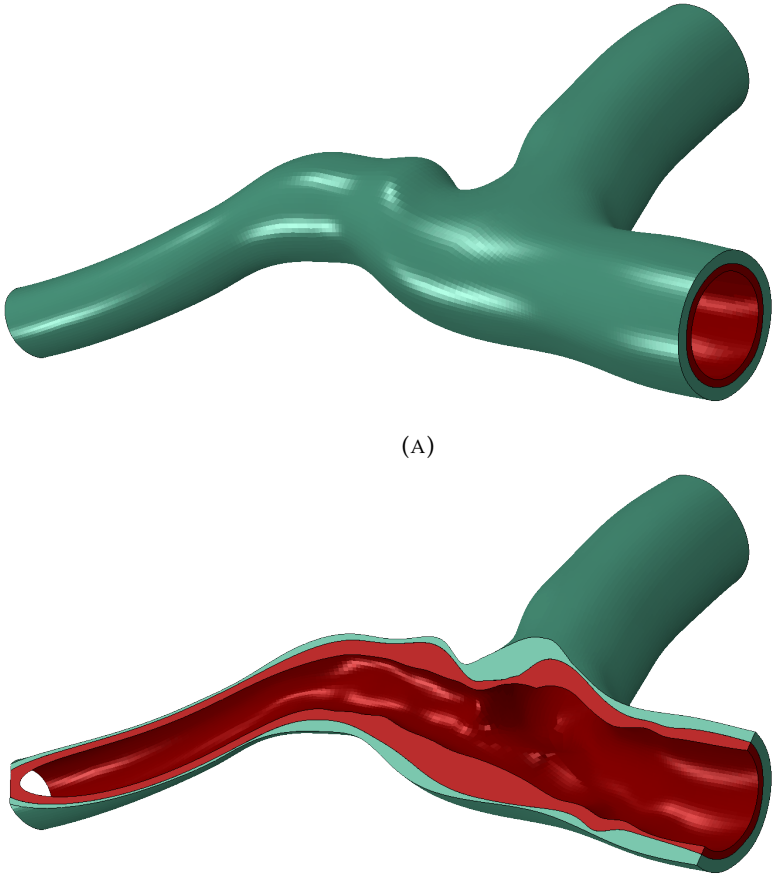

(A)

(B)

FIGURE 7.3: The left main coronary artery bifurcation model. The two layer structure is visible in the cut section (B), consisting of the artery layer (green) and plaque (red).

Holzapfel et al. (2005) studied the mechanical response of the LAD via *in-vitro* bench testing of human tissue samples which facilitated the characterisation of the material using the hyperelastic sixth order polynomial strain energy density function (Gervaso et al., 2008; Zunino et al., 2009). In turn Pant et al. (2012) used this model to capture the stress response of a single layer arterial model, in which the artery was represented by the media layer only. The same material modelling strategy is used here. The coefficients of the material model for the arterial layer are shown in Table 7.1.

The definition of the hyperelastic sixth order polynomial strain energy density function is given by:

$$\begin{aligned} U = {} & C_{10}(\bar{I}_1 - 3)^1 + C_{20}(\bar{I}_1 - 3)^2 + C_{30}(\bar{I}_1 - 3)^3 \\ & + C_{40}(\bar{I}_1 - 3)^4 + C_{50}(\bar{I}_1 - 3)^5 + C_{60}(\bar{I}_1 - 3)^6 \end{aligned} \tag{7.2}$$

in which U gives the strain energy per unit of volume, C_{i0} is a model coefficient (where $i = 1 - 6$) and $\bar{I}_1$ is the first deviatoric strain invariant, given by:

$$\bar{I}_1 = \bar{\lambda_1}^2 + \bar{\lambda_2}^2 + \bar{\lambda_3}^2 \tag{7.3}$$

where $\bar{\lambda_i}$ is defined as:

$$\bar{\lambda}_i = J^{-\frac{1}{3}}\lambda_i \tag{7.4}$$

where λ_i gives the principle stretch in each of the three material directions and $J = det(F)$ in which F is the deformation gradient.

C_{10}	C_{20}	C_{30}	C_{40}	C_{50}	C_{60}
0.00652	0.0489	0.00926	0.76	-0.43	0.0869

TABLE 7.1: Material model parameters to describe the mechanical response of the media layer of a coronary artery using a hyperelastic sixth order reduced polynomial strain energy density function.

Wong et al. (2009) and subsequently Pant et al. (2012) described the plaque layer within a single layer coronary artery using the Neo-Hookean hyperelastic model. The Cauchy stress response of this hyperelastic model is given by:

$$\sigma = \frac{\mu}{J}\, dev[\mathbf{b}^*] + \kappa\,(J-1)\,[I] \tag{7.5}$$

in which μ and κ are the model parameters that refer to the shear modulus and bulk modulus respectively, as before, $J = det(F)$, b^* is the distortional left Cauchy green tensor and I is the identity matrix (DS SIMULIA, 2018). The values of the coefficients μ and κ used to describe the mechanical response of the plaque are given in Table 7.2.

μ	κ
0.06	1200

TABLE 7.2: Material model parameters to describe the plaque layer of the coronary artery models using a Neo-Hookean hyperelastic material model.

Additionally, in the case of both the idealised and left-main bifurcation arterial models a mass proportional damping factor was applied to the material models to reduce the spurious oscillations that occurred. Based upon Rayleigh damping (Liu and Gorman, 1995), the Abaqus user guide likens mass proportional damping to the object moving through a viscous liquid (DS SIMULIA, 2018). Such a technique is physically appropriate given that coronary arteries are not free-floating in space but wrap around and are partially embedded in the heart muscle which will naturally have a damping effect

upon the vessel. After some initial simulations, an α_R value of 200 was found to appropriately reduce the amplitude and frequency of the vibrational modes that were seen to develop in the absence of material damping.

The expansion balloon was increased in length to 28 mm for the bifurcation scaffold. In addition to the expansion balloon, a post-dilatation balloon of diameter 4.0 mm and length 19 mm was parameterised to ensure the proximal scaffold rings were not under-expanded to minimise malapposition of the scaffold struts. This used the same material model and element definition as the 3.5 mm expansion balloon, as described in Subsection 3.3.2. Both the free and constrained (deployment into the coronary artery bifurcation) deployments of the bifurcation scaffold design were conducted for the Hoddy-Bressloff (HB) and Bergstrom-Boyce (BB) material models.

The free expansion simulations consisted of the following steps:

1. Folding of the expansion and post-dilatation balloons to resemble a standard tri-folded balloon, as detailed in Subsection 3.3.2.
2. In each case the scaffold was crimped to an OD of 1.1 mm onto the folded expansion and post-dilatation balloons. The staged crimping profile was used in the case of the BB model, as described in Subsection 6.2.5.
3. The scaffold was expanded using the tri-folded 3.5 mm expansion balloon, inflated to 8 atm.
4. Post-dilatation of the proximal end of the scaffold was conducted using the 4.0 mm balloon, overexpanded to 4.5 mm using 8 atm of pressure.
5. Radial crushing of the scaffold was undertaken using a displacement driven cylinder from the scaffold's post-recoil diameter to a diameter of approximately 2 mm.

Deployment of the bifurcation scaffold into the coronary artery geometry used the same process with the addition of a positioning step after the scaffold crimping to align the scaffold and balloons correctly with the vessel side branch as shown in Figure 7.4. The inflation pressures of the balloons were also increased above their nominal value of 8 atm to 12 atm to minimise malapposition of the scaffold struts and ensure it achieved a maximum diameter of 4.5 mm as used in *vitro*. A non-penetrating contact was defined between the balloon tips-balloon-scaffold assembly and the guide-wire to ensure the assembly followed the correct path as it was positioned. Displacement boundary conditions were then imposed on the balloon tips and scaffold to position them correctly within the artery. The radial crushing step was not conducted on the models deployed into the bifurcation model as the scaffold was already exposed to the crushing force of the stenosed artery.

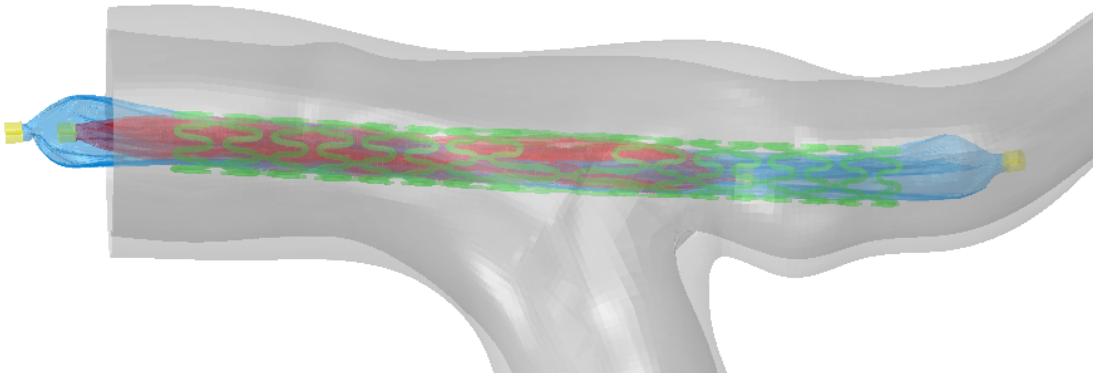

FIGURE 7.4: The bifurcation scaffold positioned within the coronary artery bifurcation model. The large central rings are aligned with the vessel side branch. The 3.5 mm expansion balloon is shown in blue and the 4.0 mm post-dilatation balloon is shown in red. The proximal scaffold end is located to the left with the distal end located to the right.

7.2.4 In-Vitro Bench Testing

The *in-vitro* bench testing conducted by Arterius Ltd for the free expansion and constrained expansions was conducted in a water bath, heated to 37 °C to mimic body temperature. In the case of the constrained scaffold expansion, a 3D printed silicon bifurcation model of the patient specific geometry was purchased from Stratasys, a specialist in additively manufactured anatomical geometry. The geometry consisted of two layers in which the inner plaque layer was designed to be approximately 10 times stiffer than the outer artery layer. The scaffolds were crimped using the same technique as described in Subsection 3.4.2. The testing then followed the same procedure as described for the *in-silico* cases. Firstly nominal expansion of the scaffold was conducted using a 3.5 mm balloon before post dilatation of the proximal end of the scaffold was conducted using a 4.0 mm balloon expanded to 4.5 mm. A radial crushing test was performed after the scaffold had elastically recoiled to obtain the radial strength of the scaffold. In the case of the bifurcation scaffold it was necessary to cut the scaffold in half at the central connectors to separate the proximal and distal ends of the scaffold. This resulted in the two halves of the scaffold being radial crushed separately.

7.2.5 Assessment of the Artery Stress State

In addition to observation of the distribution and maximum von Mises stress in the plaque layer of the arterial geometry, the volume averaged stress (*VAS*), as used by Pant et al. (2011) was assessed in the constrained deployment scenario for the idealised stenosis. An element set was defined to limit the area of observation to the plaque that

was in contact with the scaffold. Therefore, the region of +/- 6 mm either side of the stenosis mid-point was assessed.

The *VAS* is given by:

$$VAS = \frac{\int_V \sigma_{VM} dV}{\int_V dV} \tag{7.6}$$

A finite element model is already discretised and so calculating this metric numerically is simple. Therefore, this was implemented via the expression:

$$VAS = \frac{\sum_{i=1}^{i=n} \sigma_{VMi} V_i}{\sum_{i=1}^{i=n} V_i} \tag{7.7}$$

in which σ_{VMi} gives the von Mises stress in the ith of the n elements in the bounded element set that is in contact with the scaffold. V_i represents the volume of the ith element.

7.2.6 Radial Strength Measurement

In this chapter, the radial strength of the scaffold was measured from the level of force exerted upon the scaffold at a diameter of 3 mm. This is obtained via observation of the force-displacement graph. The *in-vitro* and *in-silico* data indicated that the maximum radial force occurred as the scaffold diameter was crushed below 2 mm which is well past the point at which the scaffold is considered to have failed. Therefore, the force at a diameter of 3 mm was taken as the reference for the scaffold radial strength.

7.3 Results & Discussion

7.3.1 Idealised Concentric Artery Lesion

Deployment of the baseline scaffold into the idealised coronary artery model is shown in Figure 7.5. In this case, the material behaviour was described by the Bergstrom-Boyce model calibrated to the mean stress-strain data, as described in Chapter 6. The scaffold at maximum balloon inflation pressure and recoiled post-expansion is depicted. Prior to delivery of the scaffold, the minimum lumen area was 3.80 mm^2 whilst after scaffold expansion the minimum lumen area at the location of the stenosis was 8.97 mm^2. This corresponds to an increase of 136% and almost restores the minimum lumen area to its original pre-stenosis area of 9.62 mm^2 which suggests the scaffold has a high level of efficacy in such a clinical scenario and is likely to lead to a favourable patient outcome.

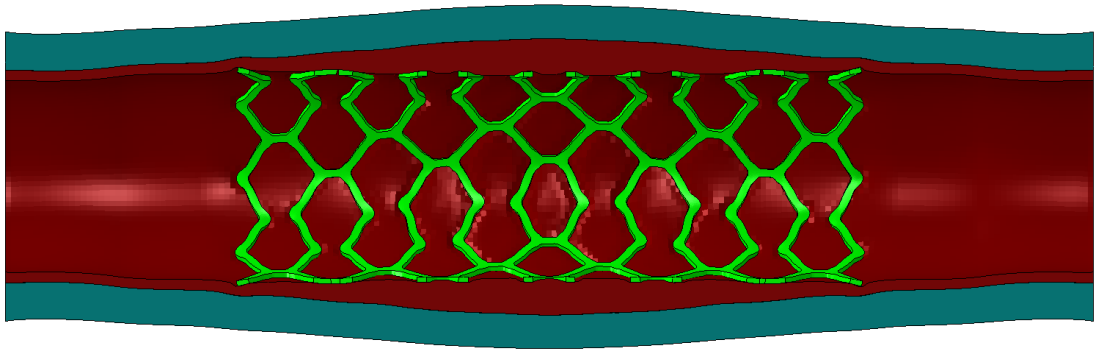

(A)

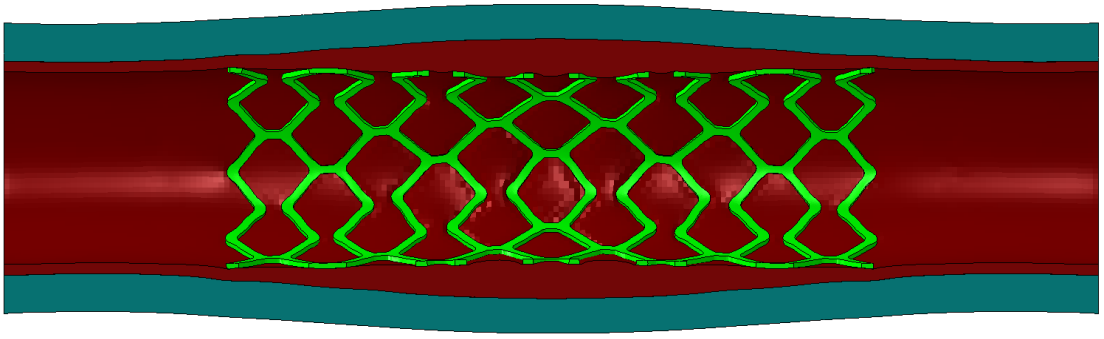

(B)

FIGURE 7.5: The baseline bioresorbable scaffold design deployed within the idealised coronary artery stenosis at; (A) maximum diameter and (B) its post recoil state.

Additionally the level of apposition of the scaffold struts against the vessel wall was excellent. Strut coverage of the walls was 100% with no struts separating from the vessel wall and protruding into the lumen, as evidenced in Figure 7.6 in which a series of cut-through images are shown along the scaffold length. This is also evident in Figure 7.7 where the stress exerted on the vessel wall remains elevated post recoil.

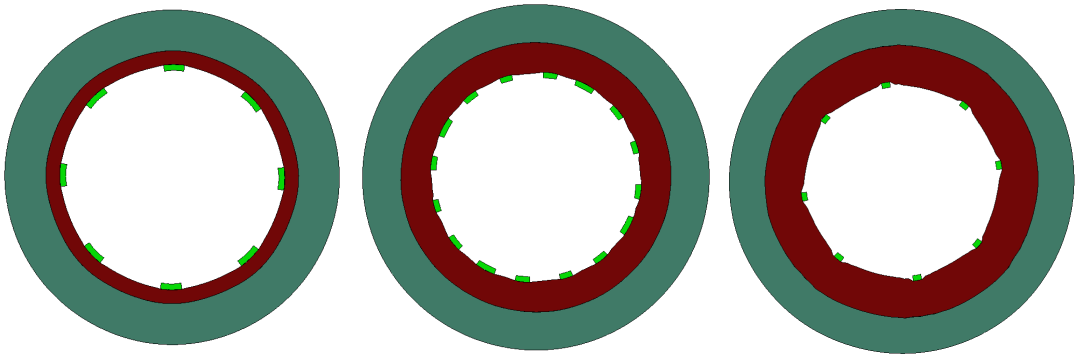

(A) (B) (C)

FIGURE 7.6: Cross-section cut through images of the deployed scaffold from; (A) the proximal end of the scaffold through to; (C) the central connectors, which show excellent apposition of the scaffold struts to the vessel wall in all locations.

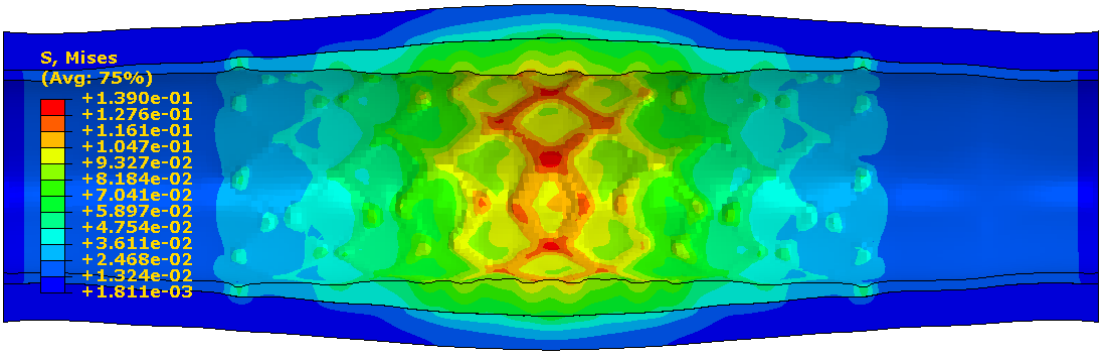

(A)

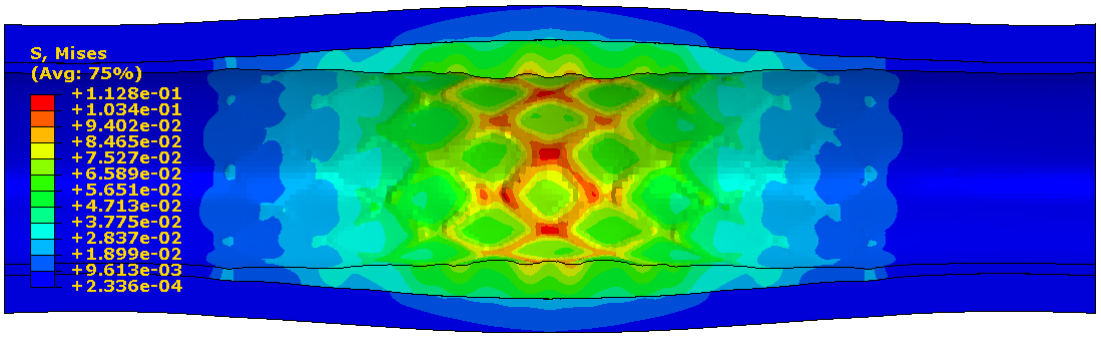

(B)

FIGURE 7.7: The von Mises stress (MPa) at the vessel wall as a result of the interaction of the plaque and scaffold at; (A) maximum diameter and (B) post recoil.

Consistent with the findings of Schiavone et al. (2016), the levels of stress exerted by the BRS within the coronary artery are low and of a very similar magnitude. As expected, the largest stresses occur at the central closed ring due to this aligning with the location of the most prominent part of the stenosis. Also, the additional connectors at the closed cells at the centre of the scaffold will cause increased stresses on the vessel wall. However, this is necessary to improve the radial strength of the scaffold in order that it can achieve an acceptable post-expansion diameter. It is widely accepted that greater stresses exerted on the vessel wall are likely to induce the onset of in-stent restenosis via the biological process of neointimal hyperplasia (Edelman and Rogers, 1998; Hoffmann et al., 1999). The von Mises stress exerted upon the vessel wall as a result of the deployment of metallic stents is generally significantly higher. Pant et al. (2011) reported maximum von Mises stress at the plaque of 0.3 MPa whilst Lally et al. (2005) observed maximum principle stresses in excess of 10 MPa. This difference in stress magnitudes reported by the two studies is notable given that both use a Young's modulus of approximately 200 GPa to describe the elastic behaviour of the stent. Whilst the source of the disparity is unclear, it may be attributed to the difference in hyperelastic models used to capture the stress response of the plaque, or a result of the coarse mesh used by Lally et al. (2005) to discretise the stent geometry.

In their detailed study of the composition of a multi-layer coronary artery stenosis model, Wei et al. (2019) reported von Mises stresses of 0.7 MPa at the vessel wall after expansion of a metallic stent via pressure applied to its inner face compared to maximum stresses in the order of 0.14 MPa for the BRS. However, the volume average stress (*VAS*) for the plaque section in contact with the scaffold based upon the ArterioSorb^{TM} is 44.2 x 10^{-3} MPa whilst the *VAS* reported by Pant et al. (2011) is 46.4 x 10^{-3} MPa. This highlights that whilst the maximum stresses exerted on the plaque by the scaffold are significantly lower, due to the wider and shorter struts, necessary to maintain sufficient radial strength in the polymer scaffold, the volume over which elevated stress is exerted is not dissimilar in the case of BRS when compared with metallic stents. It should also be noted that this metric is greatly affected by the domain chosen by the user to be included in the calculation. Pant et al. (2011) considered a section 0.5 mm either side of the scaffold's nominal length. However, in this chapter a section 0.5 mm less than the scaffold's nominal length was considered to account for the foreshortening of the scaffold in expansion. Therefore, this is a more conservative consideration of *VAS* as the section considers only the length of plaque in contact with the scaffold, suggesting that the benefit of BRS compared to metallic stents in terms of the *VAS* will be slightly greater than predicted in this case. Therefore, BRS provide a benefit in terms of the stress to which the vessel wall is exposed, particularly in terms of the maximum von Mises stress. However, it must be recognised that this is a result of the lower radial strength of BRS compared to metallic stents which is a potential drawback that leads to increased acute recoil in BRS. Although lower radial strength is a reality of BRS compared to metallic stents, *in-vitro* bench testing of the scaffold based upon the ArterioSorb^{TM} has shown similar levels of radial strength when compared with the XIENCE Sierra stent (Boston Scientific, Boston, MA).

Unsurprisingly, considering the von Mises stress within the artery rather than the plaque shows a significantly lower magnitude of stress of approximately one order of magnitude. Figure 7.8 shows the von Mises stress in the artery layer when the scaffold is at its maximum and recoiled diameters. As is the case in the plaque layer, the maximum stress exists at the central closed ring where the stenosis is greatest. The stress then gradually reduces in magnitude towards the ends of the artery segment where the pattern of the struts is no longer visible and is replaced by pools of stress of approximately 5 KPa. These are located at the crown apexes of the end rings. This highlights that the crown apexes protrude into the plaque and artery due to their outwards splaying in the radial direction in balloon expansion which has been observed in *vitro*, evidenced (albeit subtly) in Figure 7.9.

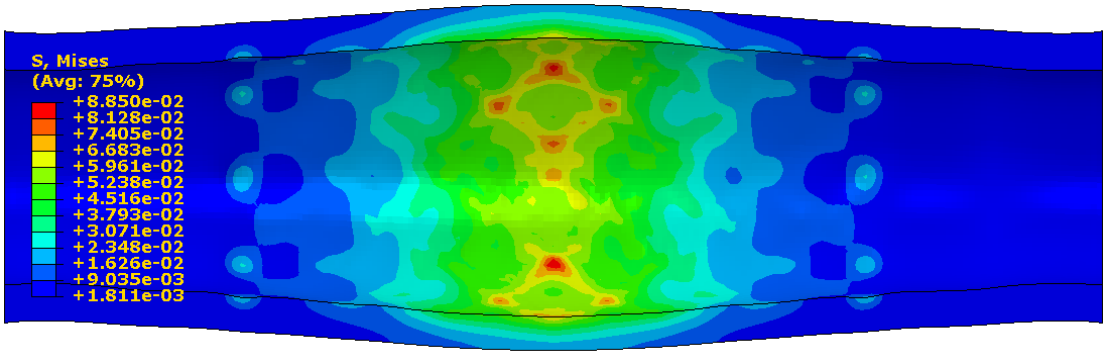

(A)

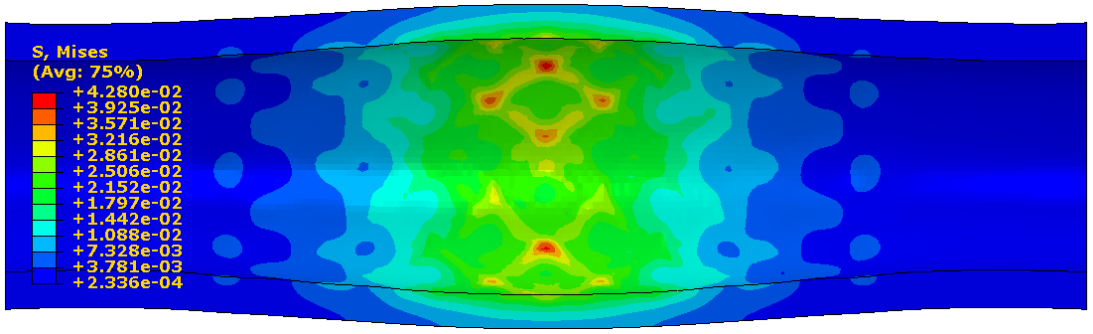

(B)

FIGURE 7.8: The von Mises stress in the coronary artery layer as a result of the interaction of the plaque and artery at; (A) the maximum diameter at maximum balloon inflation pressure and (B) post recoil after the balloon has been deflated and removed.

7.3.2 Free Expansion of the Bifurcation Scaffold

The maximum diameter (MD), final diameter (FD) and radial strength (RS) for the bifurcation scaffold is shown for the two material models and the *in-vitro* bench test in Table 7.3. The results are given for the end of both the initial expansion step (3.5 mm balloon) and the post-dilatation step (overexpanded 4.0 mm balloon).

The final diameter in free expansion for the bifurcation scaffold design is shown in Figure 7.9 for the two material models in addition to the *in-vitro* expansion using the 3.5 mm expansion balloon. Figure 7.10 shows the proximal end of the scaffold in the three cases after post-dilatation using the overexpanded 4.0 mm balloon.

Material Model	Maximum Diameter (mm)	Maximum Diameter (mm)	Final Diameter (mm)	Final Diameter (mm)	Radial Strength (N)
	Prx. Ring	Dst. Ring	Prx Ring	Dst. Ring	
in-vitro (3.5 mm Balloon)	3.69	3.69	3.61	3.54	9.73
in-vitro (4.0 mm Balloon)	4.59	-	4.45	-	-
Bergstrom-Boyce (3.5 mm Balloon)	3.94	3.86	3.69	3.63	10.96
Bergstrom-Boyce (4.0 mm Balloon)	4.56	-	4.31	-	-
Hoddy-Bressloff (3.5 mm Balloon)	3.89	3.85	3.34	3.60	6.08
Hoddy-Bressloff (4.0 mm Balloon)	4.66	-	4.24	-	-

TABLE 7.3: Results for the free expansion of the bifurcation BRS design. The *in-silico* cases using the Bergstrom-Boyce material model and Hoddy-Bressloff model are compared along with the analogous *in-vitro* test conducted by Arterius Ltd (Leeds, UK). Results for both the initial and post-dilatation expansion steps are given and in each case the proximal and distal rings are considered.

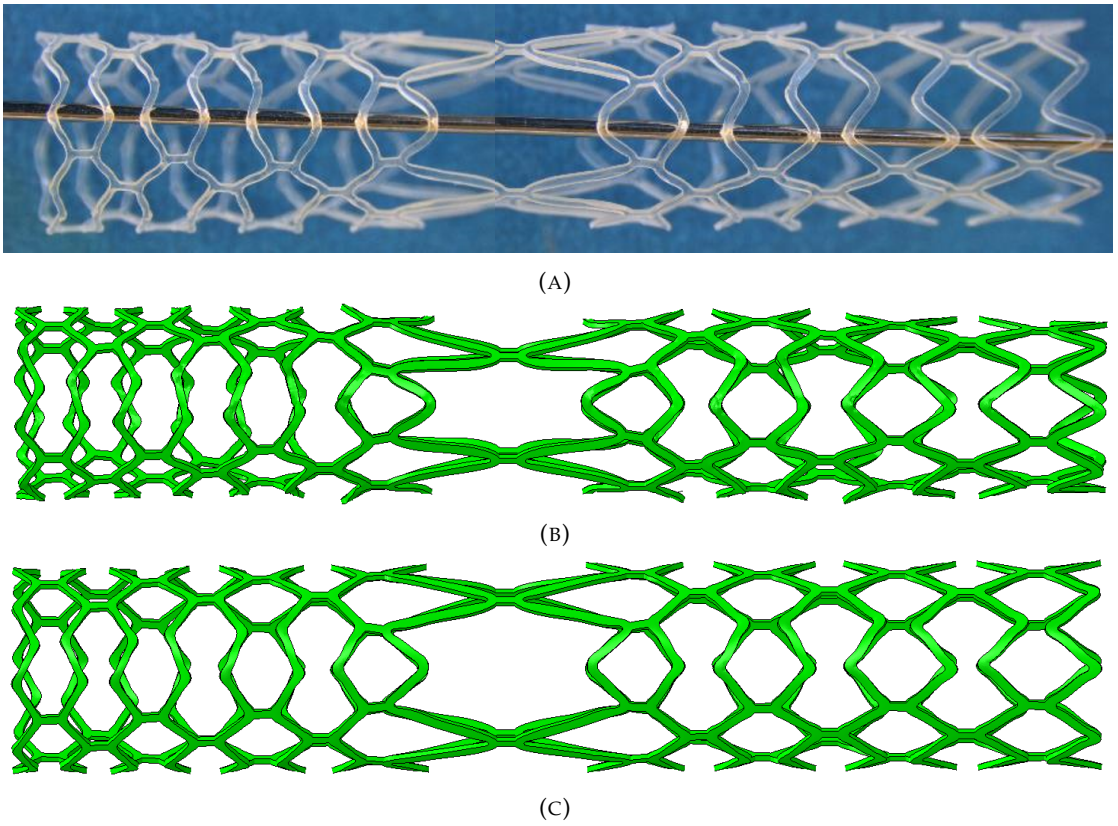

(A)

(B)

(C)

FIGURE 7.9: The final scaffold shape after expansion of the 3.5 mm balloon for; (A) the *in-vitro* test; (B) the Hoddy-Bressloff model and (C) the Bergstrom-Boyce material model. The proximal scaffold end is located to the right with the distal end located to the left.

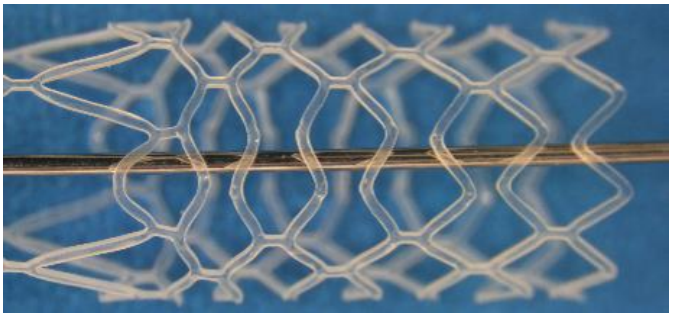

(A)

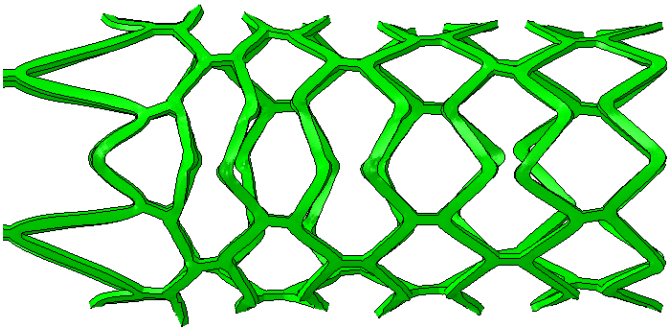

(B)

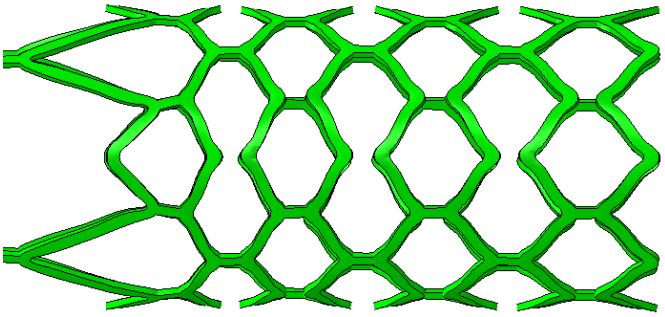

(C)

FIGURE 7.10: The final scaffold shape after expansion of the overexpanded 4.0 mm balloon at the proximal end of the scaffold for; (A) the *in-vitro* test; (B) the Hoddy-Bressloff model and (C) the Bergstrom-Boyce material model.

It is evident in Table 7.3 that both the BB and HB models over-predict the MD of the scaffold when expanded using the 3.5 mm balloon inflated to 8 atm. This results in an accurate prediction of the FD within 2.5% for the BB model. However, the HB model still predicts a FD with an error in excess of 7% from the *in-vitro* value. This is also evident in Figure 7.9 whereby the HB model has clearly recoiled more greatly at the proximal end than the BB model. Observing Figure 7.10 in addition to Figure 7.9 highlights the difference in the strut configuration predicted by the two models. In particular, three features are evident that differ between the two constitutive material models. Firstly, the aforementioned 'pinching' evident at the crown apex as a result of strain either side of the outside of the crown appears to be over-emphasised in the BB model. According to Figure 7.10(A) whilst striations or 'whitening' is evident at the outside of

the crown either side of the apex, this effect appears subtle and does not result in 'pinching' of the crown apex. The HB model appears to capture this more accurately with the crown apex maintaining a relatively smooth contour without significant evidence of 'pinching'. Secondly, the BB model predicts the post expansion strut configuration to remain circumferentially uniform. As discussed in Chapter 6 this is likely to be a result of the isotropic limitation of the BB model. Observing Figure 7.10(C) the scaffold struts appear to open equally regardless of the presence of a connector in contrast to the HB model in Figure 7.10(B). This displays a strut configuration that aligns more closely with the *in-vitro* data in which the deformation of the struts in each ring does not appear to be uniform. Lastly, the HB model shows the aforementioned splaying of the crowns in the radial direction, particularly in the case of the ring adjacent to the large central open cell (where this is over-emphasised). This splaying of the crowns is evident in both Figure 7.9(A) and Figure 7.9(B). Figure 7.10(C) does not display any evidence of crown splaying as they appear flat in the radial direction.

Returning to Table 7.3, the values of RS vary greatly between the *in-vitro* and two *in-silico* scenarios. This is partly due to the testing method, which as stated in Subsection 7.2.4, required the scaffold to be cut in half before radial crushing. This makes comparison with the *in-silico* data difficult due to a number of factors. The process of cutting the scaffold in half after expansion is likely to affect the radial strength of the scaffold due to alteration of the scaffold shape when the cutting process is conducted. Additionally, the interaction between the proximal and distal ends of the scaffold in crushing is removed which will also impact the radial strength calculated in *vitro*. Therefore, whilst both the BB and HB models present percentage errors in excess of 10% in radial strength prediction, this is likely to be a result of the *in-vitro* testing methodology.

Observing Figure 7.11 it is evident neither model accurately predicts the force-displacement profile. However, as previously stated, this is likely to be due to the disparity in the methodology used between the *in-vitro* and *in-silico* cases. Whilst the BB model provides an over estimation of the radial strength of 11% which could be attributed to the differences in methodology, the HB model presents an under prediction of 38%. This can also be attributed to the deformation of the scaffold struts that occurs in radial crushing in which two of the central long ring-length struts appear to buckle in this process, as shown in Figure 7.12. This demonstrates the interdependence between the deformation of the scaffold struts and the radial strength prediction. The manner in which the geometry deforms, as a result of the predicted final shape of the scaffold post expansion, will affect the force-displacement prediction of the scaffold. Buckling of these central struts allows axial movement of the top half of the scaffold rings in Figure 7.12 which did not manifest in *vitro*. This results in a mode of deformation that provides less resistance than radially crushing the scaffold in which the rings remain concentric. Despite this inaccuracy, the force-displacement profile of the HB model in Figure 7.11 does appear to resemble that of the *in-vitro* data, in which the force required

to crush the scaffold rapidly increases before a slower rate of increase until the maximum value at an OD of 2 mm.

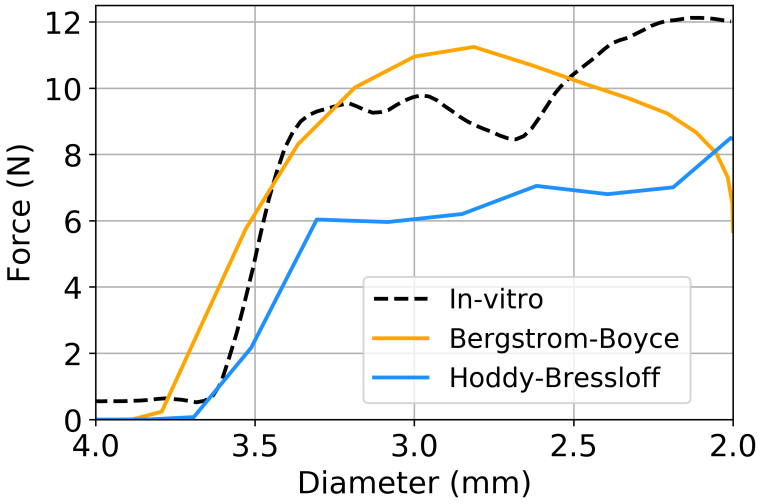

FIGURE 7.11: The force-displacement profiles of the bifurcation scaffold design in radial crushing after deployment via the 3.5 mm expansion balloon. Significant disparity between the material models and the *in-vitro* data is evident due to a number of factors.

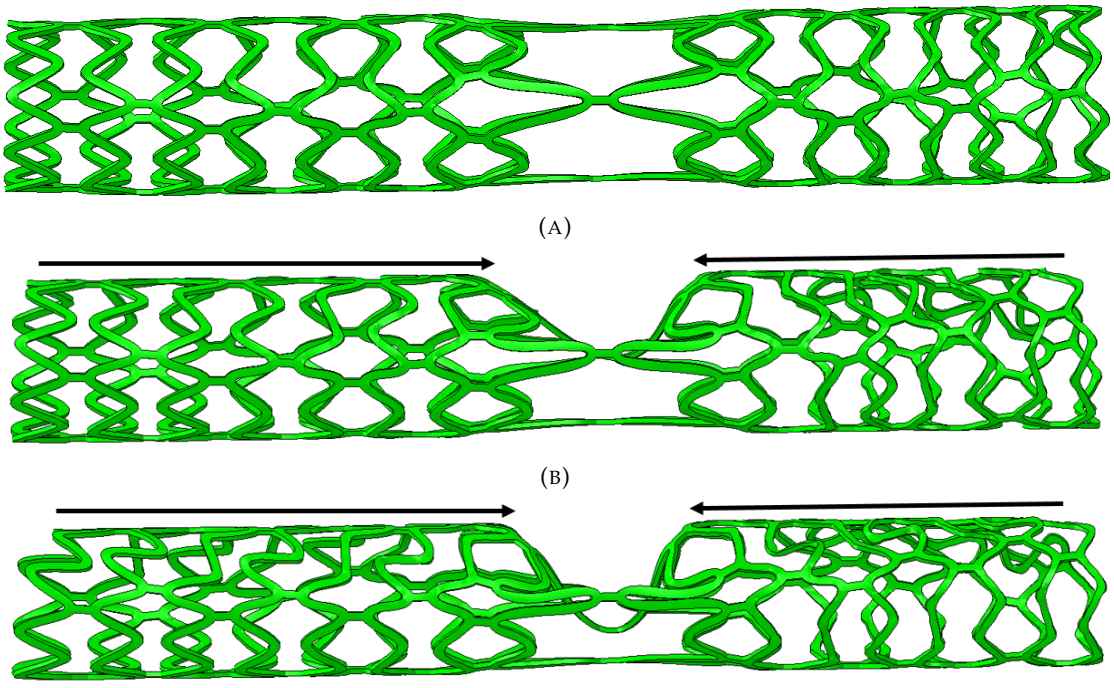

(A)

(B)

(C)

FIGURE 7.12: Buckling of the central long ring-length struts at the centre of the bifurcation scaffold in radial crushing using the Hoddy-Bressloff model which leads to under-prediction of the scaffold radial strength. The arrows show the axial movement of the rings that facilitates a lower resistance mode of radial crushing. The proximal scaffold end is located to the left with the distal end located to the right.

7.3.3 Expansion of the Bifurcation Scaffold into a Patient-Specific Left Main Bifurcation

Deployment of the scaffold into the coronary artery bifurcation provides a greatly increased level of complexity in terms of the loading environment the scaffold is exposed to. Significant tapering of the vessel diameter from almost 5 mm at the proximal end to 2.5 mm at the distal end in addition to the crushing force of plaque close to the ostium of the side branch provide this additional challenge. Unlike free expansion or deployment into an idealised concentric stenosis, the scaffold is likely to be subjected to uneven loading around its circumference given the non-circular shape of the coronary artery geometry.

The difference in strut configuration produced by the two constitutive material models in the deployment of the scaffold into the patient specific coronary artery bifurcation is significant. Whilst the BB model has generally produced reliable predictions of the overall scaffold mechanical behaviour it also appears to have misrepresented the configuration of the scaffold struts post expansion. This appears particularly true in the case of the deployment into the coronary artery bifurcation. Figure 7.13 shows a comparison of the bifurcation scaffolds after post-dilatation of the proximal end in which a clear difference in the strut configurations is evident. Figure 7.13(B) depicts the scaffold struts to have opened evenly around the ring's circumference in the post-dilatation step, in contrast to Figure 7.13(A) in which some struts remain more greatly straightened than others. This appears to be dependant upon the relative location of a connector which, as previously explored in Chapter 4, makes a significant difference to the distribution of equivalent plastic strain and in turn the post deployment strut configuration. Most noticeably, the Hoddy-Bressloff model predicts failure of three struts (shown at the location of the red asterisks) due to failure of the elements as a result of excessive strain in post-dilatation. This indicates the struts in this location should be made longer to facilitate the large overexpansion required to match the vessel diameter at the proximal end of the artery. The Bergstrom-Boyce model does not indicate a risk of such a failure, indeed, the struts appear to be undamaged in Figure 7.13(B) with no necking evident at the inside of the crown apex. A twisting phenomenon is also observed in the proximal ring in Figure 7.13(A) but not in Figure 7.13(B). This effect was discussed in Chapter 4 and observed in *vitro* in Figure 4.15.

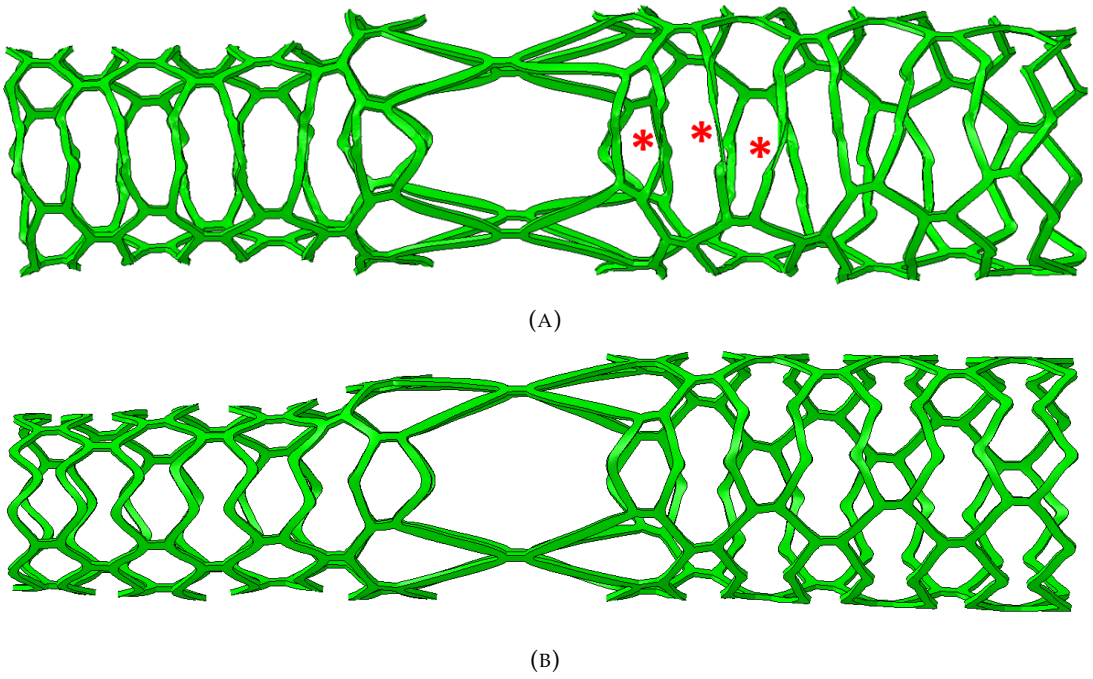

(A)

(B)

FIGURE 7.13: A comparison of the bifurcation scaffolds after post-dilatation at the proximal end deployed into the *in-silico* coronary artery bifurcation model using; (A) the Hoddy-Bressloff model and (B) the Bergstrom-Boyce model. The proximal scaffold end is located to the right with the distal end located to the left.

Returning to the strut failure observed in Figure 7.13(A), predicted by the Hoddy-Bressloff model, this is corroborated when compared with *in-vitro* test data. Figure 7.14 shows two cases of strut failure in the rings of the bifurcation scaffold when deployed in the coronary artery bifurcation model in *vitro* after post-dilatation to improve malapposition of the scaffold struts. Location of the strut failures appear to coincide with those in Figure 7.13(A) as they have occurred at the central closed ring and two rings proximal to the central ring. Whilst Foin et al. (2016b) observe strut fractures in first generation scaffolds exposed to modest over-expansions, this result demonstrates the greater tensile strain that can be tolerated by a second generation device. Figure 7.13(A) shows the scaffold struts to be fully straightened before they have failed at an OD of almost 5 mm which represents a significant overexpansion for the rings that have failed. It is encouraging that the HB model appears to correctly predict the onset of excessive plastic strain that leads to strut failure. The Bergstrom-Boyce model cannot be expected to predict strut failure in its current form as the strain to cause this lies well outside of the model calibration. If the strain does exceed 0.2, as per the maximum value in the BB model calibration then the stress response will be extrapolated and continue at approximately the same gradient as the plastic hardening reduces as the strain approaches 0.2, tending towards perfect plasticity. However, the BB model does not appear to accurately predict the strut configuration for a complex non-idealised loading scenario such as the coronary artery bifurcation model. Therefore, whilst the BB model provides

reliable predictions in terms of the scaffold mechanical behaviour, particularly in concentric loading scenarios, the HB model provides additional information regarding the scaffold mechanical behaviour that is not captured in the PRF within Abaqus/Explicit.

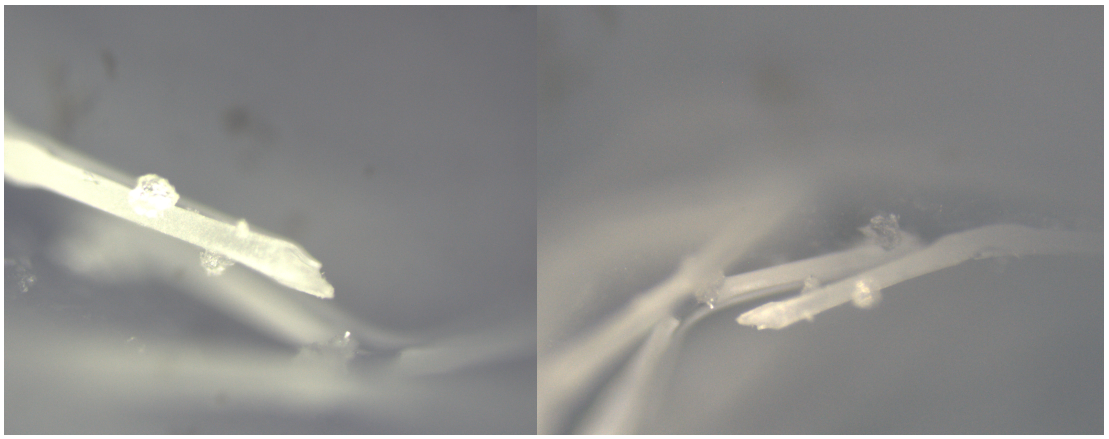

(A) (B)

FIGURE 7.14: Strut failures observed in the proximal half of the scaffold after post-dilatation in the coronary artery bifurcation model at; (A) the central closed cell ring and (B) two rings proximal to the central closed ring. The *in-vitro* testing was conducted by Arterius Ltd. These images were captured using an optical microscope in the University of Southampton materials laboratory.

With regards to the malapposition of the scaffold struts, Figure 7.15 shows a comparison of the deployed scaffolds within the plaque geometry for both the BB and HB models. Observing the scaffold which uses the HB model in Figure 7.15(A), it is evident that the two most proximal rings of the scaffold are underexpanded resulting in significant malapposition of the scaffold struts. This is also the case in Figure 7.15(B) although, as already discussed, the strut configuration is different. In both cases this highlights that to reduce malapposition of the scaffold struts at the proximal end of the scaffold, the proximal scaffold struts should be increased in ring length. However, the HB model also indicates that a significant level of twisting occurs at the proximal ring. This necessitates further consideration of the scaffold design at its proximal end. Whilst longer rings may be necessary to match the large vessel diameter and improve the apposition of the struts to the vessel wall, this will also exacerbate any twisting that might occur in the proximal rings. As discussed in Chapter 4, the twisting phenomenon results when the ratio of strut width to strut thickness becomes too large. It is imperative that the strut thickness is minimised due to the resulting increased risk of thrombus formation. Therefore, to avoid twisting of long ring-length rings for the bifurcation BRS it will be necessary to re-parameterise the crown geometry to ensure the proximal rings open in balloon expansion via cantilever bending rather than twisting. This is likely to result in lower radial strength in these rings to facilitate lower resistance in the circumferential direction to avoid strut twisting. However, this may be acceptable at the proximal end of the scaffold where the stenosis is less severe. From this study and the use of both

material models, it is evident that the bifurcation scaffold must be re-designed to avoid strut twisting and reduce malapposition at the proximal end. In both cases the distal end of the scaffold performs well as the lumen diameter is significantly increased, particularly in the case of the HB model, with excellent apposition of the scaffold struts to the vessel wall.

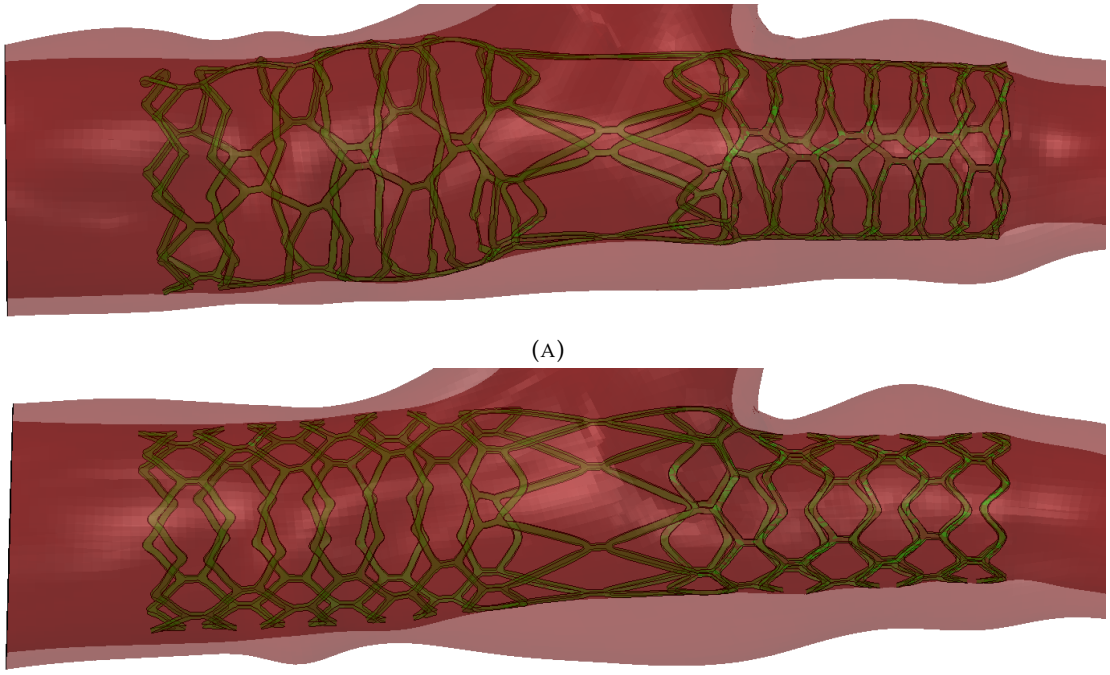

(A)

(B)

FIGURE 7.15: The bifurcation scaffold deployed in *silico* into the left main coronary artery geometry after post-dilatation using; (A) the Hoddy-Bressloff material model and (B) the Bergstrom-Boyce material model. The proximal scaffold end is located to the left with the distal end located to the right.

7.4 Conclusions

Use of both the Hoddy-Bressloff and Bergstrom-Boyce material models in the context of scaffold deployment in clinically realistic scenarios were investigated in this chapter. Balloon expansion of a next generation thin-strut bioresorbable coronary scaffold into arterial geometry of any kind has not been conducted to date in the literature. The baseline scaffold design was deployed into an idealised coronary artery model containing a concentric stenosis. The investigation of a novel scaffold design for a highly tapered coronary artery bifurcation was also conducted via free expansion and constrained deployment into patient specific geometry.

The following conclusions can be drawn from this chapter:

1. The baseline scaffold design, based upon the ArterioSorb^{TM}, exerts lower maximum stresses upon the artery wall when deployed via balloon expansion than a permanent metallic stent found in the literature. Whilst this is a result of their lower radial strength, the BRS demonstrates acceptable radial strength to successfully revascularise a concentric coronary artery with a 60% of area stenosis in *silico*. The BRS also exhibits a lower level of volume averaged stress than a permanent metallic stent found in the literature. This means BRS are likely to reduce the risk of restenosis as a result of injury to the vessel wall despite their wider and thicker struts compared to metallic stents.

2. The Bergstrom-Boyce model appears to predict the scaffold mechanical response such as final diameter and radial strength with good accuracy, particularly in concentric loading scenarios. However, deployment of scaffolds in realistic arterial geometry, such as the patient specific left main coronary artery bifurcation provides additional challenge to accurately predict the scaffold deployment. In this case, despite a less accurate prediction of the aforementioned metrics, the Hoddy-Bressloff model captures a number of phenomena that are not described by the Bergstrom-Boyce model. In particular, failure of the scaffold struts under significant over-expansion is accurately predicted and validated with *in-vitro* data in addition to twisting of the proximal ring as a result of balloon expansion. The outwards splaying of the crowns is also not captured by the Bergstrom-Boyce model. Therefore, use of both material models provide merit in the *in-silico* investigation of BRS.

3. The novel bifurcation scaffold designed for a patient specific left-main coronary artery bifurcation requires increased ring length of the proximal rings to give an improvement of strut apposition to the vessel walls in addition to re-parameterising the crown shape of the proximal rings to facilitate the cantilever bending of the long ring-length rings and resist twisting about the crown apex in balloon expansion.

Chapter 8

Concluding Remarks

8.1 Introduction

The latest generation of BRS continue to be investigated with regards to their clinical viability and potential efficacy relative to permanent metallic stents. Whilst this latest revolution in interventional cardiology began many years ago, both anticipation and scepticism remain regarding BRS and their introduction into routine clinical practice. Despite encouraging pre-clinical data from a number of scaffold designs (Katagiri et al., 2019; Koltowski et al., 2020; Song et al., 2021), until long term clinical data can be presented for BRS, there will remain many outstanding questions regarding their efficacy, particularly in terms of the rates of late stent thrombosis. In the meantime, improved modelling strategies to accurately predict their mechanical behaviour both in *vitro* and in *vivo* will help build confidence in BRS and facilitate improvements in their design that will ultimately lead to more favourable patient outcomes.

In this thesis, an investigation has been presented of the mechanical behaviour of scaffold designs based upon the ArterioSorb^{TM} BRS. Finite element analysis (FEA) has been utilised to better understand the relationship between the scaffold design variables and the equivalent plastic strain, initially investigated by Migliavacca et al. (2002) in the case of permanent DES and latterly by Wang et al. (2017) in BRS, developed in the scaffold struts in the deployment process. Particular phenomena that occur throughout balloon expansion have also been discovered and related to the scaffold design parameters to inform the future design of BRS.

Despite a number of studies providing significant insight into the material modelling of BRS in the context of their *in-silico* deployment (Eswaran et al., 2011; Debusschere et al., 2015; Bobel and McHugh, 2018; Wang et al., 2018; Blair et al., 2019b), there appeared a lack of consensus regarding the optimum choice for a material model to capture the

mechanical behaviour of polymeric BRS. Therefore, assessment of several different material models within FEA has also been undertaken to understand their appropriateness and limitations in describing the scaffold mechanical response when used to simulate crimping, balloon expansion and radial crushing. A novel user defined material model, a permutation of an existing anisotropic material model, was also implemented and investigated. The *in-silico* data from the FEA simulations was also compared with *in-vitro* bench test data to validate the accuracy of the material models in predicting the scaffold performance, which according to the literature is a rare practice. The material models were also underpinned by relevant experimentally obtained stress-strain data from different mechanical tests, conducted by our industrial partner, to which the model parameters could be calibrated.

Lastly, it was recognised that a general deficit exists regarding the *in-silico* deployment of BRS into clinically realistic scenarios, with the exception of the work by Schiavone et al. (2016). Therefore, exploration of the baseline scaffold design, deployed in *silico* into stenosed coronary artery geometry, was conducted in addition to the deployment of a novel scaffold design intended for the left main coronary artery bifurcation. Assessment of the apposition of the scaffold struts to the vessel wall, in addition to the stresses exerted on the artery as a result of the scaffold/plaque interaction, as conducted by Pant et al. (2011) and Wei et al. (2019) in the case of DES, were undertaken to gain a deeper insight into the expected BRS performance in *vivo* and the viability of the novel bifurcation scaffold design.

8.2 Conclusions

Firstly, a concise summary of the main contributions to the field as a result of this doctoral research are presented, followed by further detailed discussion of the contributions and their respective limitations as a result of the methodology employed.

8.2.1 Primary Contributions

The primary contributions made in this doctoral research are:

- The Hoddy-Bressloff model was developed in this research to utilise a variable yield ratio which facilitated the capture of the differences in plastic hardening in the axial and circumferential material directions. This allowed a more accurate prediction of the post-expansion strut configuration, compared to the Bergstrom-Boyce model, due to its anisotropic framework. Additionally, it was able to predict strut failure due to excessive strain in overexpansion and the aforementioned 'twisting' phenomenon.

- The Bergstrom-Boyce material model implemented via the parallel rheological framework in Abaqus/Explicit predicted the radial strength and post-expansion diameter of the BRS within 2% of the corresponding *in-vitro* values. However, it overemphasised the 'pinching' phenomenon at the crown apex and did not accurately capture the post-expansion strut configuration due to its isotropic limitation.

- The ratio of crown width to strut thickness was found to be a critical variable in the design of thin-strut BRS due to the 'twisting' phenomenon exhibited in long ring-length scaffolds. This was found to result in an asymmetric distribution of equivalent plastic strain either side of the crown apex and is likely to degrade patient outcome due to reduced radial strength and increased stress exerted on the vessel wall.

- The baseline scaffold design investigated in this research, based upon a second generation thin-strut BRS, offers a good level of both radial strength and side branch access compared to designs that utilise a variable ring length and strut width along their length. The BRS was also found to successfully revascularise a stenosed coronary artery segment with excellent apposition of the struts to the vessel wall.

- *In-silico* testing of a novel scaffold design intended for a left main coronary artery bifurcation demonstrated the scaffold to successfully revascularise the distal part of the vessel close to the location of the stenosis at the side branch ostium. However, the proximal ring lengths were not long enough to facilitate the necessary overexpansion and exhibited the 'twisting' phenomenon.

8.2.2 Discussion and Limitations

The strut twisting about the crown apex observed both in *silico* and in *vitro* in the radial direction is a critical behaviour that occurs in wide-strut BRS that could adversely affect patient outcome. Due to the low stiffness in the radial direction, a result of the thin struts, the cantilever bending in the axial and circumferential directions that normally occurs in balloon expansion is exchanged for a twisting movement. This would have a detrimental effect upon the radial strength of the scaffold, due to reducing the influence of the axial direction's stiffer material properties upon the scaffold's resistance to radial crushing, and the stress to which the vessel wall will be exposed, due to the protruding crown apex. This was shown to result in an asymmetric distribution of equivalent plastic strain either side of the crown apex and should be avoided in future BRS design.

The design study undertaken to explore variable ring-length and strut-width scaffolds highlighted that the baseline scaffold design lies close to the optimum specific radial strength (SRS). This is likely to be a result of the aforementioned twisting exhibited by

wide-strut designs which subsequently reduces their SRS. Wide-strut scaffolds were also found to display large levels of PEEQ at the inside of the crown apex, due to their small radius of curvature, suggesting they pose an increased risk of strut fracture in balloon expansion. Additionally, percentage recoil ($R_{\%}$) and maximum average PEEQ (PQ_{max}) were inversely proportional and the presence of a connector attached to a crown apex significantly reduced the development of PEEQ at that crown, particularly for wide-strut designs. Due to the baseline scaffold exhibiting a good level of SRS compared to alternative designs and the difficulty in improving cell area (CA) without; (i) incurring a significant penalty in SRS or (ii) initiating strut twisting, a full optimisation study was not undertaken. It was deemed that the percentage improvements in scaffold performance would be small by exploring the variable ring-length and strut-width scaffold designs. Moreover, the limited efficacy of the anisotropic elasto-plastic material model was considered a more important avenue of exploration that would ultimately facilitate design optimisation of BRS to be undertaken with greater accuracy and confidence in model predictions. As a result of this study, the parameterisation of the crown apex geometry was highlighted as a critical area to which attention should be given to avoid the twisting phenomenon.

Subsequently, the exploration of several different calibrations of the in-built Abaqus isotropic and anisotropic elasto-plastic material models yielded the following conclusions. The use of isotropic or anisotropic elasto-plastic theory to predict the metrics that define the mechanical response of thin-strut polymeric BRS is generally not appropriate. It is challenging to accurately capture both the final diameter and radial strength of BRS when using isotropic linear elastic models with Mises or Hill's plasticity. Generally, either the final diameter or the radial strength of the scaffold can be accurately predicted when tuning of the model to the underlying stress-strain data is conducted. Two possible improvements upon elasto-plastic theory are presented in this thesis for capturing the mechanical behaviour of next generation thin-strut BRS.

Firstly, the Hoddy-Bressloff (HB) model, in which a permutation of the Hill's yield function was implemented to capture the anisotropic plasticity at high strains in the axial direction of the BRS, via a variable yield ratio, provided an improved, yet conservative, estimation of the mechanical behaviour of the scaffold, compared to isotropic plasticity models and Hill's yield function models. Additionally, the failure of elements as a result of excessive strain was implemented via a relaxation of the yield stress and reduction in hardening as the PEEQ exceeded a threshold. Radial strength was predicted with a percentage error of just 1.1% using a realistic multi-balloon expansion strategy. Post-expansion scaffold shape was predicted within 6.7% of the *in-vitro* data which represented a significant improvement upon the isotropic and anisotropic elasto-plastic models within Abaqus. The Hoddy-Bressloff model was also able to capture several phenomena that occurred in the balloon expansion of BRS that were not otherwise realised in *silico*. Additionally, twisting about the crown apex of long ring-length

wide-strut rings was correctly predicted in *silico*. To validate the *in-silico* predictions, the *in-vitro* balloon expansion of the scaffold (conducted by Arterius Ltd) was undertaken at 37°C whilst submerged in a water bath to simulate the haemodynamic environment. In contrast, the underlying stress-strain data obtained via uniaxial tensile testing (conducted by Arterius Ltd) was undertaken at room temperature in dry conditions due to limitations in the testing equipment available. Therefore, whilst the HB material model was calibrated to stress-strain data obtained at room temperature in dry conditions, the predictions to which the material model was validated were more realistic and closely resembled the in *vivo* environment. Whilst this is likely to be a factor in the small disparity between the *in-silico* predictions and *in-vitro* validation of radial strength (RS) and final diameter (FD), conducting the *in-vitro* testing under these conditions facilitated a fair comparison with previous ArterioSorb^{TM} designs and derived a more realistic prediction of the strut configuration and subsequent strain distribution in the scaffold struts in *vivo*. Moreover, both room temperature (RT, 25°C) and body temperature (BT, 37°C) lie below the glass transition temperature of the PLLA and so significant changes in the polymer's mechanical behaviour would not be expected. This is corroborated by Bobel et al. (2016) and shown in Figure 2.17 in which the stress-strain response of PLLA at RT and BT show identical Young's modulii, along with a relatively modest 25% reduction in yield stress when the temperature is increased from RT to BT. This is in contrast to the stress-strain response at a temperature of 42°C in which the initial elastic modulus decreases significantly and the yield stress at zero plastic strain reduces by approximately 80%.

The second improvement concerns an implementation of the Bergstrom-Boyce (BB) material model in Abaqus/Explicit. This model is generally regarded as the optimum material model for predicting the stress response of polymers. The model was demonstrated to predict both the final diameter and radial strength of the scaffold within 2% of its *in-vitro* values in free expansion. The model should be calibrated to material stress-strain data calculated from the average of the circumferential and axial directions of the die-drawn PLLA tube, obtained at a clinically relevant displacement rate of 1 mm/min, given its isotropic limitation. The BB model can also be used to benefit the prediction of the post-crimping scaffold diameter through use of a temperature dependent model that facilitates a reduction in stress as a result of increased temperature. A staged crimping profile should also be used to exploit the stress relaxation that occurs in PLLA when held at a constant strain, a benefit of the model's time dependant behaviour. Whilst this technique improved the post-crimping diameter prediction, the recoil at this stage of the deployment was still found to exceed that exhibited in *vitro*. Therefore, a mechanism exists at the micro-structural level of the PLLA that is not described by any of the investigated material models that facilitates low levels of percentage recoil, in the order of 2-3%. Additionally, whilst the BB model can accurately predict the final diameter and radial strength of BRS, it was found to misrepresent the post-expansion strut configuration in non-idealised scenarios, due to the model's isotropic limitation. The

Hoddy-Bressloff model was able to more accurately represent the post-expansion strut configuration due to capturing the material anisotropy, despite its less accurate final diameter prediction.

Additionally, Wang et al. (2018) and Antonini et al. (2021b) both utilised the Johnson-Cook (JC) plasticity model to explore the mechanical behaviour of polymeric BRS. This material model framework was not considered in this doctoral research. However, the JC model was deemed to be similar in formulation to the HB model as it determines a yield stress via a low order polynomial, which is a function of the PEEQ only. Temperature and strain-rate dependency can be utilised in this model, although this was explored using the BB model. The JC model is also limited to an isotropic implementation in Abaqus/Explicit.

Despite the literature indicating that PLLA generally exhibits significant levels of viscoelastic recovery (Bobel et al., 2016), shown in Figure 2.19, the PLLA provided by Arterius Ltd was observed to exhibit very low levels of viscoelastic recovery, shown in Figure A.6, that contributed less than 1% recoil post expansion. The *in-vitro* study of the BRS recoil indicated the viscoelastic recovery stabilised within 6 minutes of relaxation commencing. Therefore, it is evident that the die-drawing process, unique to the PLLA used to construct the ArterioSorb^{TM}, has a significant effect upon the recoil and time-dependent properties of the PLLA and explains the cause for the low levels of recoil exhibited by the ArterioSorb^{TM} and the subsequently derived scaffold designs. The exact nature of the micro-structural mechanism that causes this behaviour is unknown and it is evident from the *in-silico* testing that the material models investigated in this research are unable to capture this behaviour. It should be noted that the *in-vitro* observations from which this conclusion is drawn are obtained from measuring the long term recoil of a BRS subjected to balloon expansion. To compare the observations directly with the work of Bobel et al. (2016) recovery tests would need to be conducted on dogbone specimens of PLLA to observe their viscoelastic recoil at an appropriate temperature and displacement rate.

The baseline scaffold design successfully revascularised a coronary artery segment with a 60% stenosis of the lumen area. The scaffold almost fully restored the lumen area with excellent apposition of the scaffold struts to the vessel wall, indicting such a scenario would yield a favourable patient outcome. Investigation of the stresses exerted on the vessel wall demonstrated that BRS offer a significant benefit in terms of reducing the maximum stress experienced, as a result of the scaffold/plaque interaction. Additionally the volume average stress exerted by the BRS was found to be lower than a permanent metallic stent, despite the scaffold's wider and shorter struts (resulting in greater contact area between the plaque and scaffold). This assessment of the baseline scaffold design only considered an idealised arterial geometry that does not contain the tortuosity and non-uniformity that would be present in a realistic coronary artery.

After *in-silico* balloon expansion of the novel scaffold design intended for the left main coronary artery bifurcation, it was evident that the struts proximal to the large central open cells were vulnerable to fracture as a result of the significant overexpansion they were exposed to. This was realised in *vitro* whereby a number of struts in this novel design were observed to fracture. Twisting about the crown apex at the proximal end of the scaffold was also predicted in *silico*, which was subsequently evidenced in *vitro*. Whilst the left main coronary artery bifurcation provides a challenging case for BRS, the patient specific geometry does not contain significant curvature in the segment in which the BRS is placed. Therefore, the flexibility, an important metric to determine the scaffold's deliverability, and the stress imparted to the artery walls via vessel straightening, as considered by Mortier et al. (2010), is not tested in this assessment of the BRS mechanical performance. Additionally only a two layer artery model was considered in this research. The model could be developed further to include all three arterial layers (the adventitia, media and intima) and realistic stenoses compositions could be modelled, as per the work of Wei et al. (2019).

8.3 Future Work

Considering the findings in this doctoral research, there are several potential lines of enquiry that should be considered in any future work relating to the mechanical behaviour of next generation thin-strut bioresorbable polymeric coronary scaffolds.

Development of a user subroutine to implement the Bergstrom-Boyce material model used in this research in Abaqus/Explicit should be undertaken. This would facilitate alteration of the model within the finite element analysis simulations to capture the anisotropy of PLLA, as undertaken by Debusschere et al. (2015) in Abaqus/Implicit. This would likely facilitate a more accurate prediction of the post-expansion strut configuration of a bioresorbable scaffold and capture the twisting of the scaffold struts exhibited in *vitro* and in *silico* via the Hoddy-Bressloff model. Additionally, consideration of a strain based failure criteria, which has proven to be successful in the Hoddy-Bressloff model, would benefit the amended Bergstrom-Boyce model to facilitate prediction of strut fracture in balloon expansion. This would allow the benefits of the Hoddy-Bressloff model to be combined with the time dependent Bergstrom-Boyce model and allow a single material constitutive theory to capture the mechanical response of thin-strut bioresorbable scaffolds, negating the need for multiple models to carry out different roles in the design and simulation process. This would also remove the necessity to calibrate the Bergstrom-Boyce model to stress-strain data calculated as an average of the axial and circumferential material directions.

The uniaxial tensile testing to determine the stress-strain response of the PLLA used to construct the ArterioSorb^{TM} should also be undertaken at an elevated temperature in

submerged conditions to simulate the haemodynamic environment. This would facilitate the material models to be calibrated to the most clinically relevant material stress-strain data, thus removing another potential source of error from the *in-silico* predictions.

It is evident that whilst next generation thin-strut BRS offer the potential to improve patient outcomes in relatively simple clinical scenarios, the use of a BRS in a complex case such as the left main coronary artery bifurcation still requires significant development. Therefore, further development of the novel bifurcation scaffold design should be undertaken. The aforementioned re-parameterisation of the proximal scaffold rings and the crown apex geometry should be conducted to provide an updated baseline design for the bifurcation scenario. This will reduce the likelihood of strut fracture when the scaffold is subjected to large over-expansions and facilitate improved apposition of the struts in the proximal end of the scaffold, in addition to reducing the likelihood of strut twisting. Indeed, a separate design study to consider twisting about the crown apex as a result of the ratio of crown width to strut thickness should be considered. This could utilise a simplified scaffold geometry that considers a single crown only to determine at what point the onset of radial twisting occurs as the ratio of crown width to strut thickness is increased.

Returning to the optimisation of the entire bifurcation scaffold design, increasing the ring length to facilitate greater overexpansion, whilst reducing the likelihood of strut twisting, presents a design challenge as they were found to be competing objectives in this research. Following this design change, the scaffold should be validated via *in-vitro* free expansion and deployment into the patient specific coronary artery bifurcation to determine whether it is an appropriate baseline design that can be used in a formalised design optimisation process. The work by Foin et al. (2016a,b) also provides an excellent framework for assessing BRS design via *in-vitro* testing in terms of their overexpansion capability and radial strength. Additionally, it is recommended that high resolution CT scans are used to assess the apposition of the scaffold struts to the wall of coronary artery models in *vitro*. Such a technique has not been observed in the literature for thin-strut BRS and would also facilitate analysis of the scaffold surface to observe micro-cracks that could initiate strut fracture. If the updated scaffold is deemed an appropriate baseline design then sensitivity analysis of the design variables should be conducted to determine their limits and which variables should be considered in a design study. Appropriate objective functions should also be selected to quantify the scaffold performance in free and constrained expansion. It is suggested that the scaffold radial strength, final diameter, volume averaged stress of the vessel wall and percentage of malapposed struts, as used by Ragkousis (2016), are considered. The scaffold flexibility, to determine how easily it can be delivered to the stenosis/plaque site and the stress it may impart on the artery wall as a result of vessel straightening, should be investigated. Use of highly curved arterial geometry into

which the bifurcation scaffold could be deployed should be considered, along with axial bending tests of the scaffold geometry. In addition, the susceptibility of strut failure due to loading at the interface of the connectors and the central long ring-length struts should be investigated. This section of the scaffold structure is inherently vulnerable to excessive deformation and fracture. In summary, significant effort is required to conduct a formal design optimisation of the bifurcation scaffold. However, prior to the optimisation study a robust process must be undertaken to ensure the design study has chosen appropriate design variables with reasonable bounds and objective functions that usefully quantify the scaffold performance and predict patient outcome. It is imperative that a good baseline design is validated to maximise the efficacy of a design optimisation study.

Despite investigation into improving the *in-silico* post-crimping recoil prediction of the thin-strut BRS, it is evident that there remains a disparity in the post-crimping and post-expansion recoil predicted by the material models investigated and that exhibited in *vitro*. The percentage recoil exhibited by the baseline scaffold design lies in the order of just 2% in both crimping and balloon expansion, unlike the *in-silico* predictions that estimate percentage recoil of at least 6%. Therefore, investigation into the micro-structural mechanism in the PLLA that results in the low levels of recoil observed in *vitro* would be beneficial. It is hypothesised that this is primarily a result of the unique patented die-drawing pre-processing that the PLLA, used to construct the ArterioSorb^{TM}, is subjected to prior to laser cutting of the scaffolds from the PLLA tubes. These low levels of recoil are not observed in the loading-unloading tests conducted at room temperature in air on the dogbone PLLA specimens and so may also be a function of the loading environment (although this is not the case with other BRS investigated in the literature). Therefore, validation of this hypothesis via uniaxial loading-unloading tests should be conducted in which PLLA dogbone samples are subjected to clinically relevant environmental conditions. Additionally, the uniaxial testing should be conducted to PLLA that has not been subjected to the die-drawing process to explore the difference this process makes to the unloading behaviour of the PLLA. Following this, understanding of the micro-structural changes that occur in the material should be sought and identification of how this can be captured within the constitutive material model framework should be considered. Use of different imaging techniques such optical microscopes, high resolution CT scans and even scanning electron microscopes could be utilised to aid this.

Lastly, whilst it is widely accepted that coronary stents/scaffolds have primarily structural implications upon the coronary environment, a significant factor in determining the patient outcome is also the haemodynamic disturbance caused by the presence of a stent/scaffold. Therefore, assessment of next generation bioresorbable coronary scaffolds using computational fluid dynamics should also be undertaken to assess the changes in wall shear stress as a result of the medical implant, as per Gogas et al. (2015)

and Tarrahi et al. (2020). This metric, highlighted in the literature in the context of permanent metallic stents by Wentzel et al. (2003); LaDisa et al. (2003); Dehlaghi et al. (2008) and Pant et al. (2011), is a significant factor in determining the risk of restenosis and thrombus formation in the short and medium term in the context of BRS. Multi-physics modelling beyond structural finite element analysis will serve to more completely assess the efficacy of BRS when deployed into coronary artery geometry.

Appendix A

Uniaxial Tensile Testing of PLLA

A.1 Introduction

To achieve accurate results using FEA it is essential that an appropriate material model is selected and calibrated to relevant stress-strain data obtained from mechanical bench testing. As the mechanical response of PLLA is highly dependant upon the pre-processing it is subjected to, it is important to calibrate material models with stress-strain data derived from PLLA that has been treated identically to that used to construct the BRS. Therefore, uniaxial tensile strain-to-break and loading-unloading tests were undertaken by Arterius Ltd to ascertain the stress response of the PLLA used to manufacturer the ArterioSorb^{TM}. Strain-to-break tests are commonly used in the literature to inform elasto-plastic materials models (Pauck and Reddy, 2015; Blair et al., 2019b), as investigated in Chapters 4 and 5, whilst loading-unloading data, as used by Eswaran et al. (2011) and Bobel and McHugh (2018), can be used to calibrate high fidelity parallel network models, investigated in Chapter 6.

A.2 Methodology

Figure A.1 shows the tensile testing setup. Uniaxial tensile tests were conducted by Arterius Ltd using a Mecmesin MultiTest 1-I tensometer with U form vice grips on dog-bone shaped specimens. A preload was applied to the samples of approximately 0.1 N to remove any slack, such that a region of zero force did not occur in the stress-strain data. Extruded PLLA tubes were processed by solid phase orientation using biaxial die drawing whereby they were heated above the glass transition temperature, then drawn over an expanding mandrel (Al-Lamee et al., 2019). This induces crystallinity and orientates the polymer chains in both the axial and circumferential directions. As a result, the PLLA displays significant anisotropy with higher strength and stiffness in

the axial direction, due to increased polymer chain crystallinity in this direction. Dogbone shaped specimens were then laser cut from the die drawn tubes in both the axial and circumferential directions. The stress-strain data obtained was relevant to scaffold design as the PLLA samples were treated identically to the PLLA used to construct the ArterioSorb^{TM} BRS platform which ensured the material properties between dogbone samples and scaffolds remained constant. The dogbone specimens had a gauge length of 10 mm and a width of 1.25 mm, as per ISO 20753.

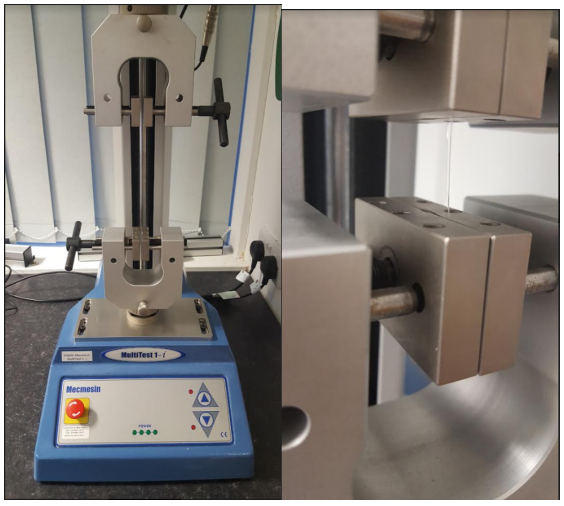

(A) (B)

FIGURE A.1: (A) The Mecmesin MultiTest 1-I tensometer and (B) a dogbone PLLA sample under uniaxial tension.

Samples cut from the tubes' axial and circumferential directions were tested such that the material anisotropy could be observed. Strain-to-break tests were conducted at four different displacement rates of 1, 5, 10 and 50 mm/min, given the time dependant stress response exhibited by PLLA. Two tests were conducted for each direction/displacement rate combination which derived the engineering stress and strain. The averaged data in the two test cases in each scenario was then used to obtain the true stress and strain via the approximations:

$$\sigma_{true} = \sigma_{eng} * (1 + \epsilon_{eng}) \tag{A.1}$$

$$\epsilon_{true} = ln(1 + \epsilon_{eng}) \tag{A.2}$$

where σ_{true} is the true stress, ϵ_{true} is the true strain, σ_{eng} is the engineering stress and ϵ_{eng} is the engineering strain (Benham et al., 1996). This was necessary as Abaqus/CAE (DS SIMULIA) requires the true stress and strain values for calibration of the material

model, which, for high levels of strain as considered in this doctoral thesis, deviate significantly from the engineering values.

The loading-unloading tests sought to strain the dogbone samples to approximately 80% of their ultimate tensile strain (UTSn), to ensure they did not fracture, before unloading the samples to zero strain.

A.3 Results & Discussion

The stress-strain data for uniaxial tensile strain-to-break tests for the four different displacement rates is shown in A.2.

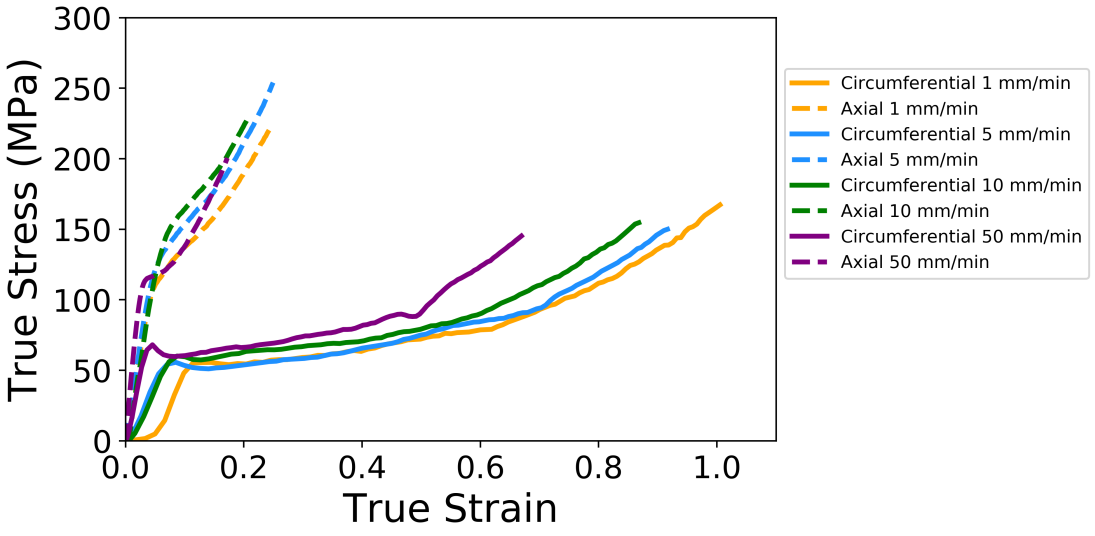

FIGURE A.2: The stress-strain response from uniaxial tensile tests of dogbone shaped specimens cut from a die-drawn PLLA tube. Samples from both the axial and circumferential directions were tested at four independent displacement rates. In each case, the sample was strained until failure.

The stress-strain response of the PLLA samples in the loading-unloading tests is given in A.3.

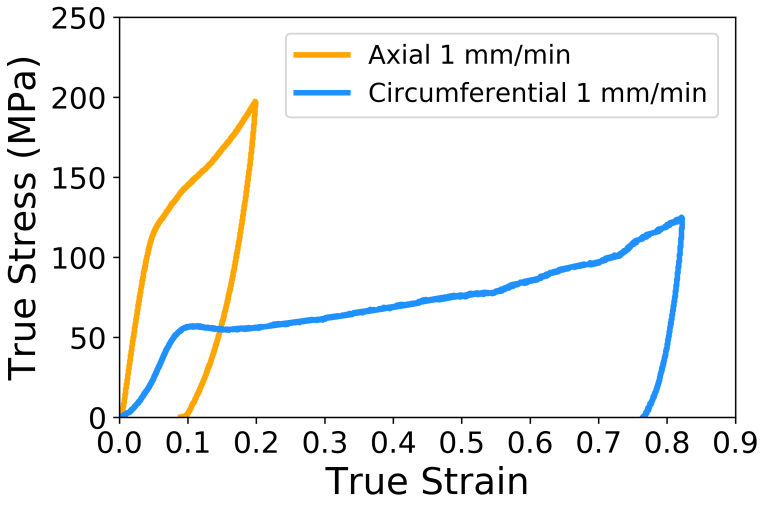

FIGURE A.3: The stress-strain response for a uniaxial loading-unloading test for dog-bone shaped samples cut from die-drawn PLLA tubes in the circumferential and axial directions. The samples were loaded at 1 mm/min before unloading at the same rate to zero stress.

The highly anisotropic properties of PLLA are evident in Figure A.2. Indeed, the axial direction has a significantly higher stiffness and yield point in comparison to the circumferential direction. However, the UTSn is much lower in the case of the axial direction. Interestingly, this is in contrast to the data obtained by Eswaran et al. (2011) in which the circumferential direction shows greater stiffness and brittleness, as detailed in Figure A.4. The crystallinity of the PLLA blend provided by Arterius Ltd was such that the polymer chains were predominantly orientated in the axial direction. High strength and low ductility are associated with properties aligned with the polymer chains, as this limits the potential of the chains to rearrange and redistribute stresses, and so these trends in material anisotropy, presented in Figure A.2, are expected (Bergström and Hayman, 2016).

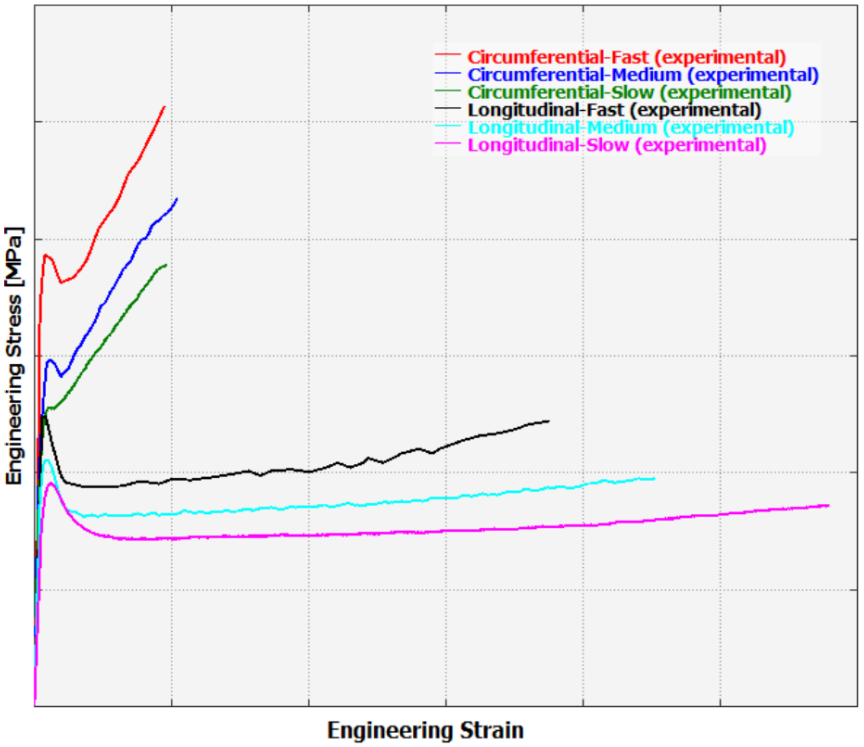

FIGURE A.4: Uniaxial tensile strain-to-break tests conducted on dogbone samples cut from an extruded PLLA tube. In this case, the circumferential direction shows greater stiffness and brittleness than the axial direction (Eswaran et al., 2011).

In the circumferential direction, the UTSn is inversely proportional to the displacement rate whilst the yield stress increases, albeit marginally, with an increase in displacement rate. The Young's modulus is proportional to the displacement rate, ranging from approximately 800 MPa at 1 mm/min to almost 3000 MPa at 50 mm/min in the circumferential direction. In the 1 mm/min case for the circumferential direction, the initial elastic portion of the graph exhibits non-linear elasticity, evidenced by the large change in gradient at low levels of strain. In the case of the axial direction, the yield point at zero plastic strain is also proportional to the displacement rate. However, the largest displacement rate of 50 mm/min subverts this trend and shows a similar yield point to the 1 mm/min case of 110 MPa. The Young's modulus also increases for the axial direction from 3000 MPa at 1 mm/min to 4500 MPa at 50 mm/min.

From this data it is evident that the anisotropic effects of PLLA are significant. Whilst the time dependant effects of the axial data are generally more subtle, the stress-strain response in the circumferential direction showed a significant range of variation in the Young's modulus and UTSn as a result of the strain rate. Considering the findings of Wang et al. (2018), it is suggested that the effect of strain rate upon the stress response of the scaffold is very limited when the scaffold is deployed in the haemodynamic environment meaning that modelling the time dependency of PLLA could be unnecessary in balloon expansion. Due to the general recommendation that scaffolds are expanded

slowly in *vivo*, a displacement rate as high as 50 mm/min is unlikely to be encountered in clinical scenarios. However, this provides a significant contrast to the slower clinically relevant displacement rates.

The loading-unloading data in Figure A.3 confirms the findings of the strain-to-break tests in Figure A.2. Additionally though, these tests provide information about the elastic relaxation of the PLLA. It is evident in Figure A.3 in the case of the circumferential direction that the unloading slope has a steeper gradient than the slope in loading, a feature that would not be captured using linear elasticity with Mises plasticity and isotropic hardening. This does not appear to be the case in the axial direction, in which the unloading slope appears shallower than the loading slope which is likely to be a result of the lower strains developed, albeit, these are a similar proportion of the UTSn in this material direction compared to the circumferential direction. The cyclic loading-unloading tests conducted by Eswaran et al. (2011), presented in Figure 2.15, suggest this is the case as the unloading slope becomes steeper as greater strains are developed in the scaffold struts.

The loading-unloading tests do not provide information regarding the viscoelastic recovery of the BRS. This is a time-dependant phenomenon, evidenced in Figure 2.15 and in the work of Bobel et al. (2016) in which the strain in a structure continues to reduce when the stress has already relaxed to zero. Figure A.5 shows a diagram of the typical stress/stain response of PLLA. The major differences in the case of the PLLA used by Arterius Ltd is that rather than softening of the PLLA post-yield the material hardens. Additionally, at low displacement rates, the PLLA exhibits non-linear elasticity, rather than linear elasticity, as suggested in Figure A.5.

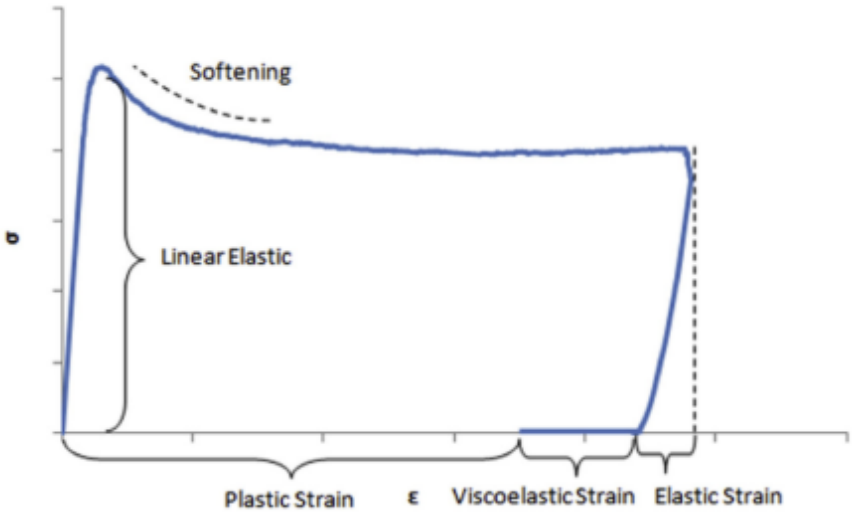

FIGURE A.5: A typical stress-strain response of PLLA used for biomedical applications, annotated to show the different phenomena exhibited by the material (Bobel et al., 2016).

To investigate the viscoelastic recovery of the PLLA used to construct the ArterioSorb^{TM}, observations of scaffold recoil, post balloon expansion, in an *in-vitro* free expansion scenario over an extended time period of 10 minutes were conducted. This time period extended beyond the initial acute elastic recoil of the scaffold to observe the time dependant effect. Four locations along the length of a variable ring length scaffold expanded to a target diameter of 4.5 mm OD were observed, the cumulative recoil at each of these locations is shown in Figure A.6

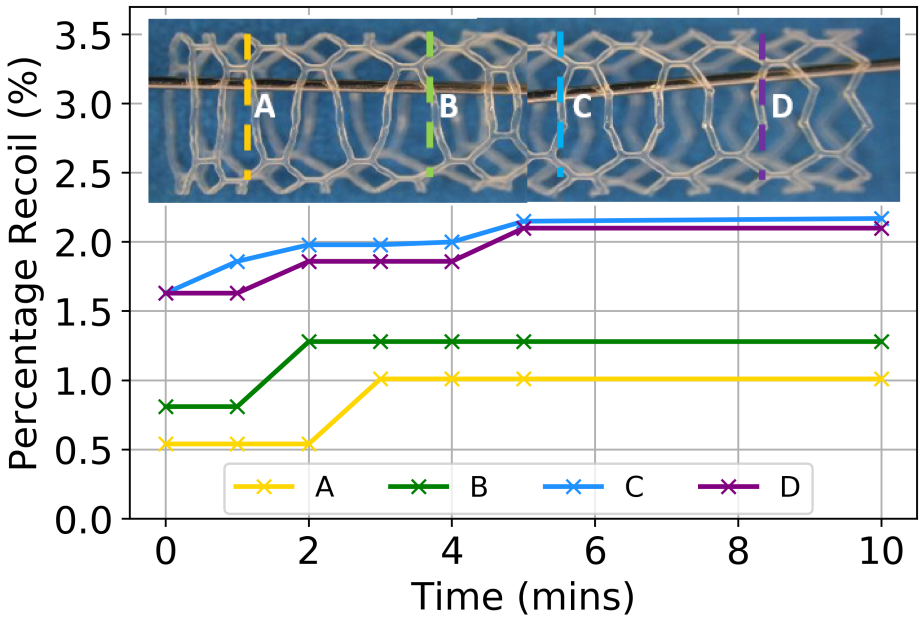

FIGURE A.6: The viscoelastic recovery of a variable ring length scaffold, measured at four locations along the scaffold length via the cumulative percentage recoil.

Observing Figure A.6, it is evident that the recoil of the scaffold due to the time dependant viscoelastic recovery stabilises in all four locations after less than 6 minutes. The magnitude of recoil due to the time dependant effects is also minimal. In each case the percentage recoil only increases by at most 0.5% over the 10 minute observation time. Therefore, in contrast to the findings of Bobel et al. (2016), the viscoelastic recovery of the PLLA appears to be negligible. It should also be remembered that the scaffold was deployed in a water bath, heated to 37 °C. According to Bobel et al. (2016) large levels of viscoelastic recovery were observed, with the sample exhibiting approximately 25% recoil post balloon expansion, when the sample was strained to 0.4. The low level of percentage recoil displayed by the scaffold manufactured from the PLLA used to construct the ArterioSorb^{TM} is an extremely promising result. In comparison to the viscoelastic recovery observed in the literature this is a significant improvement. Low levels of viscoelastic recovery will result in larger lumen areas achieved by the scaffold which will of course facilitate improved patient outcomes.

Appendix B

Explicit and Implicit Solution Methods

B.1 The Implicit Solution Method

The implicit solution method is analogous to that used in static analysis as it requires the inversion of a stiffness matrix to solve for the DOF vector. B.1 gives the equation of motion for the time step at n+1. This is then rearranged to ensure the known quantities are on the RHS of the equation and can then be written in the general form shown in B.3. Inversion of the stiffness matrix K then gives the DOF for the time step n+1.

$$[M]\{\ddot{d}\}_{n+1} + [C]\{\dot{d}\}_{n+1} + [K]\{d\}_{n+1} = \{f\}_{n+1} \tag{B.1}$$

$$[K]\{d\}_{n+1} = \{f\}_{n+1} - [M]\{\ddot{d}\}_{n+1} - [C]\{\dot{d}\}_{n+1} \tag{B.2}$$

$$[K]\{d\}_{n+1} = \{f_{eff}\}_{n+1} \tag{B.3}$$

To obtain $\{f_{eff}\}_{n+1}$ we must define the speed, $\{\dot{d}\}_{n+1}$ and acceleration $\{\ddot{d}\}_{n+1}$ in terms of known quantities. To do this the Euler formulae are utilised, shown in equations B.4 and B.5.

$$x(t) = x_0 + vt + \frac{1}{2}at^2 \tag{B.4}$$

$$v(t) = v_0 + at \tag{B.5}$$

Rewriting the Euler equations in the appropriate notation yields equations B.6 and B.7. The parameters α and β are introduced to account for acceleration that is not constant throughout the increment. These parameters weight the acceleration between the value at the current and next increments.

$$\{d\}_{n+1} = \{d\}_n + (\delta t)\{\dot{d}\}_n + \frac{1}{2}(\delta t^2)(2\alpha\{\ddot{d}\}_{n+1} + (1-2\alpha)\{\ddot{d}\}_n) \tag{B.6}$$

$$\{\dot{d}\}_{n+1} = \{\dot{d}\}_n + (\delta t)(\beta\{\ddot{d}\}_{n+1} + (1-\beta)\{\ddot{d}\}_n) \tag{B.7}$$

Rearranging B.6 for the acceleration at the next increment yields B.8. Substituting B.8 into B.7 and rearranging for the velocity at the next increment yields B.9.

$$\{\ddot{d}\}_{n+1} = \frac{1}{\alpha(\delta t)^2}\left(\{d\}_{n+1} - \{d\}_n - \delta t\{\dot{d}\}_n\right) + \left(1 - \frac{1}{2\alpha}\right)\{\ddot{d}\}_n \tag{B.8}$$

$$\{\dot{d}\}_{n+1} = \left(1 - \frac{\beta}{\alpha}\right)\{\dot{d}\}_n + \delta t\left(1 - \frac{\beta}{2\alpha}\right)\{\ddot{d}\}_n + \frac{\beta}{\alpha\delta t}(\{d\}_{n+1} - \{d\}_n) \tag{B.9}$$

Substituting B.8 and B.9 into B.1 and rearranging yields B.10. This leaves the unknown quantity $\{d\}_{n+1}$ a function of the known quantities of nodal displacements, velocities and accelerations of the current increment.

$$\begin{aligned}\left(\frac{[M]}{\alpha(\delta t)^2} + \frac{[C]\beta}{\alpha(\delta t)} + k\right)\{d\}_{n+1} &= f_{n+1} + \left(\frac{[M]}{\alpha(\delta t)^2} + \frac{[C]\beta}{\alpha(\delta t)}\right)\{d\}_n \\ - \left(\frac{[M]}{\alpha\delta t} + [C](\frac{\beta}{\alpha} - 1)\right)\{\dot{d}\}_n &+ \left([M](\frac{1}{2\alpha} - 1) + [C]\delta t(\frac{\beta}{2\alpha} - 1)\right)\{\ddot{d}\}_n\end{aligned} \tag{B.10}$$

This can be written in the form of B.3. B.6, B.7 and B.8 are utilised to calculate f_{eff} as the nodal velocities and accelerations for the current increment must be obtained using the appropriate DOF quantities from the current and prior time increment. To begin the solution procedure the initial conditions of displacement, velocity and acceleration must be known.

B.2 The Explicit Solution Method

The explicit solution method provides an alternative technique to solve a dynamic problem. Unlike the implicit method, here the stiffness matrix is stated explicitly and

so the inversion of this, often very large matrix, is not required. Rather than using Euler time integration, this technique uses the central difference method and hence displacements are initially defined in terms of the displacements at the n-1 and n+1 increments.

The equation of motion for the current time step is given by B.11. The velocity and acceleration in terms of past and future displacements are then defined using the central difference formula in B.12 and B.13. Note that B.13 defines the acceleration in terms of the velocity at half the next and previous time steps. In turn these velocities can be defined in terms of the next, current and previous time steps, shown in B.14 and B.15.

$$[M]\{\ddot{d}\}_n + [C]\{\dot{d}\}_n + [K]\{d\}_n = \{f\}_n \tag{B.11}$$

$$\{\dot{d}\}_n = \frac{1}{2\delta t}(\{d\}_{n+1} - \{d\}_{n-1}) \tag{B.12}$$

$$\{\ddot{d}\}_n = \frac{1}{\delta t}(\{\dot{d}\}_{n+\frac{1}{2}} - \{\dot{d}\}_{n-\frac{1}{2}}) \tag{B.13}$$

$$\{\dot{d}\}_{n+\frac{1}{2}} = \frac{1}{\delta t}(\{d\}_{n+1} - \{d\}_n) \tag{B.14}$$

$$\{\dot{d}\}_{n-\frac{1}{2}} = \frac{1}{\delta t}(\{d\}_n - \{d\}_{n-1}) \tag{B.15}$$

Substituting B.15 and B.14 into B.13 and then in turn substituting B.13 and B.12 into B.11 before rearranging terms and factorising leads to B.16.

$$\left(\frac{[m]}{(\delta t)^2} + \frac{[c]}{(2\delta t)}\right)\{d\}_{n+1} = \{f\}_n + \left(\frac{2[m]}{(\delta t)^2} - [k]\right)\{d\}_n - \left(\frac{[m]}{(\delta t)^2} - \frac{[c]}{(2\delta t)}\right)\{d\}_{n-1} \tag{B.16}$$

Note that for short duration events, for which the explicit solution method is often used, as the time increment reduces, the damping matrix becomes insignificant and so can be considered equal to zero. A lumped mass matrix is also used which forces [M] to become diagonal and hence no matrix inversion is required to solve for $\{d\}_{n+1}$ as it is now stated explicitly. B.17 defines a consistent mass matrix, where [N] is the shape function matrix for a given element. Computing the mass matrix and inverting it is not a trivial task and can require significant computation time. Therefore, utilising a lumped mass matrix whereby the mass is equally divided between the nodes of an element saves significant computation time. As the off-diagonal terms are now zero

the mass moment of inertia information is no longer present in the mass matrix. However, as elements become smaller the mass moment of inertia in each element becomes insignificant and so this is considered a reasonable approximation.

$$[m] = \int_V [N]^T [N] \rho dV \tag{B.17}$$

To commence time integration we require the initial condition $\{d\}_0$ as well as the DOF vector $\{d\}_{-1}$ using the Euler equation B.4.

Appendix C

Optimised Latin Hypercube

The number of instances required to populate a design space, n, and the number of design variables, k, define the design study. The design space can be sub-divided into n^k 'buckets'. The design points can then be allocated to the buckets via permutations of a k number of vectors of n terms given by:

$$\frac{1}{2n} + i\frac{1}{n} \tag{C.1}$$

where i represents the integers 0, 1, 2, ..., $n-1$. For instance, if five designs across two design variables are required then two vectors containing the terms 0.1, 0.3, 0.5, 0.7 and 0.9 are randomly permutated to give five sets of two point coordinates. These define the initial random Latin hypercube. This will guarantee uniformity of spread but not optimised space-filling. Subsequently, the maximin metric, proposed by Johnson et al. (1990), can be used to quantify the space-filling ability of a particular plan. This defines a vector $\{\zeta\}$ which contains the unique distances between all the possible pairs of points in a sampling plan. The vector $\{\eta\}$ gives the number of pairs of points separated by the distance ζ_i. The maximin plan will, according to the definition of Morris and Mitchell (1995), maximise each value of ζ_i and minimise each value of η_i among all available plans for which they are true. The distance between points can be mathematically defined as the Euclidean distance, given by:

$$\zeta_p(\mathbf{x}^{i_1}, \mathbf{x}^{i_2}) = \sqrt{\left(\sum_{j=1}^{k} |x_j^{i_1} - x_j^{i_2}|^2\right)} \tag{C.2}$$

Forrester et al. (2008) recommend the use of the definition suggested by Morris and Mitchell (1995) which combines the vectors ζ and η to evaluate the space filling properties of a sampling plan via a scalar value and aid its comparison to another plan. This is given by:

$$\Phi_q(\mathbf{X}) = \left(\sum_{i=1}^{n-1} \eta_i \, \zeta_i^{-q} \right)^{\frac{1}{q}} \tag{C.3}$$

in which a low value of Φ_q indicates a better level of space-filling. The value of q weights the effect on Φ_q of different terms in the ζ vector. Large values of q result in earlier terms in ζ dominating subsequent terms.

Lastly, an optimisation algorithm must be devised to evolve a space filling plan and then compare it with the previous plan to obtain an improved version. This can be done by mutating a plan by swapping two of its elements, which will always guarantee a Latin hypercube is obtained. This can be done iteratively until a threshold is reached whether that be a defined number of iterations based upon a computational budget or change in the value of Φ_q, at which point the optimised plan is obtained. A MATLAB implementation of this code, found in Forrester et al. (2008), was used to devise the space filling plan.

Appendix D

Surrogate Modelling

Polynomial regression models can be trained to a sparse data set to predict values of a metric that cannot be obtained via testing. Their simplicity means that the model calibration process can be relatively fast, assuming the number of design variables remains low. Otherwise the number of terms in the polynomial, and subsequent parameters to estimate, increases significantly. The general form of a polynomial model of order m containing n design variables is given by:

$$\hat{f}(\mathbf{x}) = \sum_{i=0}^{n_b} \hat{w}_i \Delta^i \tag{D.1}$$

in which Δ^i represents a vector containing all possible combinations of the n design variables contained in the vector $\mathbf{x}$, up to and including order m. n_b is the length of the vector Δ^i. To give an example, a two parameter design space in which a second order polynomial regression model is used yields:

$$\Delta^i = \{x_1, x_2, x_1 x_2, x_1^2, x_2^2\} \tag{D.2}$$

in which each term in this vector requires a different value of $\hat{w}_i$ to be estimated to obtain the polynomial model. From this example, it is clear that increasing the number of design variables or order beyond two increases the number of parameters dramatically. However, polynomial models can still be considered a subset of linear models as the design variables within the vector Δ^i can be re-labelled as new linear variables, e.g. $x_1 = z_1, ..., x_1^2 = z_5$ and hence the function becomes linear in $\{z\}$. The model parameters can then be calibrated using least-squares minimisation. This functionality affords the model good flexibility to fit the underlying data and yet can be calibrated using a simple iterative technique.

A linear polynomial regression model from the *scikit learn* library (Pedregosa et al., 2011) in Python was used to create the surface response of the PQ_{max} across the design space whilst CA and SRS used second and fifth order polynomial regression models, respectively.

A radial basis function model was used to predict the response of $R_{\%}$ as this offered an improved fit over the polynomial regression model. This type of model uses a combination of n weighted radially symmetric functions whose centres can be located anywhere in the design space. The model is summarised by:

$$\hat{f}(\mathbf{x}) = \{\hat{w}\}^T\{\psi\} = \sum_{i=0}^{n_b} \hat{w}_i \psi_i(||\mathbf{x}^{(i)} - \{c\}^{(i)}||) \tag{D.3}$$

in which $\{c\}^{(i)}$ is the i^{th} of the n_c centres of the basis functions whilst $\{\psi\}$ contains the basis functions themselves which are evaluated at the Euclidean distance between the basis function centre and the prediction site, $\mathbf{x}^{(i)}$, that is, the i^{th} term of $\mathbf{x}$, containing the sampling plan. These functions can take-on a number of different shapes. Simpler, fixed basis functions in which only one parameter must be estimated per function can be linear, $\psi(r) = r$, cubic, $\psi(r) = r^3$, or a thin plate spline $\psi(r) = r^2 lnr$. More complex parametric basis functions, such as a multiquadratic, $\psi(r) = (r^2 + z^2)^{1/2}$ can be used. In this case a further parameter, z must be estimated.

As previously stated, the basis function centres can coincide with the location of the data points. In this case D.3 can be simplified to:

$$\Psi\{\hat{w}\} = \{y\} \tag{D.4}$$

where $\{y\}$ denotes the vector of objective function values supplied by the training data and Ψ is the Gram matrix given by:

$$\Psi = \psi(||\mathbf{x}^{(i)} - \mathbf{x}^{(j)}||) \tag{D.5}$$

where $i, j = 1, 2, .., n$. This is effectively the evaluation of the radial basis functions to the Euclidean distances between each data point. Referring back to D.4, it follows that the weights, $\{\hat{w}\}$, can be estimated through a single step matrix inversion to yield:

$$\{\hat{w}\} = \Psi^{-1}\{y\} \tag{D.6}$$

which can be implemented numerically through LU decomposition. Of course, if parametric basis functions are used then estimation of their base(s) must be conducted via

an iterative process. This process should utilise further data points not considered in the estimation of the basis function weights because correctly estimated, these will guarantee the underlying data is always exactly predicted. Further information regarding radial basis functions can be found in Forrester et al. (2008). Observing D.4 it can be seen that the equation is linear in terms of the weights of the basis functions but is still able to predict non-linear responses, much like the aforementioned polynomial regression models.

References

Abbott Vascular. Absorb bioresorbable vascular scaffold system information for prescribers. https://vascular.eifu.abbott/en/hcp/home.html, 2017. Accessed: August 2020.

A Abizaid, S Kedev, RB Mohd Ali, T Santoso, A Cequier, RJM van Geuns, B Chevalier, F Hellig, R Costa, and Y Onuma. Tct-176 implantation of thin-strut sirolimus-eluting bioresorbable vascular scaffold in patients with de novo coronary artery lesions: 2-year clinical and 6-month imaging outcomes of the meres-1 extend trial. *Journal of the American College of Cardiology*, 74(13S):175, 2019.

K Al-Lamee, A Kelly, P Coates, G Thompson, and P Coton-Rose. Patent No. US 10,299,944 B2. 2019.

B Amadei. Importance of anisotropy when estimating and measuring in situ stresses in rock. *International Journal of Rock Mechanics and Mining Sciences & Geomechanics Abstracts*, 33:293–325, 1996.

HY Ang, H Bulluck, P Wong, SS Venkatraman, Y Huang, and N Foin. Bioresorbable stents: current and upcoming bioresorbable technologies. *International Journal of Cardiology*, 228:931–939, 2017.

L Antonini, F Berti, B Isella, D Hossain, L Mandelli, G Pennati, and L Petrini. From the real device to the digital twin: A coupled experimental-numerical strategy to investigate a novel bioresorbable vascular scaffold. *PLoS ONE*, 16(6), 2021a.

L Antonini, G Poletti, L Mandelli, G Dubini, G Pennati, and L Petrini. Comprehensive computational analysis of the crimping procedure of plla bvs: Effects of material viscous-plastic and temperature dependent behavior. *Journal of the Mechanical Behavior of Biomedical Materials*, 123, 2021b.

Arterius Ltd. Products. http://arterius.co.uk/products/#ArterioSorb, 2015. Accessed: December 2020.

D Barrett, M Gretton, and T Quinn. *Cardiac care an introduction for healthcare professionals*. John Wiley, 2006. ISBN 0470019832.

J Bayón, M Santás-Álvarez, R Ocaranza-Sánchez, and C González-Juanatey. Magmaris very late in-scaffold restenosis: Has the "black boxes" nightmare come back? *Catheterization and Cardiovascular Interventions*, 96(2):174–176, 2020.

PP Benham, RJ Crawford, and CG Armstrong. *Mechanics of engineering materials*. Pearson, 1996. ISBN 0582251648.

JS Bergström. *Mechanics of solid polymers: theory and computational modeling*. William Andrew, 2015. ISBN 0323322964.

JS Bergström and MC Boyce. Constitutive modeling of the large strain time-dependent behavior of elastomers. *Journal of the Mechanics and Physics of Solids*, 46(5):931–954, 1998.

JS Bergström and MC Boyce. Large strain time-dependent behavior of filled elastomers. *Mechanics of Materials*, 32(11):627–644, 2000.

JS Bergström and MC Boyce. Constitutive modeling of the time-dependent and cyclic loading of elastomers and application to soft biological tissues. *Mechanics of Materials*, 33(9):523–530, 2001.

JS Bergström and D Hayman. An overview of mechanical properties and material modeling of polylactide (pla) for medical applications. *Annals of Biomedical Engineering*, 44(2):330–340, 2016.

N Bink, VB Mohan, and S Fakirov. Recent advances in plastic stents: a comprehensive review. *International Journal of Polymeric Materials and Polymeric Biomaterials*, 70(1): 54–7, 2019.

Biotronik. Magmaris. https://www.biotronik.com/pl-pl/products/coronary/magmaris, 2019. Accessed: April 2019.

RW Blair, NJ Dunne, AB Lennon, and GH Menary. Characterisation and constitutive modelling of biaxially stretched poly (l-lactic acid) sheet for application in coronary stents. *Journal of the Mechanical Behavior of Biomedical Materials*, 97:346–354, 2019a.

RW Blair, NJ Dunne, AB Lennon, and GH Menary. Multi-objective optimisation of material properties and strut geometry for poly (l-lactic acid) coronary stents using response surface methodology. *PLoS ONE*, 14(8), 2019b.

AC Bobel and PE McHugh. Computational analysis of the utilisation of the shape memory effect and balloon expansion in fully polymeric stent deployment. *Cardiovascular Engineering and Technology*, 9(1):60–72, 2018.

AC Bobel, S Petisco, J Ramon Sarasua, W Wang, and PE McHugh. Computational bench testing to evaluate the short-term mechanical performance of a polymeric stent. *Cardiovascular Engineering and Technology*, 6(4):519–532, 2015.

AC Bobel, S Lohfeld, RN Shirazi, and PE McHugh. Experimental mechanical testing of poly (l-lactide)(plla) to facilitate pre-degradation characteristics for application in cardiovascular stenting. *Polymer Testing*, 54:150–158, 2016.

NF Boeder, M Weissner, F Blachutzik, Ullrich, R Anadol, M Tröbs, T Münzel, CW Hamm, J Dijkstra, and S Achenbach. Incidental finding of strut malapposition is a predictor of late and very late thrombosis in coronary bioresorbable scaffolds. *Journal of Clinical Medicine*, 8(5), 2019.

Boston Scientific. Rebel. http://www.bostonscientific.com/en-US/products/stents–coronary/rebel-platinum-chromium-coronary-stent-system.html, 2018. Accessed: October 2019.

MC Boyce and EM Arruda. Constitutive models of rubber elasticity: a review. *Rubber Chemistry and Technology*, 73(3):504–523, 2000.

NW Bressloff, S Pant, and K Al-Lamee. *Patent No. US 9,707,109 B2*, 2017.

British Heart Foundation. BHF Statistics Factsheet - UK. https://www.bhf.org.uk/what-we-do/our-research/heart-statistics, 2018. Accessed: March 2019.

F Burzotta, JF Lassen, Y Louvard, T Lefèvre, AP Banning, O Daremont, M Pan, D Hildick-Smith, A Chieffo, and YS Chatzizisis. European bifurcation club white paper on stenting techniques for patients with bifurcated coronary artery lesions. *Catheterization and Cardiovascular Interventions*, 96(5):1067–1079, 2020.

C Capelli, F Gervaso, L Petrini, G Dubini, and F Migliavacca. Assessment of tissue prolapse after balloon-expandable stenting: influence of stent cell geometry. *Medical Engineering & Physics*, 31(4):441–447, 2009.

Cardiac Institute of the Palm Beaches. Coronary angioplasty and stent placement, 2015. URL `https://www.thecardiacinstitute.com/cardiac-diagnostic-services-north-palm-beach/coronary-angioplasty-palm-beach-gardens/`. Accessed: March 2019.

CG Caro, TJ Pedley, RC Schroter, and WA Seed. *The mechanics of the circulation*. Cambridge University Press, 2012. ISBN 0521151775.

M De Beule, P Mortier, SG Carlier, B Verhegghe, R Van Impe, and P Verdonck. Realistic finite element-based stent design: the impact of balloon folding. *Journal of Biomechanics*, 41(2):383–389, 2008.

N Debusschere, P Segers, P Dubruel, B Verhegghe, and M De Beule. A finite element strategy to investigate the free expansion behaviour of a biodegradable polymeric stent. *Journal of Biomechanics*, 48(10):2012–2018, 2015.

V Dehlaghi, MT Shadpoor, and S Najarian. Analysis of wall shear stress in stented coronary artery using 3d computational fluid dynamics modeling. *Journal of Materials Processing Technology*, 197(1-3):174–181, 2008.

Diagnostic and Interventional Cardiology. Resolute onyx 2.0 mm stent performs well in small vessels. https://www.dicardiology.com/content/resolute-onyx-20-mm-stent-performs-well-small-vessels, 2017. Accessed: August 2021.

DS SIMULIA. Abaqus 6.21 analysis user's manual, 2018.

ER Edelman and C Rogers. Pathobiologic responses to stenting. *The American Journal of Cardiology*, 81(7):4–6, 1998.

SK Eswaran, JA Kelley, JS Bergström, and VL Giddings. Material modeling of polylactide. *SIMULIA Customer Conference*, 2011.

F Etave, G Finet, M Boivin, J Boyer, G Rioufol, and G Thollet. Mechanical properties of coronary stents determined by using finite element analysis. *Journal of Biomechanics*, 34(8):1065–1075, 2001.

S Farah, DG Anderson, and R Langer. Physical and mechanical properties of pla, and their functions in widespread applications—a comprehensive review. *Advanced Drug Delivery Reviews*, 107:367–392, 2016.

A Farb, G Sangiorgi, AJ Carter, VM Walley, WD Edwards, RS Schwartz, and R Virmani. Pathology of acute and chronic coronary stenting in humans. *Circulation*, 99(1):44–52, 1999.

N Filipovic, D Nikolic, V Isailovic, M Milosevic, V Geroski, G Karanasiou, M Fawdry, A Flanagan, D Fotiadis, and M Kojic. In vitro and in silico testing of partially and fully bioresorbable vascular scaffold. *Journal of Biomechanics*, 115, 2021.

N Foin, RD Lee, R Torii, JL Guitierrez-Chico, A Mattesini, S Nijjer, S Sen, R Petraco, JE Davies, and C Di Mario. Impact of stent strut design in metallic stents and biodegradable scaffolds. *International Journal of Cardiology*, 177(3):800–808, 2014. ISSN 0167-5273.

N Foin, R Lee, C Bourantas, A Mattesini, N Soh, JE Lim, R Torii, J Ng, LH Liang, and G Caiazzo. Bioresorbable vascular scaffold radial expansion and conformation compared to a metallic platform: insights from in vitro expansion in a coronary artery lesion model. *EuroIntervention*, 12(7):834–844, 2016a.

N Foin, R Lee, A Mattesini, G Caiazzo, E Fabris, ID Kilic, JN Chan, Y Huang, SS Venkatraman, and C Di Mario. Bioabsorbable vascular scaffold overexpansion: insights from in vitro post-expansion experiments. *EuroIntervention*, 11(12): 1389–1399, 2016b.

A Forrester, A Sobester, and A Keane. *Engineering design via surrogate modelling: a practical guide*. John Wiley & Sons, 2008. ISBN 0470770791.

F Gervaso, C Capelli, L Petrini, S Lattanzio, L Di Virgilio, and F Migliavacca. On the effects of different strategies in modelling balloon-expandable stenting by means of finite element method. *Journal of Biomechanics*, 41(6):1206–1212, 2008.

BD Gogas, B Yang, T Passerini, A Veneziani, M Piccinelli, G Esposito, E Rasoul-Arzrumly, M Awad, G Mekonnen, and OY Hung. Computational fluid dynamics applied to virtually deployed drug-eluting coronary bioresorbable scaffolds: Clinical translations derived from a proof-of-concept. *Global Cardiology Science and Practice*, 2014(4):56, 2015.

ED Grech. *ABC of interventional cardiology*. Wiley-Blackwell/BMJ Books, 2011. ISBN 9781118294024.

JA Grogan, SB Leen, and PE McHugh. Comparing coronary stent material performance on a common geometric platform through simulated bench testing. *Journal of the Mechanical Behavior of Biomedical Materials*, 12:129–138, 2012.

A Halkin and GW Stone. Polymer-based paclitaxel-eluting stents in percutaneous coronary intervention: A review of the taxus trials. *Journal of Interventional Cardiology*, 17(5):271–282, 2004.

JE Hall. *Guyton and Hall textbook of medical physiology e-Book*. Elsevier Health Sciences, 2010. ISBN 1437726747.

H Hamid and J Coltart. 'miracle stents'–a future without restenosis. *McGill Journal of Medicine*, 10(2):105–111, 2007.

RM Hicks and PA Henne. Wing design by numerical optimization. *Journal of Aircraft*, 15(7):407–412, 1978.

R Hill. A theory of the yielding and plastic flow of anisotropic metals. *Proceedings of the Royal Society of London. Series A. Mathematical and Physical Sciences*, 193(1033): 281–297, 1948.

B Hoddy, N Ahmed, K Al-Lamee, N Bullett, N Curzen, and NW Bressloff. Investigating the material modelling of a polymeric bioresorbable scaffold via in-silico and in-vitro testing. *Journal of the Mechanical Behavior of Biomedical Materials*, 120, 2021a.

B Hoddy, N Ahmed, K Al-Lamee, N Bullett, N Curzen, and NW Bressloff. Computational modelling of brs deployment into a patient-specific lm bifurcation. *EuroPCR Abstract Book*, 2021b. URL: https://eposter.europa-organisation.com/2021/europcr/.

B Hoddy, N Ahmed, K Al-Lamee, N Bullett, and NW Bressloff. Exploring a parallel rheological framework to capture the mechanical behaviour of a thin-strut polymeric bioresorbable coronary scaffold. *Journal of the Mechanical Behavior of Biomedical Materials*, 130, 2022a.

B Hoddy, N Ahmed, K Al-Lamee, N Bullett, N Curzen, and NW Bressloff. Investigating the equivalent plastic strain in a variable ring length and strut width thin-strut bioresorbable scaffold. *Cardiovascular Engineering and Technology*, pages 1–16, 2022b. ISSN 1869-4098.

R Hoffmann, GS Mintz, R Mehran, KM Kent, AD Pichard, LF Satler, and MB Leon. Tissue proliferation within and surrounding palmaz-schatz stents is dependent on the aggressiveness of stent implantation technique. *The American Journal of Cardiology*, 83(8):1170–1174, 1999.

GA Holzapfel, G Sommer, CT Gasser, and P Regitnig. Determination of layer-specific mechanical properties of human coronary arteries with nonatherosclerotic intimal thickening and related constitutive modeling. *American Journal of Physiology-Heart and Circulatory Physiology*, 289(5):2048–2058, 2005.

R Jedynak. Approximation of the inverse langevin function revisited. *Rheologica Acta*, 54(1):29–39, 2015.

ME Johnson, LM Moore, and D Ylvisaker. Minimax and maximin distance designs. *Journal of Statistical Planning and Inference*, 26(2):131–148, 1990.

JK Kahn, BD Rutherford, DR McConahay, WL Johnson, LV Giorgi, and GO Hartzler. Short-and long-term outcome of percutaneous transluminal coronary angioplasty in chronic dialysis patients. *American Heart Journal*, 119(3):484–489, 1990.

Y Katagiri, R Torii, K Takahashi, E Tenekecioglu, T Asano, P Chichareon, M Tomaniak, JJ Piek, JJ Wykrzykowska, and N Bullett. Preclinical evaluation of a thin-strut bioresorbable scaffold (arteriosorb): acute-phase invasive imaging assessment and hemodynamic implication. *Eurointervention*, 16(2):141–146, 2019.

DJ Kereiakes, Y Onuma, PW Serruys, and GW Stone. Bioresorbable vascular scaffolds for coronary revascularization. *Circulation*, 134(2):168–182, 2016.

DJ Kereiakes, SG Ellis, DC Metzger, RP Caputo, DG Rizik, PS Teirstein, MR Litt, A Kini, A Kabour, and SO Marx. Clinical outcomes before and after complete everolimus-eluting bioresorbable scaffold resorption: five-year follow-up from the absorb iii trial. *Circulation*, 140(23):1895–1903, 2019.

L Koltowski, M Tomaniak, D Ochijewicz, J Maksym, T Roleder, M Zaleska, K Proniewska, G Opolski, and J Kochman. Second generation, sirolimus-eluting, bioresorbable tyrocore scaffold implantation in patients with st-segment elevation

myocardial infarction: Baseline oct and 30-day clinical outcomes–a fantom stemi pilot study. *Catheterization and Cardiovascular Interventions*, 96(1):1–7, 2020.

A König, TM Schiele, J Rieber, K Theisen, H Mudra, and V Klauss. Influence of stent design and deployment technique on neointima formation and vascular remodeling. *Zeitschrift für Kardiologie*, 91(3):98–102, 2002.

JF LaDisa, I Guler, LE Olson, DA Hettrick, JR Kersten, DC Warltier, and PS Pagel. Three-dimensional computational fluid dynamics modeling of alterations in coronary wall shear stress produced by stent implantation. *Annals of Biomedical Engineering*, 31(8):972–980, 2003.

C Lally, FL Dolan, and PJ Prendergast. Cardiovascular stent design and vessel stresses: a finite element analysis. *Journal of Biomechanics*, 38(8):1574–1581, 2005.

GN Levine, AP Chodos, and J Loscalzo. Restenosis following coronary angioplasty: clinical presentations and therapeutic options. *Clinical Cardiology*, 18(12):693–703, 1995.

J Li, F Zheng, X Qiu, P Wan, L Tan, and K Yang. Finite element analyses for optimization design of biodegradable magnesium alloy stent. *Materials Science and Engineering: C*, 42:705–714, 2014.

M Liu and DG Gorman. Formulation of rayleigh damping and its extensions. *Computers Structures*, 57(2):277–285, 1995.

Q Luo, X Liu, Z Li, C Huang, W Zhang, J Meng, Z Chang, and Z Hua. Degradation model of bioabsorbable cardiovascular stents. *PloS ONE*, 9(11), 2014.

G Mani, MD Feldman, D Patel, and CM Agrawal. Coronary stents: a materials perspective. *Biomaterials*, 28(9):1689–1710, 2007.

Medgadget. Abbott's bioresorbable stent continues to prove itself in trials. https://www.medgadget.com, 2010. Accessed: April 2019.

F Migliavacca, L Petrini, M Colombo, F Auricchio, and R Pietrabissa. Mechanical behavior of coronary stents investigated through the finite element method. *Journal of Biomechanics*, 35(6):803–811, 2002.

F Migliavacca, L Petrini, V Montanari, I Quagliana, F Auricchio, and G Dubini. A predictive study of the mechanical behaviour of coronary stents by computer modelling. *Medical Engineering and Physics*, 27(1):13–18, 2005.

P Mincarone, A Bodini, S Sabina, R Colella, MR Tumolo, Fawdry, DI Fotiadis, and CG Leo. Simulated versus physical bench tests: The economic evaluation of the insilc platform for designing, developing, and assessing vascular scaffolds. *Medicine*, 100(25), 2021.

K Modi and SS Bhimji. *Stent thrombosis*. StatPearls Publishing, 2017.

MD Morris and TJ Mitchell. Exploratory designs for computational experiments. *Journal of Statistical Planning and Inference*, 43(3):381–402, 1995.

P Mortier, M De Beule, D Van Loo, B Verhegghe, and P Verdonck. Finite element analysis of side branch access during bifurcation stenting. *Medical Engineering & Physics*, 31(4):434–440, 2009.

P Mortier, GA Holzapfel, M De Beule, D Van Loo, Y Taeymans, P Segers, P Verdonck, and B Verhegghe. A novel simulation strategy for stent insertion and deployment in curved coronary bifurcations: comparison of three drug-eluting stents. *Annals of Biomedical Engineering*, 38(1):88–99, 2010.

H Nef, J Wiebe, N Boeder, O Dörr, T Bauer, K Hauptmann, A Latib, A Colombo, DieDter Fischer, and T Rudolph. A multicenter post-marketing evaluation of the elixir desolve® novolimus-eluting bioresorbable coronary scaffold system: First results from the desolve pmcf study. *Catheterization and Cardiovascular Interventions*, 92(6):1021–1027, 2018.

Y Onuma, PW Serruys, JA Ormiston, E Regar, M Webster, L Thuesen, D Dudek, S Veldhof, and R Rapoza. Three-year results of clinical follow-up after a bioresorbable everolimus-eluting scaffold in patients with de novo coronary artery disease: the absorb trial. *EuroIntervention*, 6(4):447–453, 2010.

JA Ormiston, PW Serruys, E Regar, D Dudek, L Thuesen, MWI Webster, Y Onuma, HM Garcia-Garcia, R McGreevy, and S Veldhof. A bioabsorbable everolimus-eluting coronary stent system for patients with single de-novo coronary artery lesions (absorb): a prospective open-label trial. *The Lancet*, 371(9616):899–907, 2008.

S Pant, G Limbert, N Curzen, and NW Bressloff. Multiobjective design optimisation of coronary stents. *Biomaterials*, 32(31):7755–73, 2011.

S Pant, NW Bressloff, and G Limbert. Geometry parameterization and multidisciplinary constrained optimization of coronary stents. *Biomechanics and Modeling in Mechanobiology*, 11(1-2):61–82, 2012. ISSN 1617-7959.

RG Pauck and BD Reddy. Computational analysis of the radial mechanical performance of plla coronary artery stents. *Medical Engineering and Physics*, 37(1): 7–12, 2015. ISSN 1350-4533.

F Pedregosa, G Varoquaux, A Gramfort, V Michel, B Thirion, O Grisel, M Blondel, P Prettenhofer, R Weiss, V Dubourg, J Vanderplas, A Passos, D Cournapeau, M Brucher, M Perrot, and E Duchesnay. Scikit-learn: Machine learning in Python. *Journal of Machine Learning Research*, 12:2825–2830, 2011.

PolymerFEM. Abaqus parallel rheological framework (prf), 2021. URL https://polymerfem.com/abaqus-parallel-rheological-framework-prf/.

PR Newswire. Abbott receives ce mark approval for world's first drug eluting bioresorbable vascular scaffold for treatment of coronary artery disease. https://www.prnewswire.com/news-releases/abbott-receives-ce-mark-approval-for-worlds-first-drug-eluting-bioresorbable-vascular-scaffold-for-treatment-of-coronary-artery-disease-113197364.html, 2011. Accessed: October 2020.

TY Qiu, M Song, and LG Zhao. A computational study of crimping and expansion of bioresorbable polymeric stents. *Mechanics of Time-Dependent Materials*, 22:273–290, 2017.

MD Radu, Y Onuma, RJ Rapoza, R Diletti, and PW Serruys. In vivo visualisation by three-dimensional optical coherence tomography of stress crazing of a bioresorbable vascular scaffold implanted for treatment of human coronary stenosis. *EuroIntervention*, 7(12):1461–1463, 2012.

GE Ragkousis. *Coronary artery stent design for challenging disease: insights into patient specific modelling*. Thesis, 2016.

C Rapetto and M Leoncini. Magmaris: A new generation metallic sirolimus-eluting fully bioresorbable scaffold: Present status and future perspectives. *Journal of Thoracic Disease*, 9(9):903, 2017.

P Ruygrok. Intracoronary stenting: From concept to custom. *The Asia Pacific Heart Journal*, 6(1):69–70, 1997.

MH Sadd. *Continuum Mechanics Modeling of Material Behavior*. Academic Press, 2018. ISBN 0128116498.

A Sakamoto, H Jinnouchi, S Torii, R Virmani, and A Finn. Understanding the impact of stent and scaffold material and strut design on coronary artery thrombosis from the basic and clinical points of view. *Bioengineering*, 5(3):71, 2018.

A Schiavone, C Abunassar, S Hossainy, and LG Zhao. Computational analysis of mechanical stress–strain interaction of a bioresorbable scaffold with blood vessel. *Journal of Biomechanics*, 49(13):2677–2683, 2016.

PW Serruys, B Chevalier, Y Sotomi, A Cequier, D Carrié, JJ Piek, AJ Van Boven, M Dominici, D Dudek, and D McClean. Comparison of an everolimus-eluting bioresorbable scaffold with an everolimus-eluting metallic stent for the treatment of coronary artery stenosis (absorb ii): a 3 year, randomised, controlled, single-blind, multicentre clinical trial. *The Lancet*, 388(10059):2479–2491, 2016.

T Simard, B Hibbert, DF Ramirez, M Froeschl, Y Chen, and ER O'Brien. The evolution of coronary stents: a brief review. *Canadian Journal of Cardiology*, 30(1):35–45, 2014.

JS Soares, JE Moore, and KR Rajagopal. Modeling of deformation-accelerated breakdown of polylactic acid biodegradable stents. *Journal of Medical Devices*, 4(4), 2010.

L Song, B Xu, Y Chen, Y Zhou, S Jia, Z Zhong, X Su, Y Ma, Q Zhang, and J Liu. Thinner-strut sirolimus-eluting bioresorbable scaffolds versus everolimus-eluting stents in patients with coronary artery disease: Future-ii trial. *JACC: Cardiovascular Interventions*, 14(13):1450–1462, 2021.

J Sweeney, P Spencer, K Nair, and P Coates. Modelling the mechanical and strain recovery behaviour of partially crystalline pla. *Polymers*, 11(8):1342, 2019.

T Tada, RA Byrne, I Simunovic, LA King, S Cassese, M Joner, M Fusaro, S Schneider, S Schulz, and T Ibrahim. Risk of stent thrombosis among bare-metal stents, first-generation drug-eluting stents, and second-generation drug-eluting stents: results from a registry of 18,334 patients. *JACC: Cardiovascular Interventions*, 6(12): 1267–1274, 2013.

H Tamai, K Igaki, E Kyo, K Kosuga, A Kawashima, S Matsui, H Komori, T Tsuji, S Motohara, and H Uehata. Initial and 6-month results of biodegradable poly-l-lactic acid coronary stents in humans. *Circulation*, 102(4):399–404, 2000.

HC Tan and R Ananthakrishna. A review of bioresorbable scaffolds: hype or hope? *Singapore Medical Journal*, 58(9):512, 2017.

I Tarrahi, M Colombo, EMJ Hartman, T Forero, R Torii, C Chiastra, J Daemen, and FJH Gijsen. Impact of bioresorbable scaffold design characteristics on local hemodynamic forces-an ex vivo assessment with computational fluid dynamics simulations. *EuroIntervention*, 16(11):930–937, 2020.

NP Taylor. Reva files for bankruptcy after bioresorbable scaffold flops. https://www.medtechdive.com/news/reva-files-for-bankruptcy-after-bioresorbable-scaffold-flops/570563/, 2020. Accessed: November 2020.

MA ul Haq, M Erickson, J Rankin, and A Whelan. Late strut fracture within a partially resorbed bioresorbable vascular scaffold: a possible cause of late scaffold thrombosis and acute coronary syndrome. *Heart, Lung and Circulation*, 26(4):e26–e28, 2017.

P Wang, FR Nezami, MB Gorji, F Berti, L Petrini, T Wierzbicki, F Migliavacca, and ER Edelman. Effect of working environment and procedural strategies on mechanical performance of bioresorbable vascular scaffolds. *Acta Biomaterialia*, 82: 34–43, 2018.

P Wang, F Berti, L Antonini, FR Nezami, L Petrini, F Migliavacca, and ER Edelman. Multimodal loading environment predicts bioresorbable vascular scaffolds' durability. *Annals of Biomedical Engineering*, 49:1298–1307, 2020.

Q Wang, G Fang, Y Zhao, G Wang, and T Cai. Computational and experimental investigation into mechanical performances of poly-l-lactide acid (plla) coronary stents. *Journal of the Mechanical Behavior of Biomedical Materials*, 65:415–427, 2017.

W Wang, D Liang, D Yang, and M Qi. Analysis of the transient expansion behavior and design optimization of coronary stents by finite element method. *Journal of Biomechanics*, 39(1):21–32, 2006.

L Wei, Q Chen, and Z Li. Influences of plaque eccentricity and composition on the stent–plaque–artery interaction during stent implantation. *Biomechanics and Modeling in Mechanobiology*, 18(1):45–56, 2019.

JJ Wentzel, FJH Gijsen, N Stergiopulos, PW Serruys, CJ Slager, and R Krams. Shear stress, vascular remodeling and neointimal formation. *Journal of Biomechanics*, 36(5): 681–688, 2003.

C Wiltz. Polymer vs. metal: The battle of bioresorbable stents. https://www.mddionline.com/polymer-vs-metal-battle-bioresorbable-stents, 2013. Accessed: April 2019.

HC Wong, KN Cho, and WC Tang. Bending of a stented atherosclerotic artery. *Comsol Conference, Boston*, 2009.

J Zheng, H Qiu, Y Tian, X Hu, T Luo, C Wu, Y Tian, Y Tang, L Song, and L Li. Preclinical evaluation of a novel sirolimus-eluting iron bioresorbable coronary scaffold in porcine coronary artery at 6 months. *JACC: Cardiovascular Interventions*, 12(3):245–255, 2019.

FF Zhou, YH Liu, PC Ge, ZH Chen, XQ Ding, JY Liu, QW Jia, FH An, LH Li, and LS Wang. Coronary artery diameter is inversely associated with the severity of coronary lesions in patients undergoing coronary angiography. *Cellular Physiology and Biochemistry*, 43(3):1247–1257, 2017.

OC Zienkiewicz, RL Taylor, and JZ Zhu. *The finite element method: its basis and fundamentals*. Elsevier, 2005. ISBN 008047277X.

P Zunino, C D'Angelo, L Petrini, C Vergara, C Capelli, and F Migliavacca. Numerical simulation of drug eluting coronary stents: mechanics, fluid dynamics and drug release. *Computer Methods in Applied Mechanics and Engineering*, 198(45-46): 3633–3644, 2009.